N d'ordre NNT : 2023ISAL0014

THESE de DOCTORAT DE L'INSA LYON,
membre de l'Université de Lyon

Ecole Doctorale 160
Électronique, Électrotechnique et Automatique

Spécialité/ discipline de doctorat :
Électronique, micro et nano-électronique, optique et laser

Soutenue publiquement le 15/03/2023, par :
Alestair Wilson

Développement de couches minces de Germanium et Silicium-Germanium microcristallin pour les détecteurs d'image above-IC en proche infrarouge

---

Devant le jury composé de :

Mme. Françoise MASSINES	Directrice de Recherche , PROMES, UPVD	Présidente
M. Père ROCA i CABARROCAS	Professeur, LPICM, Polytechnique	Rapporteur
M. Lars ZIMMERMANN	Professeur, IHP, TU Berlin	Rapporteur
M. Erwann FOURMOND	Maître de Conférence, INL, INSA Lyon	Directeur de thèse
M. Bilel SAIDI	Chef de projet Imageurs, STMicroelectronics	Co-encadrant
M. Mickaël GROS-JEAN	Chef de projet R&D, STMicroelectronics	Co-encadrant

Cette thèse est accessible à l'adresse : https://theses.insa-lyon.fr/publication/2023ISAL0014/these.pdf
© [A. Wilson], [2023], INSA Lyon, tous droits réservés

Département FEDORA – INSA Lyon - Ecoles Doctorales

SIGLE	ECOLE DOCTORALE	NOM ET COORDONNEES DU RESPONSABLE
CHIMIE	**CHIMIE DE LYON** **https://www.edchimie-lyon.fr** Sec. : Renée EL MELHEM Bât. Blaise PASCAL, 3e étage secretariat@edchimie-lyon.fr	**M. Stéphane DANIELE** C2P2-CPE LYON-UMR 5265 Bâtiment F308, BP 2077 43 Boulevard du 11 novembre 1918 69616 Villeurbanne **directeur@edchimie-lyon.fr**
E.E.A.	**ÉLECTRONIQUE, ÉLECTROTECHNIQUE, AUTOMATIQUE** **https://edeea.universite-lyon.fr** Sec. : Stéphanie CAUVIN Bâtiment Direction INSA Lyon Tél : 04.72.43.71.70 secretariat.edeea@insa-lyon.fr	**M. Philippe DELACHARTRE** INSA LYON Laboratoire CREATIS Bâtiment Blaise Pascal, 7 avenue Jean Capelle 69621 Villeurbanne CEDEX Tél : 04.72.43.88.63 **philippe.delachartre@insa-lyon.fr**
E2M2	**ÉVOLUTION, ÉCOSYSTÈME, MICROBIOLOGIE, MODÉLISATION** **http://e2m2.universite-lyon.fr** Sec. : Bénédicte LANZA Bât. Atrium, UCB Lyon 1 Tél : 04.72.44.83.62 secretariat.e2m2@univ-lyon1.fr	**Mme Sandrine CHARLES** Université Claude Bernard Lyon 1 UFR Biosciences Bâtiment Mendel 43, boulevard du 11 Novembre 1918 69622 Villeurbanne CEDEX **sandrine.charles@univ-lyon1.fr**
EDISS	**INTERDISCIPLINAIRE SCIENCES-SANTÉ** **http://ediss.universite-lyon.fr** Sec. : Bénédicte LANZA Bât. Atrium, UCB Lyon 1 Tél : 04.72.44.83.62 secretariat.ediss@univ-lyon1.fr	**Mme Sylvie RICARD-BLUM** Institut de Chimie et Biochimie Moléculaires et Supramoléculaires (ICBMS) - UMR 5246 CNRS - Université Lyon 1 Bâtiment Raulin - 2ème étage Nord 43 Boulevard du 11 novembre 1918 69622 Villeurbanne Cedex Tél : +33(0)4 72 44 82 32 **sylvie.ricard-blum@univ-lyon1.fr**
INFOMATHS	**INFORMATIQUE ET MATHÉMATIQUES** **http://edinfomaths.universite-lyon.fr** Sec. : Renée EL MELHEM Bât. Blaise PASCAL, 3e étage Tél : 04.72.43.80.46 infomaths@univ-lyon1.fr	**M. Hamamache KHEDDOUCI** Université Claude Bernard Lyon 1 Bât. Nautibus 43, Boulevard du 11 novembre 1918 69 622 Villeurbanne Cedex France Tél : 04.72.44.83.69 **hamamache.kheddouci@univ-lyon1.fr**
Matériaux	**MATÉRIAUX DE LYON** **http://ed34.universite-lyon.fr** Sec. : Yann DE ORDENANA Tél : 04.72.18.62.44 yann.de-ordenana@ec-lyon.fr	**M. Stéphane BENAYOUN** Ecole Centrale de Lyon Laboratoire LTDS 36 avenue Guy de Collongue 69134 Ecully CEDEX Tél : 04.72.18.64.37 **stephane.benayoun@ec-lyon.fr**
MEGA	**MÉCANIQUE, ÉNERGÉTIQUE, GÉNIE CIVIL, ACOUSTIQUE** **http://edmega.universite-lyon.fr** Sec. : Stéphanie CAUVIN Tél : 04.72.43.71.70 Bâtiment Direction INSA Lyon mega@insa-lyon.fr	**M. Jocelyn BONJOUR** INSA Lyon Laboratoire CETHIL Bâtiment Sadi-Carnot 9, rue de la Physique 69621 Villeurbanne CEDEX **jocelyn.bonjour@insa-lyon.fr**
ScSo	**ScSo*** **https://edsciencessociales.universite-lyon.fr** Sec. : Mélina FAVETON INSA : J.Y. TOUSSAINT Tél : 04.78.69.77.79 melina.faveton@univ-lyon2.fr	**M. Bruno MILLY** Université Lumière Lyon 2 86 Rue Pasteur 69365 Lyon CEDEX 07 **bruno.milly@univ-lyon2.fr**

*ScSo : Histoire, Géographie, Aménagement, Urbanisme, Archéologie, Science politique, Sociologie, Anthropologie

Cette thèse est accessible à l'adresse : https://theses.insa-lyon.fr/publication/2023ISAL0014/these.pdf
© [A. Wilson], [2023], INSA Lyon, tous droits réservés

Thèse réalisée conjointement à Institut des Nanotechnologies de Lyon
INSA Lyon
1, rue Enrico Fermi
69100 Villeurbanne, France

Tél : +33 (0)4 72 43 83 29
Web : https://inl.cnrs.fr/

et à STMicroelectronics
850 Rue Jean Monnet
38920 Crolles, France

Tél : +33 (0)4 76 92 60 00
Web : https://www.st.com/

Sous la direction de Erwann Fourmond erwann.fourmond@insa-lyon.fr

Co-encadrement Bilel Saidi saidibilel@yahoo.fr
Mickaël Gros-Jean mickael.gros-jean@st.com

Financement CIFRE ANRT N° 2019/1645

Cette thèse est accessible à l'adresse : https://theses.insa-lyon.fr/publication/2023ISAL0014/these.pdf
© [A. Wilson], [2023], INSA Lyon, tous droits réservés

Cette thèse est accessible à l'adresse : https://theses.insa-lyon.fr/publication/2023ISAL0014/these.pdf
© [A. Wilson], [2023], INSA Lyon, tous droits réservés

Résumé de thèse en français : Développement de couches minces de Germanium et Silicium-Germanium microcristallin pour les détecteurs d'image above-IC en proche infrarouge

Cette thèse est accessible à l'adresse : https://theses.insa-lyon.fr/publication/2023ISAL0014/these.pdf
© [A. Wilson], [2023], INSA Lyon, tous droits réservés

Cette thèse est accessible à l'adresse : https://theses.insa-lyon.fr/publication/2023ISAL0014/these.pdf
© [A. Wilson], [2023], INSA Lyon, tous droits réservés

Résumé

Le marché croissant de l'internet des objets (IoT) encourage le développement de nouveaux capteurs fiables et à faible coût. Les imageurs CMOS ne font pas exception. L'industrie automobile et téléphonique en particulier sont friands d'imageurs pour le proche infrarouge pour observer leur environnement. Leur coût peut être réduit en s'appuyant sur une approche above-IC de l'intégration CMOS dans laquelle les photodiodes du capteurs sont produites après les transistors et les interconnexions. Les procédés above-IC sont donc intrinsèquement limités en budget thermique en raison de la structure CMOS sous-jacente à la photodiode.

Dans ce contexte, l'objectif de ce travail est de produire et de caractériser des couches minces de silicium-germanium et de germanium hydrogénés déposés à basse température ($<$ 350 °C) pour imageurs above-IC sensibles dans le proche infrarouge. Une preuve de concept de l'utilisation de ces matériaux pour la détection en proche IR est donnée avec le développement et la caractérisation d'une photodiode. Compte tenu des limitations thermiques, le dépôt chimique en phase vapeur assisté par plasma (PECVD) sera utilisé pour développer des semi-conducteurs amorphes et microcristallins allant du silicium (µc-Si :H) aux alliages de silicium-germanium microcristallin (µc-$Si_{1-x}Ge_x$:H). L'incorporation de germanium est bénéfique pour l'absorption du NIR de la couche mince obtenue en raison de son faible gap par rapport au silicium.

Pour atteindre les objectifs fixés, des couches minces intrinsèques de µc-Ge :H et µc-SiGe :H sont obtenus par PECVD pour être utilisées en tant qu'absorbeur dans de futurs dispositifs. L'étude de ses matériaux se focalise sur l'impact des conditions de dépôt sur les propriétés structurelles, électriques et optiques des couches. La fabrication d'une photodiode nécessitant la réalisation d'une jonction P-I-N, le dopage de type p et de type n de couches microcristallines au phosphore et au bore est donc étudié. En s'appuyant sur ces briques individuelles, une photodiode est conçue pour tester expérimentalement l'efficacité des matériaux développés dans un dispositif réel. Ce prototype de photodiode permet de trouver la composition et l'épaisseur optimale pour l'absorbeur et mais permet également comprendre les mécanismes à l'origine des pertes dans les dispositifs.

Mots clés : microcristallin, silicium-germanium, above-IC, PECVD, photodiode, NIR

Cette thèse est accessible à l'adresse : https://theses.insa-lyon.fr/publication/2023ISAL0014/these.pdf
© [A. Wilson], [2023], INSA Lyon, tous droits réservés

Cette thèse est accessible à l'adresse : https://theses.insa-lyon.fr/publication/2023ISAL0014/these.pdf
© [A. Wilson], [2023], INSA Lyon, tous droits réservés

Introduction

Context Général

La croissance du marché de l'internet des objets (IoT) et les besoins croissants des industries de l'automobile et de la téléphonie mobile poussent au développement de capteurs fiables et peu coûteux. Qu'ils mesurent la température, les indicateurs de santé ou capturent les sons environnants, ces capteurs répondent au besoin d'interaction des objets hautement interconnectés avec leur environnement. Parmi ces capteurs, les capteurs d'image CMOS sont un type de capteur largement utilisé dans les téléphones mobiles et les appareils photo pour obtenir une image numérique.

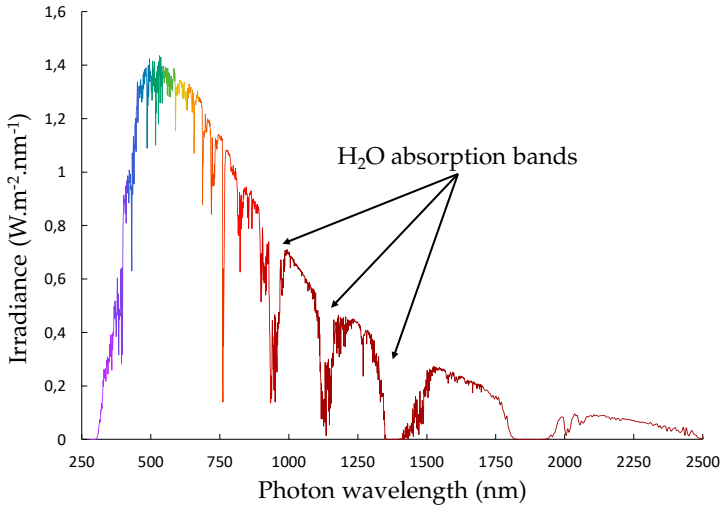

FIGURE 1 – Irradiance solaire au niveau du sol lorsque le soleil a un angle zénithal de 48,2° (AM1.5g). Le spectre solaire ressemble à un corps noir de 5250 °C, avec des bandes d'absorption dues à l'atmosphère. En particulier, la vapeur d'eau dans l'atmosphère est responsable de 3 creux dans l'irradiance à 940, 1130 et 1350 nm.

Le matériau utilisé pour la fabrication de la partie photosensible du capteur dépend nécessairement de la gamme spectrale visée. La région optiquement active de la plupart des capteurs d'images CMOS est constituée de silicium cristallin. Alors que le c-Si est parfaitement adapté à l'absorption de la lumière visible (λ = 400 - 800 nm), son absorption dans la région du proche infrarouge (NIR) (λ = 800 - 2500 nm) chute rapidement en raison de sa bande interdite de 1,12 eV. Dans cette thèse de doctorat, nous visons à développer des semi-conducteurs sensibles

Cette thèse est accessible à l'adresse : https://theses.insa-lyon.fr/publication/2023ISAL0014/these.pdf
© [A. Wilson], [2023], INSA Lyon, tous droits réservés

au NIR, adaptés aux capteurs d'images CMOS. Nous nous concentrerons en particulier sur un domaine spectral restreint entre 900 et 1350 nm. Cette plage spectrale présente un intérêt particulier en raison du spectre d'irradiation du soleil au niveau du sol, illustré par la figure 1.

Dans ce spectre, 3 chutes majeures d'irradiance apparaissent à $\lambda = 940$, 1130 et 1350 nm en raison de l'absorption par la vapeur d'eau dans l'atmosphère. Pour les applications de reconnaissance faciale par exemple, le visage est éclairé par une LED NIR invisible à l'œil humain. La lumière réfléchie qui atteint le capteur CMOS forme alors une image qui est traitée par le dispositif. En travaillant à des longueurs d'onde de 940, 1130 ou 1350 nm, le bruit environnemental dû à la lumière du soleil est minimal, ce qui permet d'obtenir un meilleur rapport signal/bruit même dans des conditions d'éclairage difficiles.

Le capteur d'images CMOS lui-même est le composant sur lequel nous allons nous concentrer. Il peut être divisé en trois types principaux en fonction de son architecture : les capteurs éclairés par la face avant, la face arrière et les capteurs éclairés par un circuit intégré supérieur (above-IC). Une représentation schématique de ces différentes architectures de capteurs est fournie dans la figure 2.

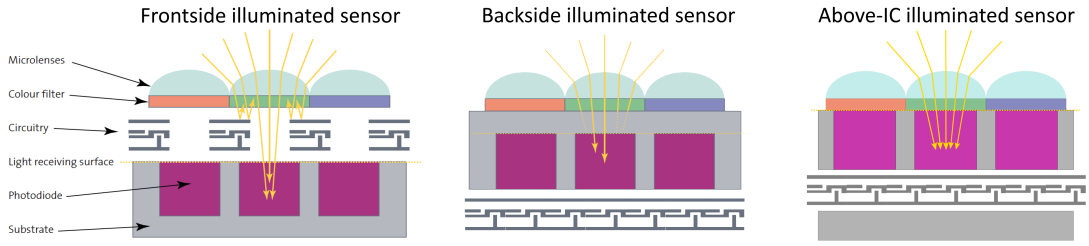

FIGURE 2 – Représentation schématique de 3 types de capteurs d'images CMOS (frontside, backside et above-IC), définis par l'emplacement de la photodiode. Adapté de STEMMER Imaging.

Les architectures fronside et backside sont basées sur une fabrication frontale de la photodiode, avant la fabrication des transistors et des interconnexions. Les capteurs CMOS above-IC, quant à eux, sont issus d'une approche d'intégration "More than Moore", visant à ajouter de nouvelles fonctionnalités aux systèmes CMOS après la fabrication des transistors et des interconnexions. Avec une telle conception, il n'y a pas d'ombrage dû aux interconnexions (contrairement aux capteurs frontaux) et le substrat n'a pas besoin d'être aminci pour éviter l'absorption parasite (contrairement aux capteurs dorsaux). Ces avantages potentiels ont un coût. La température du processus de fabrication de la photodiode doit être limitée pour éviter d'endommager la structure CMOS sous-jacente. Ceci est dû au risque de diffusion d'impuretés et de dégradation des matériaux au niveau de l'interconnexion. Une limite supérieure de l'ordre de 350 à 400°C est donc communément acceptée pour les processus de post-interconnexion. En conséquence, il est impossible de s'appuyer sur des processus à haute température comme l'épitaxie, l'oxydation du silicium, le recuit d'activation des dopants ou le durcissement des matériaux. Cette forte contrainte sur le budget thermique du procédé de dépôt de photodiode appelle au développement de matériaux sensibles au NIR qui peuvent être déposés à basse température. Au cours de ce projet, nous avons choisi d'utiliser le dépôt chimique en phase vapeur assisté par plasma pour tenir compte de cette contrainte. Avec le PECVD, une grande variété de matériaux peut être cultivée à basse température (de la température ambiante à 400 °C) à partir de précurseurs en phase gazeuse.

Cette thèse est accessible à l'adresse : https://theses.insa-lyon.fr/publication/2023ISAL0014/these.pdf
© [A. Wilson], [2023], INSA Lyon, tous droits réservés

Objectifs de la thèse

L'objectif de cette thèse est de développer des films minces obtenus par PECVD à partir de précurseurs de silicium et de germanium et de les intégrer dans un prototype de photodiode simple et fonctionnel, sensible au NIR. Les matériaux obtenus vont du germanium amorphe hydrogéné aux alliages silicium-germanium microcristallins. L'utilisation du germanium - un matériau à faible bande interdite - permet d'atteindre des coefficients d'absorption élevés dans la gamme spectrale d'intérêt. Ces matériaux pourraient donc convenir à des capteurs dans l'infrarouge proche. Les propriétés structurelles exotiques des films amorphes et microcristallins conduisent à des propriétés optoélectroniques qui diffèrent considérablement de celles de leurs homologues cristallins.

Le premier chapitre donne un aperçu des connaissances actuelles sur ces matériaux. Le deuxième chapitre se concentrera ensuite sur les équipements et les techniques nécessaires à la production et à la caractérisation des couches semi-conductrices individuelles ainsi que des dispositifs optoélectroniques complets. Les défis à relever pour la fabrication des photodiodes restent nombreux. Tout d'abord, il faut développer une couche absorbante de haute qualité avec une forte absorption optique dans la gamme spectrale NIR. Le chapitre 3 sera donc consacré au développement de films minces intrinsèques de haute qualité en Si :H, Ge :H et SiGe :H par PECVD, en mettant l'accent sur les propriétés structurelles, électriques et optiques de ces films. Ensuite, le dopage de type p et de type n des films microcristallins doit être réalisé afin de produire une jonction P-I-N. Le chapitre 4 étudiera les propriétés électriques et structurelles des films Si :H et Ge :H dopés au phosphore et au bore. En fin de compte, ces blocs de construction devront être intégrés en un seul dispositif fonctionnel avec la plus grande efficacité quantique possible, tout en s'assurant que l'ensemble du processus est compatible avec les contraintes d'intégration CMOS above-IC. Cet aspect sera abordé dans le chapitre 5 où les couches précédemment développées seront utilisées pour produire une architecture de jonction PIN intégrée à un prototype simple de photodiode.

1 Etat de l'art : des bases de la PECVD à la croissance du µc-SiGe :H

Le dépôt chimique en phase vapeur assisté par plasma (PECVD) permet de fabriquer une large gamme de films minces, en utilisant seulement un faible budget thermique. Bien que l'on trouve une littérature abondante sur le silicium amorphe et microcristallin (a/µc-Si :H) - en partie en raison de son utilisation dans l'industrie des cellules solaires - les études concernant le silicium-germanium et le germanium pur obtenus par PECVD sont moins courantes. Ces alliages à base de silicium-germanium ont un grand potentiel pour les capteurs optiques en raison de leur coefficient d'absorption élevé dans la gamme spectrale du visible au proche infrarouge, en particulier par rapport au silicium cristallin et à son énergie de bande interdite de 1,12 eV (1107 nm).

Dans ce chapitre, nous proposons un bref aperçu des photodétecteurs Ge et SiGe existants, en mettant l'accent sur les dispositifs compatibles avec les circuits intégrés supérieurs rapportés dans la littérature. Dans la suite de ce chapitre, nous chercherons à explorer les différentes conditions expérimentales nécessaires à la production de films minces de $Si_{1-x}Ge_x$: H de haute qualité, compatibles above-IC, allant du silicium pur (x=0) au germanium pur (x=1). En partant des bases du dépôt PECVD, nous donnerons ensuite un aperçu des propriétés structurelles et optoélectroniques des films Si :H, Ge :H et SiGe :H ainsi que des conditions expérimentales

Cette thèse est accessible à l'adresse : https://theses.insa-lyon.fr/publication/2023ISAL0014/these.pdf
© [A. Wilson], [2023], INSA Lyon, tous droits réservés

nécessaires à leur production.

1.1 Photodétecteurs compatibles above-IC

L'intégration CMOS above-IC est un concept qui remonte aux années 1990 [1]. Il a gagné en popularité une décennie plus tard comme moyen d'ajouter de nouvelles fonctionnalités aux systèmes CMOS dans une approche d'intégration "More than Moore" [2, 3]. Le potentiel de cette approche en termes de performance, de compacité et de coût a été discuté par des groupes de recherche du secteur de la microélectronique [3-6] mais nécessite l'introduction dans l'industrie de nouveaux matériaux compatibles avec les contraintes de la technologie CMOS et la structure CMOS sous-jacente.

Parallèlement, la recherche dans le domaine du photovoltaïque (PV) et la quête d'un rendement de conversion énergétique toujours plus élevé ont conduit à un intérêt pour les matériaux à faible bande interdite pour les cellules inférieures des structures tandem. [7-11] Afin d'obtenir des cellules solaires flexibles, peu coûteuses et à haut rendement, les matériaux développés à cet effet ont souvent été déposés à basse température. Ces semi-conducteurs amorphes et microcristallins à base de silicium et de germanium étaient donc intrinsèquement compatibles avec les températures above-IC et pouvaient être d'excellents candidats pour les applications de détection dans le proche infrarouge.

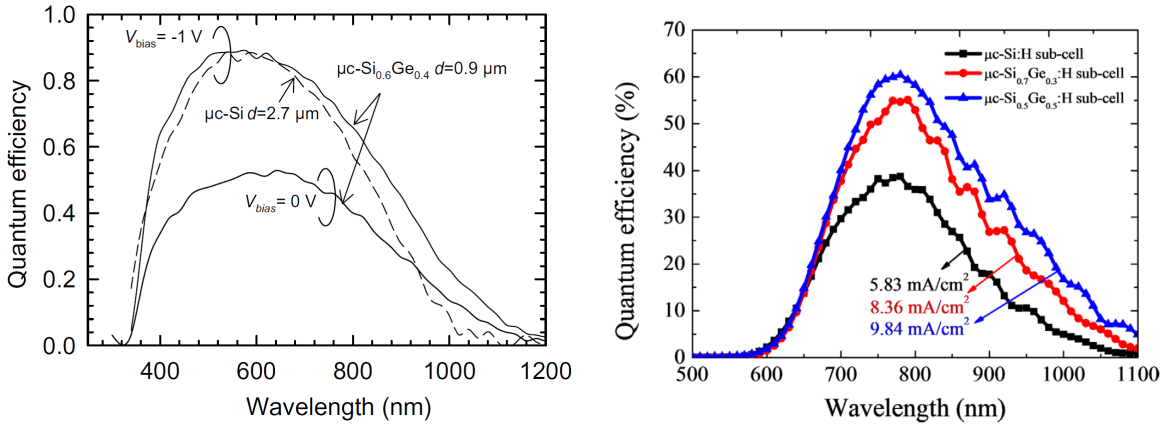

(a) (b)

FIGURE 3 – Rendement quantique de cellules solaires PIN avec un : (a) absorbeur $\mu c - Si_{0.6}Ge_{0.4} : H$ de 900 nm d'épaisseur [12] (b) absorbeur $\mu c - Si_{0.5}Ge_{0.5} : H$ de 1 µm d'épaisseur [13].

Des cellules solaires à haut rendement de collecte - également appelé rendement quantique - ont été signalées dans la littérature avec une sensibilité s'étendant au proche infrarouge grâce à l'introduction de germanium dans les alliages SiGe hydrogénés. Matsui et al. [12, 14-16] ont pu produire une cellule solaire avec une couche de $Si_{0.6}Ge_{0.4} : H$ de 900 nm d'épaisseur avec une sensibilité allant jusqu'à 1200 nm [12] (10 % à 1100 nm sous une polarisation de -1V, voir la figure 3a). D'autres groupes [13] ont obtenu des résultats similaires (voir figure 3b) avec une efficacité quantique à 1100 nm atteignant 5 %.

Ne se limitant pas seulement aux alliages SiGe :H, Krause et al. [17] ont rapporté un photodétecteur en Germanium microcristallin déposé à basse température. Le dispositif fonctionne en polarisation inverse (-0,2 V) et montre une efficacité de collecte prometteuse (voir figure 4)

Cette thèse est accessible à l'adresse : https://theses.insa-lyon.fr/publication/2023ISAL0014/these.pdf
© [A. Wilson], [2023], INSA Lyon, tous droits réservés

qui atteint 15 % à 1100 nm avec un absorbeur de 110 nm.

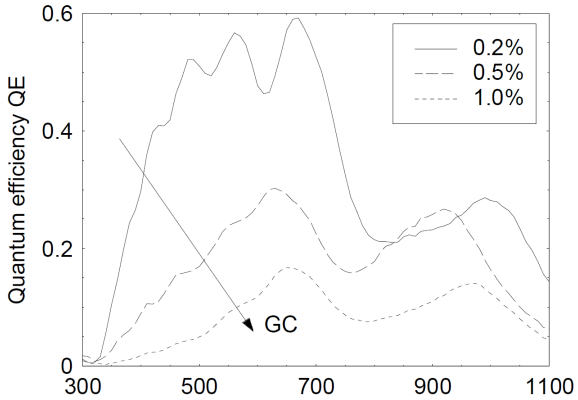

FIGURE 4 – Quantum efficiency for a PIN photodiode with a 110 nm thin µc-Ge:H absorber deposited by PECVD at different germane concentration GC. Measurements were done under -0.2 V bias at 250 K.[17]

L'intérêt de tels dispositifs réside dans le faible budget thermique nécessaire à la fabrication d'un dispositif dont l'épaisseur totale est bien inférieure à 1 µm. La figure 5 donne un exemple de l'architecture utilisée pour une cellule solaire PIN ainsi que le rendement quantique mesuré. [18]

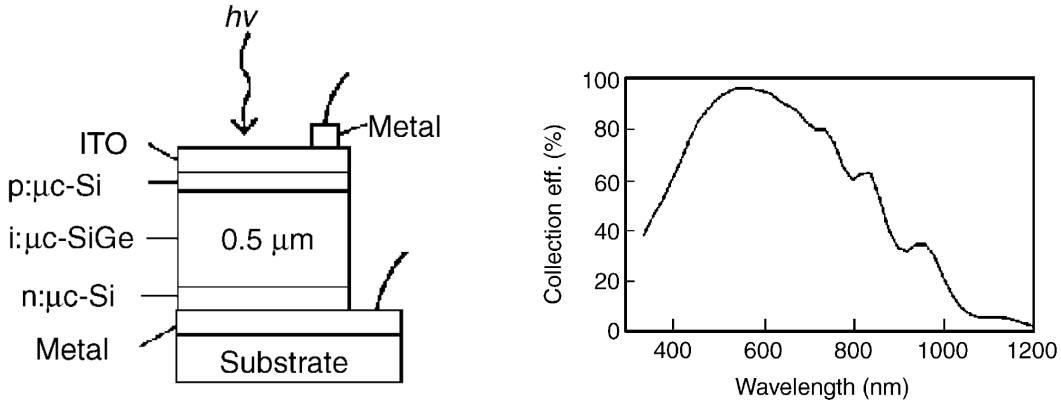

(a) (b)

FIGURE 5 – (a) Structure test et (b) rendement quantique d'une cellule solaire µc-Si:H(p)/µc$-Si_{0.27}Ge_{0.63}:H$/c-Si:H(n).[18]

Le travail avec des semi-conducteurs amorphes et microcristallins à base de silicium-germanium a été jugé prometteur. Afin de comprendre la nature de ces semi-conducteurs non conventionnels, les sections suivantes de ce chapitre sont consacrées à une introduction aux équipements de dépôt utilisés ainsi qu'aux conditions de dépôt et aux propriétés optoélectroniques des matériaux allant du silicium amorphe au silicium-germanium microcristallin.

1.2 Objectifs du projet de thèse

Dans ce projet de thèse, nous chercherons à étudier les propriétés des films minces de silicium, de germanium et de silicium-germanium hydrogénés déposés par PECVD, dans le but

Cette thèse est accessible à l'adresse : https://theses.insa-lyon.fr/publication/2023ISAL0014/these.pdf
© [A. Wilson], [2023], INSA Lyon, tous droits réservés

final de produire un photodétecteur compatible avec les circuits intégrés supérieurs et présentant une sensibilité accrue dans le proche infrarouge. Ce premier chapitre a fourni un aperçu synthétique de l'état actuel des connaissances sur ces matériaux. Le µc-Si :H a été largement étudié et offre de bonnes propriétés électriques au prix d'un coefficient d'absorption rapidement décroissant dans la gamme du proche IR [19]. Cela en fait peut-être le matériau le moins approprié pour la détection NIR à des longueurs d'onde élevées, car des films extrêmement épais seraient nécessaires. D'autre part, le µc-Ge :H s'est révélé être un matériau prometteur avec un coefficient d'absorption atteignant $10^4 cm^{-1}$ à 1 eV [14]. L'utilisation de ce matériau est cependant extrêmement rare pour les applications de photodétection [17] et ses mauvaises propriétés électriques limitent son utilisation à des absorbeurs très fins. L'étape suivante a donc été d'essayer de combiner les avantages de ces deux matériaux dans un alliage microcristallin $Si_{1-x}Ge_x : H$. Avec ce matériau, l'absorption et les propriétés électriques deviennent dépendantes de la composition. Plusieurs études ont montré une dégradation des propriétés électriques avec l'augmentation de la fraction Ge alors que l'absorption augmente continuellement dans la région de basse énergie [13, 14]. Un compromis doit être trouvé en fonction de l'application. Jusqu'à présent, ce matériau a été principalement introduit dans les cellules solaires [12, 13, 18].

Aperçu du travail réalisé

Afin de réaliser un photodétecteur NIR compatible above-IC, les matériaux présentés au cours de ce chapitre devront être développés et étudiés individuellement avant de les combiner en tant que briques élémentaires pour obtenir un dispositif fonctionnel. Dans le cadre des procédés above-IC, nous cherchons à réaliser ces étapes en veillant à ne pas dépasser des températures de 350 °C [3-6].

Les défis d'une telle entreprise résident, dans un premier temps, dans l'obtention d'un matériau de haute qualité, à faible taux de défauts et à forte absorption optique dans le domaine spectral NIR pour être utilisé comme couche absorbante. Deuxièmement, le dopage des films semi-conducteurs développés doit être étudié afin d'obtenir des films minces stables et fortement dopés. Le dopage de type p et de type n du matériau étudié doit être réalisé afin de pouvoir produire une jonction P-I-N. Enfin, les films étudiés doivent être intégrés comme un dispositif fonctionnel unique avec des contacts électriques appropriés présentant un comportement de photodiode.

Dans le but de fournir une solution aux défis susmentionnés, le chapitre 2 se concentrera sur les équipements et les techniques nécessaires pour produire et caractériser les couches semi-conductrices individuelles ainsi que les dispositifs. Le chapitre 3 sera consacré au développement de films minces intrinsèques de haute qualité en Si :H, Ge :H et SiGe :H par PECVD, en mettant l'accent sur les propriétés structurelles, électriques et optiques de ces films. Sur la base de ces résultats, les propriétés électriques et structurelles des films Si :H et Ge :H dopés au phosphore et au bore sont étudiées dans le chapitre 4. Enfin, le chapitre 5 tirera parti des connaissances acquises tout au long des chapitres précédents pour réaliser une architecture de jonction PIN intégrée à une structure prototype simple. La conception de ce prototype nous permettra de tester de manière approfondie les matériaux développés dans des conditions de fonctionnement réelles et nous permettra de travailler sur l'amélioration des performances NIR de notre dispositif.

Cette thèse est accessible à l'adresse : https://theses.insa-lyon.fr/publication/2023ISAL0014/these.pdf
© [A. Wilson], [2023], INSA Lyon, tous droits réservés

2 Matériel et Méthode

Dans ce chapitre, nous avons donné un aperçu des techniques expérimentales de dépôt et de caractérisation utilisées au cours de ce projet. Le réacteur PlasmaTherm Vision 310 PECVD utilisé à l'INL a été présenté avec ses principales spécifications. Ce réacteur a été utilisé tout au long de ce projet pour le dépôt de couches de semi-conducteurs et de diélectriques à basse température. L'équipement PECVD est au cœur du développement des matériaux sensibles au NIR. Le matériel a été adapté pour ce projet, ce qui permet de faire croître des films Si :H, SiGe :H ou Ge :H avec un dopage intrinsèque, de type p ou n. Ces films minces sont déposés sur des substrats de silicium cristallin, de verre ou d'ITO. Le processus de nettoyage de ces différents substrats avant le dépôt PECVD a été présenté dans ce chapitre.

Les films déposés peuvent ensuite être caractérisés structurellement, chimiquement, optiquement et électriquement grâce à un large éventail de techniques expérimentales. La caractérisation structurelle peut être réalisée par TEM ou par spectroscopie Raman, tandis que SIMS peut fournir des informations chimiques précises. En tant que technique non-destructive, la caractérisation Raman sera largement utilisée pour fournir des informations structurelles et chimiques sur les films déposés, en raison du faible temps d'acquisition et d'analyse.

D'autre part, l'ellipsométrie spectroscopique, la réflectométrie et l'efficacité quantique sont utilisées pour étudier les propriétés optiques des films obtenus par PECVD. L'efficacité quantique (QE) en particulier fournit une mesure de la performance du matériau une fois intégré dans un dispositif fonctionnel. Dans notre objectif de démontrer la faisabilité de photodétecteurs NIR en silicium-germanium microcristallin, l'EQ est une méthode de caractérisation clé. Enfin, les méthodes de caractérisation électrique adaptées aux matériaux microcristallins (Effet Hall et SSPG) ont été introduites.

Toutes ces techniques seront évoquées dans les chapitres suivants lors de nos travaux de recherche. Elles permettront de mieux comprendre la nature des films déposés et l'impact de leurs conditions de dépôt, qu'il s'agisse d'un simple film mince ou d'empilements de couches beaucoup plus complexes.

3 Développement et caractérisation des matériaux pour l'absorbeur

Au cours de ce chapitre, nous chercherons à développer un matériau approprié pour la couche absorbante d'une photodiode. Le matériau idéal à cette fin serait une couche très absorbante, sans défaut et mince. Une absorption élevée, en particulier dans le proche infrarouge, garantit une absorption maximale des photons. Si cette condition est remplie, l'absorbeur peut alors être mince, ce qui réduit la distance que les porteurs minoritaires photogénérés doivent parcourir pour être collectés. Enfin, avoir le moins de défauts possible réduit les chances de recombinaison des porteurs minoritaires avant leur extraction. La section suivante sera donc consacrée à la réalisation de trois matériaux introduits dans le chapitre 1, à savoir µc-Si :H, µc-Ge :H et µc-SiGe :H. Alors que nous montrerons rapidement que le premier n'est pas optiquement pertinent, µc-Ge :H et µc-SiGe :H pourraient être des candidats prometteurs.

3.1 Hydrogenated Silicon thin films development

Les films de silicium hydrogénés sont obtenus par décomposition de précurseurs de silicium, dans notre cas le silane (SiH_4), dans la chambre PECVD. L'espèce de précurseur peut être utilisée diluée dans de l'hydrogène, de l'hélium ou de l'argon, ce qui aura un impact important sur les propriétés structurelles et électriques des couches déposées. Des matériaux tels que

Cette thèse est accessible à l'adresse : https://theses.insa-lyon.fr/publication/2023ISAL0014/these.pdf
© [A. Wilson], [2023], INSA Lyon, tous droits réservés

le silicium amorphe (a-Si :H), le silicium microcristallin (µc-Si :H) et des couches similaires à phase mixte (pm-Si :H, nc-Si :H) peuvent être déposés en réglant de manière adéquate la température, la pression, la puissance et les débits de gaz. Un aperçu plus large de l'état de l'art du dépôt de µc-Si :H peut être trouvé dans le chapitre 1. Dans cette section, nous allons présenter les paramètres de notre procédé pour la production de couches de semi-conducteurs à base de Si. Comme le µc-Si :H est un matériau largement documenté, nous nous appuierons sur la littérature.

L'étude du silicium microcristallin a révélé que celui-ci n'est pas adapté à l'absorption du NIR, mais ses propriétés électriques et sa faible absorption au-dessus de 800 nm pourraient en fait être prometteuses pour produire des couches de fenêtre de type n ou p afin de former une jonction P-I-N pour nos dispositifs. Cet aspect du µc-Si :H sera abordé dans le chapitre suivant. En se concentrant sur le développement de la couche d'absorption, une alternative à faible bande interdite aux couches à base de silicium avec des propriétés structurelles similaires est le germanium, qui peut être introduit dans la chambre de réaction sous forme de précurseurs gazeux germaniques. Dans la section suivante, des films minces de Germanium microcristallin hydrogéné ont été étudiés afin d'établir leurs avantages et inconvénients pour une utilisation potentielle dans les photodiodes P-I-N.

3.2 Développement des couches minces de Germanium hydrogéné

Les films minces de µc-Si :H obtenus par PECVD ont montré leurs limites dans la section précédente, notamment en termes de coefficient d'absorption α au-dessus de $\lambda = 800\,\text{nm}$. Une approche pour résoudre ce problème est de se concentrer sur les films semi-conducteurs de Germanium amorphes et microcristallins. Dans cette section, nous nous attacherons à établir la relation entre les propriétés structurelles, les propriétés optiques et les paramètres de dépôt.

3.2.1 Propriétés structurelles

Afin d'identifier les conditions optimales pour l'obtention de µc-Ge :H, des couches de germanium hydrogéné ont été déposées sur du c-Si et du verre à des R_H croissants, allant de 20 à 400 pour deux puissances RF distinctes de 30 et 100 W respectivement. Tous les échantillons ont été déposés à 250 °C, 1000 mTorr, $\Phi_{tot} = 350$ sccm et $t_{dep} = 20$ min. X_c a ensuite été estimé à partir de la caractérisation des spectres Raman pour les films déposés sur le substrat c-Si (car les composants Ge-Ge et Si-Si TO du film et du substrat ne se recouvrent pas), l'épaisseur et la vitesse de dépôt ont été obtenues par des mesures d'ellipsométrie spectroscopique (voir chapitre 2). Les résultats sont rassemblés dans la figure 6.

Comme prévu, l'épaisseur du film et donc la vitesse de dépôt diminuent avec l'augmentation de la dilution R_H. On pourrait s'attendre à ce que la vitesse de dépôt v_{dep} dépende linéairement de la concentration en germane, et donc qu'elle dépende inversement de $R_H = (H_2 + GeH_4)/GeH_4$.

3.2.2 Propriétés optiques

A partir des données d'Ellipsométrie Spectroscopique, on peut extraire à la fois n et k. Les résultats obtenus dans la gamme de 0.5 eV à 5 eV sont montrés dans la figure 7 et comparés avec les coefficients obtenus précédemment pour a-Ge :H. Les constantes optiques pour le c-Ge ont été ajoutées pour servir de référence.

Une comparaison entre a-Ge :H et µc-Ge :H est particulièrement intéressante afin de sélectionner le matériau le mieux adapté à nos besoins. Dans les longueurs d'onde visibles, a-Ge :H

Cette thèse est accessible à l'adresse : https://theses.insa-lyon.fr/publication/2023ISAL0014/these.pdf
© [A. Wilson], [2023], INSA Lyon, tous droits réservés

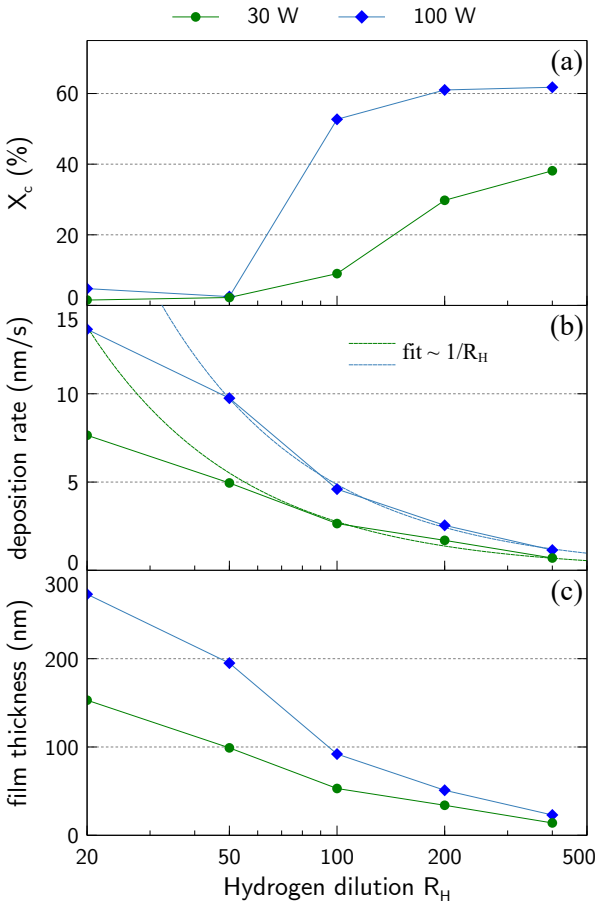

FIGURE 6 – (a) cristallinité Raman, (b) vitesse de dépôt et (c) épaisseur du film en fonction de R_H. $t_{dep.}$ a été fixé à 20 min, la température à 250°C et la pression à 1000 mTorr.

a un coefficient d'absorption plus élevé que µc-Ge :H, car il se comporte comme un matériau à bande interdite directe. Au-dessus de $\lambda = 1060$ nm, le µc-Ge :H dépasse rapidement le a-Ge :H principalement en raison de sa bande interdite plus faible. Une absorption plus élevée que celle du c-Ge dans la plupart de la gamme étudiée est également observée. Elle peut être attribuée à la bande interdite directe de la phase amorphe restante combinée à la bande interdite indirecte de la phase cristalline, ainsi qu'à l'absorption de la queue de bande due aux défauts. La plage spectrale qui nous intéresse, de 940 à 1340 nm, se situe dans une zone où le µc-Ge :H serait, en moyenne, plus performant que le a-Ge :H.

3.2.3 Conclusion : µc-Ge :H

Bien que l'absorption soit un facteur de mérite important pour le choix de notre matériau, les propriétés électroniques doivent également être prises en compte. Or la faible photocondutivité du µc-Ge :H pourrait être un inconvénient majeur pour les applications de photodétection ; elle pourrait conduire à une dégradation du rapport signal/bruit. Les films de µc-Ge :H déposés par PECVD étudiés ne répondent pas aux exigences d'un absorbeur efficace et pourraient donc ne pas être une option viable pour les photodiodes compatibles avec les circuits intégrés supérieurs, malgré leurs propriétés optiques prometteuses. Jusqu'à présent, il a été démontré

Cette thèse est accessible à l'adresse : https://theses.insa-lyon.fr/publication/2023ISAL0014/these.pdf
© [A. Wilson], [2023], INSA Lyon, tous droits réservés

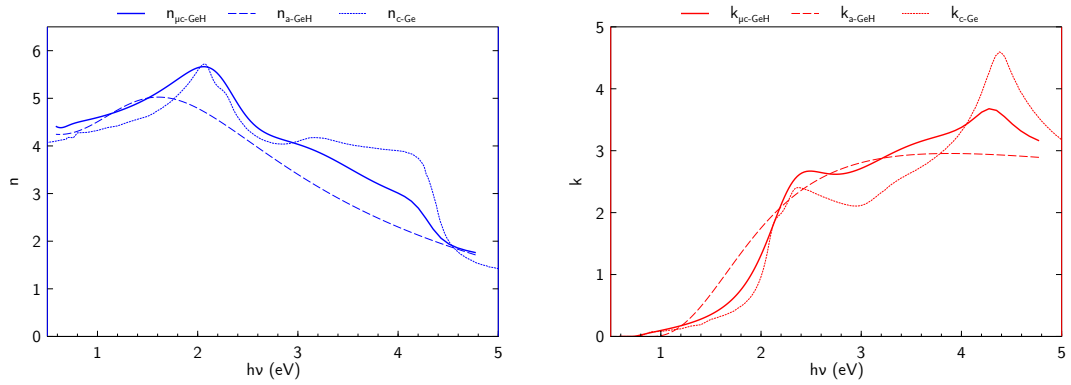

FIGURE 7 – Coefficients optiques ajustés n et k pour a-Ge:H et µc-Ge:H en fonction de l'énergie photonique $h\nu$. Les indices optiques pour c-Ge sont donnés à titre de comparaison et proviennent de [20].

que le µc-Si :H et le µc-Ge :H n'étaient pas totalement adaptés à l'utilisation que nous voulons en faire, mais ils présentent tous deux des aspects prometteurs : en travaillant avec des alliages silicium-germanium microcristallins, il pourrait être possible de trouver un compromis entre une absorption élevée et des propriétés électriques suffisantes.

3.3 Développement des alliages de silicium-germanium hydrogénés

Jusqu'ici, deux matériaux ont été étudiés pour servir de couche absorbante dans une photodiode PIN. Comme notre objectif est d'atteindre une efficacité quantique élevée dans le domaine du proche infrarouge, des matériaux efficaces doivent être développés pour les couches de type n, intrinsèque et de type p. La couche intrinsèque, également appelée couche absorbante, doit être optimisée afin de trouver le meilleur compromis entre l'absorption des photons et l'extraction des paires électron-trou de la couche. Dans les sections précédentes de ce chapitre, les propriétés optoélectroniques du µc-Si :H et du µc-Ge :H ont été étudiées. Dans la présente section, les alliages silicium-germanium hydrogénés ($\mu c - Si_{1-x}Ge_x : H$) sont explorés comme un moyen d'atteindre un compromis entre les propriétés électriques du µc-Si :H et l'absorption du µc-Ge :H. Comme présenté dans le chapitre 1, le µc-SiGe :H a été étudié dans le contexte de la recherche photovoltaïque pour des applications de cellules de fond [18, 21, 22]. Il a été constaté que les propriétés électriques des alliages µc-SiGe :H se dégradent avec l'incorporation de Ge [14]. Comme pour tout matériau microcristallin, les propriétés optiques et électriques établies sont fortement liées aux conditions de dépôt. Par conséquent, la section suivante se concentre sur la production et la caractérisation de couches SiGe :H de pointe pour l'absorption NIR.

L'ajout de germanium aux alliages µc-SiGe :H est extrêmement bénéfique pour les performances du matériau dans la gamme spectrale NIR. À $\lambda = 1000$nm par exemple, le passage d'un alliage µc-$Si_{0.6}Ge_{0.4}$:H à un alliage µc-$Si_{0.4}Ge_{0.6}$:H augmente l'absorption de $\alpha = 2\times10^3\,\mathrm{cm}^{-3}$ à $6\times10^3\,\mathrm{cm}^{-3}$. Ces résultats sont en accord étroit avec ceux obtenus par Matsui et al. [14]. L'absence d'une forte chute de l'absorption à des longueurs d'onde élevées, habituellement observée dans les semi-conducteurs cristallins, peut être interprétée comme une conséquence des défauts de sous-bande interdite des matériaux désordonnés [23].

Il a été démontré que les alliages µc-SiGe :H peuvent être obtenus pour toute fraction de Ge donnée en calibrant soigneusement les conditions de dépôt. Le film résultant peut être étudié optiquement par ellipsométrie spectroscopique si des précautions sont prises dans

Cette thèse est accessible à l'adresse : https://theses.insa-lyon.fr/publication/2023ISAL0014/these.pdf
© [A. Wilson], [2023], INSA Lyon, tous droits réservés

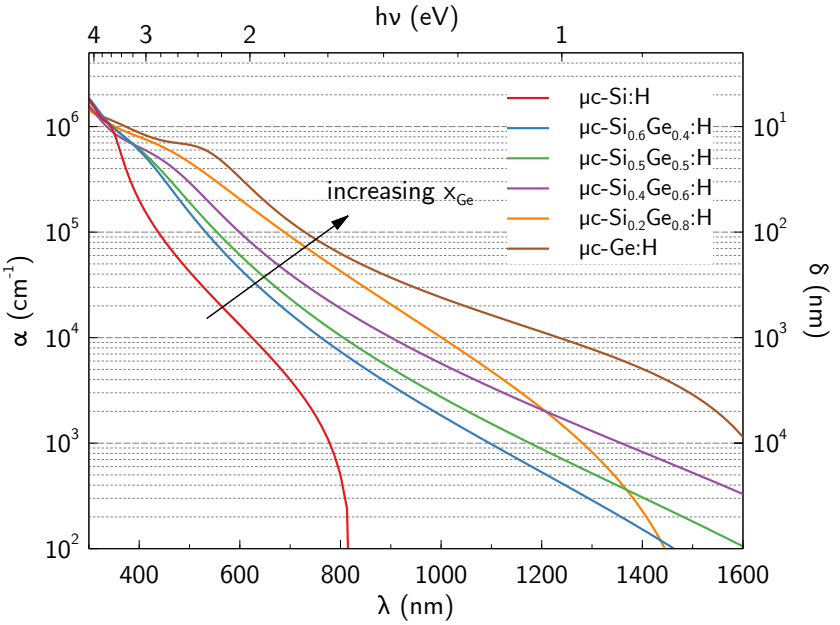

FIGURE 8 – Coefficient d'absorption α du μc-SiGe:H obtenu à partir des données fittées par ellipsométrie spectroscopique.

la construction du modèle. Avec l'augmentation de la fraction Ge, l'absorption du NIR est augmentée de façon mesurable. Un compromis entre α et la longueur de diffusion L_{diff} doit cependant être trouvé pour établir la composition optimale de l'alliage.

Dans l'ensemble, le Silicium-Germanium microcristallin fournit un matériau ajustable qui se situe entre la forte absorption du Germanium microcristallin et les bonnes propriétés électriques du Silicium microcristallin. Le degré de liberté supplémentaire apporté par la composition accordable du matériau rend son processus de fabrication plus complexe et exige une grande quantité de travail expérimental pour trouver les meilleures conditions de dépôt pour chaque nuance de l'alliage. Dans cette section, nous avons commencé par examiner les propriétés chimiques du μc-SiGe :H dans une large gamme de conditions de dépôt. Nous avons ensuite étudié en profondeur les propriétés optoélectroniques du matériau en nous concentrant sur un ensemble plus restreint de paramètres de procédé où la dilution élevée de l'hydrogène R_H assure la nucléation de la phase cristalline. Les alliages μc-SiGe :H constituent une option prometteuse pour une couche absorbante NIR efficace et seront mis en œuvre dans le cadre de la fabrication de prototypes de photodiodes.

3.4 Conclusion : Absorber layer materials development

Dans ce chapitre, des couches de semi-conducteurs microcristallins ont été produites par PECVD et caractérisées. Notre objectif était de produire des films minces de matériaux semi-conducteurs adaptés aux couches absorbantes dans le proche infrarouge (λ de 940 à 1350 nm) dans les futurs prototypes de photodiodes P-I-N. Dans une première tentative pour comprendre et maîtriser la croissance des matériaux microcristallins, des films de silicium amorphe et microcristallin ont été produits en s'appuyant sur l'abondante littérature existante. Les films obtenus ont montré des signes évidents de cristallisation et ont été caractérisés optiquement par ellipsométrie spectroscopique. En raison de sa faible absorption au-dessus de $\lambda = 800\,\text{nm}$, le μc-Si :H n'est pas une couche appropriée pour la détection dans le proche infrarouge, mais

Cette thèse est accessible à l'adresse : https://theses.insa-lyon.fr/publication/2023ISAL0014/these.pdf
© [A. Wilson], [2023], INSA Lyon, tous droits réservés

dans le contexte de la production de photodiodes P-I-N, il pourrait agir comme une couche fenêtre efficace de type n ou p sur la face avant du dispositif. Cette opportunité sera explorée dans le chapitre suivant.

Les limitations optiques du µc-Si :H ont poussé à l'étude de matériaux alternatifs. Le germanium microcristallin est un candidat de choix pour notre application, car sa bande interdite inférieure améliore l'absorption du proche infrarouge. Le germane, un précurseur du germanium en phase gazeuse, est disponible dans le commerce, ce qui signifie que sa production peut également être réalisée par PECVD. Les conditions de dépôt ont été testées afin de produire des couches hautement cristallisées. En raison de la faible énergie des liaisons covalentes dans le germanium, un facteur de dilution de l'hydrogène élevé R_H était nécessaire pour passer des films amorphes aux films microcristallins. Une approche de croissance en deux étapes a été étudiée afin de produire des films avec un X_c élevé sans compromettre la vitesse de dépôt. La caractérisation optique des films minces de Ge par ellipsométrie spectroscopique a été rendue possible par la définition d'un modèle approprié pour décrire nos échantillons. Le coefficient d'absorption extrait de l'analyse a montré les avantages du µc-Ge :H par rapport au a-Ge :H pour les longueurs d'onde supérieures à $\lambda = 1000\,nm$. Cependant, l'inspection des propriétés électriques a révélé que la photoconductivité était extrêmement faible en raison du courant d'obscurité élevé et des taux de recombinaison élevés. µc-Ge :H a conservé cet inconvénient malgré nos efforts pour trouver des paramètres de processus plus appropriés.

La dernière section de ce chapitre s'est attachée à trouver un compromis approprié entre l'absorption optique et les propriétés électriques en travaillant avec des alliages µc-SiGe :H. La complexité du réglage fin de la composition de l'alliage fait du µc-SiGe :H un matériau plus délicat à produire. Une phase de calibration a été nécessaire pour comprendre la cinétique de croissance du matériau. La caractérisation optique par Ellipsométrie Spectroscopique du µc-SiGe :H avec une fraction de Ge croissante a montré l'impact positif sur le coefficient d'absorption NIR. Une dégradation apparente des propriétés électriques avec l'augmentation de la teneur en germanium a été mise en évidence par des mesures de longueur de diffusion, les valeurs exactes ne semblant pas vraiment fiables.

4 Semiconducteurs microcristallins dopés pour les jonctions pn

Le développement d'un prototype de photodétecteur à partir de la base est un chemin qui peut être divisé en plusieurs blocs de construction. Le premier et sans doute le plus critique de ces blocs est le matériau de la couche absorbante, qui a été développé et caractérisé dans le chapitre précédent. En gardant à l'esprit que notre objectif final est de produire une photodiode de type P-I-N, deux matériaux supplémentaires doivent être étudiés avant de concevoir l'ensemble du prototype : les semi-conducteurs microcristallins de type n et p.

Le silicium cristallin est généralement dopé par implantation ionique suivie d'un recuit, mais cette méthode donne des taux d'activation très faibles dans des matériaux aussi défectueux que le µc-Si :H [24, 25]. Le dopage d'un matériau non cristallin est souvent réalisé par co-déposition, [26-28] où les précurseurs d'atomes dopants sont ajoutés aux précurseurs de Si ou de Ge dans le mélange gazeux initial. Outre le fait qu'il s'agit d'une méthode de dopage efficace, le codépôt permet de réaliser le dopage directement à l'intérieur de la chambre du réacteur PECVD en une seule étape et à basse température, sans nécessiter de recuit. Dans le contexte de notre travail, l'utilisation d'un seul équipement pour produire à la fois la couche d'absorption et les couches dopées limite le risque de contamination externe, réduit la complexité du processus et permet de gagner du temps.

Dans ce chapitre, nous nous concentrerons sur l'obtention de semi-conducteurs de type n

Cette thèse est accessible à l'adresse : https://theses.insa-lyon.fr/publication/2023ISAL0014/these.pdf
© [A. Wilson], [2023], INSA Lyon, tous droits réservés

et p en nous focalisant d'abord sur l'addition de phosphine (PH_3) et de diborane (B_2H_6) au silicium microcristallin hydrogéné. Compte tenu des difficultés à obtenir du µc-Si :H de type p fortement dopé, on a ensuite exploré le µc-Ge :H dopé au bore, ce qui a donné des résultats encourageants.

La zone de charge d'espace

Nous cherchons à obtenir des couches microcristallines avec des niveaux de dopage élevés afin que les régions de charge d'espace (SCR) aux interfaces P-I et I-N s'étendent aussi loin que possible dans la couche d'absorption intrinsèque. Le champ électrique dans l'absorbeur favoriserait alors la séparation et la collecte des paires d'électrons et de trous, sans dépendre de la faible longueur de diffusion du matériau. L'étendue du SCR dans une simple jonction p-n peut être dérivée de l'équation de Poisson [29] :

$$\Delta V = -\frac{\rho}{\epsilon_{sc}} \quad \text{on trouve} \quad W_{SCR} = \sqrt{\frac{2\epsilon_{sc}}{q}\frac{N_D + N_A}{N_A N_D}(V_{bi} - \frac{2k_B T}{q})} \tag{0.1}$$

$$\text{avec} \quad V_{bi} = k_B T \cdot ln(\frac{N_D N_A}{n_i^2})$$

où ρ est la densité de charge volumique, ϵ_{sc} est la permittivité du matériau, q la charge élémentaire, N_D la densité atomique du donneur, N_A la densité atomique de l'accepteur, $N = N_D$ ou N_A selon que $N_A \gg N_D$ ou vice versa, k_B la constante de Boltzmann et T la température.

Si le semi-conducteur de type n est fortement dopé et que l'absorbeur est de type p, il est nécessaire d'avoir $N_D \gg N_A \approx n_i$ pour que le ZCR s'étende dans la région d'intérêt, c'est-à-dire l'absorbeur. La longueur du ZCR peut alors être réécrite comme suit :

$$W_{ZCR} \approx \sqrt{\frac{2\epsilon_{sc}}{qN}\left(k_B T \cdot ln(\frac{N_D}{n_i}) - \frac{2k_B T}{q}\right)} \tag{0.2}$$

Cette formule met en évidence l'importance d'avoir à la fois un absorbeur réellement intrinsèque (faible N_A) et un N_D élevé pour obtenir un W_{SCR} de l'ordre de grandeur de l'épaisseur de l'absorbeur.

4.1 Dopage *in situ* de µc-Si :H

Notre premier aperçu des propriétés optiques du µc-Si :H a montré que le coefficient d'absorption limité du a-Si :H et du µc-Si :H en faisait un matériau de couche absorbante médiocre. Ces mêmes propriétés optiques pourraient toutefois être exploitées en utilisant du Si :H dopé au bore ou au phosphore comme couche de fenêtre dans des photodiodes P-I-N. Le terme de couche fenêtre est couramment utilisé en photovoltaïque pour décrire une couche d'émetteur à large bande interdite qui permet aux photons de faible énergie de traverser l'absorbeur sans être absorbés. Cette conception permet de réduire l'absorption dans l'émetteur où les recombinaisons de porteurs minoritaires peuvent être extrêmement élevées, ce qui dégrade l'efficacité quantique globale du dispositif.

4.1.1 µc-Si :H type-n

Nous nous sommes concentrés sur l'exploration du processus de croissance ainsi que sur les propriétés structurelles et électriques du µc-Si :H de type n (dopé au phosphore). Le µc-Si :H

Cette thèse est accessible à l'adresse : https://theses.insa-lyon.fr/publication/2023ISAL0014/these.pdf
© [A. Wilson], [2023], INSA Lyon, tous droits réservés

non dopé déposé par PECVD présente typiquement une couche d'incubation amorphe qui peut s'étendre jusqu'à 100 nm avant la nucléation de la phase cristalline. [30] Les travaux antérieurs menés par d'autres groupes de recherche sur les capteurs P-I-N µc-Si :H/µc-SiGe :H ont montré que les couches de type n et p sont typiquement conçues avec une épaisseur de l'ordre de quelques dizaines de nanomètres.[17, 27] Il est donc d'un grand intérêt de comprendre la nature structurelle des couches minces ainsi que l'impact du dopage au phosphore sur leurs propriétés. Nous avons étudié l'impact des paramètres du procédé de dépôt des couches de silicium microcristallin dopées au phosphore, tels que la puissance, la pression et la dilution de l'hydrogène sur les propriétés des films. La fraction volumique cristalline, la concentration en dopant actif et absolu ainsi que l'épaisseur de la couche d'incubation ont été mesurées et des conditions de dépôt ont été trouvées qui donnent des niveaux de dopage élevés ainsi qu'une couche d'incubation mince.

Résultats

es niveaux de dopage élevés sont atteints avec $actif\,[P] = n > 10^{20}\mathrm{cm}^{-3}$ pour les couches µc-Si :H les plus dopées, avec un [P] plus élevé pour les échantillons de faible puissance. Dans les deux ensembles d'échantillons et pour toute la gamme de dopage étudiée, le taux d'activation des atomes dopants incorporés, c'est-à-dire le taux actif, $[P]/[P]_{SIMS}$, est supérieur à 30 %. C'est encourageant si l'on considère que le µc-Si :H contient de nombreux défauts structurels par rapport à son homologue monocristallin. A niveau de phosphine équivalent β, notre échantillon présente un niveau de dopage de deux ordres de grandeur supérieur à celui rapporté par Wei et al [31] alors que Backhausen et al [32] ont atteint des niveaux de dopage similaires avec $\beta = 2$ %. Un excès de défauts ou une ségrégation du phosphore aux joints de grains aurait conduit à un taux d'activation plus faible et aurait donc rendu impossible l'atteinte de ces niveaux de dopage élevés. Les valeurs détaillées de la conductivité σ, de la mobilité μ_H et des niveaux de dopage n obtenus par mesure de l'effet Hall sont reportées dans le tableau 1. L'incertitude est inférieure à 0,1 % pour σ et inférieure à 5 % pour n et μ_H.

Pas d'incorporation préférentielle du phosphore dans le film par rapport au silicium. Dans la gamme étudiée, le rapport [P]/[Si] dépend linéairement du rapport de flux de gaz dopant β avec une légère préférence pour l'incorporation de P dans des conditions de faible puissance (r=[P]/($\beta \cdot [Si]$) = 0.94) par rapport à des conditions de forte puissance (r = 0.73). Ce comportement peut être expliqué en termes d'énergie de dissociation des liaisons Si-H et P-H, car les deux valeurs sont proches : $\mathrm{E_D(P-H)} = 3,55\,\mathrm{eV} > \mathrm{E_D(Si-H)} = 3,08\,\mathrm{eV}$ [33].

	low power			*high power*		
β	σ [S·cm^{-1}]	μ_H [cm^2·V^{-1}·s^{-1}]	n_{active} [cm^{-3}]	σ [S·cm^{-1}]	μ_H [cm^2·V^{-1}·s^{-1}]	n_{active} [cm^{-3}]
0.05 %	1.078	0.615	-1.09E+19	0.338	0.454	-4.64E+18
0.10 %	2.195	0.630	-2.18E+19	0.812	0.385	-1.33E+19
0.50 %	8.772	0.651	-8.41E+19	5.690	0.602	-5.90E+19
1.00 %	13.218	0.487	-1.70E+20	9.512	0.602	-9.86E+19

TABLE 1 – Mesure par effet Hall de la conductivité (σ), de la mobilité (μ_H) et du niveau de dopage à température ambiante dans la configuration de Van Der Pauw.

Discussion : Dopage au phosphore de µc-Si :H

Des conditions PECVD adaptées au dépôt de silicium microcristallin fortement dopé au phosphore ont été trouvées. La tendance du µc-Si :H dopé au P à subir une transition cristalline

Cette thèse est accessible à l'adresse : https://theses.insa-lyon.fr/publication/2023ISAL0014/these.pdf
© [A. Wilson], [2023], INSA Lyon, tous droits réservés

à amorphe a été empêchée en augmentant la dilution de l'hydrogène de $R_H = 25$ à 50, ce qui a entraîné une diminution de la vitesse de dépôt. Dans ces conditions, les mesures de cristallinité AFM et Raman ont révélé qu'un régime de haute puissance (100 W) et de haute pression (1 Torr) conduit à une nucléation plus continue des cristallites avec l'épaisseur du film contrairement au régime de faible puissance (30 W, 0,8 Torr) qui croît comme une couche amorphe pour les premiers 23 nm avant la nucléation de la phase cristalline. Sans une couche d'incubation entièrement amorphe, les conditions de haute puissance pourraient être mieux adaptées aux couches de contact électrique dans les jonctions PIN. Les mesures SIMS et d'effet Hall montrent que des conditions de puissance et de pression plus faibles (30 W, 800 mTorr) conduisent à une incorporation de phosphore de 20 % plus élevée dans le film provenant du plasma. Cependant, le taux d'activation du phosphore incorporé ne dépend pas des conditions de dépôt choisies et des niveaux de dopage de type n atteignant $1.7 \times 10^{20}\,\mathrm{cm}^{-3}$ ont été obtenus. Ces couches nouvellement développées ont été mises à profit dans nos structures prototypes décrites dans le chapitre 5. Cependant, le dopage au phosphore du µc-Si :H est connu pour être plus facile à obtenir que sa contrepartie, c'est-à-dire le µc-Si :H dopé au bore de type p.

4.1.2 µc-Si :H type-p

Le savoir-faire acquis sur la croissance du µc-Si :H de type n doit être complété avec le µc-Si :H de type p dans notre objectif de produire des couches empilées de semi-conducteurs N-I-P. Afin d'obtenir du silicium dopé au bore, des conditions de dépôt identiques à celles utilisées pour le dépôt *low power* de µc-Si :H dopé au phosphore ont été utilisées. Le précurseur gazeux dopant PH_3 a été remplacé par B_2H_6 (dilué à 1000 ppm dans H_2) à une concentration $\beta = B_2H_6/SiH_4$ comprise entre 0,05 % et 0,5 %.

Étude structurale et électrique du µc-Si :H dopé au bore

Les spectres Raman obtenus pour chaque échantillon sont présentés dans la figure 9 ainsi que les valeurs calculées pour X_c en fonction du rapport de gaz dopant β. Contrairement au µc-Si :H de type n déposé dans des conditions similaires, la microstructure de la couche s'est avérée être fortement affectée par l'incorporation de bore, la couche déposée passant d'un matériau hautement cristallisé ($X_c = 78\,\%$) à un matériau complètement amorphe au-dessus de $\beta = 0,3\,\%$. Cette dégradation continue des propriétés structurelles avec l'augmentation du flux de diborane a été observée par d'autres groupes [28, 34] et a été interprétée comme une conséquence du désordre local induit par la fluctuation de la longueur des liaisons. Il a également été rapporté par [35] que le bore a tendance à former un complexe bore-hydrogène-silicium dans <p> µc-Si :H, ce qui peut encore ajouter au désordre local du matériau, empêchant la nucléation de la phase cristalline.

Discussion : Dopage au bore de µc-Si :H

Le dopage au bore du Si :H est notoirement difficile à obtenir, même avec un facteur de dilution aussi élevé que $R_H = 50$. Le niveau de dopage maximal obtenu était de $p = 3,39 \times 10^{18}\,\mathrm{cm}^{-3}$, ce qui est considérablement inférieur au µc-Si :H dopé au phosphore et pourrait limiter le champ électrique s'étendant dans l'absorbeur intrinsèque d'une architecture de photodiode P-I-N. Une dilution supplémentaire de l'hydrogène pourrait être une solution pour empêcher l'amorphisation de la couche à des \bêta plus élevés en échange de taux de croissance plus faibles. Dans le contexte de notre travail, le niveau de dopage actif p atteint avec $\beta = 0,05\,\%$ est toujours une option viable bien que non idéale.

Cette thèse est accessible à l'adresse : https://theses.insa-lyon.fr/publication/2023ISAL0014/these.pdf
© [A. Wilson], [2023], INSA Lyon, tous droits réservés

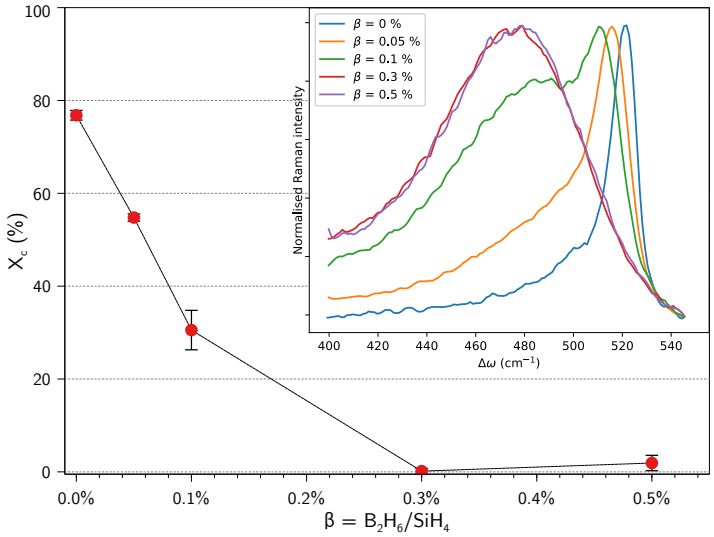

FIGURE 9 – Spectres Raman normalisés et cristallinité Raman calculée X_c de µc-Si:H dopé au bore pour différents rapports de gaz de dopage β, allant de 0 % à 0,5 %. Les données montrent la dégradation de la structure cristalline avec l'augmentation de la concentration en B_2H_6.

Si l'on considère cette question du point de vue d'une photodiode, si la couche de type p est située sur la face arrière de la photodiode, il n'est pas nécessaire d'avoir une couche fenêtre à bande interdite élevée. Une couche Ge :H ou SiGe :H dopée au bore pourrait être utilisée, à condition que des niveaux de dopage plus élevés puissent être atteints.

4.2 Dopage *in situ* de µc-Ge :H

L'amorphisation de la couche de silicium microcristallin avec l'incorporation de dopants s'est avérée être un problème, quel que soit le type de dopage. Dans le cas du dopage au phosphore, une augmentation de la dilution de l'hydrogène était suffisante pour maintenir une bonne qualité cristalline. D'autre part, le dopage au bore a conduit à une amorphisation rapide dans des conditions de dépôt équivalentes.

4.2.1 Caractérisation électrique du µc-Ge :H type-p

La conductivité \$sigma$, la concentration de dopage actif p et la mobilité Hall μ_H ont été obtenues par des mesures d'effet Hall à température ambiante avec des couches de 170 nm d'épaisseur déposées sur du verre. De l'InGa liquide a été utilisé pour obtenir un contact ohmique avec la couche semi-conductrice. Le µc-Ge :H intrinsèque ($\beta = 0\,\%$) s'est avéré avoir un niveau de dopage de fond de type p relativement élevé ($1,6\times10^{17}\,\mathrm{cm}^{-3}$) qui peut être corrélé aux courants d'obscurité élevés et à la faible photoréponse trouvés dans le chapitre 3, section 3.2. Ce dopage de fond peut provenir d'une contamination in-situ pendant le dépôt (d'un processus de dépôt antérieur impliquant du phosphore) ou être une conséquence directe des grandes queues de bande de µc-Ge :H. Il est peu probable que cette caractéristique provienne d'une exposition à des températures élevées. Il est peu probable que cette caractéristique provienne de l'exposition à l'oxygène, car un dopage de type n aurait été attendu.

Le dopage, la conductivité et la mobilité sont représentés sur la figure 10. La conductivité σ augmente de $0,086\,\mathrm{S}\cdot\mathrm{cm}^{-1}$ à $118\,\mathrm{S}\cdot\mathrm{cm}^{-1}$ avec l'ajout de diborane, ce qui est principalement lié

Cette thèse est accessible à l'adresse : https://theses.insa-lyon.fr/publication/2023ISAL0014/these.pdf
© [A. Wilson], [2023], INSA Lyon, tous droits réservés

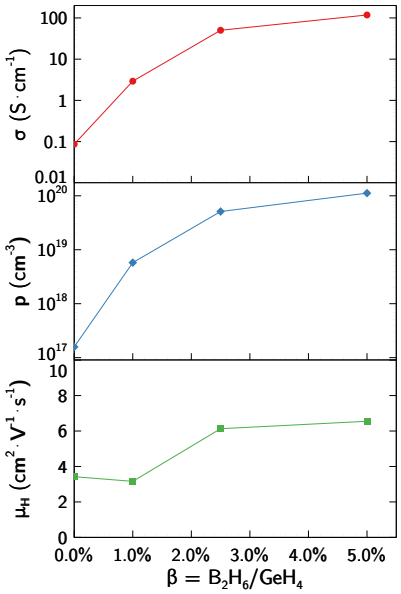

FIGURE 10 – Mesure de la conductivité et de la mobilité par effet Hall de µc-Ge:H dopé au bore.

à l'augmentation de p puisque μ_H varie à peine sur la plage étudiée et reste de l'ordre de 3 à 6 $cm^2/V \cdot s$. Il est intéressant de noter que μ_H augmente avec β et donc avec le niveau de dopage, contrairement au comportement habituel trouvé dans les semi-conducteurs cristallins tels que le silicium [36]. Ce résultat peut être interprété comme une diminution de la hauteur de la barrière de potentiel aux limites du grain qui existe en raison des états pièges, comme précédemment rapporté par [37, 38] dans le cas du µc-Si :H dopé au phosphore. Le résultat le plus intéressant concernant notre objectif est que le dopage de type p aussi élevé que $p = 1.12 \times 10^{20}\,cm^{-3}$ a été atteint. Comparé au niveau de dopage maximal de $3,4 \times 10^{18}\,cm^{-3}$ obtenu pour <p>µc-Si :H, le dopage au bore du µc-Ge :H semble assez prometteur. En effet, les films µc-Ge :H ont pu conserver leurs propriétés structurelles malgré un débit élevé de gaz diborane.

Conclusion : Dopage au bore de µc-Ge :H

Dans cette section, il a été démontré que du germanium hautement microcristallin pouvait être obtenu en dopant fortement le matériau in-situ. L'addition de diborane B_2H_6 à un mélange germanium / hydrogène peut facilement produire des couches semi-conductrices de type p avec des niveaux de dopage atteignant plus de $10^{20}\,cm^{-3}$. Aucun impact clair de l'incorporation de bore sur les propriétés structurelles du film n'a été trouvé dans la gamme étudiée, étant cependant limité par le débit maximum de gaz diborane de 100 sccm. On pense que le taux d'activation des atomes de bore incorporés dans le film est extrêmement faible et peut induire des états de défauts indésirables ayant un impact sur les longueurs de diffusion des porteurs. Puisqu'il a été démontré précédemment que le µc-Ge :H avait des propriétés électriques médiocres (chapitre 3, section 4.2.1), le remplacement du µc-Si :H de type p par le µc-Ge :H de type p ne peut être réalisé que si une couche cristalline suffisamment fine peut être obtenue afin de limiter l'absorption et la recombinaison indésirables dans la partie dopée au bore de la jonction P-I-N.

Cette thèse est accessible à l'adresse : https://theses.insa-lyon.fr/publication/2023ISAL0014/these.pdf
© [A. Wilson], [2023], INSA Lyon, tous droits réservés

4.3 Conclusion

Dans ce chapitre, nous avons cherché à développer une couche de semi-conducteurs de type n et p obtenue par PECVD pour les futurs prototypes de photodiodes P-I-N. L'obtention de couches microcristallines minces avec des niveaux de dopage élevés était un objectif clé pour améliorer les performances optiques et électriques des futurs dispositifs. Une couche optiquement mince est nécessaire pour minimiser l'absorption parasite dans la gamme spectrale NIR tandis que les niveaux de dopage élevés ont un impact direct sur le champ électrique dans la couche absorbante.

Dans la première section du chapitre, il a été montré que le phosphore empêchait la nucléation des cristallites et conduisait à des couches amorphes. L'adaptation des conditions de dépôt à un facteur de dilution élevé R_H a permis de maintenir une forte cristallinité et d'atteindre des niveaux de dopage $n > 10^{20}\,\mathrm{cm}^{-3}$. Le dopage au bore du µc-Si :H a été mis en œuvre en utilisant la même approche mais a conduit à une amorphisation rapide de la couche avec l'augmentation du précurseur de bore en phase gazeuse. A faible débit de gaz diborane, une couche cristalline a cependant pu être obtenue, au prix de niveaux de dopage n'atteignant que $p = 3.4 \times 10^{18}\,\mathrm{cm}^{-3}$.

Les inconvénients du µc-Si :H de type p nous ont conduits à explorer une autre option dans la deuxième section : le µc-Ge :H dopé au bore. L'ajout de diborane à un mélange germane / hydrogène n'a pas affecté de manière significative la cristallinité des films déposés. Alors que X_c est resté pratiquement constant (~63 %), l'incorporation de bore dans la couche a augmenté la conductivité de 3 décades, avec un niveau de dopage maximal $p = 1.1 \times 10^{20}\,\mathrm{cm}^{-3}$. Le principal inconvénient de ce matériau est le faible taux d'incorporation et d'activation du bore, qui pourrait se traduire par une augmentation des défauts électriques. Le coefficient d'absorption élevé du µc-Ge :H dans la gamme spectrale visible et NIR implique que le µc-Ge :H ne devrait être utilisé que comme une couche très mince sur la face arrière du dispositif.

Cette étude de 3 matériaux distincts a surtout porté sur l'intégrité structurelle et l'efficacité du dopage de notre procédé. Les améliorations potentielles futures pourraient inclure les aspects d'ingénierie du diagramme de bande ainsi que la compatibilité de la fonction de travail. On pourrait en effet affiner le dopage et la composition chimique des couches p/n afin d'obtenir des contacts sélectifs efficaces pour les trous ou les électrons. Ces aspects nécessiteraient toutefois de considérer le dispositif dans son ensemble afin d'optimiser chaque couche les unes par rapport aux autres. Dans le dernier chapitre, nous nous attacherons à prendre les trois briques de construction de notre prototype de photodiode, c'est-à-dire la couche de type p, l'absorbeur et la couche de type n, et à concevoir un dispositif fonctionnel.

5 Conception, fabrication et caractérisation de prototypes de photodiodes

Dans ce dernier chapitre, notre approche passera de l'optimisation des matériaux individuels à la construction d'un dispositif photosensible simple. Certains aspects de notre prototype jugés trop éloignés de la portée de notre travail sur les semi-conducteurs microcristallins ne seront pas étudiés en profondeur. Des considérations telles que l'ingénierie des diagrammes de bande ou la conception de revêtements anti-reflets seront donc laissées de côté.

Les trois principaux éléments constitutifs de notre prototype de photodiode P-I-N ont été développés individuellement dans les chapitres précédents. Le dopage au phosphore et au bore du µc-Si :H et du µc-Ge :H pour les couches N et P a été abordé dans le chapitre 4 tandis qu'il a été constaté dans le chapitre 3 que la couche absorbante intrinsèque (I) devait être basée sur

Cette thèse est accessible à l'adresse : https://theses.insa-lyon.fr/publication/2023ISAL0014/these.pdf
© [A. Wilson], [2023], INSA Lyon, tous droits réservés

des alliages µc-SiGe :H.

5.1 Conception du prototype

Plusieurs contraintes doivent être prises en considération lors de la conception de la géométrie du prototype. Ces contraintes se répartissent en trois catégories principales : la robustesse, la compatibilité avec les processus et la complexité. Après quelques essais, la conception présentée dans la figure 11 a été sélectionnée. Il consiste en un substrat revêtu d'ITO sur lequel des couches de semi-conducteurs de type n, i et p sont déposées pour former la partie photosensible du dispositif. Une tranchée centrale est laissée non déposée pour que la cathode soit formée directement sur l'ITO. Les 8 anodes sont placées sur le dessus de la couche de type p. Avec cette architecture, la lumière doit traverser le substrat de verre et l'ITO pour atteindre la photodiode PIN. Cette structure pourrait être améliorée car aucune couche de passivation de surface n'a été utilisée.

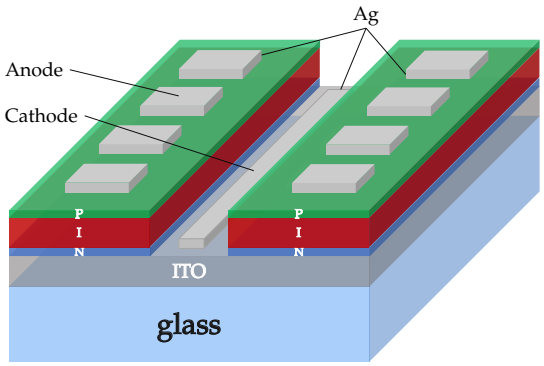

FIGURE 11 – Représentation schématique de la conception du prototype proposé pour les photodiodes P-I-N. Chaque échantillon contient 8 contacts électriques définissant 8 photodiodes indépendantes.

Un tel échantillon mesure 20 mm de long, 15 mm de large et 1,1 mm d'épaisseur. Il est obtenu par un procédé en 3 étapes sans lithographie, schématisé dans la figure 12. Cette structure et ce procédé particuliers présentent quelques avantages essentiels par rapport aux contraintes définies ci-dessus, au prix de quelques inconvénients.

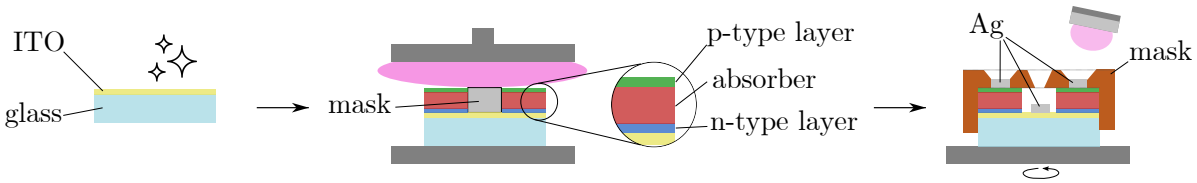

(a) ITO Cleaning

(b) PECVD deposition of N-I-P junction

(c) Sputtering of Silver Contacts

FIGURE 12 – Processus de production du dispositif prototype (a) le verre revêtu d'ITO est nettoyé (b) les parties N, I et P de la diode sont déposées par PECVD avec un masque central afin d'avoir accès à l'ITO (c) pulvérisation de l'anode et de la cathode métalliques en utilisant un masque imprimé en 3D.

Cette thèse est accessible à l'adresse : https://theses.insa-lyon.fr/publication/2023ISAL0014/these.pdf
© [A. Wilson], [2023], INSA Lyon, tous droits réservés

5.2 Influence de la composition de l'absorbeur sur les performances du dispositif

Le chapitre 3 nous a laissé des questions en suspens concernant les performances opto-électroniques des alliages µc-SiGe :H. En mettant en œuvre différentes compositions de l'alliage comme couche absorbante pour notre structure précédemment définie, nous cherchons à trouver le compromis optimal entre absorption et longueur de diffusion en conditions réelles. Afin de passer en revue l'ensemble des compositions de l'alliage µc-SiGe :H, onze prototypes ont été produits avec une structure identique et une fraction de germanium absorbante croissante.

5.2.1 Caractérisation structurale

Les sections transversales TEM obtenues à partir des échantillons SiGe55% et SiGe60% sont présentées dans les figures 13a et 13b respectivement. Les films ITO, µc-Si :P, µc-SiGe :H et µc-Si :B peuvent être clairement identifiés grâce à leur contraste en nombre atomique. Des caractéristiques de croissance colonnaire sont visibles dans les deux couches absorbantes de l'échantillon. Aucun signe de fissures ou de cloques n'a été trouvé aux interfaces.

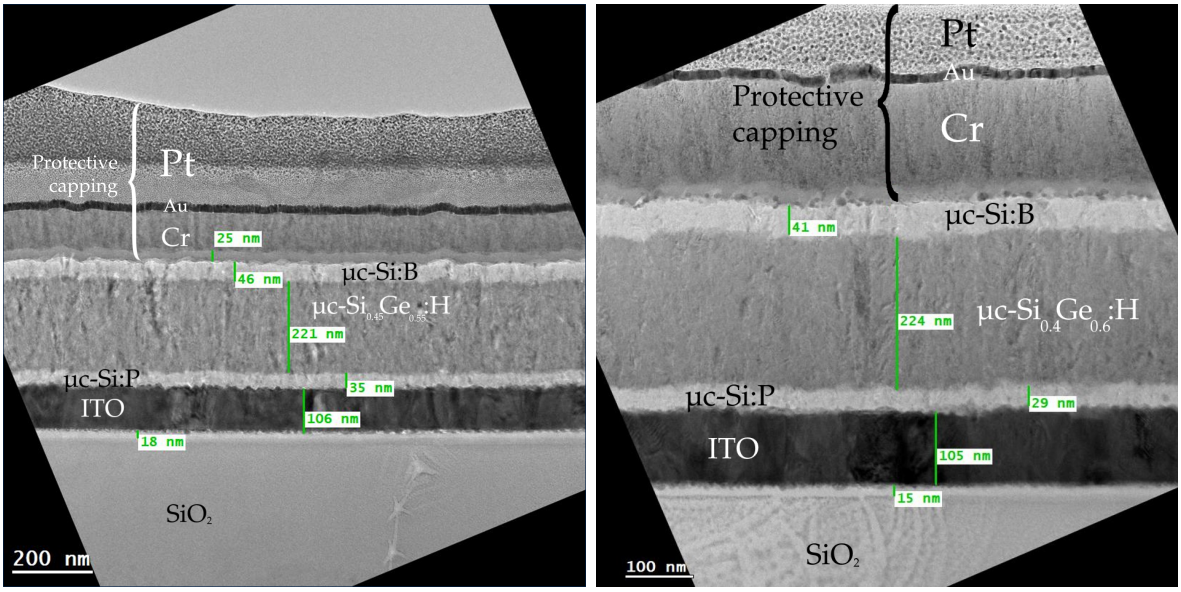

(a) (b)

FIGURE 13 – Coupe transversale TEM de la pile de couches verre / ITO / µc-Si:P / µc-SiGe:H / µc-Si:B pour les échantillons (a) SiGe55% (b) SiGe60%.

Les mesures d'épaisseur montrent que l'objectif de 50 nm / 200 nm / 50 nm de l'épaisseur du film NIP ne correspondait pas parfaitement. La couche de µc-Si :H de type n s'est avérée aussi mince que 29 nm avec une épaisseur moyenne de l'ordre de 33 nm. La rugosité de l'interface induite par la cristallisation joue certainement un rôle dans la déviation de l'épaisseur. La couche µc-Si :H de type p, déposée dans des conditions presque identiques, était plus proche de l'épaisseur cible de 50 nm (46 nm pour SiGe55%). Nous soupçonnons que la cinétique de croissance du film µc-Si :P a été affectée par le film ITO sous-jacent car la vitesse de croissance du film a été calibrée avec des substrats c-Si (voir chapitre 4).

La couche absorbante a été mesurée comme étant 11 % plus épaisse que ce qui avait été anticipé en utilisant notre modèle d'extrapolation. En tenant compte de la rugosité de l'interface, l'épaisseur de la couche absorbante de l'échantillon SiGe60% a été mesurée à 223 ± 8 nm.

Cette thèse est accessible à l'adresse : https://theses.insa-lyon.fr/publication/2023ISAL0014/these.pdf
© [A. Wilson], [2023], INSA Lyon, tous droits réservés

Les deux échantillons analysés ont donné des résultats comparables ; par conséquent, seules les données concernant SiGe60% seront présentées par souci de clarté.

La présence d'un absorbeur microcristallin a été confirmée précédemment pour tous les échantillons par spectroscopie Raman. La haute résolution des images TEM obtenues permet de voir les structures périodiques caractéristiques de la phase cristalline.

5.2.2 Efficacité quantique des photodiodes N-I-P

L'efficacité quantique (QE) est l'une des principales valeurs de mérite utilisées pour évaluer les performances des photodiodes dans le domaine du proche infrarouge. Cette méthode de caractérisation opto-électronique fournit une vue d'ensemble des performances du dispositif en mesurant le rapport entre les porteurs de charge extraits et les photons entrants. Un bon QE ne peut être obtenu que si de bonnes propriétés optiques rencontrent de bonnes propriétés de transport.

Nos échantillons avec une fraction croissante de Ge absorbant ont été caractérisés à incidence normale dans la gamme $\lambda = 300 - 1100$ nm. Des mesures s'étendant plus loin dans la gamme NIR ont été effectuées plus loin dans ce chapitre sur les échantillons les plus prometteurs. L'efficacité quantique externe (EQE) pour les échantillons allant de $x_{Ge} = 0à75\,\%$ est indiquée dans la figure 14, le Ge100% n'a pas été affiché car les valeurs EQE étaient inférieures à 0,2 %.

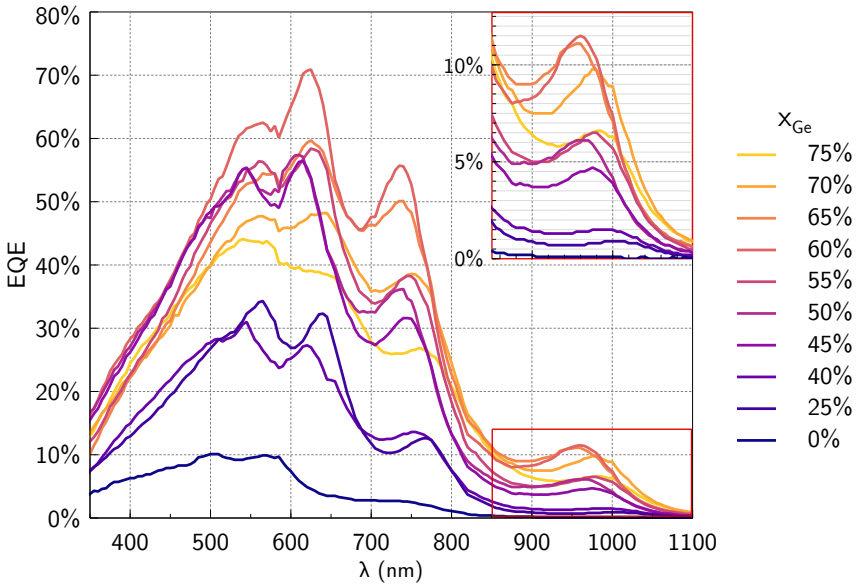

FIGURE 14 – Rendement quantique externe en fonction de la longueur d'onde pour les dispositifs SiGe NIP. L'absorbeur a une épaisseur de 200 nm et sa composition x_{Ge} varie dans la gamme de 0 à 75 %.

Comme l'EQE comptabilise le nombre d'électrons extraits par rapport au nombre total de photons entrants, certaines oscillations dans les courbes apparaissent, correspondant à des interférences constructives et destructives se produisant à des longueurs d'onde spécifiques. La période de ces oscillations est directement liée à l'épaisseur globale de notre jonction NIP et à l'indice de réfraction de notre couche. La similitude de la période d'oscillation entre tous les échantillons est donc due à la similitude de leur épaisseur et de leur indice de réfraction. Les résultats de la figure 14 permettent de tirer plusieurs conclusions.

Cette thèse est accessible à l'adresse : https://theses.insa-lyon.fr/publication/2023ISAL0014/these.pdf
© [A. Wilson], [2023], INSA Lyon, tous droits réservés

Résultats Expérimentaux

IQE(\lambda) a été calculé pour tous les échantillons précédemment caractérisés avec une fraction Ge croissante de l'absorbeur. Les tendances observées précédemment pour l'EQE sont toujours valables pour l'IQE :

- Un IQE élevé est obtenu dans le domaine visible (plus de 80 % pour les meilleurs échantillons). Ce résultat est encourageant compte tenu de la simplicité de la structure conçue.
- la valeur optimale pour la composition de l'alliage est $\mu c - Si_{0.4}Ge_{0.6} : H$. L'échantillon SiGe60% est plus performant sur toute la gamme spectrale, avec un IQE(1000 nm) atteignant 17,6 %. Ceci est dû à la réflectivité élevée de l'échantillon à ces longueurs d'onde qui a été prise en compte.
- Les absorbeurs $\mu c - Si_{1-x}Ge_x : H$ avec x_{Ge} supérieur à 60 % voient leur IQE se dégrader sur toute la gamme testée, ce qui suggère que la longueur de diffusion dans l'absorbeur devient sensiblement plus petite que son épaisseur.
- l'IQE de tous les dispositifs chute brusquement au-delà de \lambda=800 nm et ne dépasse pas 4 % à λ=1100 nm.

5.3 Performances optoélectroniques des photodiodes NIP polarisées en inverse

Jusqu'à présent dans ce chapitre, les prototypes de jonctions NIP produits ont été testés dans des conditions de court-circuit, c'est-à-dire en l'absence de toute polarisation inverse externe. Cette méthode de mesure a permis d'obtenir des spectres EQE même pour des échantillons à faible résistance de shunt et a aidé à comparer nos échantillons sur une base commune. L'application d'une polarisation inverse à nos photodiodes nous rapproche des conditions de fonctionnement réelles et constitue donc la prochaine étape de ce projet.

5.3.1 Efficacité quantique des jonctions NIP polarisées en inverse

Les résultats obtenus en polarisant SiGe60%400nm ont dépassé nos attentes. La figure 15 montre l'EQE du dispositif obtenu à une polarisation inverse croissante, allant de 0mV à -900 mV par pas de 150 mV.

5.4 Conclusion

Ce dernier chapitre a été consacré à l'utilisation des connaissances acquises sur les semiconducteurs microcristallins intrinsèques et dopés pour produire un dispositif photosensible simple. Nous avons proposé une conception simple pour notre photodiode qui répond aux contraintes du budget thermique des capteurs d'image CMOS above-IC en maintenant l'ensemble du processus sous 250 °C. Pour arriver à cette preuve de concept, un processus de production en 3 étapes a été développé tout en essayant de maximiser la robustesse et de minimiser la complexité. Pour répondre à ces deux aspects, certains compromis ont dû être faits concernant le choix des couches de contact électrique et les dimensions des photodiodes. Le prototype a donc certainement pu être amélioré grâce à l'ingénierie des diagrammes de bande, à la passivation des interfaces et à la conception de revêtements anti-reflets. Bien que la conception soit connue pour être imparfaite, certains résultats encourageants ont été obtenus.

Un ensemble d'échantillons avec une fraction croissante de Ge dans la couche absorbante a été testé afin de trouver l'alliage µc-SiGe :H offrant le meilleur compromis entre l'absorption de la lumière et l'extraction des charges. La structure testée était composée de verre / ITO(100 nm) / <n>µc-Si :H(50 nm) / µc-$Si_{1-x}Ge_x$:H(200nm) / <p>µc-Si :H(50 nm) / Ag. Les tests

Cette thèse est accessible à l'adresse : https://theses.insa-lyon.fr/publication/2023ISAL0014/these.pdf
© [A. Wilson], [2023], INSA Lyon, tous droits réservés

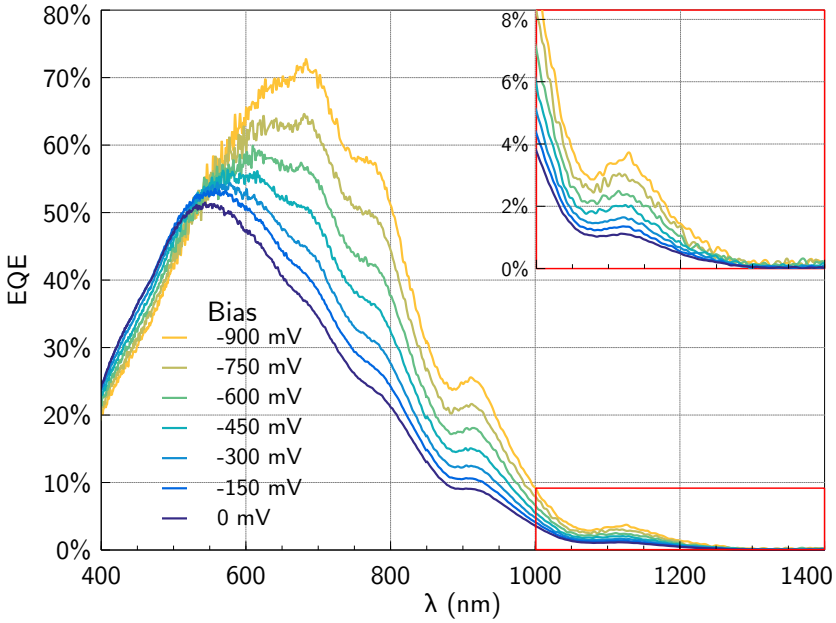

FIGURE 15 – Impact sur l'EQE d'une polarisation inverse externe appliquée à la jonction NIP avec un absorbeur $\mu c - Si_{0.4}Ge_{0.6} : H$ de 400 nm (SiGe60%400nm).

électriques ont confirmé que nos dispositifs se comportent comme des diodes et les mesures d'efficacité quantique interne ont révélé que leur sensibilité pouvait s'étendre à 1100 nm avec seulement un absorbeur de 200 nm d'épaisseur. Comme prévu, l'utilisation de µc-Si :H ou de µc-Ge :H comme couches absorbantes a conduit aux pires performances en raison de limitations optiques et électriques respectivement. Un optimum pour la composition du film a été trouvé avec une couche de $\mu c - Si_{0.4}Ge_{0.6} : H$ avec un IQE aussi élevé que 17.6 % à λ=1000 nm. La modélisation optique du dispositif à l'aide de SILVACO a permis de mieux comprendre les limites de la photodiode. L'efficacité quantique externe du dispositif s'est avérée proche de son maximum théorique dans le domaine visible, mais a commencé à diminuer dans le proche infrarouge.

L'impact de l'épaisseur de l'absorbeur sur les propriétés opto-électroniques a ensuite été étudié dans le but d'étendre la sensibilité dans le proche infrarouge. Une structure identique à la précédente a été utilisée, avec un absorbeur $\mu c - Si_{0.4}Ge_{0.6} : H$ d'épaisseur variable. Les résultats ont montré que l'absorbeur de 200 nm d'épaisseur était toujours plus performant en moyenne, avec un IQE atteignant plus de 80 % dans le domaine visible. Cependant, l'échantillon de 400 nm d'épaisseur s'est avéré plus performant à λ=1100 nm avec un IQE de 5 %.

La sensibilité des photodiodes testées jusqu'à présent est conforme à nos attentes dans le domaine visible mais se dégrade rapidement lorsqu'on atteint le NIR, en partie à cause de la couche d'ITO. Les IQE de nos échantillons ont été obtenus sans polarisation externe. L'application d'une polarisation inverse à la jonction NIP a montré qu'un gain de 250 % en EQE pouvait être obtenu dans la région NIR. Le gain de l'EQE avec la polarisation est attribué à l'extension du champ électrique dans l'absorbeur qui modifie le mécanisme de transport de charge qui n'est plus régi par la longueur de diffusion mais par la vitesse de dérive. La modélisation optique détaillée dans l'annexe A a prouvé l'existence d'une limite supérieure pour l'efficacité quantique externe du dispositif. La polarisation externe a permis de pousser l'EQE expérimentale près de cette limite théorique.

Cette thèse est accessible à l'adresse : https://theses.insa-lyon.fr/publication/2023ISAL0014/these.pdf
© [A. Wilson], [2023], INSA Lyon, tous droits réservés

Ce chapitre a montré que les semi-conducteurs µc-SiGe :H déposés par PECVD peuvent effectivement être utilisés pour produire des photodétecteurs robustes et simples à faible budget thermique. La conception simple de notre photodiode a permis de fournir un prototype fonctionnel pour tester l'influence de la composition et de l'épaisseur de l'absorbeur sur les propriétés opto-électroniques globales. Le comportement de la diode et la possibilité de polariser notre jonction est une preuve que ces matériaux, bien que très défectueux, peuvent être utilisés en tant que capteurs.

Conclusion et perspectives

Au cours de ce projet, nous avons cherché à développer des films minces de silicium-germanium hydrogénés à faible budget thermique, englobant des matériaux allant du a-Ge :H pur aux alliages $\mu c - Si_{1-x}Ge_x : H$. Notre objectif final consistait à intégrer ces films nouvellement développés dans un prototype de photodiode dont la sensibilité dans la gamme spectrale NIR pouvait s'étendre jusqu'à 1350 nm. Dans le contexte du développement de ces dispositifs pour des capteurs d'images CMOS above-IC, nous devions nous assurer que la température du processus tout au long des étapes de fabrication ne dépassait pas 350 °C.

Le chapitre 2 a présenté les techniques expérimentales de dépôt et de caractérisation utilisées au cours de ce projet. Les spécifications de l'équipement PECVD, pièce centrale du dépôt de films SiGe :H, ont été présentées. Dans le chapitre 3, nous avons cherché à produire des films minces de matériaux semi-conducteurs adaptés aux couches d'absorption dans le proche infrarouge (λ= 940 à 1350 nm) dans les futurs prototypes de photodiodes P-I-N. Dans le chapitre 4 nous avons cherché à obtenir des couches minces microcristallines avec des niveaux de dopage élevés. Les critères d'épaisseur et de niveau de dopage étaient essentiels pour améliorer les performances optiques et électriques des futurs dispositifs. Dans le chapitre 5, un design simple pour un prototype de photodiode a été proposé. La structure de test consistait en un empilement verre / ITO / <n>µc-Si :H / µc-$Si_{1-x}Ge_x$:H / <p>µc-Si :H / Ag avec un absorbeur d'environ 200 nm d'épaisseur. L'application d'une polarisation inverse de 0,9 V à l'échantillon avec un absorbeur µc-$Si_{0.4}Ge_{0.6}$:H de 400 nm d'épaisseur a montré qu'un gain de 250 % en EQE pouvait être obtenu dans la région NIR jusqu'à λ=1250 nm. Le gain d'EQE sous polarisation est probablement dû au fait que le mécanisme de transport de charge n'est plus régi par la longueur de diffusion mais par la vitesse de dérive. Les prototypes développés au cours de ce chapitre ont montré que les photodétecteurs NIR compatibles CMOS above-IC basés sur les alliages µc-$Si_{1-x}Ge_x$:H sont expérimentalement réalisables.

Cette thèse est accessible à l'adresse : https://theses.insa-lyon.fr/publication/2023ISAL0014/these.pdf
© [A. Wilson], [2023], INSA Lyon, tous droits réservés

Bibliographie

[1] Henry Baltes. “CMOS as sensor technology”. In : *Sensors and Actuators A : Physical*. Proceedings of Eurosensors VI 37-38 (1er juin 1993), p. 51-56. doi : 10.1016/0924-4247(93)80011-5.

[2] A.J. Walton et al. “Silicon - Post Processing CMOS Wafers to Create Integrated Sensors, Mems and Electro-Optic Systems”. In : *SAIEE Africa Research Journal* 101.1 (mars 2010), p. 3-10. doi : 10.23919/SAIEE.2010.8532213.

[3] Jurriaan Schmitz. “Microchip Post-Processing : There is Plenty of Room at the Top”. In : *Future Trends in Microelectronics*. John Wiley & Sons, Ltd, 2013, p. 110-119.

[4] J. A. Theil. “Advances in elevated diode technologies for integrated circuits : progress towards monolithic instruments”. In : *IEE Proceedings - Circuits, Devices and Systems* 150.4 (1er août 2003), p. 235-249. doi : 10.1049/ip-cds:20030529.

[5] C. Miazza et al. “Performance analysis of a-Si :H detectors deposited on CMOS chips”. In : *MRS Online Proceedings Library* 808.1 (1er déc. 2003), p. 269-274. doi : 10.1557/PROC-808-A4.46.

[6] Jurriaan Schmitz. “Adding functionality to microchips by wafer post-processing”. In : *Nuclear Instruments and Methods in Physics Research Section A : Accelerators, Spectrometers, Detectors and Associated Equipment*. Proceedings of the 8th International Workshop on Radiation Imaging Detectors 576.1 (11 juin 2007), p. 142-149. doi : 10.1016/j.nima.2007.01.142.

[7] Gautam Ganguly et Akihisa Matsuda. “Defect formation during growth of hydrogenated amorphous silicon”. In : *Physical Review B* 47.7 (15 fév. 1993), p. 3661-3670. doi : 10.1103/PhysRevB.47.3661.

[8] Shingo Okamoto et al. “Towards large-area, high-efficiency a-Si/a-SiGe tandem solar cells”. In : *Solar Energy Materials* (2001), p. 10.

[9] M. Krause et al. “Role of Bandgap Grading for the Performance of Microcrystalline Silicon Germanium Solar Cells”. In : *MRS Online Proceedings Library Archive* 557 (1999). doi : 10.1557/PROC-557-591.

[10] Amaresh Dey et Debajyoti Das. “Narrow band gap high conducting nc-Si1-xGex :H absorber layers for tandem structure nc-Si solar cells”. In : *Journal of Alloys and Compounds* 806 (25 oct. 2019), p. 1529-1535. doi : 10.1016/j.jallcom.2019.07.320.

[11] B. Rech et al. “Microcrystalline silicon for large area thin film solar cells”. In : *Thin Solid Films*. Proceedings of Symposium K on Thin Film Materials for Large Area Electronics of the European Materials Research Society (E-MRS) 2002 Spring Conference 427.1 (3 mars 2003), p. 157-165. doi : 10.1016/S0040-6090(02)01210-5.

[12] T. Matsui et al. “Microcrystalline silicon–germanium alloys for solar cell application : Growth and material properties”. In : *Journal of Non-Crystalline Solids*. Amorphous and Nanocrystalline Semiconductors - Science and Technology 352.9 (15 juin 2006), p. 1255-1258. doi : 10.1016/j.jnoncrysol.2005.11.144.

Cette thèse est accessible à l'adresse : https://theses.insa-lyon.fr/publication/2023ISAL0014/these.pdf
© [A. Wilson], [2023], INSA Lyon, tous droits réservés

[13] Yu Cao et al. “Non-uniform distribution in µc-Si1−xGex :H and its influence on thin film and device performance”. In : *Solar Energy Materials and Solar Cells* 151 (1er juill. 2016), p. 1-6. DOI : 10.1016/j.solmat.2016.02.009.

[14] Takuya Matsui et al. “Influence of alloy composition on carrier transport and solar cell properties of hydrogenated microcrystalline silicon-germanium thin films”. In : *Applied Physics Letters* 89.14 (2 oct. 2006), p. 142115. DOI : 10.1063/1.2358318.

[15] Takuya Matsui et al. “Microcrystalline Si1-xGex Solar Cells Exhibiting Enhanced Infrared Response with Reduced Absorber Thickness”. In : *Applied Physics Express* 1.3 (7 mars 2008), p. 031501. DOI : 10.1143/APEX.1.031501.

[16] Takuya Matsui et al. “Application of microcrystalline Si1−xGex infrared absorbers in triple junction solar cells”. In : *2010 35th IEEE Photovoltaic Specialists Conference*. 2010 35th IEEE Photovoltaic Specialists Conference. Juin 2010, p. 000311-000316. DOI : 10.1109/PVSC.2010.5615904.

[17] M. Krause et al. “Microcrystalline Germanium Photodetectors”. In : *MRS Proceedings* 664 (2001), A26.5.1. DOI : 10.1557/PROC-664-A26.5.1.

[18] M Isomura et al. “Microcrystalline silicon–germanium solar cells for multi-junction structures”. In : *Solar Energy Materials and Solar Cells* 74.1 (oct. 2002), p. 519-524. DOI : 10.1016/S0927-0248(02)00069-7.

[19] O Vetterl et al. “Intrinsic microcrystalline silicon : A new material for photovoltaics”. In : *Solar Energy Materials and Solar Cells* 62.1 (15 avr. 2000), p. 97-108. DOI : 10.1016/S0927-0248(99)00140-3.

[20] Edward D. Palik. *Handbook of Optical Constants of Solids*. Academic Press, 1998. 1019 p.

[21] R. Cariou et al. “Low temperature epitaxial growth of SiGe absorber for thin film heterojunction solar cells”. In : *Solar Energy Materials and Solar Cells* 134 (1er mars 2015), p. 15-21. DOI : 10.1016/j.solmat.2014.11.018.

[22] Yu Cao et al. “Hydrogenated microcrystalline silicon germanium as bottom sub-cell absorber for triple junction solar cell”. In : *Solar Energy Materials and Solar Cells* 114 (juill. 2013), p. 161-164. DOI : 10.1016/j.solmat.2013.03.004.

[23] Akihisa Matsuda. “Amorphous and Microcrystalline Silicon”. In : *Springer Handbook of Electronic and Photonic Materials*. Sous la dir. de Safa Kasap et Peter Capper. Springer Handbooks. Cham : Springer International Publishing, 2017, p. 573-587. DOI : 10.1007/978-3-319-48933-9_25.

[24] V. Chu et al. “Ion implantation of microcrystalline silicon for low process temperature top gate thin film transistors”. In : *Thin Solid Films* 337.1 (11 jan. 1999), p. 203-207. DOI : 10.1016/S0040-6090(98)01177-8.

[25] P. G. Le Comber et al. “Electrical and photoconductive properties of ion implanted amorphous silicon”. In : *Journal of Non-Crystalline Solids* 35-36 (1er jan. 1980), p. 327-332. DOI : 10.1016/0022-3093(80)90615-8.

[26] Anna Di Nocera, Alberto Mittiga et Alfredo Rubino. “Electrical properties of heavily doped μc-Si :H”. In : *Journal of Applied Physics* 78.6 (15 sept. 1995), p. 3955-3960. DOI : 10.1063/1.359916.

[27] Q. Guo et X. Geng. “Deposition High Quality P-type Microcrystalline Silicon Thin Films by RF-PECVD”. In : *2019 6th International Conference on Systems and Informatics (ICSAI)*. 2019 6th International Conference on Systems and Informatics (ICSAI). Nov. 2019, p. 263-267. DOI : 10.1109/ICSAI48974.2019.9010228.

[28] R. Saleh et N. H. Nickel. “Raman spectroscopy of B-doped microcrystalline silicon films”. In : *Thin Solid Films*. Proceedings of Symposium K on Thin Film Materials for Large Area Electronics of the European Materials Research Society (E-MRS) 2002 Spring Conference 427.1 (3 mars 2003), p. 266-269. DOI : 10.1016/S0040-6090(02)01203-8.

Cette thèse est accessible à l'adresse : https://theses.insa-lyon.fr/publication/2023ISAL0014/these.pdf
© [A. Wilson], [2023], INSA Lyon, tous droits réservés

[29] "*p* - *n* Junctions". In : S.M. Sze et Kwok K. Ng. *Physics of Semiconductor Devices*. Hoboken, NJ, USA : John Wiley & Sons, Inc., 10 avr. 2006, p. 77-133. DOI : 10.1002/9780470068328.ch2.

[30] P Roca i Cabarrocas. "Plasma enhanced chemical vapor deposition of amorphous, polymorphous and microcrystalline silicon films". In : *Journal of Non-Crystalline Solids* 266-269 (1er mai 2000), p. 31-37. DOI : 10.1016/S0022-3093(99)00714-0.

[31] Wensheng Wei et al. "Raman spectra of intrinsic and doped hydrogenated nanocrystalline silicon films". In : *Vacuum* 81.5 (5 jan. 2007), p. 656-662. DOI : 10.1016/j.vacuum.2006.09.006.

[32] U. Backhausen et al. "Hall-Effect Studies on Microcrystalline Silicon with Different Structural Composition and Doping". In : *MRS Online Proceedings Library* 452.1 (1er déc. 1996), p. 833-838. DOI : 10.1557/PROC-452-833.

[33] D. P. Stevenson. "The Strengths of Chemical Bonds". In : *Journal of the American Chemical Society* 77.8 (1er avr. 1955), p. 2350-2350. DOI : 10.1021/ja01613a116.

[34] N. H. Nickel, P. Lengsfeld et I. Sieber. "Raman spectroscopy of heavily doped polycrystalline silicon thin films". In : *Physical Review B* 61.23 (15 juin 2000), p. 15558-15561. DOI : 10.1103/PhysRevB.61.15558.

[35] X. L. Jiang, Y. L. He et H. L. Zhu. "The effect of passivation of boron dopants by hydrogen in nano-crystalline and micro-crystalline silicon films". In : *Journal of Physics : Condensed Matter* 6.3 (jan. 1994), p. 713. DOI : 10.1088/0953-8984/6/3/011.

[36] S. M. Sze et Kwok Kwok Ng. *Physics of semiconductor devices*. 3rd ed. Hoboken, N.J : Wiley-Interscience, 2007. 815 p.

[37] T. I. Kamins. "Hall Mobility in Chemically Deposited Polycrystalline Silicon". In : *Journal of Applied Physics* 42.11 (1er oct. 1971), p. 4357-4365. DOI : 10.1063/1.1659780.

[38] T Weis et al. "Barrier-limited carrier transport in highly n-doped μc-Si :H thin films". In : *Journal of Non-Crystalline Solids*. 19th International Conference on Amorphous and Microcrystalline Semiconductors 299-302 (1er avr. 2002), p. 380-384. DOI : 10.1016/S0022-3093(01)00954-1.

Cette thèse est accessible à l'adresse : https://theses.insa-lyon.fr/publication/2023ISAL0014/these.pdf
© [A. Wilson], [2023], INSA Lyon, tous droits réservés

Cette thèse est accessible à l'adresse : https://theses.insa-lyon.fr/publication/2023ISAL0014/these.pdf
© [A. Wilson], [2023], INSA Lyon, tous droits réservés

Remerciements

Ce manuscrit est l'aboutissement de trois années consacrées à accroître, à mon échelle, les connaissances scientifiques dans le domaine des nanotechnologies. Aucun aspect de ce projet n'aurait pu avoir le jour sans mes encadrants, Erwann Fourmond, Bilel Saidi et Mickaël Gros-Jean. Mener à bien ce travail de recherche aura en effet nécessité de la patience, des remises en questions, mais surtout d'être bien entouré.

Merci donc en tout premier lieu à STMicroelectronics et particulièrement à Bilel et Mickaël pour m'avoir confié ce projet où tout était à faire et pour m'avoir accompagné lors de mes premiers pas dans la R&D. Merci à Bilel pour la confiance qu'il m'a accordé et pour son accueil au sein de l'équipe TT. Bien que le COVID ait rendu mes venues sur Crolles plus rares que prévues, ça aura toujours été un plaisir de partager nos perspectives sur les résultats et l'avancement de la thèse.

Je remercie également l'Institut des Nanotechnologies de Lyon (INL), mon laboratoire d'accueil à Lyon qui m'a permis de mener à bien une large partie des aspects expérimentaux présentés dans ce manuscrit. Avant toute autre personne merci à Erwann pour m'avoir accordé toute son attention pendant ces trois années, que ça soit autour d'un pain au chocolat ou à s'arracher les cheveux devant un tableau blanc. Sa disponibilité, son exigence scientifique et son incomparable sens de l'humour ont apporté une délectable sérénité à cette thèse – qui par bien d'autres égards pouvait avoir ses hauts et ses bas. Merci à la plateforme Nano-Lyon d'avoir permis le bon fonctionnement de ce rouage complexe qu'est une plateforme de micro/nano-fabrication. Ma gratitude va en tout particulier à Benjamin Fornacciari, pour son humeur invariablement joviale, les longs repas au Pied du Saule et sans qui aucun dépôt n'aurait probablement vu le jour. Je n'oublierai pas de mentionner Jean-Charles Roux, MacGyver de la salle blanche, et Céline Chevalier, mon ancienne tutrice de PFE et véritable moteur au sein de cette plateforme. J'en profite également pour remercier l'équipe i-Lum ainsi que tous les permanents avec qui j'ai eu l'occasion de discuter et de maniper pendant ces trois années. Merci à Fabien Mandorlo pour m'avoir initié aux mesures de réponse spectrales et pour sa passion partagée des cimes. Merci à Virginie Lagarde pour sa patience et sa pédagogie face à ma phobie administrative. Merci enfin à Hala Houmsi pour son investissement au cours de son PFE, ses simulations ayant permis d'élever notre compréhension des résultats de cette thèse. Puisqu'en science on avance pas seul, merci à Élodie Roméo de l'Institut Lumière Matière pour l'accès à la spectroscopie Raman. Merci à Christophe Longeaud du GeePs pour son expertise lors des mesures par SSPG et de réponse spectrale. Merci enfin à Jean-Gabriel Mattei et Marc Juhel pour les analyses TEM et SIMS.

Toutes ces journées passées au laboratoire n'aurait pas eu la même saveur sans l'équipe de choc des non-permanents du laboratoire, qu'ils soient doctorant.e.s, post-doc, ou autres... Merci donc à Jérémy mon rival des questions en réunion et guerrier du dancefloor, à Théo co-bureau de légende, mon Sam Gamegie pendant la rédaction et frère de San Francisco, à Robin dont le mystère des sandwichs au jambon ne fut élucidé que trop tard, à Huiru et Oksana les

Cette thèse est accessible à l'adresse : https://theses.insa-lyon.fr/publication/2023ISAL0014/these.pdf
© [A. Wilson], [2023], INSA Lyon, tous droits réservés

deux inséparables comparses, à Paule et son humour décapant, à Maxime le recordman du monde du trajet La Doua - Ecully, à Eva, Baptiste, Giovanni, Charif, Hugo et tous les autres.

Voilà qui m'amène aux acteurs de l'ombres... Les potes de l'INSA, Stany, Thib, Benya, Ccil, Ogo, Robich, Eloi, Pénélope, dont les prémices de l'amitié furent forgés il y a pratiquement dix ans. Les grimpeurs, Adèle (x2), Adrien, Fantou, Linon et Colin avec qui on grimpe moins qu'on fait la sieste. Ma famille, Yohann et Jason, et surtout mes parents sans qui je n'écrirai pas ces mots aujourd'hui. Et pour finir Gabrielle, qui m'a soutenu pendant ces trois années et même plus, avec qui j'ai partagé mes joies, mes peines et ma vie.

Cette thèse est accessible à l'adresse : https://theses.insa-lyon.fr/publication/2023ISAL0014/these.pdf
© [A. Wilson], [2023], INSA Lyon, tous droits réservés

Development of Microcrystalline Germanium and Silicon-Germanium Thin Films for Above-IC Near Infrared Image Sensors

Cette thèse est accessible à l'adresse : https://theses.insa-lyon.fr/publication/2023ISAL0014/these.pdf
© [A. Wilson], [2023], INSA Lyon, tous droits réservés

Cette thèse est accessible à l'adresse : https://theses.insa-lyon.fr/publication/2023ISAL0014/these.pdf
© [A. Wilson], [2023], INSA Lyon, tous droits réservés

Résumé

Le marché croissant de l'internet des objets (IoT) encourage le développement de nouveaux capteurs fiables et à faible coût. Les imageurs CMOS ne font pas exception. L'industrie automobile et téléphonique en particulier sont friands d'imageurs pour le proche infrarouge pour observer leur environnement. Leur coût peut être réduit en s'appuyant sur une approche above-IC de l'intégration CMOS dans laquelle les photodiodes du capteur sont produites après les transistors et les interconnexions. Les procédés above-IC sont donc intrinsèquement limités en budget thermique en raison de la structure CMOS sous-jacente à la photodiode.

Dans ce contexte, l'objectif de ce travail est de produire et de caractériser des couches minces de silicium-germanium et de germanium hydrogénés déposés à basse température (< 350 °C) pour imageurs above-IC sensibles dans le proche infrarouge. Une preuve de concept de l'utilisation de ces matériaux pour la détection en proche IR est donnée avec le développement et la caractérisation d'une photodiode. Compte tenu des limitations thermiques, le dépôt chimique en phase vapeur assisté par plasma (PECVD) sera utilisé pour développer des semi-conducteurs amorphes et microcristallins allant du silicium (µc-Si:H) aux alliages de silicium-germanium microcristallin (µc-$Si_{1-x}Ge_x$:H). L'incorporation de germanium est bénéfique pour l'absorption du NIR de la couche mince obtenue en raison de son faible gap par rapport au silicium.

Pour atteindre les objectifs fixés, des couches minces intrinsèques de µc-Ge:H et µc-SiGe:H sont obtenus par PECVD pour être utilisées en tant qu'absorbeur dans de futurs dispositifs. L'étude de ses matériaux se focalise sur l'impact des conditions de dépôt sur les propriétés structurelles, électriques et optiques des couches. La fabrication d'une photodiode nécessitant la réalisation d'une jonction P-I-N, le dopage de type p et de type n de couches microcristallines au phosphore et au bore est donc étudié. En s'appuyant sur ces briques individuelles, une photodiode est conçue pour tester expérimentalement l'efficacité des matériaux développés dans un dispositif réel. Ce prototype de photodiode permet de trouver la composition et l'épaisseur optimale pour l'absorbeur et permet également comprendre les mécanismes à l'origine des pertes dans les dispositifs.

Mots clés : microcristallin, silicium-germanium, above-IC, PECVD, photodiode, NIR

Cette thèse est accessible à l'adresse : https://theses.insa-lyon.fr/publication/2023ISAL0014/these.pdf
© [A. Wilson], [2023], INSA Lyon, tous droits réservés

Cette thèse est accessible à l'adresse : https://theses.insa-lyon.fr/publication/2023ISAL0014/these.pdf
© [A. Wilson], [2023], INSA Lyon, tous droits réservés

Abstract

The growing internet of things (IoT) market pushes for the development of reliable and low cost sensors. CMOS image sensors are no exception. In particular, near infrared sensitive image sensors are needed to map their surroundings. Their cost can be driven down by relying on an above-IC approach to CMOS integration in which the photodiodes are produced after the transistors and interconnections. Above-IC processes are thus intrinsically limited in terms of process temperature due to the presence of the underlying CMOS structure.

In this context, the goal of this work is to produce and characterize hydrogenated Silicon-Germanium and Germanium thin films deposited at low temperature (< 350 °C) for NIR sensitive above-IC CMOS image sensors. On top of that, we aim to prove the validity of our concept by fabricating and testing a photodiode based on these materials. With the thermal limitations in mind, plasma enhanced chemical vapor deposition (PECVD) will be used to develop amorphous and microcrystalline semiconductors ranging from microcrystalline silicon (µc-Si:H) to microcrystalline silicon-germanium alloys (µc-$Si_{1-x}Ge_x$:H). Incorporating Germanium is beneficial to NIR absorption of the thin film obtained due to its low bandgap compared to silicon.

In an effort to reach our objective, intrinsic µc-Si:H, µc-Ge:H and µc-SiGe:H thin films are obtained by PECVD to be used as an absorber layer in future devices. The emphasis is put on establishing the impact of deposition conditions on the structural, electrical and optical properties of the films. Producing a photodiode requires a P-I-N junction to be made. In a second phase, p-type and n-type doping of microcrystalline films using phosphorus and boron is thus investigated. With all the necessary building blocks available, a photodiode is designed to test the relevance of the developed material in practical conditions. With this test structure an optimal absorber layer composition and thickness is found and insight is gained on the mechanisms responsible for losses in the devices.

Keywords: microcrystalline, silicon-germanium, above-IC, PECVD, photodiode, NIR

Cette thèse est accessible à l'adresse : https://theses.insa-lyon.fr/publication/2023ISAL0014/these.pdf
© [A. Wilson], [2023], INSA Lyon, tous droits réservés

Contents

Remerciements i

Résumé v

Abstract vii

Contents viii

Introduction 1

1 State of the Art : from basics of PECVD to µc-SiGe:H growth 5
1 Near Infrared SiGe photodetectors : an overview 5
1.1 Monocrystalline photodetectors 5
1.2 Above-IC compatible photodectectors 6
2 Basics of Plasma Enhanced Chemical Vapor Deposition 9
2.1 A Brief Introduction to Plasmas 9
2.2 Plasma-Enhanced Chemical Vapor Deposition (PECVD) 11
3 Hydrogenated Silicon thin films 14
3.1 Microcrystalline Hydrogenated Silicon 15
4 Hydrogenated Germanium films 21
4.1 Hydrogenated Germanium film deposition 21
4.2 Optoelectronic properties of Ge:H films 23
5 $Si_{1-x}Ge_x$:H alloy production and properties 26
5.1 PECVD deposition of µc-SiGe:H films 26
5.2 Optoelectronic properties 27
6 Goal of the Ph.D thesis project 29

2 Materials and Methods 31
1 Deposition and cleaning process 31
1.1 PECVD equipment at INL 31
1.2 Substrate cleaning procedure 35
2 Chemical and Structural characterization 37
2.1 Raman Spectroscopy 38
2.2 Transmission Electron Microscopy 43
2.3 Secondary Ion Mass Spectrometry 46
3 Optical characterization 48
3.1 Spectroscopic Ellipsometry 48
3.2 Optical Reflectometry 52

Cette thèse est accessible à l'adresse : https://theses.insa-lyon.fr/publication/2023ISAL0014/these.pdf
© [A. Wilson], [2023], INSA Lyon, tous droits réservés

3.3 Quantum Efficiency . . . 53
4 Electrical characterization . . . 55
4.1 Hall Effect characterization . . . 55
4.2 Diffusion length measurement using Steady State Photocarrier Grating Method . . . 57
5 Conclusion . . . 59

3 Development and Characterization of Absorber Layer Materials 61
1 Hydrogenated Silicon thin films development . . . 61
1.1 From amorphous to microcrystalline Silicon films . . . 62
1.2 Insight into µc-Si:H micro-structure . . . 62
1.3 Optical properties of µc-Si:H . . . 65
1.4 Conclusion : µc-Si:H thin films . . . 66
2 Hydrogenated Germanium thin films development . . . 67
2.1 Structural properties of µc-Ge:H thin films . . . 67
2.2 Optical properties of µc-Ge:H . . . 71
2.3 Electrical properties of µc-Ge:H . . . 74
2.4 Conclusion : µc-Ge:H thin films . . . 76
3 Hydrogenated Silicon- Germanium alloys development . . . 76
3.1 From gas phase SiH_4 + GeH_4 to solid $Si_{1-x}Ge_x$: H films . . . 77
3.2 Optical properties of µc-SiGe:H alloys . . . 82
3.3 Minority carriers diffusion length in µc-SiGe:H alloys . . . 86
3.4 Conclusion : µc-SiGe:H thin films . . . 88
4 Conclusion : Absorber layer materials development . . . 88
Key Points . . . 90

4 Doped Microcrystalline Semiconductors for pn Junctions 91
1 Doping requirements for pin structure . . . 91
2 *In situ* doping of µc-Si:H . . . 92
2.1 n-type µc-Si:H . . . 93
2.2 p-type µc-Si:H . . . 99
3 *In situ* doping of µc-Ge:H . . . 102
3.1 Boron-doped µc-Ge:H . . . 102
4 Conclusion . . . 105
Key Points . . . 106

5 Design, Fabrication and Characterization of Photodiode Prototypes 107
1 Prototype design and fabrication . . . 107
1.1 Prototype design . . . 107
1.2 Substrate and front contact selection . . . 109
1.3 N-I-P Junction . . . 111
1.4 Back contact selection . . . 112
1.5 Sample testing . . . 113
2 Influence of absorber composition on device performance . . . 113
2.1 Deposition conditions of N-I-P stacks . . . 114
2.2 Structural characterization of prototype photodiodes . . . 116
2.3 Opto-electronic characterization and modeling . . . 119

Cette thèse est accessible à l'adresse : https://theses.insa-lyon.fr/publication/2023ISAL0014/these.pdf
© [A. Wilson], [2023], INSA Lyon, tous droits réservés

2.4 Discussion : influence of absorber Ge fraction of opto-electronic performance . . . 129
3 Influence of µc-$Si_{0.4}Ge_{0.6}$:H layer thickness on opto-electronic properties . . . 130
3.1 Deposition conditions . . . 130
3.2 Opto-electronic characterization . . . 131
3.3 Discussion : Influence of absorber thickness on opto-electronic performances . . . 133
4 Opto-electronic performance of reverse biased NIP photodiodes . . . 133
4.1 Experimental setup and sample selection . . . 133
4.2 Quantum efficiency of reverse biased NIP junctions . . . 134
5 Conclusion . . . 136
Key Points . . . 138

Conclusion and Outlooks **139**

A Optical modeling of NIP devices with SILVACO **143**
1 Modeling setup . . . 143
2 *SiGe60%200nm* NIP photodiode modeling . . . 144
3 *SiGe60%400nm* NIP photodiode modeling . . . 144

List of Figures **149**

List of Tables **155**

Bibliography **156**

Cette thèse est accessible à l'adresse : https://theses.insa-lyon.fr/publication/2023ISAL0014/these.pdf
© [A. Wilson], [2023], INSA Lyon, tous droits réservés

Introduction

General context

The growing internet of things (IoT) market and the increasing needs of the automotive and mobile phone industries are pushing for the development of reliable, low cost sensors. Whether they measure temperature, health indicators or capture surrounding sounds, these sensors meet the need for highly interconnected objects to interact with their environment. Among these sensors, CMOS image sensors are a widely used type of sensor found in mobile phones and cameras to obtain a digital image.

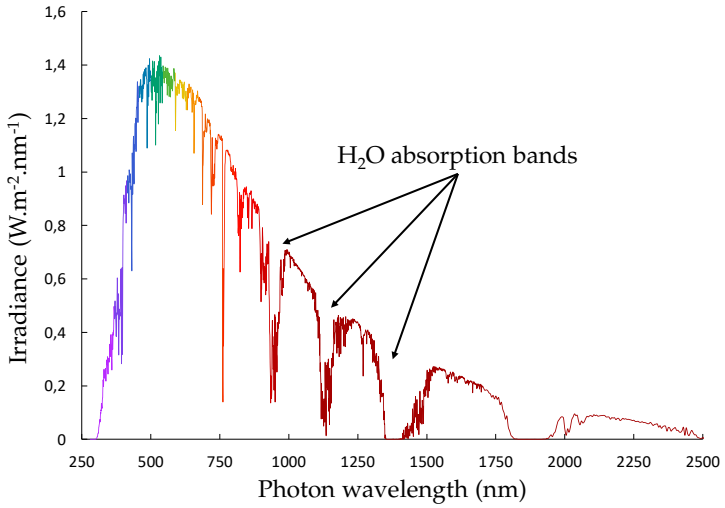

Figure 0.1: Solar irradiance at ground level when the sun is at a 48.2° zenith angle (AM1.5g). The solar spectrum resembles a 5250 °C black body, with absorption bands due to the atmosphere. In particular water vapor in the atmosphere is responsible for 3 dips in the irradiance at 940, 1130 and 1350 nm.

The material used for the manufacture of the photosensitive part of the sensor necessarily depends on the targeted spectral range. The optically active region of most CMOS image sensors is made of crystalline silicon. While c-Si is perfectly suited for visible light ($\lambda = 400$ – 800 nm) absorption, its absorption in the near-infrared (NIR) region ($\lambda = 800$ – 2500 nm) drops rapidly due to its indirect 1.12 eV band-gap. In this Ph.D thesis we will aim to develop NIR sensitive semiconductors suitable for CMOS image sensors. We will focus in particular on a restricted spectral range between 900 and 1350 nm. This spectral range is of particular interest due to the Sun's irradiance spectrum at ground level, shown in figure 0.1.

In this spectrum, 3 major drops in irradiance appear at $\lambda = 940$, 1130 and 1350 nm due to absorption by water vapor in the atmosphere. For face recognition applications for instance,

Cette thèse est accessible à l'adresse : https://theses.insa-lyon.fr/publication/2023ISAL0014/these.pdf
© [A. Wilson], [2023], INSA Lyon, tous droits réservés

the face is lit by a NIR LED invisible to the human eye. The reflected light reaching the CMOS sensor then forms an image which is processed by the device. By working at wavelengths of 940, 1130 or 1350 nm the environmental noise due to sunlight is minimal, allowing better signal to noise ratio even in difficult lighting conditions.

The CMOS image sensor itself is the component on which we will focus. It can be divided into three main types according to its architecture : Frontside, Backside and Above Integrated Circuit (above-IC) illuminated sensors. A schematic representation of these different sensor architectures is provided in figure 0.2.

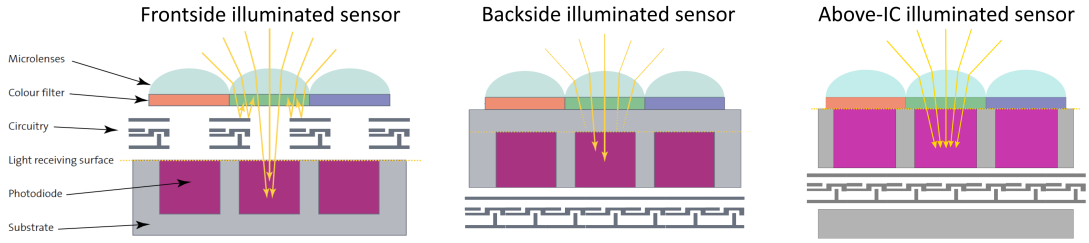

Figure 0.2: Schematic representation of 3 CMOS types of image sensors (frontside, backside and above-IC), defined by the location of the photodiode. Adapted from STEMMER Imaging.

The fronside and backside architectures are based on a front-end fabrication of the photodiode, prior to transistors and interconnections being made. Above-IC CMOS sensors on the other hand come from a "More than Moore" approach to integration, aiming to add new functionalities to CMOS systems after the fabrication of transistors and interconnections. With such a design no shading occurs from the interconnections (unlike frontside sensors) and the substrate doesn't need to be thinned to prevent parasitic absorption (unlike backside sensors). These potential advantages come at a cost. The photodiode fabrication process temperature has to be limited to avoid damaging the underlying CMOS structure. This is due to the risk of impurity diffusion and material degradation at the interconnection level. A higher limit in the order of 350 to 400°C is thus commonly accepted for post-interconnection processes. As a consequence it is impossible to rely on high temperature processes like epitaxy, silicon oxidation, dopant activation annealing or materials curing. This strong constraint on the thermal budget of the photodiode deposition process calls for the development of NIR sensitive materials which can be deposited at low temperature. During this project, we chose to use Plasma Enhanced Chemical Vapor Deposition to account for this constraint. With PECVD, a wide variety of materials can be grown at low temperatures (from room temperature to 400 °C) from gas phase precursors.

Objectives of the Ph.D project

The goal of this Ph.D thesis is to develop PECVD grown thin films from silicon and germanium precursors and integrate them into a simple and functional, NIR sensitive, prototype photodiode. The materials obtained range from hydrogenated amorphous germanium to microcrystalline silicon-germanium alloys. The use of germanium – a low band-gap material – makes it possible to reach high absorption coefficients in the spectral range of interest. These materials could thus be suitable for near infrared sensors. The exotic structural properties of amorphous and microcrystalline films lead to optoelectronic properties which differ significantly from their crystalline counter-part.

Cette thèse est accessible à l'adresse : https://theses.insa-lyon.fr/publication/2023ISAL0014/these.pdf
© [A. Wilson], [2023], INSA Lyon, tous droits réservés

In the first chapter, an overview of the current knowledge gathered on these materials will be given. The second chapter will then focus on the equipments and techniques necessary to produce and characterize individual semiconductor layer as well as completed optoelectronic devices. The challenges faced for photodiode fabrication remain numerous. First, a high quality absorber layer with strong optical absorption in the NIR spectral range has to be developed. Chapter 3 thus will be dedicated to the development of high quality intrinsic Si:H, Ge:H and SiGe:H thin films by PECVD, with an emphasis on the structural, electrical and optical properties of such films. Secondly, p-type and n-type doping of microcrystalline films should be achieved so as to produce a P-I-N junction. Chapter 4 will investigate the electrical and structural properties of Phosphorus and Boron doped Si:H and Ge:H films. Ultimately, these building blocks will have to be integrated as a single functional device with the highest quantum efficiency possible, while making sure the whole process is compatible with CMOS above-IC integration constraints. This aspect will be addressed in chapter 5 were previously developed layers will be used to produce a PIN junction architecture integrated to a simple prototype photodiode.

Cette thèse est accessible à l'adresse : https://theses.insa-lyon.fr/publication/2023ISAL0014/these.pdf
© [A. Wilson], [2023], INSA Lyon, tous droits réservés

Cette thèse est accessible à l'adresse : https://theses.insa-lyon.fr/publication/2023ISAL0014/these.pdf
© [A. Wilson], [2023], INSA Lyon, tous droits réservés

Chapter 1

State of the Art : from basics of PECVD to µc-SiGe:H growth

Plasma-Enhanced Chemical Vapor Deposition (PECVD) makes it possible to manufacture a wide range of thin films, using only a low thermal budget. Although abundant literature can be found concerning amorphous and microcrystalline silicon (a/µc-Si:H) - in part due to its use in the solar cells industry - studies regarding PECVD grown Silicon-Germanium and pure Germanium are less common. Such silicon-germanium based alloys have a great potential for optical sensors due to their high absorption coefficient in the visible to near-infrared spectral range, especially when compared to crystalline Silicon and its 1,12 eV bandgap energy (1107 nm).

In this chapter, a brief overview of existing Ge and SiGe photodetectors will be proposed, with an emphasize on above-IC compatible devices reported in the literature. In further section we will seek to explore the different experimental conditions necessary for the production of high quality, above-IC compatible $Si_{1-x}Ge_x$: H thin films ranging from pure Silicon ($x = 0$) to pure Germanium ($x = 1$). Starting from the basics of PECVD deposition we will then provide an overview of structural and optoelectronic properties of Si:H, Ge:H and SiGe:H films as well as the experimental conditions necessary for their production.

1 Near Infrared SiGe photodetectors : an overview

The need for near infrared sensitive photodetectors emerged with the democratization of fast optical communication. Indeed, optical fiber's attenuation is minimal at a wavelength $\lambda = 1.55$ µm which led to a need for new high performing sensors since silicon sensors responsivity was limited by its 1.12 eV band gap. [1, 2] For wavelengths above 1100 nm, Germanium and its 0.66 eV band gap was an straightforward option and was used as early as the 1950's [3].

1.1 Monocrystalline photodetectors

To reach the high responsivity and extreme operating frequencies by far exceeding the gigahertz [4, 5], crystalline Germanium photodetectors are typically grown by Molecular Beam Epitaxy (MBE) and Vapor Phase Epitaxy (VPE) on a GaAs or Si substrate at high temperatures [6]. The 4 % mismatch in lattice size between the Si substrate and the Ge photodiode

Cette thèse est accessible à l'adresse : https://theses.insa-lyon.fr/publication/2023ISAL0014/these.pdf
© [A. Wilson], [2023], INSA Lyon, tous droits réservés

calls for the use of a finely tuned strain-relaxed buffer layer [7, 8] which allows the growth of micron thick Ge layers with minimal crystalline defects. Ge deposition and subsequent annealing stepsof such devices typically take place in the 700 to 1050 °C range [5] and yield fast and NIR sensitive photodectectors. Some examples of the optical properties of such devices are given in figures 1.1a and 1.1b. The responsivity $R = EQE \times \frac{q}{h\nu}$ as a function of photon wavelength is given for SiGe and Ge photodiodes in a PIN configuration in figure 1.1a. Although only the data at 850, 1300 and 1550 nm were measured experimentally, the impact of Ge incorporation on NIR sensitivity is clear.

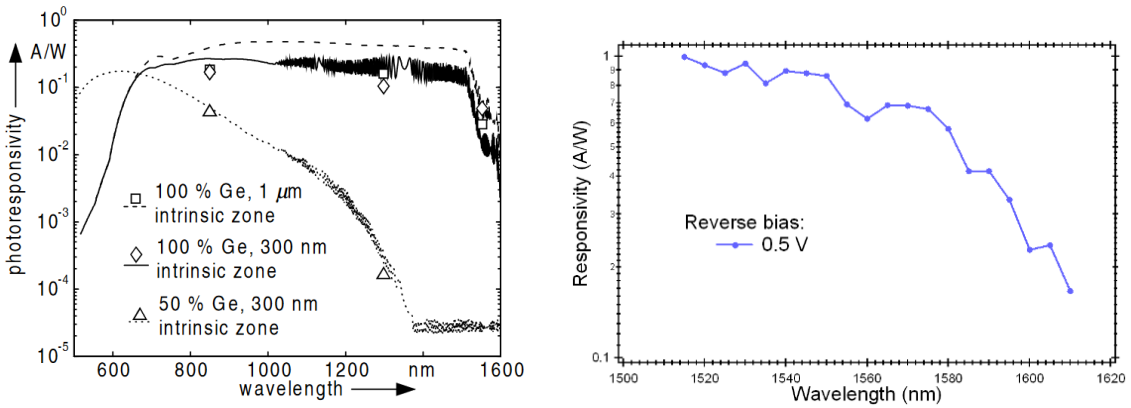

(a) (b)

Figure 1.1: (a) Simulated (solid and dotted lines) and experimental (points) responsivity for SiGe and Ge photodectectors at -1 V bias [4] (b) Responsivity of a 15 µm thick Ge photodectector at -0.5 V bias [5]

Since our spectral range of interest (940 to 1340 nm) does not extend as far as 1.55 µm, Germanium is not the only suitable material for our intended use. SiGe which performed poorly at higher wavelengths (figure 1.1a) can be a valuable option as shown in figure 1.2 Schmitz et al. [9] simulated the responsivity for 10 µm thick, above-IC, c-$Si_{1-x}Ge_x$ PIN photodiodes. According to the spectral range of interest, the composition of the SiGe alloy can be tuned to fit our needs. These results were however only obtained from simulation.

1.2 Above-IC compatible photodectectors

In practice the thermal limitations for above-IC of CMOS post-processing [10, 11] are fundamentally incompatible with MBE and VPE processes and monocrystalline growth of devices such as those described by Schmitz et al. [9].

The rise of above-IC technologies

Above-IC or CMOS post-processing is a concept which dates back to the 1990's [12]. It gained traction a decade later as a mean to add new functionalities to CMOS systems in a "More than Moore" approach to integration [10, 11]. The potential of this approach in terms of performance, compactness and cost has been discussed by research groups in the microelectronics sector [10, 13–15] but calls for the introduction of new materials in the industry which are compatible with the constraints of CMOS technology and the underlying CMOS structure.

Cette thèse est accessible à l'adresse : https://theses.insa-lyon.fr/publication/2023ISAL0014/these.pdf
© [A. Wilson], [2023], INSA Lyon, tous droits réservés

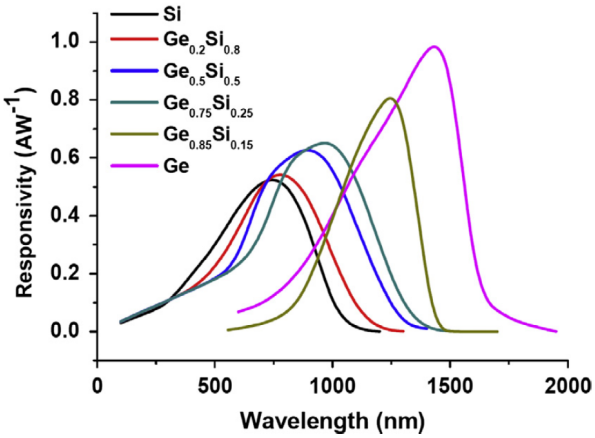

Figure 1.2: Responsivity for a 10 µm thick c-SiGe PIN photodiode at variable Ge fraction obtained by Silvaco simulation. [9]

The photovoltaic push for NIR absorption

In parallel, research in the photovoltaic (PV) domain and the quest for ever-increasing energy conversion efficiency has led to an interest for low band-gap materials for bottom cells for tandem structures. [16–20] In order to achieve flexible, low cost and high efficiency solar cells the materials developed for that purpose were often deposited at low temperatures. These amorphous and microcrystalline silicon and germanium-based semiconductors were thus inherently above-IC compatible and could be great candidates for NIR sensing application.

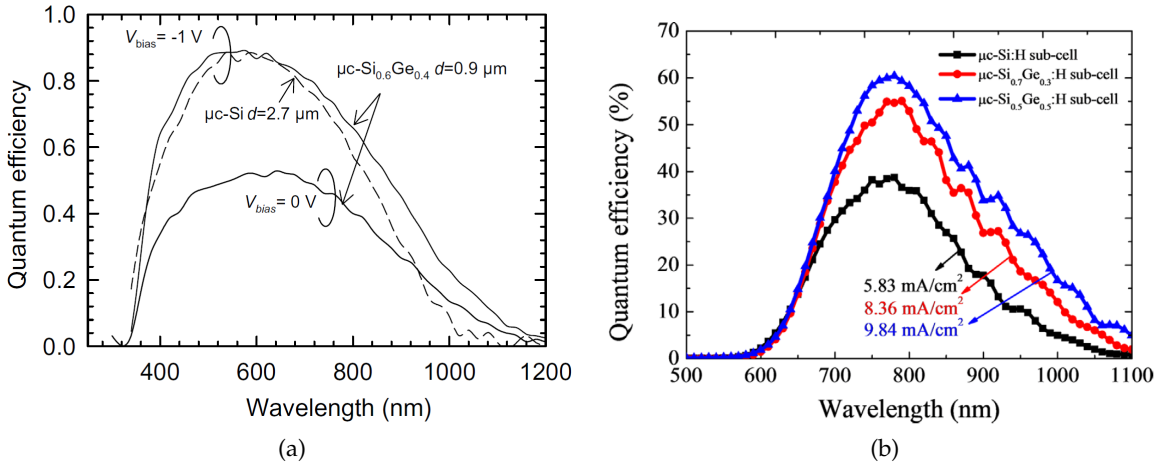

Figure 1.3: Quantum efficiency of PIN solar cells with a : (a) 900 nm thick µc-$Si_{0.6}Ge_{0.4}$:H absorber [21] (b) 1 µm thick µc-$Si_{0.5}Ge_{0.5}$:H absorber [22].

Solar cells with high collection efficiency - also named quantum efficiency - were reported in the literature with sensitivity extending into near infrared thanks to the introduction of Germanium in hydrogenated SiGe alloys. Matsui et al. [21, 23–25] were able to produce a solar cell with a 900 nm thick microcrystalline $Si_{0.6}Ge_{0.4}$:H absorber with a sensitivity extending into to 1200 nm [21] (10 % at 1100 nm under -1V bias, see figure 1.3a). Other groups [22] obtained similar results (see figure 1.3b) with a quantum efficiency at 1100 nm reaching 5 %.

Cette thèse est accessible à l'adresse : https://theses.insa-lyon.fr/publication/2023ISAL0014/these.pdf
© [A. Wilson], [2023], INSA Lyon, tous droits réservés

Not being only limited to SiGe:H alloys, Krause et al. [26] reported a microcrystalline Germanium photodetector deposited at low temperature. The device was reported to work under reverse bias (-0.2 V) and showed promising collection efficiency (see figure 1.4) which reached 15 % at 1100 nm with a 110 nm absorber.

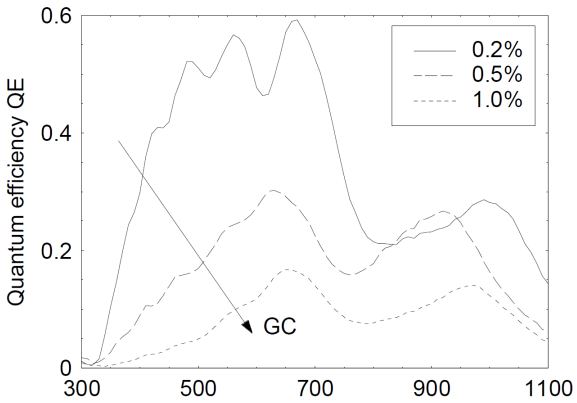

Figure 1.4: Quantum efficiency for a PIN photodiode with a 110 nm thin µc-Ge:H absorber deposited by PECVD at different germane concentration GC. Measurements were done under -0.2 V bias at 250 K.[26]

The interest of such devices lied in the low thermal budget needed for manufacturing a device with a total thickness well under 1 µm. Figure 1.5 provides example of an architecture used for a PIN solar cell together with the measured quantum efficiency. [27]

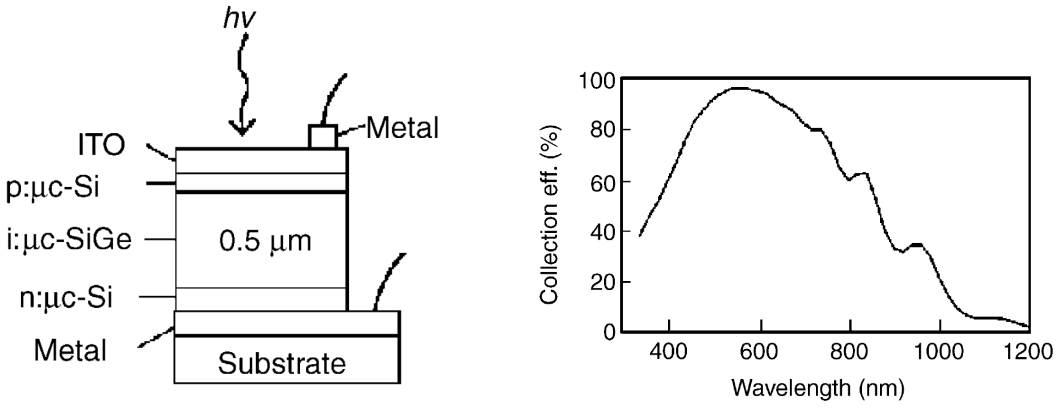

(a) (b)

Figure 1.5: (a) Test structure and (b) quantum efficiency of a µc-Si:H(p)/µc-$Si_{0.27}Ge_{0.63}$:H/c-Si:H(n) solar cell.[27]

Working with amorphous and microcrystalline Silicon-Germanium based semiconductors was deemed promising. In order to understand the nature of these unconventional semiconductors the following sections of this chapter will be dedicated to providing an introduction to the deposition equipments used as well as the deposition conditions and optoelectronic properties of materials ranging from amorphous silicon to microcrystalline silicon-germanium.

Cette thèse est accessible à l'adresse : https://theses.insa-lyon.fr/publication/2023ISAL0014/these.pdf
© [A. Wilson], [2023], INSA Lyon, tous droits réservés

2 Basics of Plasma Enhanced Chemical Vapor Deposition

2.1 A Brief Introduction to Plasmas

A plasma is a quasi-neutral gas whose atoms or molecules have been at least partially ionized [28]. In this state, sometimes considered as the fourth state of matter, the gas is composed of atoms stripped of their outer shell electrons, resulting in a system composed of positive ions and free electrons besides non ionized matter. The large range of Coulomb interactions compared to the collisional dynamics usually governing gases gives the ions and electrons a collective behavior.

2.1.1 Hot and Cold Plasma

To reach such ionized state, it is necessary to provide the system with enough energy to allow the electrons to escape from the Coulomb attraction binding them to the atomic nucleus. Once separated, we consider that the ions and electrons each have their own energy, which is translated into the form of ionic temperature T_i and electronic temperature T_e.

Considering the velocity of the species composing the plasma follows a Maxwell-Boltzmann distribution [29], their average energy is :

$$< E_c >= \frac{1}{2} m \hat{v}^2 = \frac{3}{2} k_b T \tag{2.1}$$

With m the mass of the species considered, $\hat{v}$ the mean square velocity, k_b the Boltzmann constant and T the temperature in Kelvin, ionic or electronic. We define the temperature - electronic in this case - as :

$$T_e = \frac{m_e \hat{v_e}^2}{3 k_b} \tag{2.2}$$

We therefore distinguish two major families of plasmas according to their degree of ionization α_i, defined as the ratio between the number of electrically charged species/particles and the total number of species in the plasma.

- Hot plasmas when $T_i \approx T_e$: they have a degree of ionization α close to 1. They are obtained in conditions of high temperature ($T \geq 3000K$), in stars or in the prototypes of nuclear fusion reactors or plasma torches for instance [30]. In these conditions, both electrons and ions are highly energetic.

- Cold plasmas when $T_i \ll T_e$: they are weakly ionized, α ranging from 10^{-5} to 10^{-1}. They are generally less dense than hot plasmas and can easily be created artificially. The ions remaining "cold" ($T_i \simeq 500K$) they contribute little to the collisions taking place in the plasma while the electrons, having typically energies of the order of the electron-Volt (1eV $\leftrightarrow$ $T_e \approx 11\,000$K) [28], participate strongly in the ionization of neutral species of the gas, creating new reactive and positively charged radicals as well as neutral radicals. This type of plasma is found in the earth's ionosphere, in plasma lamps or in Plasma-Enhanced CVD reactors.

In this section we will focus on cold plasmas only as they allow to accelerate gas phase reaction kinetics at low thermal cost [31], which one of the key characteristics of PECVD.

Cette thèse est accessible à l'adresse : https://theses.insa-lyon.fr/publication/2023ISAL0014/these.pdf
© [A. Wilson], [2023], INSA Lyon, tous droits réservés

2.1.2 Plasma Sheath and Debye length

Cold plasmas are quasi-neutral ionized gases. Although electrons and ions are dissociated, the plasma keeps its electrical neutrality at the macroscopic scale. However this electrical neutrality hypothesis is not valid at the microscopic scale, in particular at the boundaries of the plasma where a positively polarized "sheath" is formed. The rise of this polarized region can be roughly explained by a difference in thermal velocity between ions and electrons ($\hat{v}_i \ll \hat{v}_e$). The number of collisions per unit area per second in a closed reactor chamber for ions N_{col_i} is much lower than for electrons N_{col_e} [32], thus a negative potential appears "encapsulating" the ionized gas due to the walls accumulating a surplus of electrons [29]. At equilibrium the negative potential of the surfaces in contact with the plasma V_S can be expressed as :

$$V_S = \frac{k_b T_e}{e} \ln(\frac{\hat{v}_i}{\hat{v}_e}) = \frac{k_b T_e}{2e} \ln(\frac{m_e T_i}{m_i T_e}) \tag{2.3}$$

As a first order approximation for a hydrogen based plasma, V_S is of the order of 3 to 4 times $^{kT_e}/_q$. [32] In a simple 1D plasma, the potential away from the surface is thus obtained from Poisson's equation :

$$\nabla^2 V(x) = \frac{\rho(x)}{\varepsilon_0} = \frac{e n_\infty}{\varepsilon_0} (\exp(\frac{eV(x)}{k_b T_e}) - 1) \tag{2.4}$$

By making the approximation that $eV(x) \ll k_b T_e$ we get :

$$V(x) = V_S \exp(-^x/_{\lambda_D}) \quad \text{with} \quad \lambda_D = \sqrt{\frac{\varepsilon_0 k_b T_e}{e^2 n_\infty}} \tag{2.5}$$

where λ_D is the Debye length. The typical profile of the potential near a wall is shown in figure 2.1.

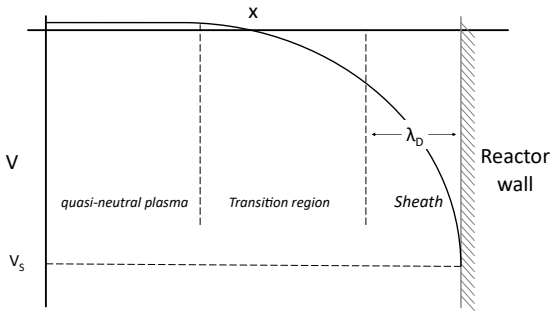

Figure 2.1: Diagram of the evolution of the potential near the plasma-wall interface, with V_S the surface potential and λ_D the Debye length [33].

This length is characteristic of the thickness of the negative sheath surrounding the plasma, the smaller it is, the stronger the shielding of the potential by the plasma. For a cold plasma of a PECVD reactor this length is generally of the order of a few hundred microns [31]. In terms of thin films deposition , this sheath close to the surface drives the ion bombardment mechanism of the surface which in turn play an important role in chemical bond annealing during film growth.

Cette thèse est accessible à l'adresse : https://theses.insa-lyon.fr/publication/2023ISAL0014/these.pdf
© [A. Wilson], [2023], INSA Lyon, tous droits réservés

2.2 Plasma-Enhanced Chemical Vapor Deposition (PECVD)

PECVD is a well established chemical vapor deposition (CVD) technique widely used in the photovoltaic and microelectronic industry [34]. Like any CVD techniques it relies on the interaction of precursor gases and a surface (the substrate) inside a temperature and pressure controlled chamber to obtain a solid film.

While CVD relies on thermal activation during precursor/substrate interactions, PECVD uses an electric field to obtain a partial ionization of a gas and thus create a cold plasma (see section 2.1.1) in which the generated ions constitute highly reactive species, in turn creating neutral radicals. This process is widely used for the production of oxides, nitrides, amorphous materials, microcrystalline materials but also exotic materials such as carbon nanotubes and graphene.

In the context of microelectronics, Plasma-Enhanced CVD is advantageous due to :

- its ease to generate dissociated precursor gases, thus generating a large number of neutral radicals despite a low ionization rate
- its deposition rates, which can be close to nm/s for industrial processes of hydrogenated amorphous silicon deposition
- the lower temperatures and higher pressures working point compared to conventional CVD deposition (less than 350°C vs over 600°C)
- the compatibility with a large variety of substrates, including glass and polymers due to possibility of low temperature deposition
- the ion bombardment of the substrate by the ionized species of the plasma, which favors the densification of the deposited layers

Yet no technology comes without compromise, hence PECVD has its share of disadvantages among which :

- the ion bombardment which participates in the sputtering of undesirable species in the gas phase, which can then be redeposited and contaminate the substrate and the deposited layers
- the anisotropy of the deposition, vertical and horizontal surfaces not undergoing the same ionic bombardment
- the risk of powder formation in high power plasma which compromises film quality and is incompatible with clean room environments
- the difficulty of depositing conductive films which short-circuit the power injection circuit
- the generation of UV light in the plasma which can damage the most sensitive components

In the following subsection we will introduce the key parameters used to operate a PECVD reactor.

Cette thèse est accessible à l'adresse : https://theses.insa-lyon.fr/publication/2023ISAL0014/these.pdf
© [A. Wilson], [2023], INSA Lyon, tous droits réservés

2.2.1 PECVD Reactors

In 1965, Sterling and Swann [35] unveiled what they called "Vapor Deposition assisted by Radio Frequency Discharge". They demonstrated that it was possible to deposit thin layers of Silicon, Silica and Silicon nitride at high speeds (2-4 µm/h) without reaching high temperatures ($T \sim$ [200°C - 400°C]). They had then developed one of the first PECVD reactors.

Plasma coupling methods

Nowadays, PECVD reactors allow the deposition of a wide variety of materials, from polymers to oxides, nitrides, metals and semiconductors. Two types of reactors can be distinguished according to the nature of the coupling between the generator and the plasma.

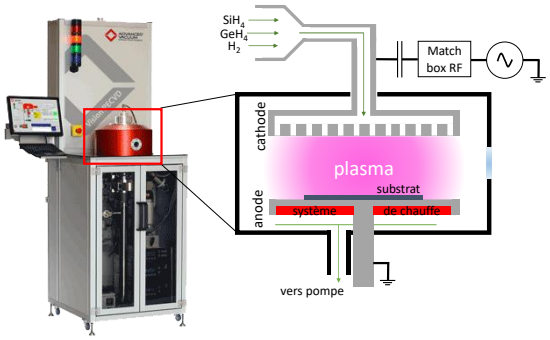

Figure 2.2: INL's capacitive PECVD reactor, with a representation of the chamber's design.

Inductive reactors (ICP) ignite the plasma through coils and the variable magnetic field they generate in the reactor vessel. Capacitive reactors (CCP) generate a variable electric field using two electrodes in the reactor chamber, one being connected to the generator and the other to the ground. In the context of this work we will focus on CCP-PECVD equipements (figure 2.2).

Working Frequency

As previously mentioned, capacitive reactors operate at a given frequency. The choice of the working frequency will strongly impact the way the plasma receives the input energy. Three operating regimes can be identified, corresponding to a different behavior of ions and electrons in the presence of an electromagnetic perturbation. Indeed, the oscillation frequency of the charges of a plasma (Langmuir frequency) around their equilibrium position is :

$$f_{p(i/e)} = \frac{1}{2\pi}\sqrt{\frac{n_{(i/e)}q^2}{m_{(i/e)}\varepsilon_0}}$$

With f_{pe} the frequency of electrons, f_{pi} the frequency of ions, $n_{(i/e)}$ the charge density of ions / electrons and $m_{(i/e)}$ the mass of ions / electrons. This frequency accounts for the capacity of the charges to follow a periodic variation of the field $\overrightarrow{E}$ of frequency f. These frequencies depend on the density of charges of the plasma, or for a cold plasma we can consider that $n_e = n_i \simeq 10^{16}\mathrm{m}^{-3}$ and $m_i = m_{proton}$ which leads to $f_{pe} \simeq 1\,\mathrm{GHz}$ and $f_{pi} \simeq 1\,\mathrm{MHz}$ [36]. These two frequencies define three domains:

Cette thèse est accessible à l'adresse : https://theses.insa-lyon.fr/publication/2023ISAL0014/these.pdf
© [A. Wilson], [2023], INSA Lyon, tous droits réservés

- Low frequency (LF) plasmas for frequencies below the megahertz, $f < f_{pi}$. The ions and electrons are driven by the electric field. This configuration favors ion bombardment of the chamber walls and the substrate.
- Radio frequency (RF) plasmas when f is between 1 and 500 MHz, i.e, $f_{pi} < f < f_{pe}$. Ions are in some sense «transparent» to the electromagnetic field, unlike electrons which are easily excited. Most reactors operate in this range, often at $f = 13.56\,\text{MHz}$ – due to regulation on communication frequencies – and more rarely up to 100 MHz.
- Microwave plasmas ($\sim$2.45 GHz) when $f_{pi} < f_{pe} < f$. They have the advantage of not requiring an electrode to be generated and do not induce a potential on the surrounding surfaces.

The equipment available at INL (figure 2.2) is capable of working both at low and radio frequency simultaneously. In order to restrict our area of research our future work will rely on the industry standard 13.56 MHz frequency.

2.2.2 Main Process Parameters

Within the PECVD reactor chamber, temperature, pressure, power or gas flow entering the chamber can be adjusted. The experimental range will be presented in chapter 2, section 1.1. All these parameters are more or less correlated and will have an impact on the quality of the film obtained, on its growth rate and on the precursor/substrate interactions.

Temperature

When discussing process temperature, we imply we are focusing on substrate temperature as there is no thermodynamic temperature for cold plasmas (see subsection 2.1.1).Increasing the substrate's temperature we favor mechanisms like surface mobility and desorption of volatile species from the substrate [29]. The increase in temperature results in a lower growth rate and a more homogeneous film. Temperature can be limited by the thermal constraints of the device, such as not exceeding 350°C for a substrate integrating CMOS elements with copper interconnections [10, 13–15] or working below the glass transition for polymers.

Pressure

The pressure in the chamber during PECVD processes is of the order of magnitude of one Torr [37] or a hundred milliTorr ($1\,\text{atm} = 760\,\text{Torr}$) . These pressure conditions are necessary for the creation of a plasma and its adjustment is a matter of compromise between limiting ion bombardment [38] (dominant at low pressures due to an increase in mean free path), avoiding powder formation in the gas phase which can occur in high power/high pressure regimes.

RF-Power Density

The power supplied by the RF generator allows the decomposition of the precursors in gas phase. This power is normalized with respect to the surface of the PECVD reactor electrode to define a power density, often given in mW/cm^2. An increase in this power density increases gas phase precursor dissociation and therefore increases the concentration of reactive species and ions in the plasma[29]. Depending on the gas mixture in the chamber as well as pressure, a low power density can lead to an unstable plasma or even to the impossibility of igniting it.

Cette thèse est accessible à l'adresse : https://theses.insa-lyon.fr/publication/2023ISAL0014/these.pdf
© [A. Wilson], [2023], INSA Lyon, tous droits réservés

Gas flow rate

Finally gas flow rate is adjusted for each gas, whether they are used as a precursor or a dilution gas. The total gas flow rate is typically given in standard centimeter cube per minute (sccm) and has an impact of deposition rate since it is directly correlated to the amount of species available for deposition. Even more crucial than total gas flow rate is the relative gas flow rates of the different gases in the mixture, which controls the chemistry and the structural properties of the film.

2.2.3 Thin Film Growth Mecanisms

The interactions governing the deposition of a thin film on a substrate placed in contact with the plasma are numerous and well described in the literature [29]. The predominant mechanisms in the case of a PECVD growth are :

- Formation of radical sites on the surface
- Adsorption of species on the surface (physisorption)
- Chemisorption on the radical sites
- Mobility of the adsorbed species on the surface
- Passivation of radical sites by hydrogen
- Inter-radical cross-linking
- Desorption from the surface to the plasma

Once nucleation is initiated as shown in figure 2.3, island growth takes place until coalescence is reached. These individual islands then merge to minimize their surface energy. In turn, microcrystalline semiconductor growth relies on the impact of high hydrogen concentration on the kinetics of these fundamental mechanisms. The growth process for these materials will be discussed in further sections.

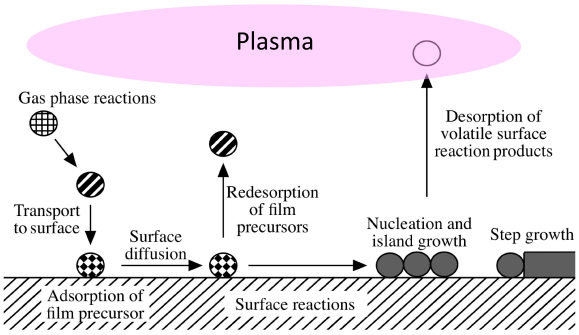

Figure 2.3: Simplified model for thin film growth on the surface of a substrate during PECVD deposition, adapted from [39]

3 Hydrogenated Silicon thin films

Growing thin films at low temperature as done in PECVD processes makes it almost impossible to obtain fully crystalline films. The lack of thermal energy during film growth is

Cette thèse est accessible à l'adresse : https://theses.insa-lyon.fr/publication/2023ISAL0014/these.pdf
© [A. Wilson], [2023], INSA Lyon, tous droits réservés

detrimental to the formation of a crystalline lattice. However workarounds exist and make it possible to obtain partially crystalline materials such as hydrogenated microcrystalline silicon at low temperature and epitaxial silicon growth on crystalline substrates.

3.1 Microcrystalline Hydrogenated Silicon

Crystalline silicon is a very mature material and dominates the microelectronics industry. It's main drawbacks are the energy-intensive processes and high material losses caused from its shaping. Unlike crystalline silicon, amorphous silicon (a-Si:H) and microcrystalline silicon (µc-Si:H) do not exhibit a long range periodic and ordered arrangement of atoms (see figure 3.1). This disorder contributes to give a-Si:H and µc-Si:H electronic and optical properties which differ significantly from crystalline silicon (c-Si). µc-Si:H is thus a complementary material to crystalline silicon [40].

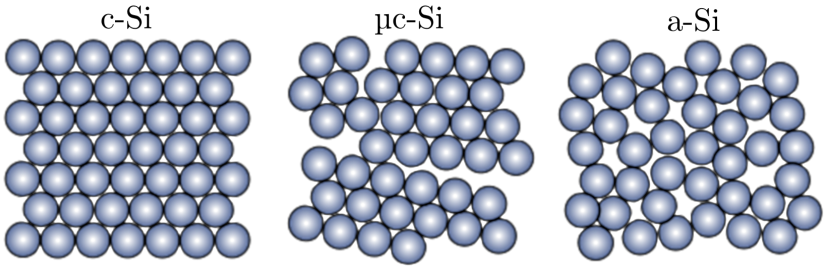

Figure 3.1: Diagram of a monocrystalline, microcrystalline and amorphous arrangement of Silicon atoms.

Both are mainly produced by PECVD from gaseous mixtures of silane and hydrogen, sometimes combined with a noble gas. This process leads to the growth of highly disordered films incorporating high amounts of hydrogen passivated bonds. Adapting the deposition condition can lead the material to stay fully amorphous – with no identifiable order beyond a few atoms – or become microcrystalline – with highly ordered regions embedded in a disordered matrix. a-Si:H has a high optical band-gap (above 1.8 eV) and consequently low absorption at high wavelengths [41]. In this section we will thus focus on microcrystalline silicon film growth and properties, highlighting both the advantages and drawbacks of this well established material.

3.1.1 PECVD growth of µc-Si:H

The mechanisms governing the growth of µc-Si:H films have been studied since the early 1980's [42], shortly after the appearance of amorphous silicon. The deposition conditions for microcrystalline silicon are very similar to those of a-Si:H. Film growth is frequently attributed to radicals rather than ions, the latter participating in the ionic bombardment of the surface and being less numerous than neutral radicals (see subsection 2.1.1). In a SiH_4/H_2 gaseous mixture the main species participating in the growth of the film are typically the neutral radicals H and SiH_3 [43] (see figure 3.2).

PECVD deposition of µc-Si:H typically takes place at substrate temperature of around 200 °C with a power density and pressure in the reactor of around 100 mW/cm² and 1 Torr respectively. The dilution is much higher, with a hydrogen dilution factor $R_H = H_2/SiH_4 > 10$ with X_n being the gas flow rate for the given specie in standards centimeter cube per minute (sccm).

Cette thèse est accessible à l'adresse : https://theses.insa-lyon.fr/publication/2023ISAL0014/these.pdf
© [A. Wilson], [2023], INSA Lyon, tous droits réservés

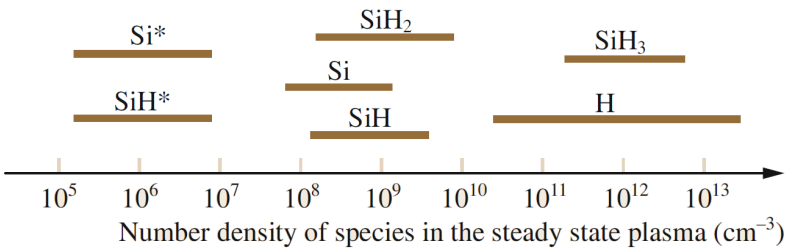

Figure 3.2: Density of the different radicals and ions present in a SiH_4/H_2 steady state plasma. The species marked with a * correspond to ionic species. [43]

RF-power density [44][45], substrate temperature [42], and pressure [20] all impact the structural properties of the material and can lead to interesting gains in deposition rate. The most critical process parameter however is undoubtedly hydrogen dilution.

The dilution of silane in hydrogen can be found expressed as the concentration of silane $SC = SiH_4/H_2$ or the dilution factor $R_H = 1/SC$. To aim for a crystalline volume fraction (the crystalline to amorphous phase ratio) close to 100% it is then essential to have $SC < 10\,\%$ or $R_H > 10$. In order to obtain a film with homogeneous crystalline volume fraction throughout its thickness, R_H can easily exceeds 50 [41] (i.e. $SC < 2.5\,\%$, see figure 3.3). In such conditions, incubation and nucleation steps necessary for µc-Si:H growth are short. Consequently crystalline phase growth rapidly reaches a steady state and is no longer thickness dependent.

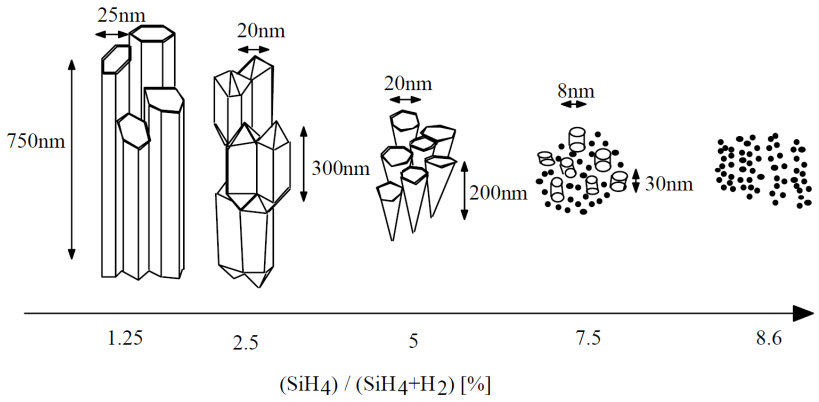

Figure 3.3: Schematic representation of the impact of the gas mixture silane concentration on the morphology of the crystalline phase [41].

Playing with hydrogen dilution can lead to the growth of films with vastly different morphology of crystalline phases although they are gathered under the name "µc-Si:H". This is highlighted in the mapping of the power density and hydrogen dilution of figure 3.4 from Matsuda [43]. To reach a crystallinity close to 100% it is necessary to exceed $R_H = 10$, otherwise for moderate powers the final material will be amorphous or at best partially crystalline. It is also noted that the amorphous phase appears for very high power densities ($> 1\,W/cm^2$) but these deposition conditions are not widely used in the literature due to an increased risk of powder formation in the gas phase.

Cette thèse est accessible à l'adresse : https://theses.insa-lyon.fr/publication/2023ISAL0014/these.pdf
© [A. Wilson], [2023], INSA Lyon, tous droits réservés

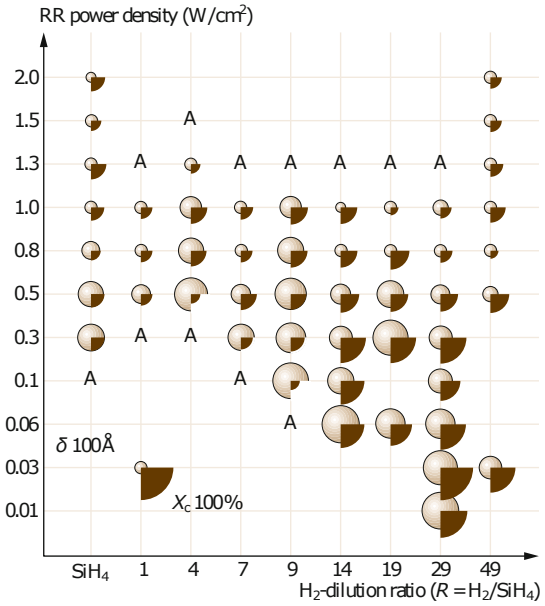

Figure 3.4: Size (*light:*δ) and volume fraction (*dark:*X_C) of microcrystallites as a function of process conditions. From [43].

However, using high hydrogen dilution R_H comes at the expense of decreasing the growth rate. Three models – presented below – have attempted to explain the importance of hydrogen on the growth of microcrystalline thin films [43].

3.1.2 Hydrogen enhanced surface diffusion model

This model proposed in 1983 by Matsuda [42] suggests that the high hydrogen dilution generates an important flux of H radicals towards the surface. The hydrogen is then captured by the Si- dangling bonds on the surface to form Si-H. By doing so, the excess hydrogen fills a majority of the nucleation sites, thus making them inactive. SiH_3 radicals reaching the surface can no longer bond with these sites, forcing them to diffuse on longer distances before finding a bonding sites. With an increased diffusion distance the radicals increase their probability of reaching a site with better energy stability. Since ordered states correspond to more stable states, the radicals will tend to cluster preferentially on crystal nucleation sites (see figure 3.5a). The surface area occupied by these crystalline phases thus increases during the deposition.

3.1.3 Hydrogen induced etching model

The etching model was developed to account for the decrease in growth rate with increasing hydrogen dilution at constant silane flux. According to Tsai et al. [46] the surface reactions can be summarized to:

$$\mathrm{SiH_{n\,(plasma)}} \underset{R_2}{\overset{R_1}{\rightleftharpoons}} \mathrm{Si_{solid}} + \mathrm{nH_{plasma}} \tag{3.1}$$

In the R_1 direction, the reaction corresponds to deposition and etching in direction R_2. During etching, the hydrogen atoms reaching the growing layer break the weaker Si-Si bonds, which correspond to the less stable bonds in the amorphous areas of the film. The unstable Si

Cette thèse est accessible à l'adresse : https://theses.insa-lyon.fr/publication/2023ISAL0014/these.pdf
© [A. Wilson], [2023], INSA Lyon, tous droits réservés

atom is desorbed from the surface in the form of silane and the site thus made available will allow the SiH_3 radicals to position themselves in a more ordered and stable configuration (see figure 3.5b).

3.1.4 Chemical annealing model

Finally, the latest model is that of Nakamura et al. [47]. It attempts to explain the recrystallization of amorphous silicon films when exposed to a pure hydrogen plasma. It is indeed possible to alternate cycles of amorphous deposition followed by hydrogen plasma annealing to obtain a microcrystalline material. Atomic hydrogen penetrates below the surface and can then recombine with other hydrogen atoms into H_2, releasing around 4.52 eV per H_2 molecule formed [48]. The local energy input from the recombinations allows the material to crystallize (see figure 3.5c)

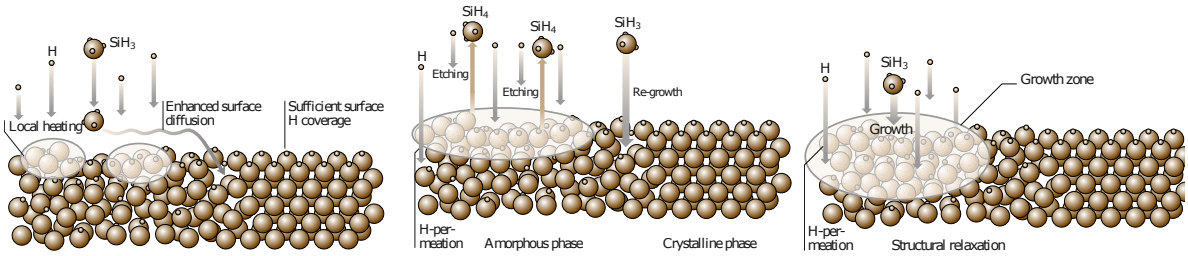

(a) Surface diffusion (b) Etching (c) Chemical Etching

Figure 3.5: Schematic representation of the three growth models of µc-Si:H [43]

3.1.5 µc-Si: growth phases

The actual mechanisms for responsible the growth of µc-Si:H are likely to be a combination of the three models presented above [49]. It is fundamental to take into account the wide variety of plasma conditions that can lead to a crystalline film. Depending on the parameters chosen one mechanism could take over the others and vice versa.

In practice, these growth mechanisms lead to three phases during µc-Si:H film growth [50]:

1. *Incubation* : An amorphous porous layer is formed which becomes charged with hydrogen. This layer can extend over a hundred nanometres and will be longer the lower the hydrogen dilution R_H. Once a porosity level of about 30% is reached, the layer is sufficiently unstable to allow chemical annealing to initiate crystallization.

2. *Nucleation* : The nucleation centers that appear as a result of incubation allow the deposit to rearrange itself, even below the surface of the material. Radicals reaching the surface diffuse and preferentially attach to these more stable centers until they occupy the majority of the surface.

3. *Growth* : Once nucleation is complete, growth takes place in a stationary manner. The grains are brought into contact with each other and extend in the growth direction, perpendicularly to the substrate.

To maximize the final crystallinity of the film, the first two phases should be minimized as much as possible. Using a layer-by-layer method involving alternating cycles of deposition

Cette thèse est accessible à l'adresse : https://theses.insa-lyon.fr/publication/2023ISAL0014/these.pdf
© [A. Wilson], [2023], INSA Lyon, tous droits réservés

and plasma annealing, Roca i Cabarrocas et al. [50] (figure 3.6b) succeeded in reducing the incubation phase to 6 nm.

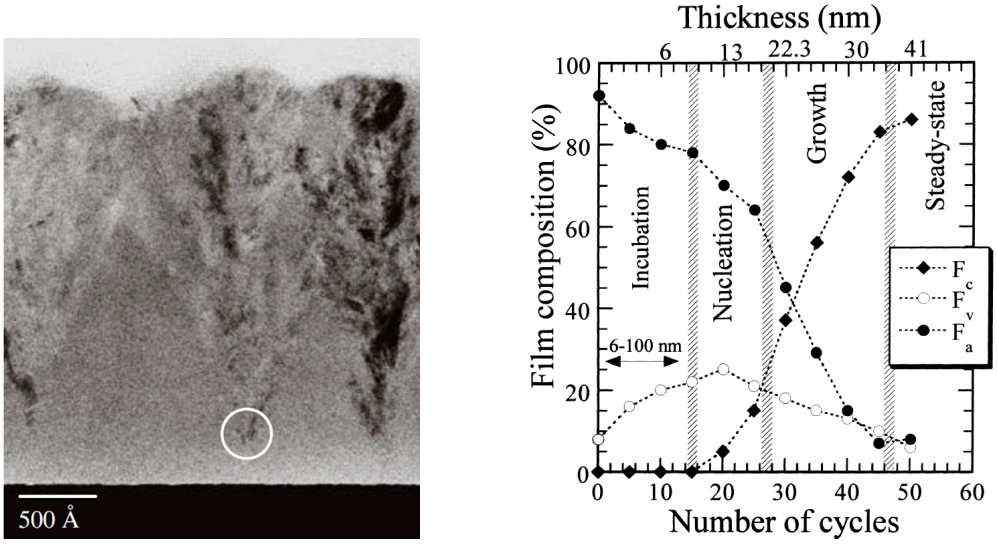

(a) TEM cross section of a µc-Si:H film. The smooth areas correspond to the amorphous region. [43]

(b) Growth phases of µc-Si:H films with a layer-by-layer deposition method. F_c: crystalline fraction, F_v: void fraction, F_a: amorphous fraction [50]

Figure 3.6: The growth of µc-Si:H starts from an incubation phase where the material is mainly amorphous.

3.1.6 Optoelectronic properties of µc-Si:H

Charge transport in µc-Si:H

Although from a transport properties point of view a high X_c is desirable [51], tensile stresses within the columnar micro-structure can lead to the formation of vertical cracks in the film which favor contamination by the external environment (oxidation) and increase the risk of short-circuiting the layer for photovoltaic applications [41]. Multijunction solar cells with µc-Si:H sub-cells [52] are deposited at R_H close to the amorphous/microcrystalline transition in order to minimize this risk while taking advantage of a good mobility [53] of the charge carriers (see table 1.1).

	Electron mobility μ_e ($cm^2/V.s$)
c-Si	$100 - 1500$
a-Si:H	$1 - 10$
µc-Si:H	$1 - 100$

Table 1.1: Electron mobility in crystalline, amorphous and microcrystalline silicon (order of magnitude).

Cette thèse est accessible à l'adresse : https://theses.insa-lyon.fr/publication/2023ISAL0014/these.pdf
© [A. Wilson], [2023], INSA Lyon, tous droits réservés

Absorption in µc-Si:H

Highly crystalline µc-Si:H films exhibit a periodic arrangement over distances ranging from tens of ångstroms to tens of nanometers, which preserves the indirect nature of the c-Si band-gap, unlike a-Si:H. As less and less amorphous phase remains in the film, the band-gap will shift from being near the 1.8 eV of a-Si:H to becoming close to $E_{g\,(c-Si)} = 1.12\,\text{eV}$. Despite an indirect energy gap close to c-Si, µc-Si:H films have an absorption coefficient much higher than their crystalline counterparts on the domains where $h\nu \in [0.5; 1.1[\cup]1.6; 3.0]$ eV (see figure 3.7). However, these performances cannot be justified by a relaxation of the conservation of momentum rule (which states that $\Delta k \sim 0$) during transitions as was done for amorphous silicon. [54]

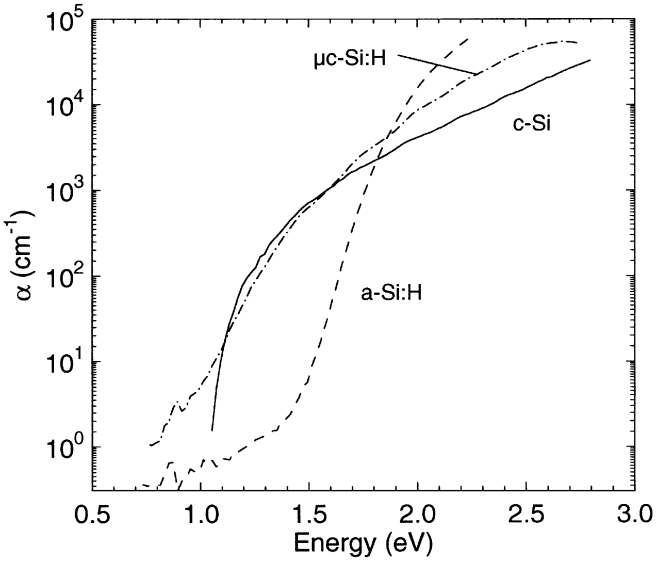

Figure 3.7: Absorption coefficient of c-Si, a-Si:H and µc-Si:H measured by PDS [40]

The sub-bandgap region below $h\nu = 1.1$ eV, still has non-zero absorption since the defects in the material constitute localized states in the band-gap that participate in the capture of low energy incident photons. These states are schematically shown in figure 3.8.

Cette thèse est accessible à l'adresse : https://theses.insa-lyon.fr/publication/2023ISAL0014/these.pdf
© [A. Wilson], [2023], INSA Lyon, tous droits réservés

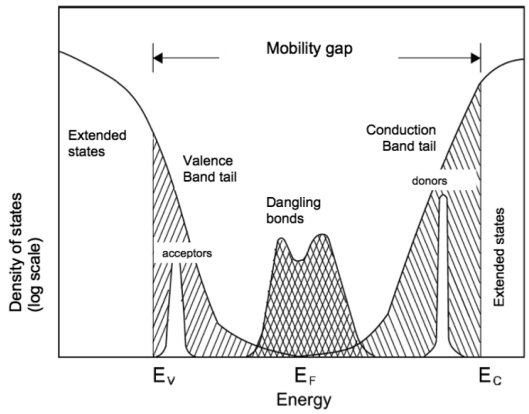

(a)

Figure 3.8: Density of state of disordered silicon. The continuum of defects (band tails) prevents the formation of a sharp band-gap [45].

In our quest for highly absorbing materials in the NIR spectral range, µc-Si:H is far from being an ideal candidate. The exponential drop in absorption below 1.5 eV means the required layer thickness to absorb the low energy photon increases drastically. For reference, a 100 µm thick layer would be needed to capture 63 % of photons at $\lambda = 1000$ nm. Its transparency in that region can however be turned to our advantaged if it is not used for light absorption purposes.

4 Hydrogenated Germanium films

Germanium in its crystalline state was the first semiconductor to be used to make a transistor in 1947 and was only replaced by silicon in the 1970's. With an inter-atomic distance of 2.45 Å compared to crystalline silicon's 2.35 Å, crystalline germanium (c-Ge) has a much smaller band gap $E_g = 0.66$ eV at 300 K. As shown in the band structure of figure 4.1, c-Ge is also an indirect gap material but has a direct transition $E_{\Gamma 1}$ with energy 0.8 eV, very close to the gap E_g. Its most obvious applications given its gap are in detection, infrared emission and high frequency applications (germanium has the highest hole mobility of all semiconductors) driven among other things by the needs of fiber optics. The early use of germanium is reflected in the equally early discovery of amorphous (a-Ge) [55, 56] and microcrystalline (µc-Ge)[57] germanium films in the late 1960's and 1970's respectively, with plasma-assisted deposition emerging shortly after.

The advantages of these materials over their crystalline counterpart are their low cost, low deposition temperatures and the ability to deposit on flexible substrates. Despite these advantages, a-Ge and µc-Ge remain less explored than their silicon counterparts.

4.1 Hydrogenated Germanium film deposition

Just like hydrogenated silicon, hydrogenated germanium (Ge:H) films are obtained from a gaseous precursor such as germane GeH_4 highly diluted in hydrogen ($R_H = H_2/GeH_4$).

Originally, Ge:H layers were developed starting from the deposition parameters of a-Si:H and adapting them slightly. This approach was not sufficient according to some authors [59, 60] who subsequently highlighted the need for high dilution of germane in hydrogen

Cette thèse est accessible à l'adresse : https://theses.insa-lyon.fr/publication/2023ISAL0014/these.pdf
© [A. Wilson], [2023], INSA Lyon, tous droits réservés

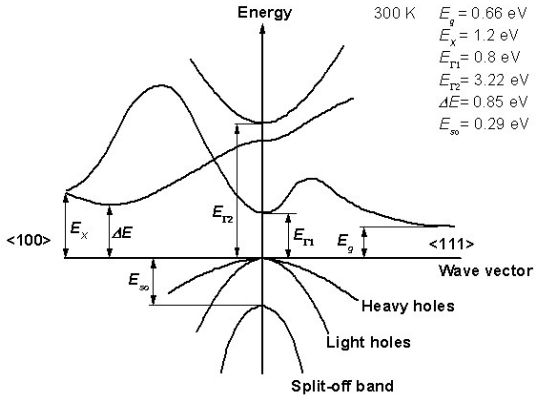

Figure 4.1: Band structure of crystalline Germanium at 300 K.[58]

as well as high RF power, regardless of the desired phase (see sections 4.1.1 and 4.1.2). As a counterpart to this high hydrogen dilution growth rates for µc-Ge:H films below 0.5 Å.s^{-1} are observed [61]. This can be considered as a drawback for industrial applications. For a-Ge:H this drawback could be overcome at high power densities and good quality deposits were obtained by Bouizem et al. [62] with deposition rates up to 7.8 Å.s^{-1} ($R_H = 40$). Examples of the conditions for high quality films gathered from the available literature are listed in table 1.2.

	Temperature [°C]	Pressure [Torr]	Power density [W.cm^{-2}]	Dilution -	Crystallinity -	Ref. -
a-Ge:H	$150-250$	$0.45-0.75$	0.77	$R_H = 20$	-	[59]
	250	0.95	0.2	$R_H = 40$	-	[60]
	$150-250$	$0.08-0.26$	0.1	$R_H = 100$	-	[63]
	250	0.75	0.15	$R_H = 4-11$	-	[64]
	175	2.3	0.15	$R_H = 40$ + Argon	-	[65]
µc-Ge:H	250	1.5	0.23	$R_H = 100-300$	> 70 %	[64]
	200	0.2	0.3	$R_H = 500$	"high"	[26, 66][1]
	200	-	30 W/?	$R_H = 890$	-	[23]
	260	1	5-35 W/?	$R_H = 1000$	62.4%	[61]

Table 1.2: Deposition parameters of a-Ge:H and µc-Ge:H films gathered from the literature. Unless stated otherwise, all the films were deposited with a 13,56 MHz capacitively coupled PECVD.

4.1.1 Growth of a-Ge:H films

In the case of a-Ge:H, the mechanisms of growth of the amorphous layer are quite similar to those of a-Si:H [43]. Upon ignition of the plasma the germane molecules are first ionized and electron-precursor collisions then generate GeH_x radicals and atomic hydrogen. a-Ge:H layers were shown to form starting from a porous incubation layer a few nanometers thick which then densified [67]. Film density can be improved by increasing ion bombardment

[1] $f_{plasma} = 95.7$ MHz

Cette thèse est accessible à l'adresse : https://theses.insa-lyon.fr/publication/2023ISAL0014/these.pdf
© [A. Wilson], [2023], INSA Lyon, tous droits réservés

of the surface through an increase in RF-power or a decrease in pressure. The main risk in increasing ion bombardment come from accidental substrate degradation and sputtering of impurities present in the reactor chamber.

4.1.2 Growth of µc-Ge:H films

A study following a similar approach also showed the interest of ion bombardment for the production of microcrystalline germanium films [68, 69]. Overall, µc-Ge:H film deposition requires a higher energy input to trigger the transition from the amorphous to the crystalline phase. The effect can be seen from the high hydrogen dilution used by authors gathered in table 1.2 to obtain crystallinity above 60 % [61, 64]. This need for additional energy input can likely be explained by the fact that, for the same deposition conditions, Drevillon et al. [68] observed an order of magnitude lower ion flux towards the surface for a GeH_4/H_2 plasma than for a SiH_4/H_2 plasma (at $R_H = 50$). It can also be in part attributed to the lower dissociation energy E_D for Ge-H bond than Si-H bonds as $\mathrm{E_D(GeH_3 - H)} = 3,58\,\mathrm{eV}$ and $E_D(\mathrm{SiH_3 - H}) = 3,9\,\mathrm{eV}$ [70, 71] at 0 K. The lower dissociation energy leads to higher growth rate which limits surface diffusion by creating numerous nucleation centers. Similarly, increasing substrate temperature was found to improve film crystallinity and density due to an improvement in surface diffusion and hydrogen desorption (see figure 4.2, from [64]).

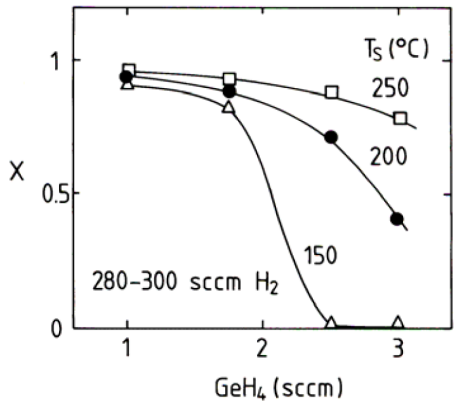

Figure 4.2: Raman crystallinity (see chapter 2, section 2.1) as a function of ϕ_{GeH_4} for different substrate temperatures. [64]

Overall, µc-Ge:H is more reluctant to transition from amorphous to microcrystalline than µc-Si:H films. The main evidence for it being the level of hydrogen dilution needed to trigger the transition (see table 1.2 for µc-Ge:H and figure 3.4 for µc-Si:H).

4.2 Optoelectronic properties of Ge:H films

The optical properties of PECVD deposited Germanium make it an appealing material for NIR photodetection. In 2001, Krause et al. [26] reported the successful implementation of µc-Ge:H as an absorption layer in a PIN photodiode. A quantum efficiency as high as 15 % was reached at 1100 nm in wavelength despite the absorber being only 110 nm thick (see section 1.2). Although studies of the material itself can be found in the literature [61, 64, 68, 72, 73], its implementation in solar cells or photodetectors is sparse [26, 74].

Cette thèse est accessible à l'adresse : https://theses.insa-lyon.fr/publication/2023ISAL0014/these.pdf
© [A. Wilson], [2023], INSA Lyon, tous droits réservés

4.2.1 NIR absorption of Ge:H films

Investigation of the optical properties of Ge:H demonstrated the interest of these materials as early as 1970 for a-Ge:H (see figure 4.3a, [75]). The absorption coefficient α for a-Ge:H follows similar variations to that of a-Si:H but shifted to lower energies by roughly 0.7 eV. At $\lambda = 1000$ nm where a-Si:H would be close to being transparent, the absorption $\alpha_{aGe:H}$ is still close to 10^5 cm^{-1}. This high absorption level in the near infrared range is a critical condition for the studied material. The amorphous nature of the film increases the optical bandgap, in turn reducing absorption at lower energies.

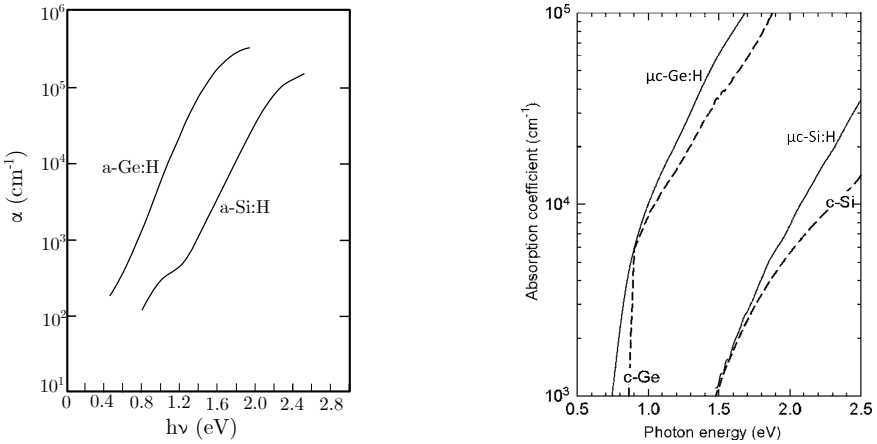

(a) (b)

Figure 4.3: Absorption coefficient α for (a) a-Ge:H vs a-Si:H adapted from [75] and (b) μc-Ge:H vs μc-Si:H with crystalline materials as reference (dashed lines) [23]

Microcrystalline Germanium avoids this issue due to the high crystalline volume fraction. Optical properties of μc-Ge:H [23, 26] were thus found to exceed those of a-Ge:H in the 1 eV region and are thus preferable to a-Ge:H for NIR absorption. A comparison of $\alpha_{\mu cGeH}$ and $\alpha_{\mu cSiH}$ is given in figure4.3b. The absorption of μc-Ge:H drops sharply below 0.9 eV but remains higher than c-Ge due to absorption by localized states, similarly to μc-Si:H. Overall, μc-Ge:H would be a better candidate than a-Ge:H or Si:H films thanks to its enhanced absorption in NIR resulting from Germanium's low band gap.

4.2.2 Transport properties of μc-Ge:H

The charge transport properties of μc-Ge:H are far from its bulk c-Ge equivalent, exhibiting record hole mobility among semiconductors (μ_p~ 1900 cm²/V/s, μ_n~ 3900 cm²/V/s) at room temperature [76]. Some authors reported an electron mobility as low as 0.16 cm²/V/s for a 20 nm thin μc-Ge:H film used in thin film transistors (TFT) [61]. The 5 order of magnitude difference found highlighting the sacrifice made in terms of electrical properties when growing films at low temperature.

Few papers deeply investigate and seek to optimize μc-Ge:H electrical properties. In studies focusing on μc-SiGe:H alloys, the photosensitivity however seems to sharply degrade as the material tends towards pure μc-Ge:H. [22, 23] This aspect will be discussed in the following section. In a paper from 2009, Badran et al. [66] however conducted an extensive study on the electrical properties of μc-Ge:H deposited at low pressure (200 mTorr) in a VHF PECVD

Cette thèse est accessible à l'adresse : https://theses.insa-lyon.fr/publication/2023ISAL0014/these.pdf
© [A. Wilson], [2023], INSA Lyon, tous droits réservés

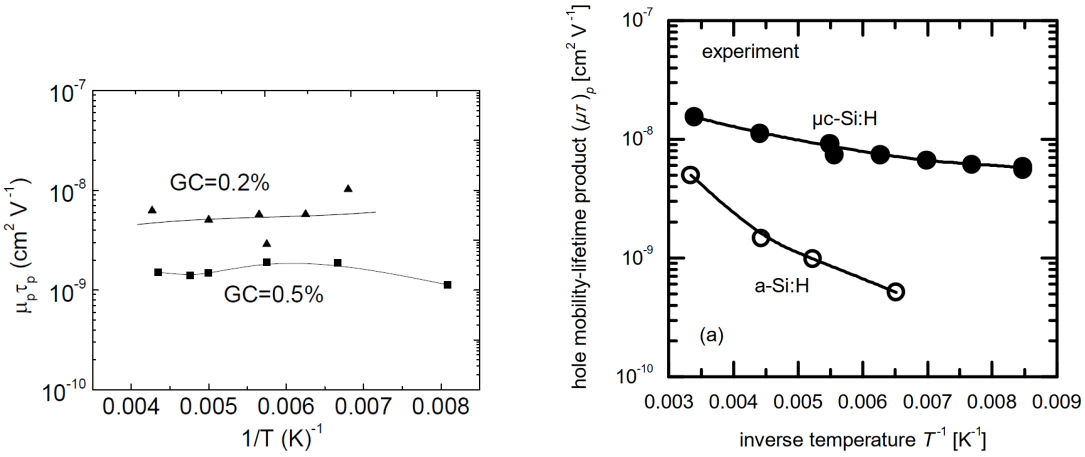

(a) (b)

Figure 4.4: Mobility lifetime product $\mu_p\tau_p$ of holes for (a) µc-Ge:H deposited at different germane concentration GC [66] and for (b) a-Si:H and µc-Si:H films. [77]

reactor (95.7 MHz) in high hydrogen dilution conditions ($R_H = 100 - 500$). In figure 4.4a mobility-lifetime product of the films were measured and found to be strongly dependent of R_H. For reference, the µτ product is compared to µc-Si:H [77] given in figure 4.4b.

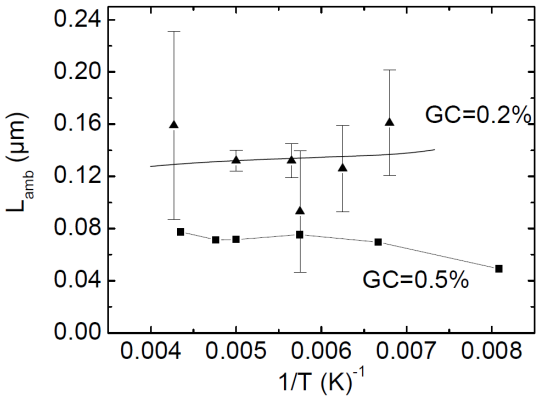

Figure 4.5: Ambipolar diffusion length of µc-Ge:H deposited at different hydrogen dilution levels.[66]

By performing several steady state photocarrier grating method (SSPG) [78, 79] measurements, the authors were able to estimate the ambipolar diffusion length L_{amb} for µc-Ge:H which could reach up to 150 nm. The emphasis was put on the importance of high dilution levels which strongly improves the material's diffusion length.

µc-Ge:H could be a promising material for above-IC NIR photodetectors and will be studied during this PhD project. The fact that µc-Ge:H and µc-Si:H can be deposited in similar experimental conditions opens the door to a wide range of new materials : hydrogenated silicon germanium alloys.

Cette thèse est accessible à l'adresse : https://theses.insa-lyon.fr/publication/2023ISAL0014/these.pdf
© [A. Wilson], [2023], INSA Lyon, tous droits réservés

5 $Si_{1-x}Ge_x$:H alloy production and properties

SiGe:H alloys emerged as an obvious solution to the problem of the inefficiency of µc-Si:H films for infrared photon collection. Production of µc-SiGe:H films were reported in literature since the late 90's up to present day mostly driven by tandem solar cell research. Indeed, the race for efficiency in multi-junction solar cells quickly implemented bottom cells made of amorphous or microcrystalline SiGe alloys [25, 80–82] as Ge contributed to an enhanced infrared response. As those benefits must come with a drawback, Mackenzie et al. [83] saw a rapid degradation of the electronic properties of a-Si:H upon incorporation of Ge. This section will mainly focus on microcrystalline Silicon Germanium films.

5.1 PECVD deposition of µc-SiGe:H films

PECVD remains the most widely used technique to produce these amorphous or microcrystalline alloys [84] although some were made by Hot-Wire CVD, sputtering etc. The deposition conditions are largely inspired by those of $a/\mu c - Si : H$, to which is added the precursor gas GeH_4 mixed with silane, hydrogen, and more rarely with a noble gas such as He or Ar. For further discussions, we define

5.1.1 Challenges in SiGe:H film elaboration

The challenges with low-temperature deposition (as low as 165 °C [85]) of SiGe:H films are numerous. Indeed, we seek to simultaneously grow a film with two species whose precursor gases and radicals have different reactivity and dissociation energies: $E_D(GeH_3 - H) = 3,58\,eV$ and $E_D(SiH_3 - H) = 3,9\,eV$ [70, 71]. These differences in reactivity give rise to preferential incorporation of Ge into the film, potential segregation of Ge in the amorphous phase and preferential bonding of hydrogen with silicon. [38, 86]. The preferential incorporation concerns both amorphous and microcrystalline films and can be attributed to a difference in reactive species generation rate which translates into a higher deposition rate for GeH_x species [21].

One solution proposed by Ni et al. [38] to slow down the incorporation of Ge into the alloy is to increase the ion bombardment during deposition. By comparing the gas-phase germane concentration $GC = GeH_4/(SiH_4 + GeH_4)$ and the germanium content x_{Ge} of the final solid film for different regimes (high and low ion bombardment) they were able to show the more gradual incorporation of Ge into the alloy (see figure 5.1). This difficulty in precisely controlling the chemical composition of the deposit is also reflected in the work of Cosme et al. [86] in which adjusting the dilution $R_H = H_2/(SiH_4 + GeH_4)$ at constant precursor flow ($\phi_{GeH_4} = \phi_{SiH_4} = 0.5\,sccm$) led to a change of the Ge fraction in the deposited film (from 50 to 70 at.%).

5.1.2 Deposition conditions for µc-SiGe:H production

A synthetic (but non-exhaustive) review of the deposition conditions for $\mu c - Si_{1-x}Ge_x : H$ is gathered in table 1.3.

[2]Plasma VHF : $f_{plasma} = 95\,MHz$
[3]Plasma VHF : $f_{plasma} = 95.7\,MHz$

Cette thèse est accessible à l'adresse : https://theses.insa-lyon.fr/publication/2023ISAL0014/these.pdf
© [A. Wilson], [2023], INSA Lyon, tous droits réservés

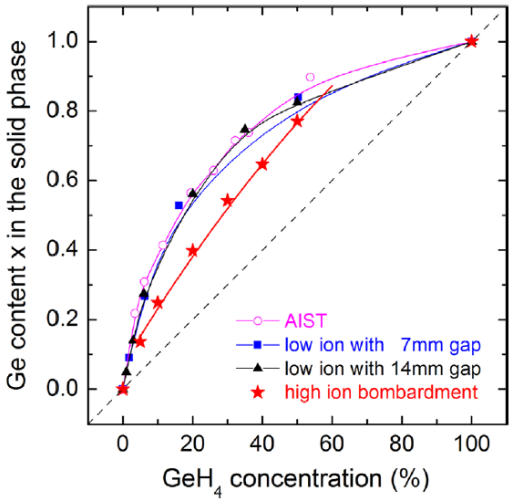

Figure 5.1: Ge content of the film as a function of the germane concentration ($GeH_4/(SiH_4/GeH_4)$) of the gas phase under low and high ion bombardment conditions, taken from [38]. The AIST data come from ref. [21].

Temperature [°C]	Pressure [mTorr]	RF-Power [mW.cm^{-2}]	R_H and GC -	Ge fraction -	Microstructure -	Ref. -
250	$30-500$	$25-1270$	$GC = 9.1\,\%$ $R_H = 50-300$	$x \sim 0.45$	µc	[87]
200	«low pressure»	«low power»[2]	$R_H = 20-50$	$x: 0.1 \rightarrow 0.9$	µc	[88]
200	200	30[3]	$GC = 10-30\,\%$ $R_H = 50-200$	$x: 0.26 \rightarrow 0.6$	µc	[89]
220	1200	700	$GC = 10\,\%$ $R_H = 25$	heterogeneous	nc-Si + a-SiGe	[19]
190	750	$180-240$	$GC = 6\%$ $R_H = 10-40$	heterogeneous	pc-SiGe	[90]
200	600	48	$GC = 0-50\,\%$ $R_H = 60$	$x: 0 \rightarrow 0.8$	µc	[38]

Table 1.3: Deposition parameters for µc-SiGe:H films gathered from the literature.

This overview of µc-SiGe:H deposition conditions shows the parameters are often inspired by µc-Si:H and µc-Ge:H deposition (see 3.1.1 and 4.1). A high hydrogen dilution level R_H compared to µc-Si:H is typically used, highlighting the increased difficulty in achieving the crystalline phase transition when adding Germanium. We still remain far from the dilution in the 200 to 1000 range found for µc-Ge:H (see table 1.2). Some authors have chosen less conventional approach to tackle the loss in crystallinity by adding helium to contribute to the ionic bombardment of the surface [84].

5.2 Optoelectronic properties

A wide range of studies tend to show that the optoelectronic properties of silicon-germanium alloys, whether crystalline or amorphous, are degraded compared to those observed for a/µc-Si:H. Among others, photosensitivity collapses with the incorporation of Ge [23, 90–92]. Photosensitivity is the difference between conductivity σ under illumination and in the dark. It can be expressed as :

$$\Delta\sigma = e \cdot \mu \cdot \tau \cdot \eta \cdot G \tag{5.1}$$

Cette thèse est accessible à l'adresse : https://theses.insa-lyon.fr/publication/2023ISAL0014/these.pdf
© [A. Wilson], [2023], INSA Lyon, tous droits réservés

[93] where G is the photo-generation rate ($cm^{-3} \cdot s^{-1}$), $\mu\tau$ the mobility-lifetime product and η the quantum efficiency. The drop in $\Delta\sigma$ can be attributed to a decrease in $\mu\tau$. Indeed, the absorption coefficient α - and thus G - increases steadily with increasing Ge fraction (see figure 5.2a) yet the behavior of the material is dominated by the loss in transport properties. The defect induced drop in minority carriers collection can be seen with the overall drop in quantum efficiency of Ge-rich solar cells found by Matsui et al. [23] (p-i-n solar cell with 1 µm absorber, see figure 5.2b).

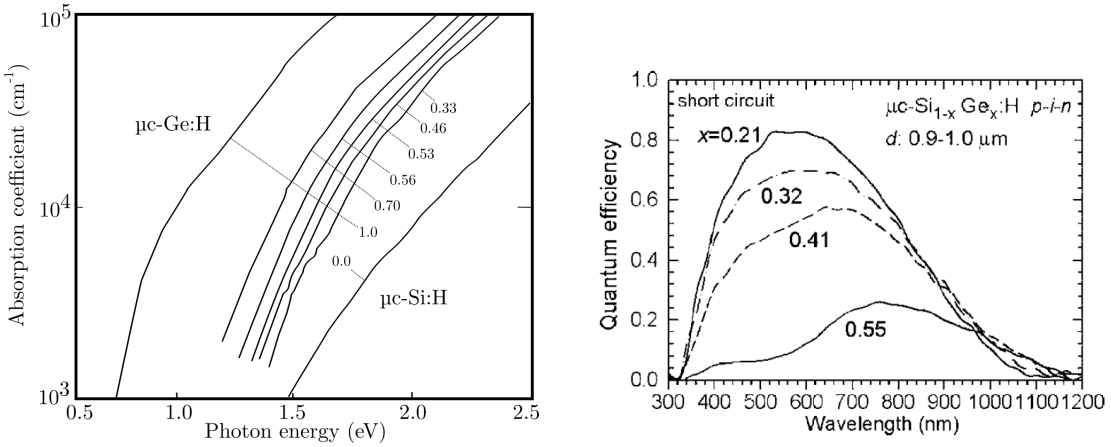

Figure 5.2: (a) Absorption spectrum and (b) Quantum efficiency of p-i-n solar cells of various grades of µc-SiGe:H alloy. [23]

5.2.1 Proto and Nano crystalline materials

In order to prevent the sharp rise in σ_{dark} for Ge-rich alloys ($x_{Ge} > 50\,\%$) a more recent approach consisted in working at the *transition edge*, i.e. as close as possible to the transition between amorphous and microcrystalline phase. [19, 90, 91] Working at that limit can be reached by adjusting the hydrogen dilution of the silane and germane precursors. Fan et al. [90] refer to these heterogeneous materials as *protocrystalline* (pc-SiGe:H) or *nanocrystalline* (nc-SiGe:H) (see figures 5.3a and 5.3b) depending on whether they are grown below or above the crystalline transition respectively.

By comparing the photosensitivity $\Delta\sigma$ obtained by the authors for microcrystalline and protocrystalline SiGe:H we find the latter reaches a $\Delta\sigma$ of 10^5 (figure 5.4b). That is orders of magnitude higher than reported photosensitivity of µc-SiGe:H films [23] ($\Delta\sigma_{max} \approx 10^3$).

The authors state this performance is based on the contribution of the crystalline phase's transport properties and the amorphous phase's and passivation capability. This *goldilocks zone* for film growth was also discussed by Das et al. [94] who suggest that percolation between nano-crystals happening at an optimal crystalline volume fraction leads charge transport to occur by tunneling between nano-crystals. Protocrystalline silicon-germanium was found to be insensitive to light induced degradation (LID) found with some amorphous films [95] and due to their low R_H, its deposition rate can reached 6 Å/s. [96]

Cette thèse est accessible à l'adresse : https://theses.insa-lyon.fr/publication/2023ISAL0014/these.pdf
© [A. Wilson], [2023], INSA Lyon, tous droits réservés

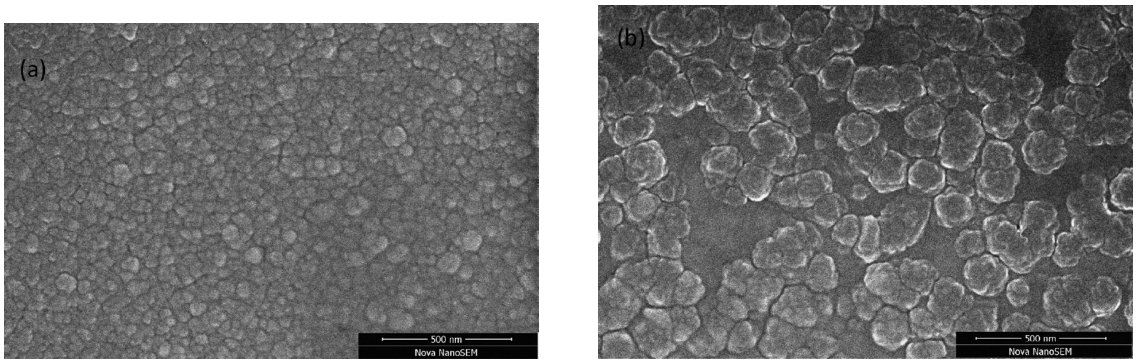

(a) pc-SiGe:H (b) nc-SiGe:H

Figure 5.3: SEM images of the surface of SiGe:H samples deposited at 190 °C, 750 mTorr, 240 mW/cm² and (a) $R_H = 20$ (b) $R_H = 25$ [90]. Images were taken at the same magnification (500 nm scale).

5.2.2 Towards enhanced NIR sensitivity for µc-SiGe:H films

These exotic pc/nc-SiGe:H films may be a viable alternative to µc-SiGe:H, yet they have not been widely studied and are rarely used. Indeed, the study by Fan et al. [90] only focuses on a Si-rich pc-SiGe:H layer, with no indication of its optical performance. The advantages of pc/nc-SiGe:H may not be so obvious for Ge-rich films. Additionally, one must bear in mind that our aim to develop NIR sensitive materials. In Ge-rich pc-SiGe:H it is likely the presence of high amounts of amorphous phase would increase the optical bandgap and thus degrade NIR absorption.

In a recent paper Dey et al., [97] showed the feasibility of Ge-rich nc-SiGe:H. Unfortunately no information on film composition was given to enable quantitative absorption coefficient comparison between nc-SiGe:H and µc-SiGe:H. These recent studies on PECVD grown SiGe:H films suggest much is still left to understand about this complex material.

6 Goal of the Ph.D thesis project

State-of-the-Art

In this Ph.D thesis project, we will seek to study the properties of PECVD deposited hydrogenated Silicon, Germanium and Silicon-Germanium thin films in a final goal to produce an above-IC compatible photodectector with enhanced near infrared sensitivity. This first chapter has provided a synthetic overview of the current state of knowledge regarding these materials. µc-Si:H has been widely studied and offer good electrical properties at the cost of a quickly decreasing absorption coefficient in the NIR range [40]. This makes it perhaps the less suitable material for NIR sensing at high wavelengths since extremely thick films would be needed. µc-Ge:H on the other hand was shown to be a promising material with an absorption coefficient reaching 10^4 cm^{-1} at 1 eV [23]. Use of this material is however extremely scarce for photodetection applications [26] and its poor electrical properties limits its usage to very thin absorbers. The next step was thus to try and combine the advantages of both materials into a microcrystalline $Si_{1-x}Ge_x$:H alloy. With this material, absorption and electrical properties becoming dependent on composition. Several studies have shown a degradation of electri-

Cette thèse est accessible à l'adresse : https://theses.insa-lyon.fr/publication/2023ISAL0014/these.pdf
© [A. Wilson], [2023], INSA Lyon, tous droits réservés

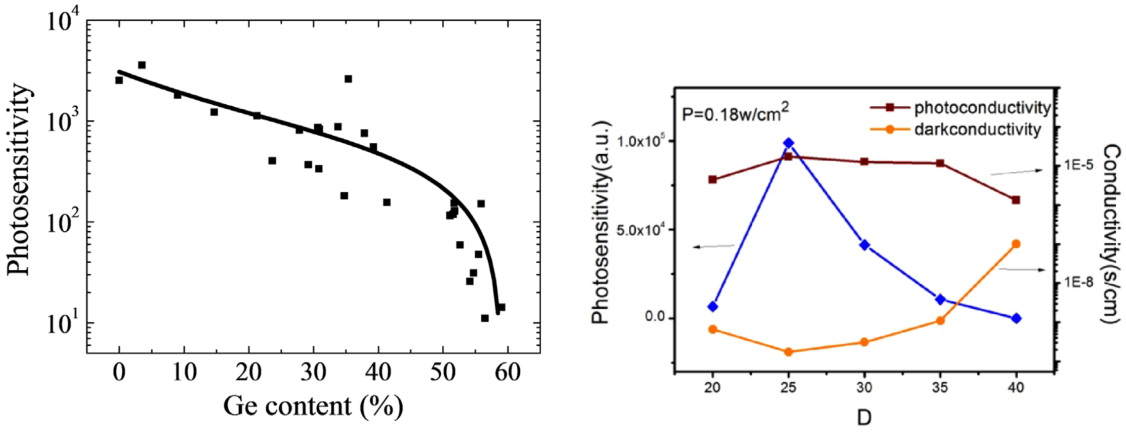

(a) (b)

Figure 5.4: $\Delta\sigma = \sigma_{ph} - \sigma_{dark}$ for: (a) µc-$Si_{1-x}Ge_x$:H [22] (b) proto/nano-crystalline SiGe:H alloy deposited at $GC = GeH_4/(SiH_4 + GeH_4) = 6$ %. $D = R_H$ is the hydrogen dilution factor. [90]

cal properties with increasing Ge fraction while absorption continuously increases in the low energy region [22, 23]. A compromise has to be reached depending on the application. So far, this material has been mainly introduced in solar cells [21, 22, 27].

Outline of this work

In order to produce an above-IC compatible NIR photodectector, the materials introduced over the course of this chapter will have to be developed and studied individually before combining them as elementary building blocks to obtain a functional device. In the context of above-IC processes, we seek to carry out these steps by taking care not to exceed temperatures of 350 °C [10, 13–15] (see section 1.2).

The challenges of such an endeavor lie, for a first part, in obtaining a high quality, low defect material with strong optical absorption in the NIR spectral range to be used as an absorber layer. Secondly, doping of the developed semiconductor films should be studied so as to achieve stable, highly doped thin films. Both p-type and n-type doping of the studied material should be achieved in order to be able to produce a P-I-N junction. Ultimately, the studied films should be integrated as a single functional device with appropriate electrical contacts exhibiting a photodiode behavior.

With the aim of providing a solution to the aforementioned challenges, chapter 2 will focus on the equipments and techniques necessary to produce and characterize individual semiconductor layer as well as devices. Chapter 3 will be dedicated to the development of high quality intrinsic Si:H, Ge:H and SiGe:H thin films by PECVD, with an emphasis on the structural, electrical and optical properties of such films. Based on these results, electrical and structural properties of Phosphorus and Boron doped Si:H and Ge:H films are investigated in chapter 4. Finally, chapter 5 will take advantage of the knowledge acquired throughout the previous chapters to produce a PIN junction architecture integrated to a simple prototype structure. This prototype's design will allow us to extensively test the developed materials in real operating conditions and will enable us to work on improving the NIR performance of our device.

Cette thèse est accessible à l'adresse : https://theses.insa-lyon.fr/publication/2023ISAL0014/these.pdf
© [A. Wilson], [2023], INSA Lyon, tous droits réservés

Chapter 2

Materials and Methods

In this second chapter, we will introduce the experimental techniques which are involved in preparing and characterizing our samples. Most of the techniques used over the course of this project have previously been described elsewhere in the literature. This chapter will thus focus on the motivation behind using these experimental techniques specifically for our samples. Additional references will be given for the reader seeking a more detailed description of the equipment in question.

1 Deposition and cleaning process

The Plasma Enhanced Chemical Vapor Deposition (PECVD) technique is at the very heart of this research project. It is inherently a low temperature deposition method. As such, PECVD limits the thermal budget for device production. Considerations regarding the physical and chemical mechanisms involved in PECVD are discussed in chapter 1, section 2. The substrate cleaning procedures prior to PECVD deposition will also be discussed here.

1.1 PECVD equipment at INL

Plasma-Enhanced Chemical Vapor Deposition (PECVD) can be summarized as a deposition technique relying on the gas phase dissociation of reactive precursors by a cold plasma to produce thin films. In this subsection we will provide an overview of the PECVD equipment in use at INL.

1.1.1 Deposition chamber specifications

The equipment used over the course of this Ph.D project is a commercially available PlasmaTherm Vision 310 PECVD (figure 1.1a). It is a capacitively coupled PECVD with a 13.56 MHz radiofrequency generator and a low frequency 100-460 kHz generator which can be used simultaneously. The low-frequency capability was only used for post-deposition cleaning of the chamber. A summary of main characteristics are given in table 2.1.

The top electrode seen in figure 1.1b is a shower-head electrode from which the gas mixture is injected into the chamber. The bottom electrode can be heated up to 380 °C and can hold substrates up to 12″ in diameter.

Cette thèse est accessible à l'adresse : https://theses.insa-lyon.fr/publication/2023ISAL0014/these.pdf
© [A. Wilson], [2023], INSA Lyon, tous droits réservés

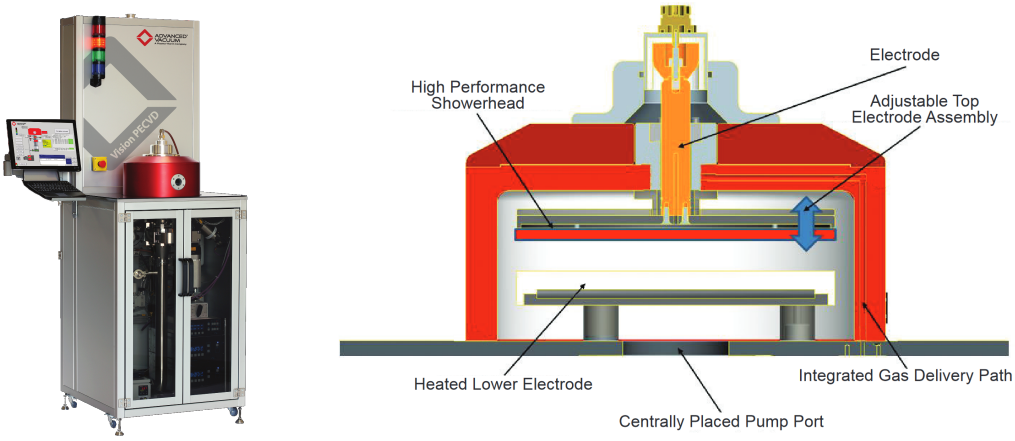

(a) (b)

Figure 1.1: (a) Photo of the PlasmaTherm Vision 310 PECVD equipment used (b) Schematic cross-section of the reactor chamber © PlasmaTherm

Electrode dimension	12″ – 305 mm
Inter-electrode spacing	22 mm
Temperature range	50 – 380 °C
Maximum Power supply	300 W (at 13.56 MHz)
Pressure range	0 – 1000 mTorr
Available gas lines	10

Table 2.1: PlasmaTherm Vision 310 PECVD specifications.

1.1.2 Gas lines specifications

Among the 10 available gas lines, 5 gases are predominantly used for semiconductor layer deposition. Gases have purity levels of 99.9999 % to prevent any unwanted species to be incorporated in the film. The concentration and gas flow rate specifcation for each of these gases is given in table 2.2. A 5 % dilution in H_2 for the GeH_4 source was chosen due to the need for high dilution factors R_H to produce µc-Ge:H films (see chapter 1, section 4). Phosphine (PH_3) and Diborane (B_2H_6) being dopant precursors they are further diluted in hydrogen in order to reach extremely low dopant to Si (or Ge) ratios.

Gas line	Dilution in H_2	Min. - Max. Flow Rates
H_2	-	15 – 1000 sccm
SiH_4	-	1.5 – 100 sccm
GeH_4	5 %	15 – 1000 sccm
B_2H_6	1000 ppm	1.5 – 100 sccm
PH_3	1000 ppm	1.5 – 100 sccm

Table 2.2: Gas lines, concentration and flow rate specifications.

Safety precautions (gas detectors, glove box, ventilation) are put in place as most of the gases used are either highly toxic (GeH_4, B_2H_6, PH_3) or highly flammable (H_2, SiH_4). The limited range in gas flow rates with the current configuration will later limit the maximum

Cette thèse est accessible à l'adresse : https://theses.insa-lyon.fr/publication/2023ISAL0014/these.pdf
© [A. Wilson], [2023], INSA Lyon, tous droits réservés

hydrogen dilution level R_H as well as the maximum Germane concentration in silane-germane plasmas.

1.1.3 Gas flow rate calculation

Working in comparable gas flow conditions is crucial to understand the impact of a single parameter on the film's properties. Consequently, the gas flow for each precursor has to be calculated from the parameters we want to set (R_H, GC or other).

Silane-Germane plasma

In order to set a parameter like R_H, GC or Φ_{tot} for a given film, it is necessary to establish the relation between the known parameters of our system and the final gas flows to input for production. The following parameters are set by the operator and the hardware itself :

$[SiH_4]_{tank}$	the Silane concentration in the gas tank used. As Silane is often found undiluted, its value is set to 1.
$[GeH_4]_{tank}$	the Germane concentration in the gas tank. The current experimental setup has Germane diluted at 5 % in hydrogen. Its value is thus set to 0.05.
Φ_{tot}	total gas flow in standard centimeter cube per minute (sccm). This value is set by the operator.
$R_H = \frac{\Phi_{H2}}{\Phi_{SiH4}+\Phi_{GeH4}}$	the hydrogen dilution factor, i.e. the ratio of hydrogen to precursor gas flow. The dilution is set by the operator.
$GC = \frac{\Phi_{GeH_4}}{\Phi_{SiH_4}+\Phi_{GeH_4}}$	germane concentration, which is the ratio of germane gas flow to total precursor gas flow.

From these known parameters three process parameters are calculated, namely the Silane gas flow Φ_{SiH4}, the diluted Germane gas flow $\Phi_{GeH4+H2}$and the hydrogen gas flow Φ_{H2}. Φ_{SiH4} is first obtained, from which Germane and Hydrogen gas flow can then be easily deduced. The expression used to obtain these parameters are the following :

$$\Phi_{SiH4} = \Phi_{tot} \cdot \Big(\frac{[SiH_4]_{tank} \cdot GC \cdot R_H}{1-GC} + [SiH_4]_{tank} \cdot R_H + \frac{GC \cdot [SiH_4]_{tank}}{[GeH_4]_{tank} \cdot (1-GC)} - \frac{GC \cdot [SiH_4]_{tank} \cdot (1-[GeH_4]_{tank})}{[GeH_4]_{tank} \cdot (1-GC)} + [SiH_4]_{tank}\Big)^{-1} \quad (1.1)$$

$$\Phi_{GeH4+H2} = \frac{\Phi_{SiH4} \cdot GC \cdot [SiH_4]_{tank}}{[GeH_4]_{tank} \cdot (1-GC)} \quad (1.2)$$

$$\Phi_{H2} = \Phi_{tot} - \Phi_{GeH4+H2} - \Phi_{SiH4} \quad (1.3)$$

These expressions make it possible to vary a single parameter like GC while keeping R_H and Φ_{tot} constant.

Cette thèse est accessible à l'adresse : https://theses.insa-lyon.fr/publication/2023ISAL0014/these.pdf
© [A. Wilson], [2023], INSA Lyon, tous droits réservés

Silane - Phosphine / Diborane plasma

Similarly to a Silane-Germane plasma, Silane can be mixed with Phosphine or Diborane precursors. The doping gas to silane ratio β can be varied while keeping R_H and Φ_{tot} constant. On top of $[SiH_4]_{tank}$ and Φ_{tot} defined above (section 1.1.3), the following parameters are set by our needs :

$R_H = \frac{\Phi_{H2}}{\Phi_{SiH4}+\Phi_{Dopant}} \approx \frac{\Phi_{H2}}{\Phi_{SiH4}}$ — the hydrogen dilution factor, i.e. the ratio of hydrogen to precursor gas flow. The dilution is set by the operator. Φ_{Dopant} is typically much smaller than Φ_{SiH_4} and can thus be neglected.

$\beta = \frac{\Phi_{Dopant}}{\Phi_{SiH_4}+\Phi_{Dopant}} \approx \frac{\Phi_{Dopant}}{\Phi_{SiH4}}$ — the doping gas to silane ratio, which gives the gas phase concentration of precursor.

From these parameters the Silane gas flow Φ_{SiH4}, the diluted Phosphine/Diborane gas flow $\Phi_{Dopant+H2}$ and the hydrogen gas flow Φ_{H2} can be calculated (in sccm). The following formulas are used :

$$\Phi_{SiH4} = \frac{\Phi_{tot}}{R_H} \tag{1.4}$$

$$\Phi_{Dopant+H2} = \frac{\Phi_{SiH4} \cdot \beta}{[Dopant]_{tank}} \tag{1.5}$$

$$\Phi_{H2} = \Phi_{tot} - \Phi_{Dopant+H2} - \Phi_{SiH4} \tag{1.6}$$

This makes it possible to vary a single parameter like β while keeping R_H and Φ_{tot} constant.

1.1.4 Hardware improvement for µc-Si:H production

Film thickness uniformity issues were encountered while working with highly hydrogenated plasmas. Due to hardware limitations of our PECVD equipment maximum H_2 gas flow rate was limited thus maximum chamber pressure was restricted. In this configuration it could not exceed 400 mTorr. Deposition of a-Si:H (with low R_H) worked as expected yet as R_H was increased to 20, unusual deposition pattern appeared as shown in figure 1.2. The center of the electrode showed no sign of film deposition while the edges where covered in a thick Si layer.

No similar problem was found to be described in literature. In order to overcome this critical limitation extensive tests where performed after upgrading the equipment's H_2 mass flow to reach $max(\Phi_{H2}) = 1000$ sccm.

Experimental setup improvement

Impact of chamber pressure, RF power, H_2 gas flow and dilution factor were examined. For each deposition conditions 4 glass substrates were positioned along the radial direction of the bottom electrode (anode) at 0, 5, 10 and 15 cm from the center. Thickness d was then measured by spectroscopic ellipsometry (SE, see chapter 2). Results are presented in figure 1.3 where relative thickness $D = d(r)/d(15cm)$ is plotted as a function of radial distance.

Out of all the parameters tested the most critical one by far was found to be chamber pressure (see figure 1.3a). Increasing the pressure from 300 mTorr to 600 mTorr led $D(r = 0)$ to

Cette thèse est accessible à l'adresse : https://theses.insa-lyon.fr/publication/2023ISAL0014/these.pdf
© [A. Wilson], [2023], INSA Lyon, tous droits réservés

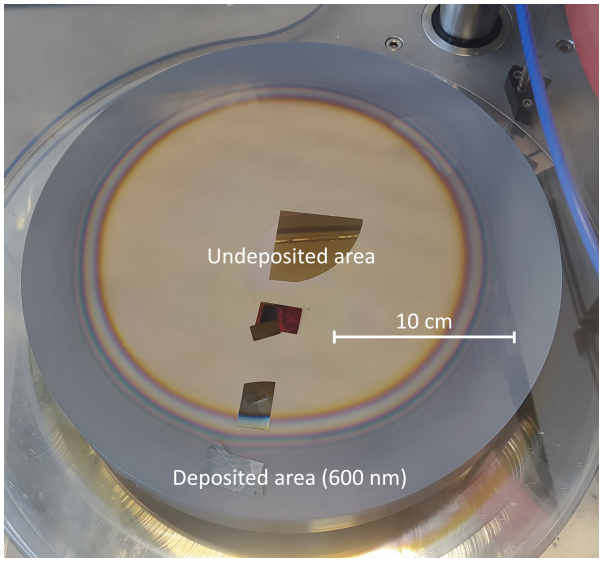

Figure 1.2: Top view of the PECVD chamber bottom electrode after a 120 min deposition (process parameters R_H=20 - 50W - 400 mTorr - Φ_{total}=100 sccm). The radial inhomogeneity is extremely important with a 600 nm thick layer deposited at the edges.

increase from 0% (no deposition) to over 60% of the film thickness found at the edges in the worst case. Increasing pressure again to 900 mTorr further improves uniformity, especially in high dilution ($R_H = 50$) and high power (60 W) conditions. From figures 1.3b and 1.3c a clear picture emerges as an increase of either RF power or Φ_{H2} will be detrimental to uniformity in the tested range. Neither of them are as critical as chamber pressure hence for future developments of hydrogen diluted gas mixtures a working point above 600 mTorr should be chosen to prevent any similar issue.

Additional data would be needed to clearly identify the mechanism responsible for this problem. Our hypothesis is that lack of uniformity occurs due to a combination of excessive pumping of the chamber, low residence time of reactive species as well as electrostatic edge effect. Due to the reactor geometry, the gaseous mixture is injected from the showerhead electrode and excess gas is then pumped below the anode. This causes the injected gas to flow radially in such a way that the flow reaching edges is greater than at the center (see figure 1.4).

At constant gas flow, a lower pressure will mean species spend less time in the chamber as they are pumped out faster. With less residence time deposition only occurs where the concentration of species is highest, i.e. at the edges. The increased electrical field formed at the edges due to the 90° angle [98, 99] may also cause increased reactive specie concentration around the edges, in turn leading to increased deposition rate. These are still assumptions however as plasma and fluid mechanics modeling was deemed to be beyond the scope of our work.

1.2 Substrate cleaning procedure

Working with sub-micrometric systems requires the production process to take place in a controlled environment. Contamination in the form of dust or organic compounds can jeopardize the proper functioning of the system. The control of the production environment start

Cette thèse est accessible à l'adresse : https://theses.insa-lyon.fr/publication/2023ISAL0014/these.pdf
© [A. Wilson], [2023], INSA Lyon, tous droits réservés

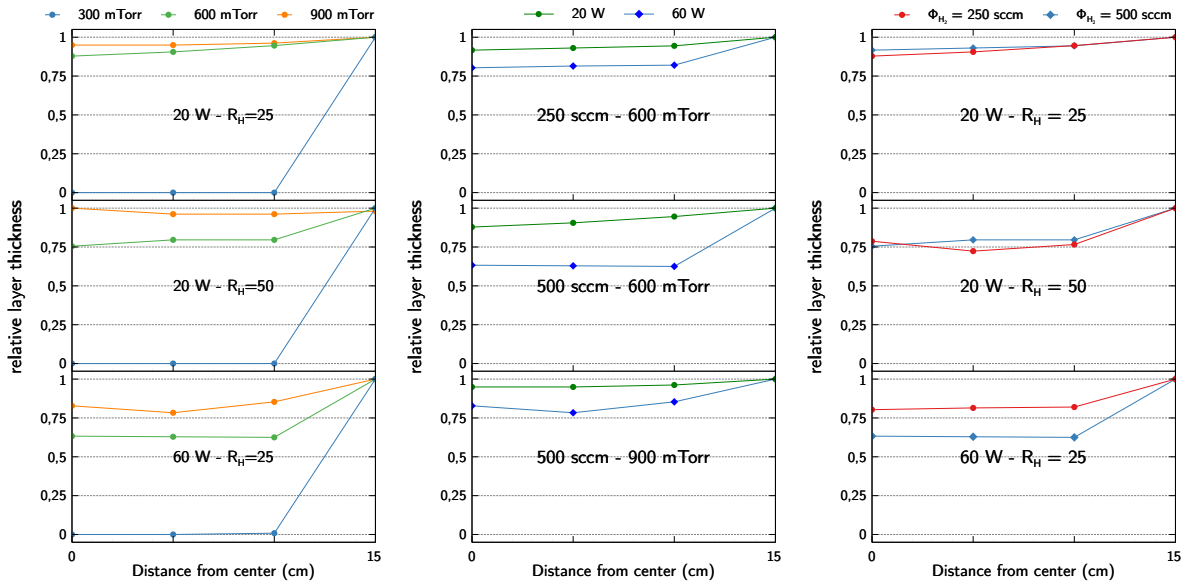

(a) (b) (c)

Figure 1.3: Film growth radial uniformity as a function of : (a) pressure, at fixed $\Phi_{H2} = 500$ sccm, (b) RF-Power, at fixed $R_H = 25$, (c) Φ_{H2}, at 600 mTorr.

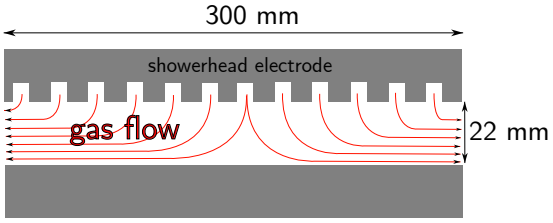

Figure 1.4: Schematic cross-sectional view of the gas flow direction between electrodes in the PECVD reaction chamber.

with adequate substrate cleaning.

1.2.1 c-Si substrate cleaning

Monocrystalline Silicon (100)-oriented substrates cut from 4″ or 12″ wafers are used as substrates. Their low surface roughness (< 1 nm) make them ideal for spectroscopic ellipsometry measurements or atomic force microscopy. Due to the inevitable formation of a native oxyde layer when exposing bare c-Si to the atmosphere, c-Si substrates are cleaned prior to deposition according to the process schematized in figure 1.5. c-Si substrate is rinsed with deionized (DI) water before being dipped in a 5 % fluoridric acid solution (HF 5 %) for 30 seconds to remove the native oxyde layer. c-Si is then re-oxydized with a 10 minute ozone treatment to get rid of organic contaminants. The oxyde layer formed is removed from the surface using 5 % diluted HF before being rinsed and blow-dried. Samples are finally sealed under a primary vacuum for transportation, thus avoiding immediate re-oxydation of the surface.

This procedure was successfully tested for c-Si surface cleaning prior to a-Si:H passivation

Cette thèse est accessible à l'adresse : https://theses.insa-lyon.fr/publication/2023ISAL0014/these.pdf
© [A. Wilson], [2023], INSA Lyon, tous droits réservés

in photovoltaic processes. It is also more simple than a standard RCA clean which as standard in the industry. More examples of silicon cleaning procedures can be found in the following book [100].

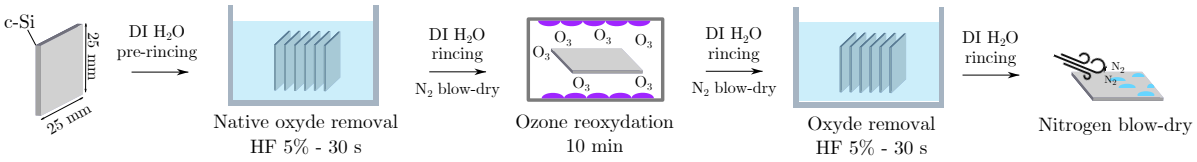

Figure 1.5: c-Si substrate cleaning process prior to PECVD deposition.

1.2.2 Glass substrate cleaning

Commercially available glass substrate were used as a non-crystalline substrate for sample deposition. The glass substrates bought from OSSILA[1] are 12×15 mm^2 in width and length and 550 µm in thickness. Before being used for PECVD deposition, each substrate is cleaned as shown in figure 1.6. The glass substrate is rinsed with DI water before being cleaned in an ultra-sonic bath with pure ethanol at 40 °C for 10 minutes. The samples are then rinsed from any trace of ethanol and blow-dried using nitrogen. Similarly to c-Si samples, the glass substrates are sealed under a primary vacuum for transportation to avoid any dust contamination.

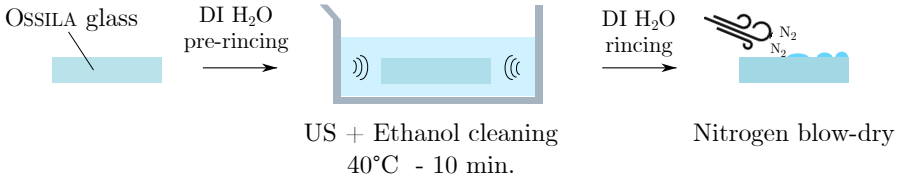

Figure 1.6: Glass substrate cleaning process prior to PECVD deposition.

1.2.3 ITO cleaning

Indium-Tin-Oxyde (ITO) can be used as a transparent electrical contact layer for device fabrication. ITO coated glass slides are commercially available from OSSILA. The substrate is a 1.1 mm thick, 15×20 mm glass slide coated with 100 nm of ITO. Prior to being used for PECVD material growth, the ITO layer is cleaned according to the process schematized in figure 1.7. The glass + ITO substrates are rinsed with DI water before being cleaned for 10 minutes by ultrasonic (US) cleaning in ethanol at 40 °C. The samples are then rinsed and blow dried using nitrogen. Finally ITO's surface is activated and cleaned from any remaining organic contaminants by exposing it to an ozone and UV treatment.

2 Chemical and Structural characterization

The peculiar structural, crystallographic and chemical properties of amorphous and microcrystalline films calls for suitable characterization techniques. In this section, Raman spec-

[1] www.ossila.com

Cette thèse est accessible à l'adresse : https://theses.insa-lyon.fr/publication/2023ISAL0014/these.pdf
© [A. Wilson], [2023], INSA Lyon, tous droits réservés

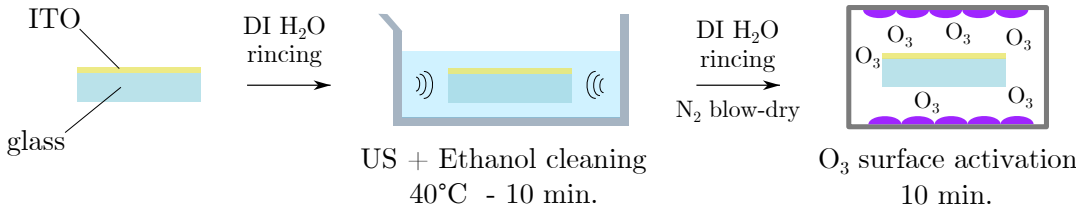

Figure 1.7: ITO cleaning process prior to PECVD deposition.

troscopy, Scanning Transmission Electron Microscopy and Secondary Ion Mass Spectrometry will be introduced, with a focus put on microcrystalline sample analysis.

2.1 Raman Spectroscopy

Raman spectroscopy is a non-destructive analysis technique which can provide chemical and structural information of a sample. It relies on the inelastic scattering of light, known as Raman scattering [101]. Inelastic scattering of light is the physical phenomenon through which photons are scattered at a different wavelength from the incoming light due to an exchange of energy with a phonon. The intensity of the scattered light and the value for the shift, called the Raman shift and noted $\Delta\omega$, provide useful information of the chemical and physical nature of the sample. The measured $\Delta\omega$ typically lies in the 50 to 2000 cm^{-1} range and is a consequence of the molecular bond energy between the atoms of the sample.

2.1.1 Equipment Specification

Measurements were performed at the CECOMO platform of the Institut Lumière Matière (ILM)[2] on a Horiba Jobin-Yvon Raman micro-spectrometer. Figure 2.1 provides a schematic overview of the equipment. A LASER beam is sent to a beam splitter and then focused via a microscope lens on the surface of the sample. The inelastic back scattered light will pass through a set of filters, mirrors and gratings before being collected by a CCD detector. The data is finally extracted in the form of a number of counts as a function of Raman shift $\Delta\omega$ (in cm^{-1}).

In the setup used throughout this project, a 473 nm LASER source was used. This wavelength is highly absorbed by the semiconductor layer of interest and thus strongly probes the surface of the sample. Precautions were taken to check the focused LASER beam did not lead to a crystallization of the studies layers. An high working distance x50 magnification microscope lens was used with a numerical aperture of 0.5. The high working distance allowed the measurements to be less sensitive to the focus plane and thus probe the film more homogeneously. The probed area was in the order of 5×5 μm^2. All spectra were averaged several times at the same location to improve the signal to noise ratio and a spectral resolution of 1.1 cm^{-1} was used.

2.1.2 Raman spectroscopy of Si/Ge films

Raman scattering was used to characterize a-Si:H films as early as 1977 [102]. Since the Raman shift is dependent on molecular bond energy, it can be used to probe the Si–Si bonds, Ge–Ge

[2]UMR5306, Villeurbanne, France

Cette thèse est accessible à l'adresse : https://theses.insa-lyon.fr/publication/2023ISAL0014/these.pdf
© [A. Wilson], [2023], INSA Lyon, tous droits réservés

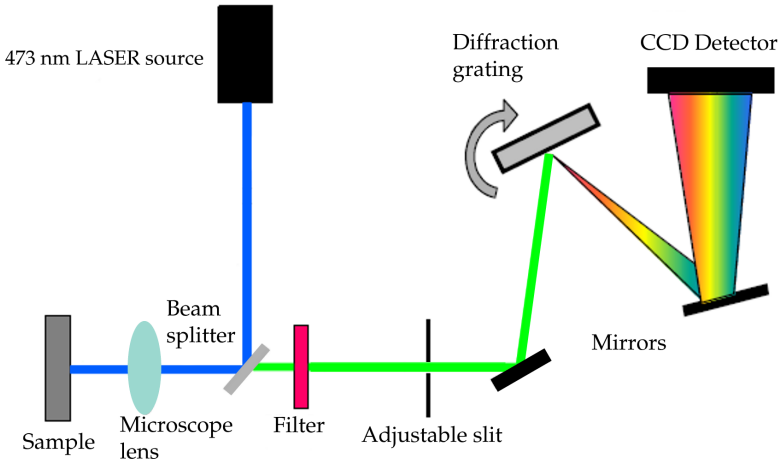

Figure 2.1: Schematic view of the backscattering Raman micro-spectrometer used, adapted from physicsopenlab.org.

bonds and Si–Ge bonds. The bond energy not only depends on the chemical species but also on the structural properties on the material.

Raman characterization of Silicon films

The Raman spectra for silicon thin films is a sum of optical and acoustic gaussian peaks, as displayed in the case of a-Si:H in figure 2.2a. The transverse optical (TO) has the highest intensity and can be used to provide structural information about the sample. In crystalline silicon, the Si–Si bond TO peak is a sharp, symmetric peak at 521 cm^{-1} while for a-Si:H it is a broad gaussian peak centered at 480 cm^{-1}. As crystalline volume fraction is increased the raman spectrum of the film becomes a combination of an amorphous spectrum and a crystalline spectrum (see figure 2.2b). The position of the crystalline $\Delta\omega_{Si-Si}$ peak is thus dependent on crystalline volume fraction but also on grain size ([103, 104]).

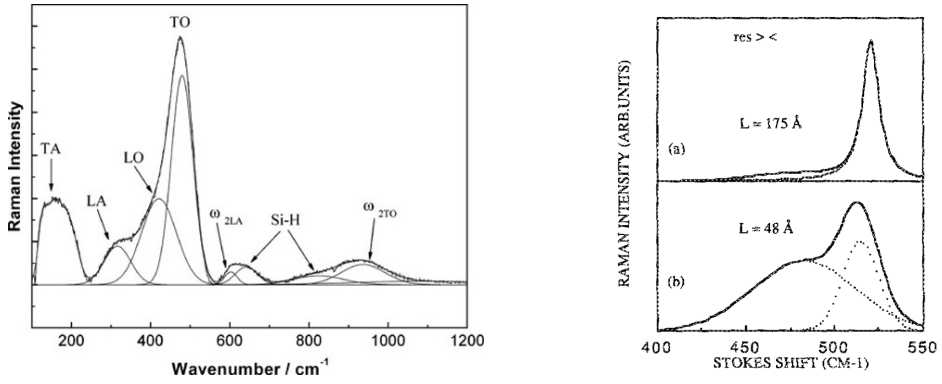

(a) (b)

Figure 2.2: (a) Raman spectrum of a-Si:H [105] (b) Raman spectra of µc-Si:H with different crystallite size L. [103]

Cette thèse est accessible à l'adresse : https://theses.insa-lyon.fr/publication/2023ISAL0014/these.pdf
© [A. Wilson], [2023], INSA Lyon, tous droits réservés

An estimation for the crystalline volume fraction called Raman crystallinity and noted X_c can be obtained from a careful analysis of the spectrum. X_c is obtained by deconvolution of the spectra into 3 gaussian components : an amorphous component in the 470 – 490 cm^{-1} range, a grain-boundary component near 500 cm^{-1} and a crystalline component in the 512 – 521 cm^{-1} range [105]. X_c (equation 2.1) is calculated from ratio in area of these gaussian peaks I_a, I_{gb} and I_c respectively.

$$X_c = \frac{I_{gb} + I_c}{\gamma \cdot I_a + I_{gb} + I_c} \tag{2.1}$$

where γ is a correction factor accounting for the difference in scattering cross section of the amorphous and crystalline phase. It was proposed by Bustarret et al. [103] and is given by equation 2.2.

$$\gamma = 0.1 + \exp(-\frac{D_{cryst}}{250}) \quad \text{with} \quad D_{cryst} = 2\pi\sqrt{\frac{B}{521 - \Delta\omega_{\max}}} \tag{2.2}$$

This correction factor is dependent on grain size D_{cryst} (in nm, with the factor $B = 2.0$ $cm^{-1}{\cdot}nm^2$) which can be estimated from $\Delta\omega_{\max}$, the difference in peak position between crystalline silicon (521 cm^{-1}) and our sample [105]. The estimation of D_{cryst} can be difficult to estimate if there is residual stress in the film as peak position will to lower or higher wavenumbers if their is tensile or compressive stress respectively [106]. Measurements were performed on glass-deposited films to avoid any contribution of the c-Si substrate to the spectrum which would lead to an overestimation of X_c.

Data analysis of Silicon films

We have developed a python code to automate the Raman data processing. The raw data obtained is smoothed using a Savitzky-Golay filter on a 7 data point window with a 3rd order polynomial [107] to make peak position identification less sensitive to noise. A linear baseline is then subtracted the 400 to 550 cm^{-1} range. From the peak position D_{cryst} and γ are obtained. The spectrum is then fitted with 3 gaussian curves each requiring 3 parameters : amplitude a, peak position ω_0 and standard deviation σ with boundary conditions on peak position as defined above. The area of each gaussian is $I = a\sigma\sqrt{2\pi}$ which is then used to obtain X_c. An example of the fitted Raman data is shown in figure 2.3. Measurements repeated at different points on a given sample yield an absolute uncertainty on X_c lower than 5 %.

Raman characterization of Germanium films

Similarly to Silicon films, the Raman spectra for germanium has an intense transverse optical (TO) peak which gives structural information about the sample. In crystalline Germanium, the Ge–Ge bond creates a sharp peak centered at 300 cm^{-1}. For amorphous Germanium this peak is shifted to lower $\Delta\omega$ around 275 cm^{-1} as seen in figure 2.4. In microcrystalline Germanium, the TO peak position $\Delta\omega_{Ge-Ge}$ can vary between 275 and 300 cm^{-1}. The same approach as the one detailed for Si:H films is used, [108, 109] that is, the measured spectrum is deconvoluted into 3 gaussians components corresponding to the amorphous, grain boundary and crystalline phases. The Raman crystallinity is obtained from the area of these gaussian curves :

$$X_c = \frac{I_{gb} + I_c}{I_a + I_{gb} + I_c} \tag{2.3}$$

Cette thèse est accessible à l'adresse : https://theses.insa-lyon.fr/publication/2023ISAL0014/these.pdf
© [A. Wilson], [2023], INSA Lyon, tous droits réservés

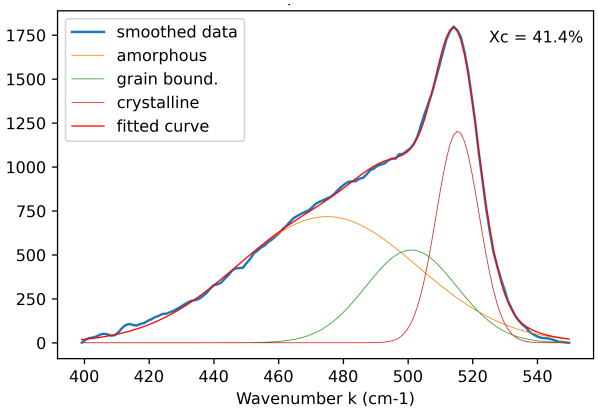

Figure 2.3: Fitted Raman spectrum for a µc-Si:H ($X_c = 41.4$ %) film deposited on glass. The fitted curve is the sum of the 3 individual gaussian curves and closely matches our experimental data.

Depending on the paper, the grain boundary component is not always used [109]. A scattering cross section correction factor (similar to γ for µc-Si:H, see section 2.1.2) is sometimes applied to the amorphous component yet the values used in literature differ. In our case we chose to set this parameter to 1. Vrijer et al. [109] worked with 0.85 while Hao et al. [108] very recently established an expression $y(D_{cryst})$ for this factor similarly to the work done by Bustarret et al. [103] for µc-Si:H.

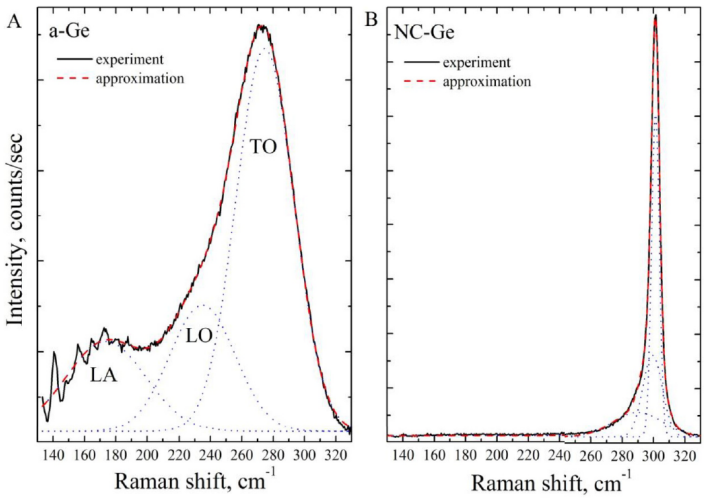

Figure 2.4: Fitted Raman spectra for a-Ge:H and µc-Ge:H films. [108]

The data analysis was performed identically to that of µc-Si:H films (see section 2.1.2) but applied to the 200 to 350 cm^{-1} range. After data smoothing, baseline subtraction and gaussian fitting, X_c is obtained. An example of a deconvoluted µc-Ge:H spectrum is given in figure 2.5. Since the Si–Si and Ge–Ge peaks do not overlap, it is possible to conduct this analysis for films grown on a c-Si substrate.

Cette thèse est accessible à l'adresse : https://theses.insa-lyon.fr/publication/2023ISAL0014/these.pdf
© [A. Wilson], [2023], INSA Lyon, tous droits réservés

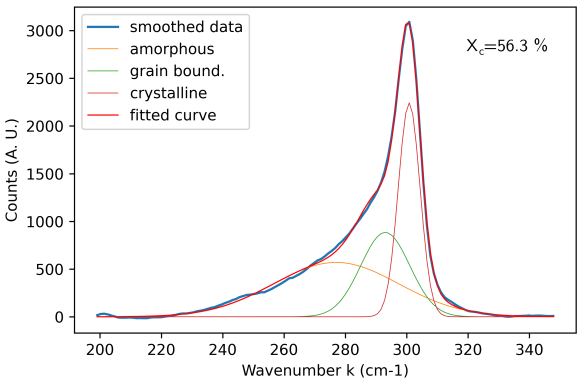

Figure 2.5: Fitted Raman spectrum for a µc-Ge:H ($X_c = 56.3$ %) film deposited on glass. The fitted curve closely matches our experimental data.

Raman characterization of Silicon-Germanium films

In Microcrystalline Silicon-Germanium films Si–Si, Ge–Ge and Si–Ge bonds coexist [88, 110]. This makes them more difficult to characterize by Raman Spectroscopy as these bonds not only vary in position and in broadening due to crystallinity but also due to composition [111, 112]. The interdependence of both parameters is too strong for us to be able to confidently extract a value for X_c. The crystallinity can however be qualitatively appreciated as a-SiGe:H and µc-SiGe:H spectra differ significantly from one another . An amorphous SiGe:H film will lead to 3 broad overlapping gaussian peaks while µc-SiGe:H has a spectra with 3 distinguishable asymmetric peaks (see figure 2.6a and 2.6b). For a more quantitative assessment of crystallinity, TEM analysis can be performed on the sample.

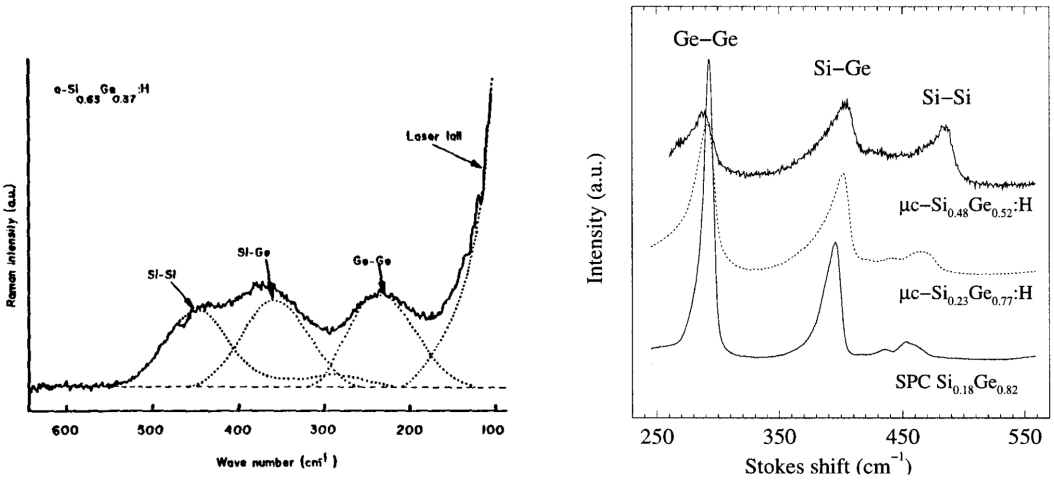

(a) (b)

Figure 2.6: (a) Raman spectrum of a-$Si_{0.65}Ge_{0.35}$:H [113] (b) Raman spectra of µc-SiGe:H films with increasing Ge fraction. [110]

Cette thèse est accessible à l'adresse : https://theses.insa-lyon.fr/publication/2023ISAL0014/these.pdf
© [A. Wilson], [2023], INSA Lyon, tous droits réservés

2.2 Transmission Electron Microscopy

Transmission electron microscopy (TEM) is a high resolution imaging technique which relies on the interaction of a high energy electron beam with a thin sample to obtain atomic resolution images. It was used to obtain local crystalline and chemical information about the PECVD-grown thin films. All TEM sample preparation and analysis were performed by the Physical Charaterization teams at STMicroelectronics. A very basic presentation of TEM and its applications to our samples will be given in this section. A more detailed approach to the technique is presented in Pennycook and Nellist's book [114].

2.2.1 Working Principle

TEM uses a high energy electron beam (100 - 1000 keV) and requires ultra-thin samples (< 100 nm). The resulting image is formed from the interaction of the electrons transmitted through the sample (lamella). The image's contrast is based on differences in atomic number and in crystallinity. TEM is a complex technique, requiring extremely controlled environments to achieve a resolution in the order of 0.5 nm. This improvement in resolution compared to Scanning Electron Microscopy (SEM) comes at the cost of increased complexity in sample preparation.

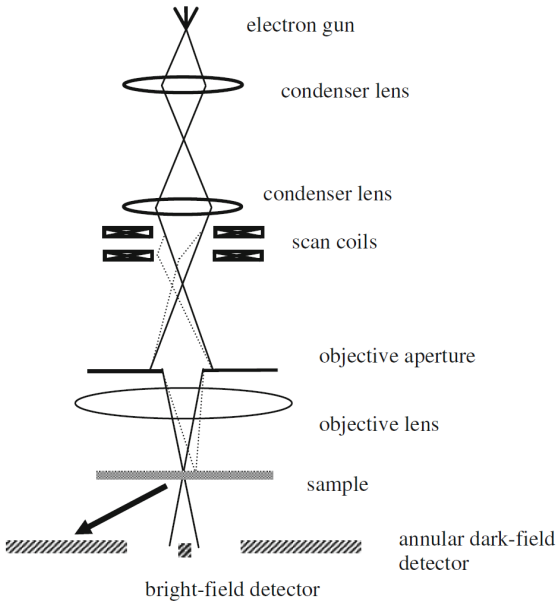

Figure 2.7: Schematic diagram of a TEM column, taken from [114].

The high energy electron beam is obtained by accelerating electron under vacuum using high voltage which can reach up to 1 MV. The accelerated electrons exit the electron gun and are then focused using a set of electromagnetic lens. This step is crucial to reach a sub-nanometric beam size when hitting the sample. Scan coils are then used to scan the beam across the sample, thus forming a 2D image acquired point by point. The signal extracted from the beam's interaction with the sample can be of several types (Bright Field, Annular Dark Field, Electron Energy Loss Spectroscopy, Energy Dispersive X-ray) which highlight different information about the sample (Crystallinity, Chemical Contrast, Composition,...). For our samples, the Annular Dark Field (ADF) and Electron Energy Loss Spectroscopy (EELS)

Cette thèse est accessible à l'adresse : https://theses.insa-lyon.fr/publication/2023ISAL0014/these.pdf
© [A. Wilson], [2023], INSA Lyon, tous droits réservés

where mostly used.

2.2.2 Dark Field Imaging

ADF collects electrons scattered at high angles from the main beam and EELS analyzes the energy loss of transmitted electrons, hence both can be used simultaneously to provide both a structural image of the sample and a chemical image of the sample. ADF leads to high resolution images with good atomic number contrast (Z-contrast). An ADF-TEM image of a c-Si sample is shown in figure 2.8 where atomic columns can be clearly identified. The error of distances obtained through this technique is on the order of 5 %.

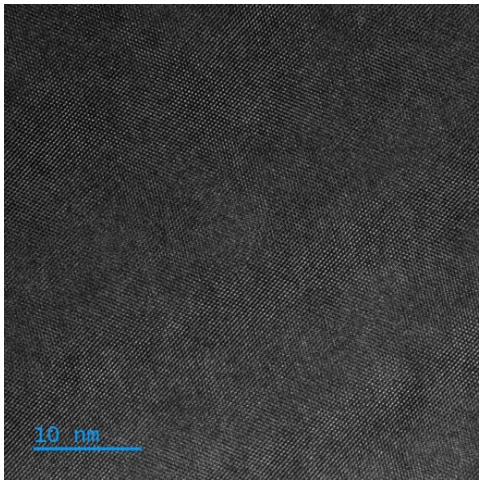

Figure 2.8: Annular dark field STEM imaging of a monocrystalline silicon sample.

2.2.3 Electron Energy Loss Spectroscopy

Unlike ADF which works thank to elastically scattered electrons, EELS uses the inelastic scattering of the electron beam to provide chemical information about a sample [115]. As fast electrons travel through the TEM lamella, fast electrons can loose some kinetic energy. This energy is loss by emitting photons in a wide range of energy (from a few eV to 1 keV). The energy loss of transmitted electrons is measured by and electron spectrometer which separates charges according to their energy using a magnetic field. An energy loss spectra is obtained at each point of the scan and careful analysis of this data provides information about the material scanned by the beam. This is done by identifying the peaks in the energy loss spectrum corresponding to the ionization energy of inner shell electrons of a given atom. By carefully gathering information on a wide energy range one can determine the nature and amount of a specific atom present in a sample. Unfortunately, thus method cannot quantify hydrogen due to its low energy transitions. An EELS image of a µc-SiGe:H film deposited on c-Si is shown in figure 2.9 with the Silicon and Germanium contents displayed as yellow and turquoise pixel colors, respectively. A line profile is also provided for element quantification.

In parallel to EELS, Energy Dispersive X-Ray Spectroscopy (EDS or EDX) was used to provide a chemical mapping of the sample. Both EELS and EDX rely on the energy lost by the beam passing through the material. Based on the energy of the X-rays emitted by the sample – corresponding to energy difference between the ionized inner shell level and the outer shell level – the composition can be estimated.

Cette thèse est accessible à l'adresse : https://theses.insa-lyon.fr/publication/2023ISAL0014/these.pdf
© [A. Wilson], [2023], INSA Lyon, tous droits réservés

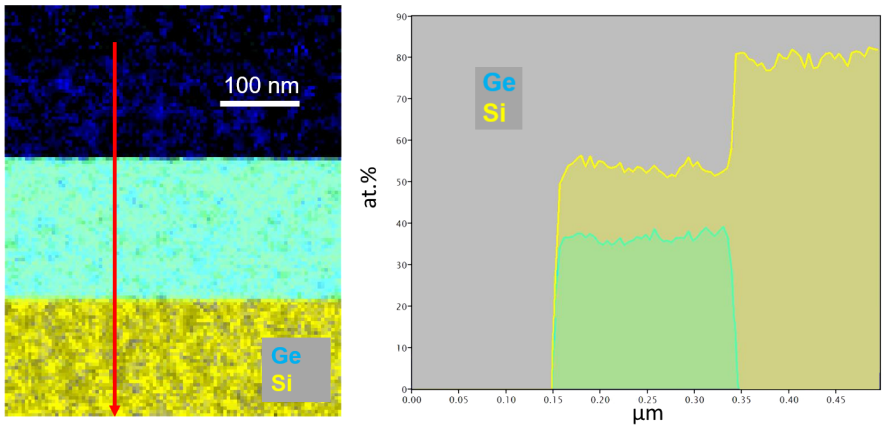

Figure 2.9: EELS Image and composition profile of a µc-SiGe:H film deposited on c-Si.

2.2.4 TEM Lamella Preparation

We previously mentioned that in order to carry out a TEM characterization ultra-thin samples of around 100 nm in thickness were needed for the sample to be transparent to electrons. This step is perhaps the most critical one as the process can alter or break the film. The two most common means of preparation for the TEM lamella are chemical-mechanical polishing and Focused Ion Beam (FIB) milling. Chemical-mechanical polishing is slow and costly as the lamella is obtained by grinding down a small sample using abrasives. The final step usually relies on an ion polishing of the surface using accelerated Ar^+ ions (~ 10 keV).

FIB milling was used for our samples. It allows to precisely select the area of interest as the milling is performed in combination with SEM imaging. The focused ion beam name comes from the accelerated Gallium ions which are used to physically etch the surface of the sample. Similarly to SEM, FIB acccelerates Ga ionized from its contact with a tungsten needle in a high electric field. The Ga^+beam is then focused to the specific area to be etch by a set of electro-magnetic lenses [116]. The lamella itselft is prepared by etching trenches around a small area of the sample for a single lamella to stand out (figure 2.10a). Once the trenches were etched and the sample thinned to less than 100 nm it was extracted for TEM observation. This step (the lift-out) was done using a nano-manipulator which was soldered to the lamella using local Platinum CVD deposition [117] (see figure 2.10b).

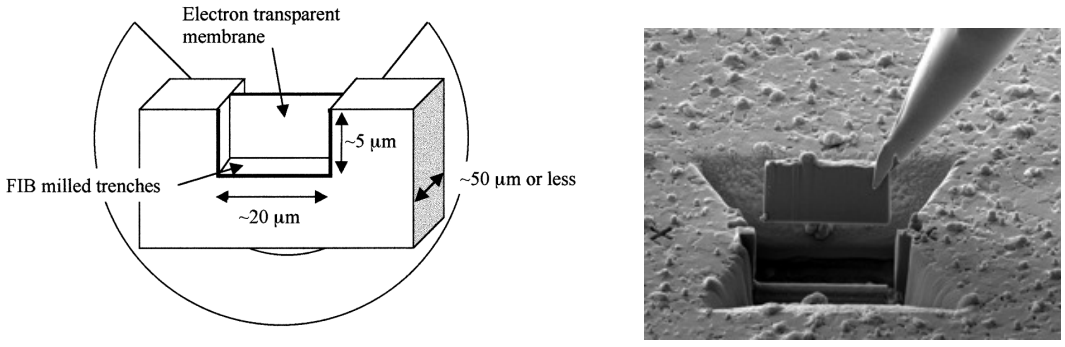

(a) (b)

Figure 2.10: (a) TEM lamella diagram from [116] (b) Micromanipulator lift-out of a lamella.

Cette thèse est accessible à l'adresse : https://theses.insa-lyon.fr/publication/2023ISAL0014/these.pdf
© [A. Wilson], [2023], INSA Lyon, tous droits réservés

In the case of microcrystalline semiconductor for which TEM aims to provide local structural information about the sample precaution should be taken during the lamella preparation. Indeed, the FIB milling process is know to damage the material's structure due to the high energy of the Ga^+ions (~ 25 keV, [116]). In particular crystalline Germanium lamellas were reported to experience amorphization at the surface (20 nm) of the lamella when milled using Gallium FIB [116, 118]. However no explicit sign of FIB induced amorphous phases were found in our samples when comparing TEM and Raman spectroscopy data.

Overall, TEM is a extremely powerful analysis tool. It can provide atomic scale structural and chemical information about a sample. However the slow throughput of this technique means we cannot only rely on TEM to study our samples. Its extremely high magnification also means the measurements are only local and do not provide a clear view of the whole sample.

2.3 Secondary Ion Mass Spectrometry

Secondary Ion Mass Spectrometry (SIMS) is a chemical analysis technique which was used to determine the chemical composition of the deposited films. Its high sensitivity made it possible to quantify the presence of atoms embedded in a matrix at low concentrations. SIMS characterization were performed by the Physical Characterization team at STMicroelectronics. This method was used for Germanium content measurement in SiGe:H alloys and for Phosphorus dopant concentration in doped films.

2.3.1 Working Principle

SIMS mesures the composition of a solid sample by sputtering its surface with a primary ion beam. The ionized sputtered material (secondary ions) originating from the surface are then collected and analyzed by a mass spectrometer as shown in figure 2.11 [119–121]. The role of this spectrometer is to identify the different ions by their mass to charge ratio. Ionization probability is highly dependent of the primary ion beam and on the analyzed material. Consequently element quantification could only be achieved by calibrating the method using references of known composition. For this reason the experimental uncertainty for the measured atomic concentration is in the order of 5 to 20 %.

This technique has a depth resolution in the 0.3 to 1 nm range and can reach a sensitivity in the ppm to ppb range [121]. The extreme sensitivity and fine depth resolution come at the cost of a lateral resolution of a few micrometers. For our purpose, two types of analysis were used : SIMS and ToF-SIMS.

2.3.2 SIMS

SIMS and Time-of-Flight (ToF-) SIMS both rely on the mass analysis of secondary ions. SIMS is sometimes referred to as "dynamic" SIMS as the ion beam etches the depth of the sample as the analysis takes place. A 3 keV Cesium primary ion beam (Cs^+) was used to sputter the surface of the sample through which a depth profile of the film composition could be obtained. This method was used for Germanium content quantification in µc-SiGe:H films. $CsGe^+$ and $CsSi^+$ ions were analyzed for quantification.

Cette thèse est accessible à l'adresse : https://theses.insa-lyon.fr/publication/2023ISAL0014/these.pdf
© [A. Wilson], [2023], INSA Lyon, tous droits réservés

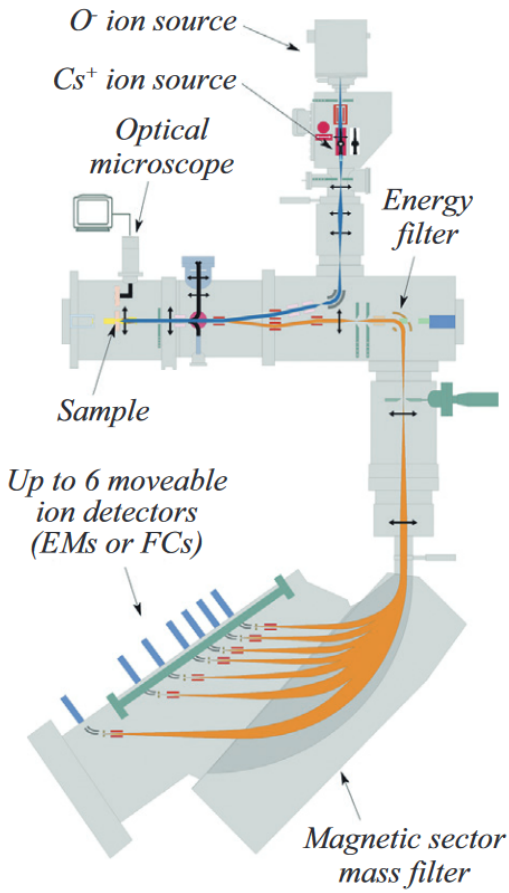

Figure 2.11: Schematic diagram of a SIMS instrument, the primary ion beam is generated at the top and secondary ions are analyzed in the mass spectrometer at the bottom, taken from [121].

2.3.3 ToF-SIMS

Time-of-Flight SIMS can be referred to as "static" SIMS. It differs from the previous method in the nature of its primary ion beam. Low ion beam doses in ToF-SIMS lead to low sputtering of the surface which virtually does not alter it. In our case, a Bismuth ion beam was used (Bi^+). Quantification of elements at low atomic concentration is made possible with ToF-SIMS. This method was thus used for dopant concentration measurement in doped microcrystalline thin films. Since ToF-SIMS does not etch the surface during the analysis, a complementary 2 keV Cs^+ ion beam was used to remove a few mono layers of material before the next Bi^+ beam. This process made it possible to obtain a ToF-SIMS depth profile similar to that presented in figure 2.12.

The absence of Phosphorus in the first 10 nm are due to the gold capping layer used for charge extraction. The depth value of the profile is calibrated using a profilometer following the analysis by supposing the etch rate is constant. This hypothesis may not hold true when analyzing layer of very different chemical nature (µc-Si:H vs µc-Ge:H). The depth profile should thus be used with a lot of precaution. For further details regarding this complex analysis technique, we recommend referring to the book written by Dr. F.A. Stevie on the topic [121].

Cette thèse est accessible à l'adresse : https://theses.insa-lyon.fr/publication/2023ISAL0014/these.pdf
© [A. Wilson], [2023], INSA Lyon, tous droits réservés

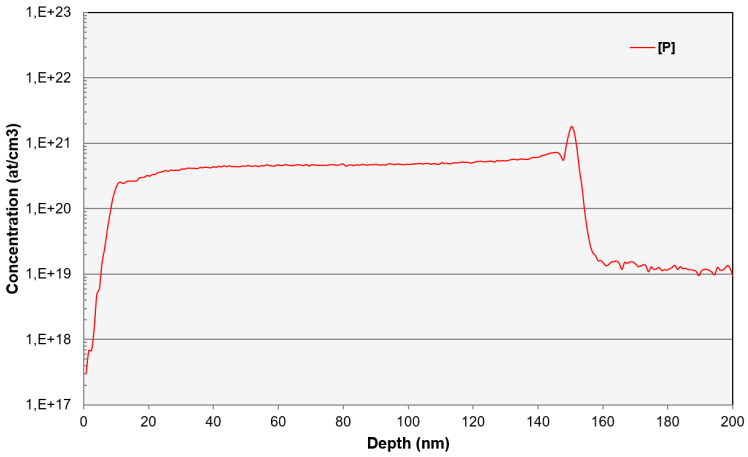

Figure 2.12: ToF-SIMS Depth profile for Phosphorus of an n-type µc-Si:H thin film deposited on glass.

3 Optical characterization

In our endeavor to design NIR sensitive devices, studying the optical properties of the deposited films is paramount. In this section we will introduce Spectroscopic Ellispometry and the considerations to be taken into account when using this technique. Reflectometry and Quantum effiency will then be presented as they are fundamental in characterizing photosensitive devices.

3.1 Spectroscopic Ellipsometry

Spectroscopic ellipsometry (SE) is a non-destructive optical characterization technique commonly used to obtain optical and dimensional properties of thin films. Its working principle is based on the change in the polarization state of light as it is reflected at an angle from a thin film sample. Through appropriate modeling and fitting of the data, information about refractive index, layer thickness and surface roughness can be obtained. For an in depth presentation of the principles of SE, one can refer to Fujiwara's book [122].

3.1.1 Working Principle of SE

Spectroscopic ellipsometry measures the output elliptical polarization of light through parameters Δ and ψ. These parameters are linked to the complex Fresnel reflection coefficients $\widetilde{r_p}$ and $\widetilde{r_s}$ of the s- and p- polarized light by the following equation.

$$\rho = \frac{\widetilde{r_p}}{\widetilde{r_s}} = \tan\psi \cdot e^{i\Delta} \tag{3.1}$$

$\tan\psi$ represents the ratio of amplitudes between the outgoing polarizations and Δ is their phase difference. In order to obtain Δ and ψ, an unpolarized polychromatic beam passes through a polarizer in order to obtain linearly polarized light. Light is then reflected from the sample and passes a modulator and an analyzer before being collected by a monochromator and a detector. A schematic of the optical setup is shown in figure 3.1.

Cette thèse est accessible à l'adresse : https://theses.insa-lyon.fr/publication/2023ISAL0014/these.pdf
© [A. Wilson], [2023], INSA Lyon, tous droits réservés

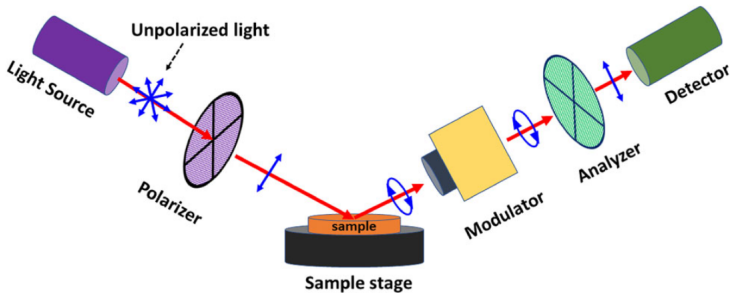

Figure 3.1: Optical setup of a spectroscopic ellipsometer, taken from [123].

3.1.2 Ellipsometric measurement and data fitting

In this work, we used a Horiba UVISEL[3] Phase Modulated Ellipsometer (PME) which can perform measurements in the UV to NIR range (0.6 eV to 5 eV). Measurements are typically done at a constant step of 5 nm or less and the angle of incidence of the beam is set to 70°. The modulator and analyzer are set at 0° and +45° respectively. In this configuration, the measurement is given as I_s and I_c as a function of photon wavelength which relate to Δ and ψ as follows.

$$I_s = \sin 2\psi \cdot \sin \Delta \quad I_c = \sin 2\psi \cdot \cos \Delta \tag{3.2}$$

The experimental data is fitted using Horiba's DeltaPsi2 software. SE is by essence a model-based technique, it requires the user to have some amount of knowledge about the sample (thickness or other) to be appropriately used. Once a model has been built to describe the characterized sample, the parameters of this model can be fitted to best match the observables I_s and I_c obtained. This is achieved by a Marquardt minimization algorithm.

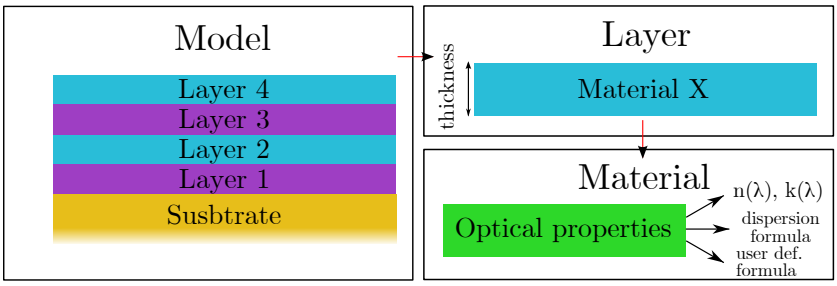

Figure 3.2: Building blocks of an ellipsometric model.

A model is defined by an "infinite" substrate and a stack of one or several layers defined by their thickness and the material(s) composing them. The materials are then defined by their optical properties, generally with fixed $n(\lambda)$ and $k(\lambda)$ or as dispersion formulas. The building blocks of ellipsometric models are schematized in figure 3.2. In the fitting process, the thickness of the layer and the parameters of the dispersion formula can be obtained. The quality of fit is measured by χ^2 (equation 3.3) which should be minimized.

$$\chi^2 = \min \sum_{i=1}^{n} \left[(\psi_{theoretical} - \psi_{experimental})^2 + (\Delta_{theoretical} - \Delta_{experimental})^2 \right] \tag{3.3}$$

[3] www.horiba.com

Cette thèse est accessible à l'adresse : https://theses.insa-lyon.fr/publication/2023ISAL0014/these.pdf
© [A. Wilson], [2023], INSA Lyon, tous droits réservés

In other to restrict the degrees of freedom of the model, we suppose our materials are isotropic and homogeneous. For materials at the amorphous to microcrystalline transition the homogeneity hypothesis may not be valid along the growth direction. This can be accounted for by subdividing the grown layer into several layers in our model which can be fitted independently.

3.1.3 Dispersion Formulas for Amorphous and Microcrystalline Semiconductors

Spectroscopic ellipsometry is a versatile tool but it is very sensitive to the choice of the model used for fitting the data. As such choosing the appropriate dispersion formulas to retrieve the refractive index of our layers is critical. According to the expected nature and chemistry of the fitted material, different dispersion formulas should be used. The dispersion formula is used to calculate the complex dielectric function of the material ε.

Kato-Adachi dispersion formula

The Kato-Adachi formula is commonly used to described the dielectric function of crystalline semiconductors near and below the transitions of the material. Indeed, in semiconductors, $\varepsilon(E)$ is directly related to the band structure. Kato-Adachi was found to best describe microcrystalline layers such as µc-Si:H and µc-SiGe:H ([124, 125]). The formula is defined as follows from a constant term ε_∞ and 4 transitions ε_1, ε_2, ε_3 and ε_4 with 11 parameters.

$$\varepsilon = \varepsilon_\infty + \varepsilon_1 + \varepsilon_2 + \varepsilon_3 + \varepsilon_4$$

$$\varepsilon_1 = \frac{A_0}{E_0^{\frac{3}{2}}} . \frac{2 - \sqrt{1+\chi} - \sqrt{1-\chi}}{\chi^2}$$

$$\varepsilon_2 = -\frac{B_1}{\xi^2} . \ln\left(1 - \xi^2\right)$$

$$\varepsilon_3 = \frac{B_{1X}}{E_1 - E - i.\Gamma_1}$$

$$\varepsilon_4 = \frac{C}{1 - \left(\frac{E}{E_2}\right)^2 - i.\frac{E}{E_2}.\Gamma_2}$$

$$\chi = \frac{E + i.\Gamma_0}{E_0}, \ \xi = \frac{E + i.\Gamma_1}{E_1},$$

where E is the photon energy, A_0, B_1, B_{1X} and C are the amplitude values and Γ_j the broadening values. E_j represent the energy position of the transitions.

Double New Amorphous dispersion formula

The Double New Amorphous (DNA) dispersion formula is a variation of the formula proposed by Forouhi and Bloomer [126] for amorphous material. The New Amorphous formula proposes a more intuitive parameterization from which the DNA formula can be obtained by adding an oscillator. It is defined as follows :

Cette thèse est accessible à l'adresse : https://theses.insa-lyon.fr/publication/2023ISAL0014/these.pdf
© [A. Wilson], [2023], INSA Lyon, tous droits réservés

$$n(\omega) = n_\infty + \frac{B_1 \cdot (\omega - \omega_1) + C_1}{(\omega - \omega_1)^2 + \Gamma_1^2} + \frac{B_2 \cdot (\omega - \omega_2) + C_2}{(\omega - \omega_2)^2 + \Gamma_2^2}$$

$$k(\omega) = \left\{ \begin{array}{cc} \frac{f_1 \cdot (\omega - \omega_g)^2}{(\omega - \omega_1)^2 + \Gamma_1^2} + \frac{f_2 \cdot (\omega - \omega_g)^2}{(\omega - \omega_2)^2 + \Gamma_2^2} & \text{if } \omega > \omega_g \\ 0 & \text{if } \omega \leq \omega_g \end{array} \right\}$$

where B_j and C_j are defined as

$$B_j = \frac{f_j}{\Gamma_j} \cdot \left(\Gamma_j^2 - (\omega_j - \omega_g)^2 \right)$$

$$C_j = f_j \cdot \Gamma_j \cdot (\omega_j - \omega_g)$$

The parameter n_∞ is the refractive index at low energy. ω_j is the energy of maximum absorption, f_j is the oscillator strength, Γ_j is the oscillator broadening and $\hbar\omega_g$ is the band gap energy below which $k(\omega) = 0$.

It can be used for extracting the refractive index of amorphous materials such as a-Si:H or a-Ge:H which do not exhibit critical points due to the absence of a band structure.

5x Amorphous user defined formula

Unlike the previously presented formulas, the 5x Amorphous dispersion is purely empirical and is based off the dispersion proposed by Forouhi and Bloomer [126]. We built this model in an attempt to describe the complex band structure of µc-Ge:H and its subsequent dielectric function. It is used to fit the ellipsometric data from µc-Ge:H films. The Kato-Adachi dispersion was not suitable for such films due to the high number of peaks in the dielectric function of c-Ge which can still be found in µc-Ge:H. In order to account for those peaks, 5 amorphous oscillators were used :

$$n(E) = \sqrt{\epsilon_\infty} + \sum_{j=1}^{5} \frac{B_{0j} \cdot E + C_{0j}}{E^2 - B_j \cdot E + C_j}$$

$$k(E) = \left\{ \begin{array}{cc} \sum_{j=1}^{5} \frac{A_j \cdot (E - E_g)^2}{E^2 - B_j \cdot E + C_j} & \text{if } E > E_g \\ 0 & \text{if } E \leq E_g \end{array} \right\}$$

where B_{0j} and C_{0j} are defined as

$$B_{0j} = \frac{2 \cdot A_j}{\sqrt{4 \cdot C_j - B_j^2}} \cdot \left(-\frac{B_j^2}{2} + E_g \cdot B_j - E_g^2 + C_j \right)$$

$$C_{0j} = \frac{2 \cdot A_j}{\sqrt{4 \cdot C_j - B_j^2}} \cdot \left((E_g^2 + C_j) \cdot \frac{B_j}{2} - 2 \cdot E_g \cdot C_j \right)$$

Each oscillator is defined by 3 parameters A_j, B_j and C_j to which are added ϵ_∞ the high energy dielectric constant and E_g the band gap energy, reaching a total of 17 parameters. In a simple Amorphous model, A is a factor while B and C relate to the optical band gap and the width of the band tail absorption [126]. In our custom formula no physical meaning can be attributed to each parameter. Other author were able to perform ellipsometric measurements on µc-Ge:H [69] but no information about the dispersion used was given.

Cette thèse est accessible à l'adresse : https://theses.insa-lyon.fr/publication/2023ISAL0014/these.pdf
© [A. Wilson], [2023], INSA Lyon, tous droits réservés

3.2 Optical Reflectometry

3.2.1 Working Principle

Reflectometry measures the reflectance R resulting from the interaction of light with a sample at normal incidence. It ressembles Spectroscopic Ellipsometry as it relies on the interaction of light at different wavelengths to obtain structural information such as thickness. Reflectometry does not however measure changes in polarization but merely changes in light intensity as it is bounced back from a sample. The change in intensity is measured at different wavelengths in the UV to NIR range to obtain a reflectance spectra $R(\lambda)$ as shown in figure 3.3.

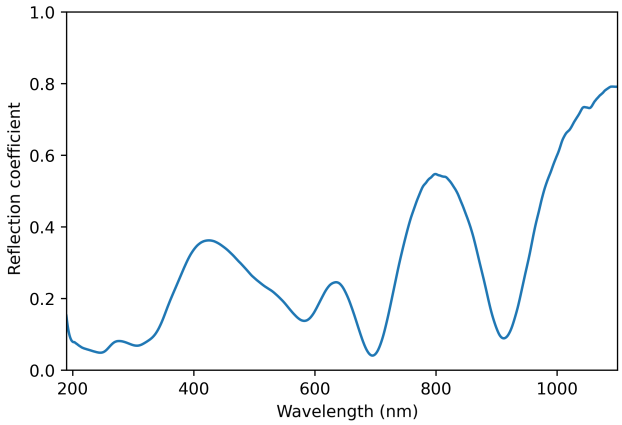

Figure 3.3: Reflectance spectrum of a glass / ITO / µc-Si:H / µc-SiGe / µc-Si:H / Ag stack.

When transparent or quasi-transparent thin films are involved, the reflectance spectra can exhibit oscillations due to the optical path difference between reflected photons of same wavelengths. At normal indicence, the valleys (low reflectance) correspond to an anti-reflective coating behavior and occur when

$$2 \cdot n_{film} \cdot d = (m - 1/2 \cdot \lambda) \tag{3.4}$$

where n_{film} is the refractive index of the thin film, d its thickness, λ the photon wavelength and m is an integer. The peaks (high refectance) on the other hand occur when

$$2 \cdot n_{film} \cdot d = m \cdot \lambda \tag{3.5}$$

.

3.2.2 Equipment specification and measurement

A FILMETRICS F20-UV reflectometer (figure 3.4) was used to measure the reflectance spectra of thin film photodiodes. The reflectance was calibrated using a reference c-Si wafer after stabilization of the light source. $R(\lambda)$ spectra were measured between $\lambda = 190 - 1100$ nm. 3 measurement were made per sample in order to account for the variation in thickness of the thin films. The spot size was adjusted to 2 mm in diameter.

The reflectance measurements were mainly used in combination with photodiode External Quantum Efficiency measurements (EQE, see section 3.3) to account for the losses due to parasitic reflections.

Cette thèse est accessible à l'adresse : https://theses.insa-lyon.fr/publication/2023ISAL0014/these.pdf
© [A. Wilson], [2023], INSA Lyon, tous droits réservés

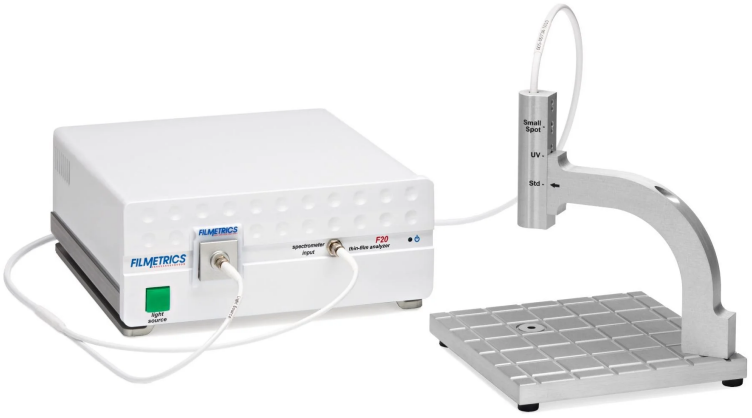

Figure 3.4: FILMETRICS F20-UV reflectometer used for reflectance spectra measurement. The sample is placed on the metallic grid on the right side of the image.

3.3 Quantum Efficiency

3.3.1 Working Principle

Quantum Efficiency (QE) or Incident Photon to Charge Carrier Efficiency (IPCE) is a characteristic photosensitive devices such as photodiodes or solar cells. It which measures the probability of an incident photon to be collected as an electrical charge by the device, at a given wavelength. We can distinguish two types of QE :

External Quantum Efficiency or EQE is the ratio of the number of charge carriers collected by the device to the number of photons reaching the surface of the device. If we consider N_e the number of collected electrons, N_{ph} the number of incident photons, I the generated photocurrent and $P_{ph} = N_{ph} \cdot E_{ph} \cdot \partial t$ the incident photon power we can express the EQE as follows :

$$EQE(\lambda) = \frac{\partial N_e / \partial t}{\partial N_{ph} / \partial t} = \frac{I \cdot P_{ph}}{q \cdot \frac{hc}{\lambda}}$$

Internal Quantum Efficiency or IQE is the ratio of the number of charge carriers collected by the device to the number of photons *absorbed* in the device. Considering the sum of the reflection on the front surface R, transmission at the backside T and absorption in the device A at any given wavelength should be equal to 1, we have :

$$IQE(\lambda) = \frac{EQE(\lambda)}{1 - R - T}$$

In order to measure the EQE we need to precisely measure the photogenerated current I, the photon wavelength λ and the incident photon power P_{ph}. The experimental setup schematized in figure 3.5 make this measurement possible.

A Xenon lamp is used as a polychromatic light source (200 – 1300 nm) and is focused towards a chopper to pulse the signal at a 30 Hz frequency. A signal wavelength is then selected by the mirrors and diffraction gratting of a monochromator before being focused onto the tested device. The resulting output current I_{diode} is a 30 Hz pulsed signal resulting from the sum of the dark and photogenerated current. This current is generally extremely

Cette thèse est accessible à l'adresse : https://theses.insa-lyon.fr/publication/2023ISAL0014/these.pdf
© [A. Wilson], [2023], INSA Lyon, tous droits réservés

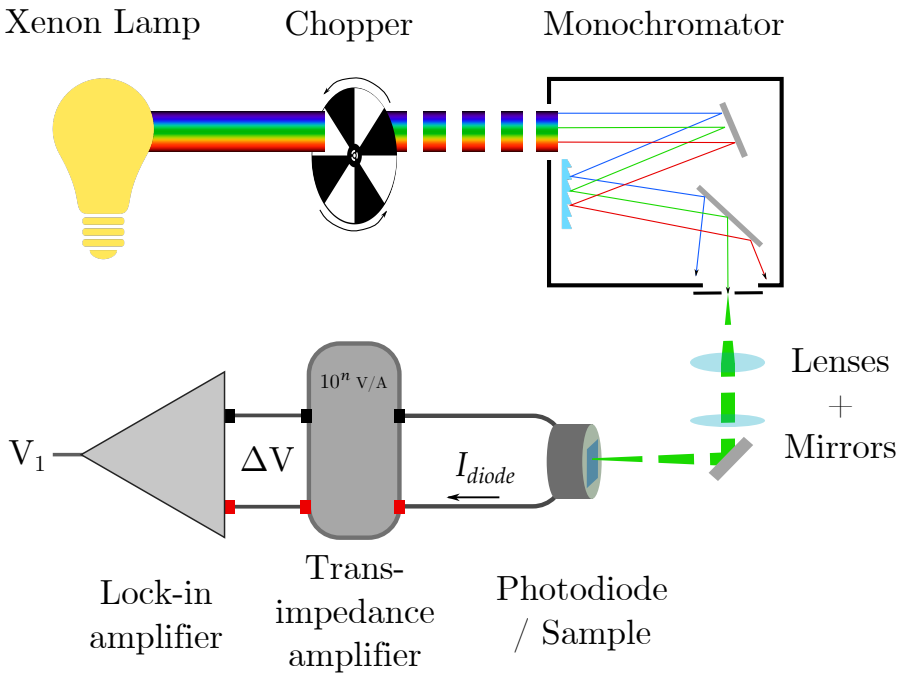

Figure 3.5: Schematic representation of the EQE acquisition, from the light source to the output voltage.

low due to the low number of photons reaching the structure and is thus amplified using a transimpedance amplifier with a gain in the order of $10^4 - 10^6$ Volt/Amp. The resulting signal ΔV is fed to a lock-in amplifier tuned to the chopper's frequency in order to extract the low-amplitude photogenerated signal from the background noise. A potential V_1 is then obtained and recorded are a function of λ with the appropriate software.

3.3.2 Data acquisition and calibration

Precise measurement of the EQE requires knowing precisely the number of photons reaching the sample's surface. This is done by calibrating the light source using a reference Silicon photodiode of known EQE. The final voltage $V_{1\,ref}$ is measured and is proportional to $N_{ph}(\lambda)$, the transimpedance amplifier gain G_{ref} and $EQE_{ref}(\lambda)$. The measurement are then performed on the sample to characterize. Since $N_{ph}(\lambda)$ is stable once the Xenon lamp has heated up, the measured potential $V_{1\,sample}$ can be expressed as :

$$V_{1\,sample} = \frac{G_{ref}}{G_{sample}} \cdot \frac{EQE_{sample}(\lambda)}{EQE_{ref}(\lambda)} \cdot V_{1\,ref} \tag{3.6}$$

Then the external quantum efficiency of the sample is obtained by :

$$EQE_{sample}(\lambda) = \frac{G_{sample}}{G_{ref}} \cdot \frac{V_{1\,sample}}{V_{1\,ref}} \cdot EQE_{ref}(\lambda) \tag{3.7}$$

Due to the 1.12 eV band gap of the crystalline silicon reference photodiode, the experiment was only conducted in the 200 – 1100 nm range despite the Xenon source's emission spectrum reaching 1300 nm. The spectral resolution was adjusted to 5 nm by closing the exit slits of the

Cette thèse est accessible à l'adresse : https://theses.insa-lyon.fr/publication/2023ISAL0014/these.pdf
© [A. Wilson], [2023], INSA Lyon, tous droits réservés

monochromator (see figure 3.5). The spot size was set to approximately 1 mm^2 in order for all incoming photons to be directed at the active part of the tested photodiode.

Obtaining the IQE requires additional measurement of the transmission and reflection coefficients $T(\lambda)$ and $R(\lambda)$. The latter can be obtain through reflectivity measurements presented in section 3.2.

4 Electrical characterization

The performance of a photosensitive device is ultimately a combination of its optical and electrical properties. Characterization technique adapted to thin films with poor electrical properties such as Hall Effect and Steady State Photocarrier Grating will be presented.

4.1 Hall Effect characterization

4.1.1 Working Principle

The Hall effect is the physical phenomenon through which a current flowing through a semiconductor produces a transverse difference of potential in the presence of a magnetic field (see figure 4.1).

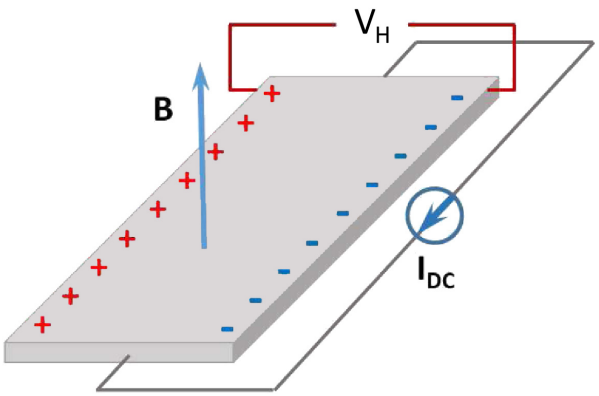

Figure 4.1: Hall effect in a semiconductor thin film.

This effect is used in hall effect measurements, an electrical characterization technique used to measure the resistivity ρ and the charge carrier density n/p of a semiconductor thin film. Resistivity is inversely proportional to $\mu_H$and carrier concentration.

$$\rho = \sigma^{-1} = (nq\mu_e + pq\mu_h)^{-1} \tag{4.1}$$

The different parameters are determined from separately measuring the resistivity and the charge carrier density. ρ is obtained from a four-point probe measurement in the Van der Pauw configuration [127, 128] with no external magnetic field applied. In the presence of a magnetic field, the Hall coefficient R_{Hall} is measured and links sample thickness t, the Hall voltage V_H, the magnetic field B and the current I to the carrier density [127].

$$R_{Hall} = \frac{t \cdot V_H}{B \cdot I} = \frac{r(p - n \cdot (\frac{\mu_n}{\mu_p})^2)}{q(p + \frac{\mu_n}{\mu_p} n)^2} \tag{4.2}$$

Cette thèse est accessible à l'adresse : https://theses.insa-lyon.fr/publication/2023ISAL0014/these.pdf
© [A. Wilson], [2023], INSA Lyon, tous droits réservés

where r is the scattering factor set to 1 [127]. In the case where $p \gg n$, $R_{Hall} = r/qp$ while for n-type layer ($n \gg p$) $R_{Hall} = -r/qn$. Due to the high resistivity of intrinsic microcrystalline materials, Hall effect is used to measure the carrier density in doped layers only. From the resistivity measurement and the Hall coefficient measurement, one can deduce mobility as $\mu = \rho \cdot |R_{Hall}|/r$.

It should be noted Hall effect measurement should not be used with amorphous semiconductors without consideration as anomalies in the sign of the carriers are know to occur in a-Si:H [129].

4.1.2 Equipment specification and sample preparation

The Ecopia HMS5000 measurement system of figure 4.2 was used. The magnetic field is applied via a permanent magnet of 0.55 T magnetic flux density. The range of measurement for the different parameters is given in table 2.3.

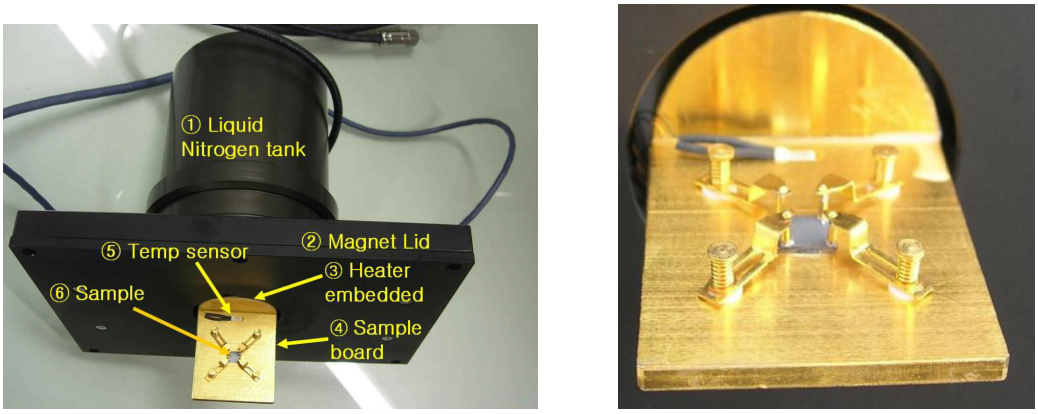

(a) (b)

Figure 4.2: (a) HMS5000 sample mount and N_2 cooling reservoir (b) Sample mount with 4 pin contacts.

Thin films were deposited on an insulator material (glass) in order to avoid any contributions from the substrate. The corner metallic contacts were either obtained applying a small drop of liquid Indium-Gallium alloy on the film of by sputtering a fine silver layer on each corner. The ohmic bevahiour of the contact were systematically checked prior to measurement. Thickness of the films is either obtained from SE (see section 3.1) or from cross-sectionnal SEM imaging.

Parameter	Measurable range
ρ	$10^{-4} - 10^{7}$ Ω·cm
μ	$1 - 10^{7}$ cm$^2 \cdot$ V$^{-1} \cdot$ s^{-1}
n/p	$10^{7} - 10^{21}$ cm^{-3}
V_H	min. 1 µV
I	1 nA – 20 mA

Table 2.3: Ecopia HMS5000 specifications.

Although this equipment can work in the 80 K to 350 K temperature range, measurement were mostly performed at room temperature.

Cette thèse est accessible à l'adresse : https://theses.insa-lyon.fr/publication/2023ISAL0014/these.pdf
© [A. Wilson], [2023], INSA Lyon, tous droits réservés

4.2 Diffusion length measurement using Steady State Photocarrier Grating Method

The Steady State Photocarrier Grating (SSPG) method is used to retrieve the minority carrier diffusion length L_{diff} of semiconductor thin films. Diffusion length is the average length a charge carrier will move between photogeneration and recombination. It can be expressed in terms of the carrier lifetime τ and diffusivity D as $L_{diff} = \sqrt{D\tau}$.

4.2.1 Working Principle

SSPG uses an optical perturbation combined with an electrical measurement to deduce the diffusion length of semiconductor materials with diffusion lengths in the 20 nm to 1 µm range approximately. The method was introduced by Ritter et al. [78] in 1987 and was soon applied to a-Si:H films which were found to have a diffusion length in the order of 150 nm at best.

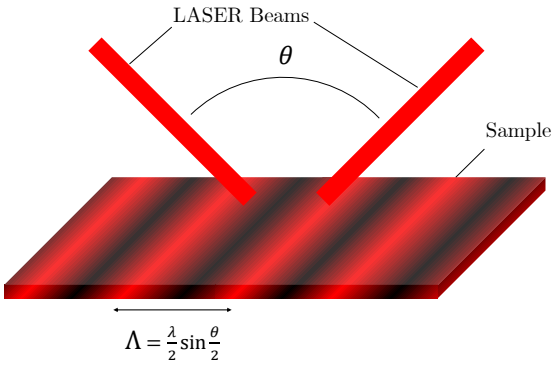

Figure 4.3: Interference fringes from two LASER beams interfering at an angle θ.

In SSPG, two LASER beams of same wavelength interfere on the surface of a sample. Interference fringes are formed on the surface of the sample causing a spacial variation of light intensity in the plane of the beams. The fringes thus generate an optical grating as seen in figure 4.3 whose period Λ is a function of the angle of incidence θ and the wavelength λ.

$$\Lambda = \frac{\lambda}{2} \cdot \sin\frac{\theta}{2}$$

Since the thin film absorbs light at the laser's wavelength the minority carrier density will be increased by Δn_{ph}, the photogenerated charge carriers. If $\Lambda > L_{diff}$ then the spacial distribution of Δn_{ph} will closely match the interference pattern on the surface of the sample. In this case the conductivity of the film in direction of the fringes only slightly increases due to dark areas of low conductivity. On the other hand if $\Lambda < L_{diff}$ then the diffusion of the charge carriers will be more of less insensitive to the interference pattern and Δn_{ph} should remain spacially uniform, yielding a higher increase in conductivity.

The diffusion length can be extracted by applying a fixed difference of potential and by measuring the current flowing through the sample. The current is measured in the case where the LASERs have parallel polarization (and thus interference fringes occur) and in the case where their polarization as perpendicular (no fringes). The ratio of those currents is written β and is a function of the diffusion length and a factor ϕ.

Cette thèse est accessible à l'adresse : https://theses.insa-lyon.fr/publication/2023ISAL0014/these.pdf
© [A. Wilson], [2023], INSA Lyon, tous droits réservés

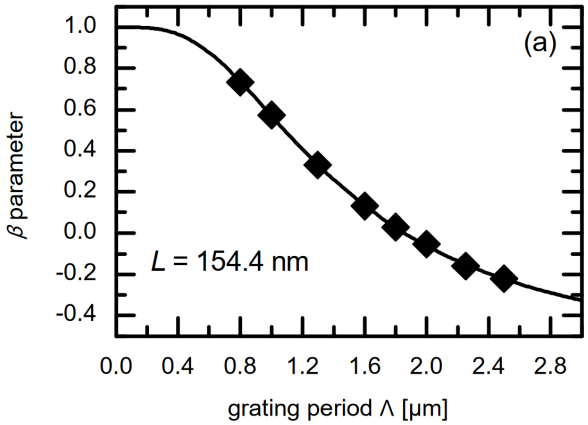

Figure 4.4: SSPG plot of β as a function of Λ for a a-Si:H film [77]. The fitted L_{diff} was found to be equal to 154 nm.

$$\beta = \frac{I_{fringes}}{I_{no\ fringes}} = 1 - \frac{2\phi}{\left(1 + \left(2\pi \cdot \frac{L_{diff}}{\Lambda}\right)^2\right)^2} \tag{4.3}$$

The working principle of the SSPG method is then to vary the grating period Λ by adjusting the incident beam angles and thus perform several measurements of β. $\beta = f(\Lambda)$ can then be plotted and the data is fitted using ϕ and L_{diff} (see figure 4.4 from [77]). The detailed calculations which lead to this expression for β can be found in papers from Ritter et al. [78] and Longeaud et al. [79].

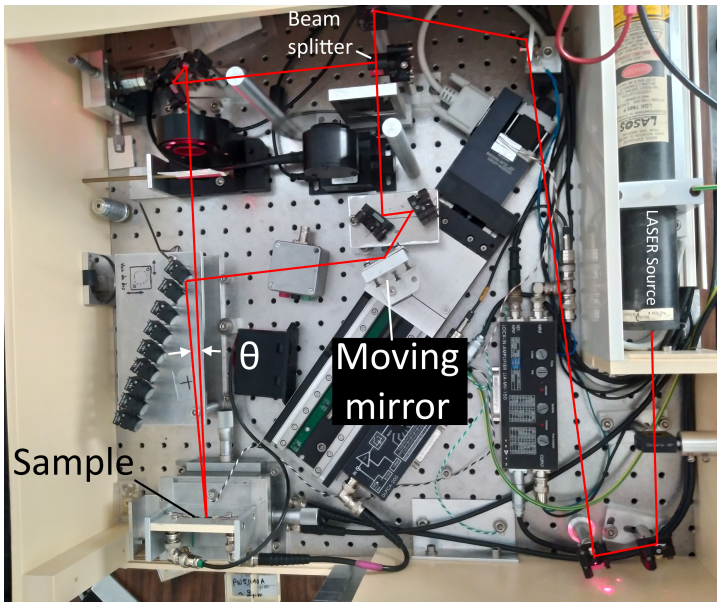

Figure 4.5: Top view photo of the automated steady state photocarrier grating equipment at GeePs. The LASER beam path has been added in red form better comprehension.

Cette thèse est accessible à l'adresse : https://theses.insa-lyon.fr/publication/2023ISAL0014/these.pdf
© [A. Wilson], [2023], INSA Lyon, tous droits réservés

4.2.2 Experimental measurement bench

SSPG measurement were performed thanks to Dr. Longeaud at GeePs[4] laboratory in Gif-sur-Yvette, France. A picture of the experimental setup is shown in figure 4.5. The setup uses a 633 nm LASER source together with a set of 9 mirrors which lead to 9 measurements of β from a grating period Λ ranging from 1.14 µm to 22.1 µm. A constant 18 V difference of potential is applied to the sample and a lock-in amplifier is then used to improve the signal to noise ratio. A schematic view of the setup is given in figure 4.6. This automated setup for diffusion length measurement is made extremely efficient thanks to the moving mirrors. It was extensively described in this paper from 2013 [79].

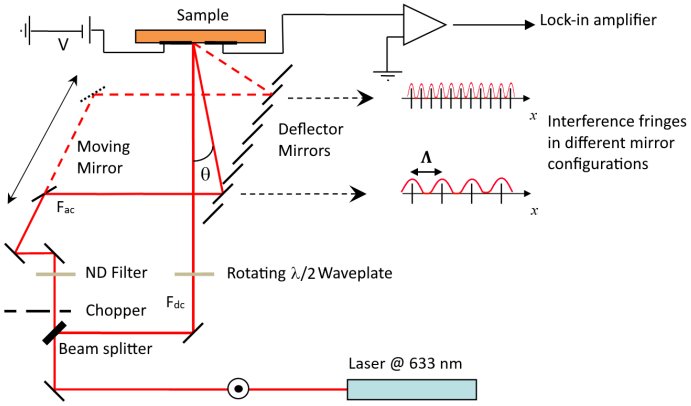

Figure 4.6: Schematic of the automated steady state photocarrier grating setup at GeePs, taken from geeps.centralesupelec.fr.

5 Conclusion

In this chapter we provided an overview of the experimental deposition and characterization techniques used over the course of this project. The PlasmaTherm Vision 310 PECVD reactor used at INL was introduced together will its main specifications. This reactor was used throughout this project for low temperature semiconductor and dielectric layer deposition. The PECVD equipment is at the heart of the development of NIR sensitive materials. The hardware was adapted for this project, making it feasible to grow Si:H, SiGe:H or Ge:H films with intrinsic, p-type or n-type doping. These thin films are deposited on crystalline silicon, glass or ITO substrates. The cleaning process for these different substrates prior to PECVD deposition were presented in this chapter.

The deposited films can then be characterized structurally, chemically, optically and electrically thanks to a wide range of experimental techniques. Structural characterization can be achieved through TEM or Raman Spectroscopy while SIMS can provide precise chemical information. As a non-destructive technique, Raman characterization will be extensively used to provide structural and chemical information about the deposited films due to the low acquisition and analysis time.

Spectroscopic Ellipsometry, Reflectometry and Quantum Efficiency on the other hand are used to investigate the optical properties of PECVD-grown films. Quantum Efficiency (QE) in

[4]Laboratoire de Génie Electrique et Electronique de Paris

Cette thèse est accessible à l'adresse : https://theses.insa-lyon.fr/publication/2023ISAL0014/these.pdf
© [A. Wilson], [2023], INSA Lyon, tous droits réservés

particular provides a measurement of the material's performance once integrated in a functional device. In our objective to show microcrystalline silicon-germanium NIR photodetectors are feasible, QE is a key characterization method. Finally, electrical characterization methods adapted to microcrystalline materials (Hall Effect and SSPG) were introduced.

All these techniques will be referred to in further chapters when conducting our research work. They will help provide a better understanding of the nature of the deposited films and the impact of their deposition conditions whether we are looking at a simple thin film or at much more complex layer stacks.

Cette thèse est accessible à l'adresse : https://theses.insa-lyon.fr/publication/2023ISAL0014/these.pdf
© [A. Wilson], [2023], INSA Lyon, tous droits réservés

Chapter 3

Development and Characterization of Absorber Layer Materials

Over the course of this chapter we will seek to develop a suitable material for the absorber layer of a photodiode. The ideal material for that purpose would be a highly absorbing, defect free and thin layer. High absorption, in particular in NIR, ensures photon absorption can be maximum. If this condition is met the absorber can then be thin, which reduces the distance photogenerated minority carriers should travel to be collected. Finally, having as little defects as possible reduces the chances of minority carrier recombining prior to being extracted. The following section will thus be dedicated to producing three materials introduced in chapter 1, namely µc-Si:H, µc-Ge:H and µc-SiGe:H. While we will quickly show the first one is not optically relevant, µc-Ge:H and µc-SiGe:H could be promising candidates.

1 Hydrogenated Silicon thin films development

Hydrogenated Silicon films are obtained from a decomposition of silicon precursors, in our case silane (SiH_4), in the PECVD chamber. The precursor can be used diluted in a hydrogen, helium or argon which will strongly impact the structural and electrical properties of the deposited layers. Materials such as amorphous silicon (a-Si:H), microcrystalline silicon (µc-Si:H) and similar mixed-phase layers (pm-Si:H, nc-Si:H[1]) can be deposited by adequately tuning temperature, pressure, power and gas flow rates. A broader overview of the state of the art of µc-Si:H deposition can be found in Chapter 1, section 3. In this section, we will introduce our process parameters for Si-based semiconductor layer production. As µc-Si:H is a widely documented material we will be relying on literature.

Optical limitations of hydrogenated amorphous silicon (a-Si:H) are discussed in section 3.1.6. Among other criteria, its low absorption coefficient below 1.8 eV [40] is unsuitable for our goal of working in the NIR range (~ 0.9 to 1.3 eV). µc-Si:H on the other hand can reach a 1.2 eV mobility gap [130]. While we do not expect µc-Si:H to be an effective absorber under this mobility gap energy, it may still be suited for the high energy part of the spectral range of interest. Additionally, managing µc-Si:H film growth and analysis will help apprehend useful concepts common to microcrystalline semiconductors.

[1] Hydrogenated *polymorphous / nanocrystalline* Silicon

Cette thèse est accessible à l'adresse : https://theses.insa-lyon.fr/publication/2023ISAL0014/these.pdf
© [A. Wilson], [2023], INSA Lyon, tous droits réservés

1.1 From amorphous to microcrystalline Silicon films

Among the many available ways of obtaining PECVD grown µc-Si:H, hydrogen dilution is one of the most straightforward options. Hydrogen is added to the gas mixture containing silane, which will has a threefold effect : etching, annealing, and surface passivation (refer to subsection 3.1.1). Increasing the dilution factor $R_H = \Phi_{H2}+\Phi_{SiH4}/\Phi_{SiH4}$ in the range of 10 to 20 will lead to a phase transition from a fully amorphous material to a partially crystallized one [43].

1.1.1 Towards high quality µc-Si:H

The deposition uniformity issues mentioned in chapter 2, section 1.1.4 were tackled by being able to increase simultaneously R_H and Pressure. This meant we could obtain uniform layers of partially crystalline materials. The nature of the crystalline phase is easily assessed by Raman Spectroscopy by identifying the position and intensity of the Raman peak associated to Si-Si bonds. The details of the method used to obtain a value for X_c can be found in chapter 2. Figure 1.1 provides a comparison of Raman spectra of a-Si:H, µc-Si:H and c-Si. The deposition conditions for both samples are gathered in table 3.1. The increase of R_H from 5 to 25 changed the structure from an amorphous to a microcrystalline film. The presence of Raman signal in the 480 cm^{-1} region of the µc-Si:H sample shows the film still has an important amorphous content which could be further reduced by increasing R_H. A more in-depth study of µc-Si:H's micro-structure is developed in the following subsection.

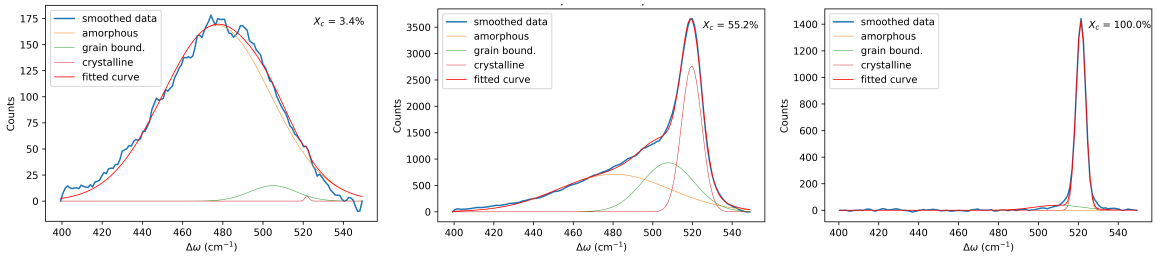

Figure 1.1: Raman spectra comparison of a-Si:H (left), µc-Si:H (center) and standard c-Si (right), obtained for a laser excitation wavelength $\lambda_{exc} = 473$ nm.

Sample	X_c -	Thickness [nm]	t_{dep} [min]	Temperature [°C]	Power [W]	Pressure [mTorr]	R_H -	Φ_{tot} [sccm]	H_2 [sccm]	SiH_4 [sccm]
aSi:H (#243)	-	660	40	200	30	800	5	200	160	40
µcSi:H (#253)	55 %	163	40	250	30	800	25	250	240	10

Table 3.1: Typical deposition conditions for Silicon based thin films. A higher R_H yields a microcrystalline structure at the cost of a decreased deposition rate.

1.2 Insight into µc-Si:H micro-structure

Having obtained µc-Si:H and confirmed the crystalline nature of the film through Raman spectroscopy we further investigated their structural properties. SEM images together with Raman spectroscopy and Grazing Incidence X-Ray Diffraction (GI-XRD) were used in order to built a more detailed picture of the material's morphology.

Cette thèse est accessible à l'adresse : https://theses.insa-lyon.fr/publication/2023ISAL0014/these.pdf
© [A. Wilson], [2023], INSA Lyon, tous droits réservés

As discussed in chapter 1 the structural properties of µc-Si:H are strongly dependent on film thickness, usually in the first few tens of nanometers of film growth. [49, 50, 131] In order to minimize the impact of this interface layer between film and substrate, longer deposition times were chosen to obtain thicker layers.

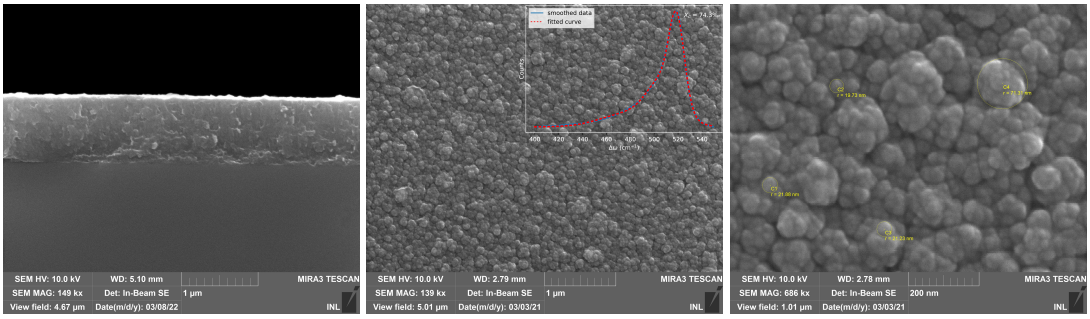

(a) (b) (c)

Figure 1.2: (a) Cross-section and (b)-(c) Top view SEM images of 1050 nm thick µc-Si:H deposited on c-Si substrate (sample #264, see table 3.2)

Figure 1.2 shows SEM images (In-Beam Secondary Electron detector mode) of a 1050 nm thick µc-Si:H layer deposited on c-Si substrate. The texture seen in the side view image as well as the "cauliflower-like" surface seen on the top-view is a good indication of the potential microcrystalline nature of the film [43, 132] although we have to rely on Raman measurements for quantitative crystalline volume fraction. The provided Raman spectrum has been measured for an identical layer deposited on glass in order to avoid unwanted contribution of the substrate's c-Si peak which can lead to an overestimation of X_c (see chapter 2). A 74 % crystalline volume fraction is reached, mainly due to the high $R_H = 50$ factor. Detailed deposition conditions can be found in table 3.2.

Sample	X_c [ ]	Thickness [nm]	t_{dep} [min]	Temperature [°C]	Power [W]	Pressure [mTorr]	R_H [ ]	Φ_{tot} [sccm]	H_2 [sccm]	SiH_4 [sccm]
µcSi:H (#264)	74 %	1050	150	250	100	1000	50	500	490	10
µcSi:H (#280)	79 %	161	60	200	30	800	50	350	343	7
µcSi:H (#285)	72 %	339	60	250	100	1000	50	350	343	7

Table 3.2: Deposition conditions for "thick" µc-Si:H samples #264, #280, #285.

Grazing-Incidence X-ray Diffraction

Raman spectrocopy can provide a rough estimation for grain size due to shifts in peak position. A method for providing this estimation has been proposed by Bustarret et al. [103], details of which can be found in chapter 2. In the case of highly crystalline films however, peak position is also strongly influenced by internal mechanical stress.[104] Relying on X-Ray diffraction (XRD) is then a safer approach. In practice, Grazing Incidence XRD (GI-XRD) is preferred when dealing with sub-micron thin films in order to maximize the signal/noise ratio. Incidence angle was set to 1° with $\lambda_{X-ray} = 1.54$ Å. The diffractogram presented in figure 1.3 was obtained by scanning µc-Si:H sample #285 (see table 3.2) on a limited range to reduce acquisition time. The diffractogram shows evidence of a crystalline phase in accordance with our Raman measurements. From each of the peak's position one can determine its crystalline

Cette thèse est accessible à l'adresse : https://theses.insa-lyon.fr/publication/2023ISAL0014/these.pdf
© [A. Wilson], [2023], INSA Lyon, tous droits réservés

orientation as well as distance between lattice planes d. The crystalline orientations found where identical to those described by Carambe et al.[133] which are gathered in table 3.3. (1 1 1) oriented crystals are found in greater amounts followed by (3 1 1) and (2 2 0). Fitting the corresponding peaks with a Voigt-function makes it possible to obtain a precise estimation for the full-width half-maximum (FWHM) of the peak. Relying on the Debye-Scherrer equation (see equation 1.1, [134]) we can get an estimate for crystallite size D_{avg}, with some assumptions regarding the crystallites' geometry contained in the factor K.

$$D_{avg} = \frac{K \cdot \lambda_{X-ray}}{(FWHM - FWHM_{tool}) \cdot cos\theta} \tag{1.1}$$

with $K = 0.94$ and $FWHM_{tool} = 0.17°$. The calculated D_{avg} are for the µc-Si:H sample of figure 1.3 are given in table 3.3.

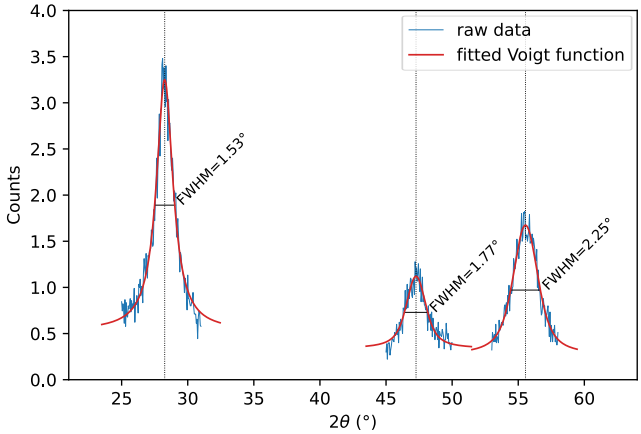

Figure 1.3: Grazing-Incidence XRD diffractogram of a 339 nm thick µc-Si:H film. Three peaks were identified at 28.4°, 47.3° and 56.1°, respectively.

2θ (°)	d (Å)	Orientation	FWHM[2]	D_{avg} (nm)
28.4	3.14	1 1 1	1.53°	6.3
47.3	1.92	2 2 0	1.77°	5.7
56.1	1.64	3 1 1	2.25°	4.5

Table 3.3: X-ray diffraction peak and corresponding crystallographic parameters for $\lambda_{X-ray} = 1.54$ Å (from [133])

The three identified peaks were found in µc-Si:H independently from deposition conditions. Crystallite size D_{avg} however was found to be strongly influenced by the increased RF-Power as higher growth rates leaves less time for the growing film to rearrange itself. Figure 1.4 shows the peak broadening observed as RF-Power was increased leading to a decrease in D_{avg} from 14.3 nm to 6.3 nm.

Hydrogenated microcrystalline Silicon's structural properties are sensitive to deposition conditions. Slight variation on deposition conditions can yield vastly different films in terms of X_c, crystallite size, or surface roughness. Additionally, the thickness dependence of some of these properties makes precise control of film properties even more challenging.

[2]Full-Width Half-Maximum

Cette thèse est accessible à l'adresse : https://theses.insa-lyon.fr/publication/2023ISAL0014/these.pdf
© [A. Wilson], [2023], INSA Lyon, tous droits réservés

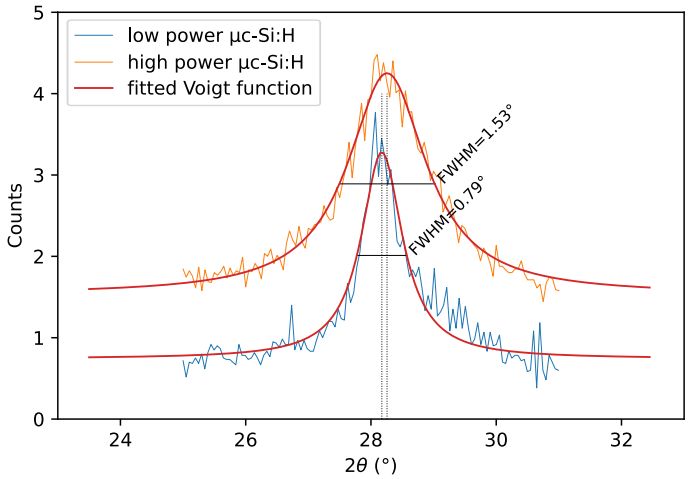

Figure 1.4: GI-XRD diffractogram and FWHM of µc-Si:H in two deposition conditions, *low power* (#280, $D_{avg} = 14.3\,\text{nm}$) and *high power* (#285, $D_{avg} = 6.3\,\text{nm}$). See table 3.2.

1.3 Optical properties of µc-Si:H

Obtaining the optical constants of our layers is a critical part of characterization. The real part of the optical index $\tilde{n} = n + \imath k$ can be used to design effective anti-reflective coatings [135] while k gives the material's absorption through the relation $\alpha = 4\pi k/\lambda$.

In order to find an appropriate modeling method, a 270 nm thick layer of µc-Si:H was deposited on c-Si at 250 °C. SEM images of the sample are shown in figure 1.5. Spectroscopic Ellipsometry (SE, see chapter 2, section 3.1) measurement was performed in the 1.5 eV to 5 eV energy range. The model used for fitting of I_s and I_c consisted of a c-Si substrate, a 1 nm thin native oxide, a *pSi_fine grain* [124] Kato-Adachi dispersion formula (detailed in chapter 2, section 3.1.3) and a surface roughness layer. Considering GI-XRD showed crystallites were less than 15 nm in diameter the *fine grain* model was deemed appropriate. The fit obtained is shown as a solid line in figure 1.5 and corresponding thicknesses and dispersion parameters are gathered in table 3.4.

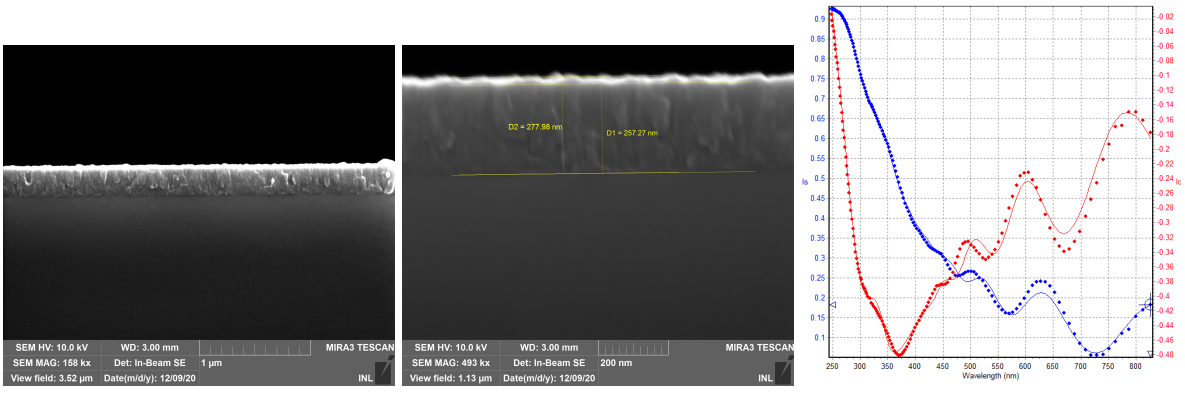

Figure 1.5: Cross-sectional SEM image of µc-Si:H deposited on c-Si and corresponding ellipsometric data fitted using a Kato-Adachi dispersion formula ($\chi^2 = 1.17$).

One has to bear in mind the optical properties obtained here may vary depending of crystalline volume fraction X_c. It was however found the high energy range was the most im-

Cette thèse est accessible à l'adresse : https://theses.insa-lyon.fr/publication/2023ISAL0014/these.pdf
© [A. Wilson], [2023], INSA Lyon, tous droits réservés

pacted, lower crystallinity leading to a broadening of the peaks at 3.4 and 4.3 eV. Figure 1.6a shows the extracted values for n and k as function of photon wavelength for a-Si:H, µc-Si:H and a reference c-Si bulk material.

Parameter	$d_{\mu c\text{-}Si:H}$	$d_{roughness}$	ϵ_∞	E_0	A_0	Γ_0	E_1	B_1	B_{1X}	Γ_1	E_2	C	Γ_2
Fitted value	286 nm	8 nm	0.935	0.936	-22.926	3.386	3.560	4.478	2.993	0.217	4.121	5.258	0.196

Table 3.4: Model result for µc-Si:H deposited on c-Si modeled with a Kato-Adachi dispersion formula.

The similarity between µc-Si:H and c-Si means ellipsometry can be used as a way to identify the presence of microcrystalline phase. However considering the many advantages of Raman spectroscopy in that task, this path was not pursued.

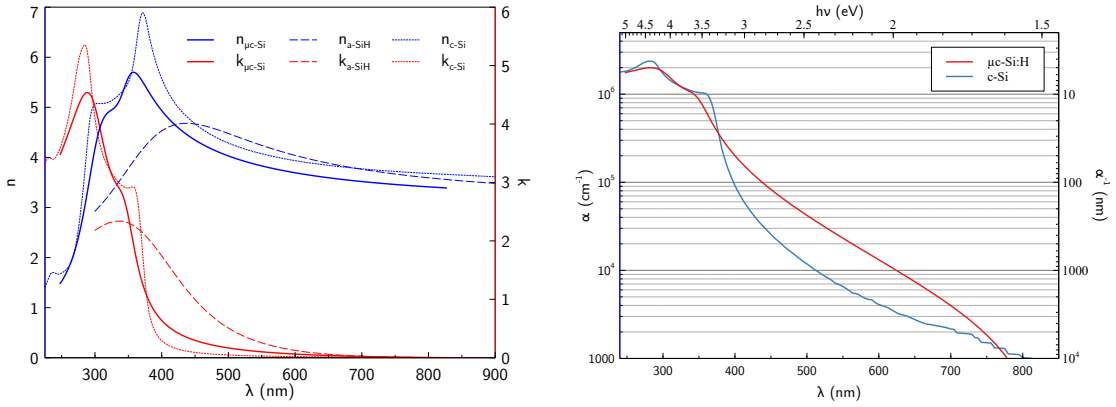

(a) (b)

Figure 1.6: (a) Optical indices n and k of a-Si:H, µc-Si:H and c-Si obtained by Spectroscopic Ellipsometry (SE). (b) Absorption coefficient comparison of µc-Si:H and c-Si. The evaluation by SE of α below 10^3 cm^{-1} comes with a lot of uncertainty.

From the material's optical index, the absorption coefficient $\alpha_{\mu c\text{-}Si:H}$ was derived and is plotted in figure 1.6b together with α_{c-Si}. As expected, µc-Si:H has an extremely low absorption above 800 nm. The estimated penetration depth of photons at 800 nm would be above 10 µm. Working in the near infrared range would imply depositing extremely thick layers by PECVD while deposition rate were found to be lower than 10 nm/min. Production time would ramp up to several days just to grow such a layer. Providing such a process were feasible, the low diffusion length of charge carriers in µc-Si:H (~ 150 nm) means the generated e^-/h^+ pairs would recombine before being extracted.

1.4 Conclusion : µc-Si:H thin films

Microcrystalline Silicon is not suited for NIR absorption, yet its electrical properties and low absorption above 800 nm could actually be promising to produce n or p-type window layers to form a P-I-N junction for our devices. This aspect of µc-Si:H will be discussed in the following chapter. Focusing on the absorber layer development, a low band-gap alternative to Silicon-based layers with similar structural properties is Germanium, which can be introduced in the reaction chamber as a Germane gaseous precursors. In the following section,

Cette thèse est accessible à l'adresse : https://theses.insa-lyon.fr/publication/2023ISAL0014/these.pdf
© [A. Wilson], [2023], INSA Lyon, tous droits réservés

hydrogenated microcrystalline Germanium thin film were studied in order to establish its advantages and drawbacks for potential use in P-I-N photodiodes.

2 Hydrogenated Germanium thin films development

PECVD grown µc-Si:H thin films have shown its limitations in the previous section, in particular in terms of its absorption coefficient α above $\lambda = 800\,\text{nm}$. One approach to solve this issue is to focus on amorphous and microcrystalline Germanium semiconductor films. In this section we will focus on establishing the relationship between structural properties, optical properties and deposition parameters.

2.1 Structural properties of µc-Ge:H thin films

Hydrogen dilution in Germane plasma

Due to its lower dissociation energy compared to $Si-H$ bonds, the $Ge-H$ bonds of germane (GeH_4) are broken apart more easily [70, 71] yielding more reactive species, in turn translating into high growth rates (see chapter 1, section 5.1.1). In similar deposition conditions (given in table 3.5) growth rate for Ge:H films is 1.85 times higher than Si:H films. Although higher growth rates might seem like an advantage in the context of industrial production, the consequences on the structural properties are detrimental. The deposited layer moves on from a highly crystallized morphology to a fully amorphous layer (see table 3.5). This experimental evidence is in agreement with data gathered from the literature [59, 60] in chapter 1, subsection 4.1. Obtaining microcrystalline layers implies limiting the amount of dangling bonds at the film's surface to ensure atomic rearrangement happens faster than film growth as well as providing hydrogen to "chemically anneal" the film and overcome the metastable amorphous phase formation [50] (see section 3.1.1). Conversely, we can forcefully limit the material's growth rate to ensure crystallization by dramatically increasing hydrogen dilution.

Sample	X_c [ ]	Thickness [nm]	t_{dep} [min]	v_{dep} [nm·min^{-1}]	Temperature [°C]	Power [W]	Pressure [mTorr]	R_H [ ]	Φ_{tot} [sccm]
µc-Si:H (#280)	79 %	161	60	2.68	200	30	800	50	350
a-Ge:H (#296)	0 %	99	20	4.95	250	30	1000	50	350

Table 3.5: Growth rate and Raman crystallinity for silane-based and germane-based plasmas in similar dilution and power deposition conditions. Temperature and Pressure have much less impact on growth rate.

In order to identify optimal conditions for obtaining µc-Ge:H, hydrogenated Germanium layers were deposited on c-Si and glass at increasing R_H, ranging from 20 to 400 for two separate RF-Power of 30 and 100 W respectively. All samples were deposited at 250 °C, 1000 mTorr, $\Phi_{tot} = 350$ sccm and $t_{dep} = 20$ min. X_c was then estimated from Raman spectra characterization for films deposited on c-Si substrate (as Ge-Ge and Si-Si TO[3] components of the film and substrate do not overlap), thickness and deposition rate were obtained through spectroscopic ellipsometry measurements (see chapter 2). Results are gathered in figure 2.1.

[3]Transverse Optical

Cette thèse est accessible à l'adresse : https://theses.insa-lyon.fr/publication/2023ISAL0014/these.pdf
© [A. Wilson], [2023], INSA Lyon, tous droits réservés

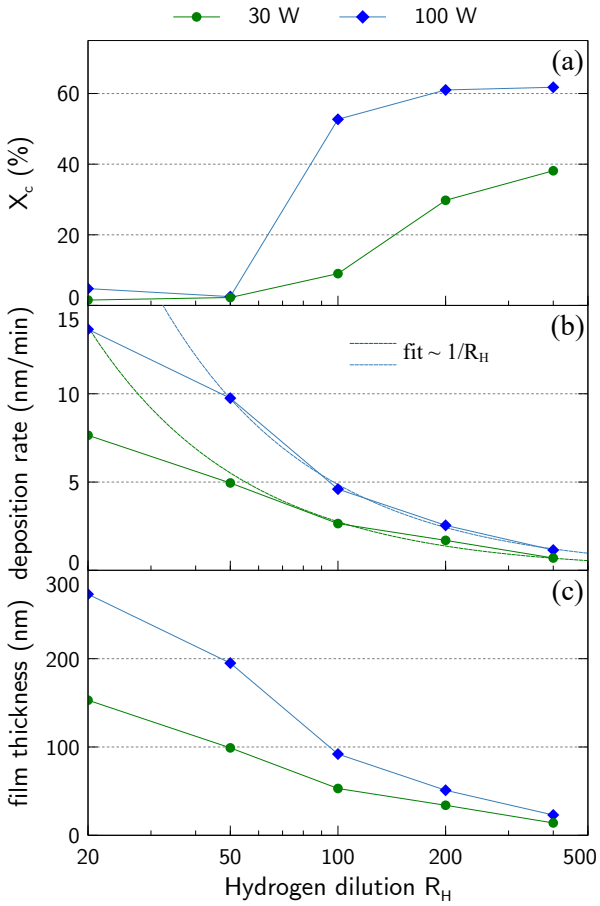

Figure 2.1: (a) Raman crystallinity, (b) deposition rate and (c) film thickness as a function of R_H. $t_{dep.}$ was set at 20 min., temperature at 250°C and pressure at 1000 mTorr.

As expected, film thickness and therefore deposition rate decreases with increasing dilution R_H. One could expect the deposition rate v_{dep} to be linearly dependent on germane concentration, and thus inversely depend on $R_H = (H_2 + GeH_4)/GeH_4$. A fit on $v_{dep} = f(R_H)$ with a simple a/R_H function yields a good correlation with our experimental data as long as $R_H > 50$ (see figure 2.1). As Φ_{tot} is maintained constant, R_H is inversely related to the amount of GeH_4 in the system. The correlation of deposition rate v_{dep} with GeH_4 at high R_H suggests the v_{dep} is precursor-limited. In an analogy to the thermodynamics of CVD growth, this is equivalent to the deposition rate no longer following an Arrhenius function when plotting $v_{dep} = f(1/T)$ [136, 137] but rather it starts reaching a plateau. Conversely, at low R_H deposition rate is limited by the system's energy input rather than precursor availability.

Similarly to µc-Si:H, the dependence of X_c on hydrogen dilution is characterized by a threshold value for R_H under which the film stays amorphous. In the tested range of deposition conditions a-Ge:H is obtained for R_H up to 50 and crystalline phase nucleation starts somewhere in the range $R_H \in [50, 100]$ (to be compared with $R_H \in [10, 20]$ for µc-Si:H [43]). From figure 2.1 it is quite clear *high power* (100 W) conditions lead to a more abrupt phase transition as well as highly crystalline layers (up to 60 %). A little nuance should be added since deposition time was kept constant (at 20 min) for both conditions, meaning the "100 W" samples led to thicker films. Crystalline phase nucleation in known to strongly depend on

Cette thèse est accessible à l'adresse : https://theses.insa-lyon.fr/publication/2023ISAL0014/these.pdf
© [A. Wilson], [2023], INSA Lyon, tous droits réservés

film thickness in the case of µc-Si:H [50, 131] and similar growth mechanism can be expected for µc-Ge:H.

Influence of RF-Power on crystallinity

Figure 2.1 showed the crucial importance of dilution in obtaining a microcrystalline morphology for PECVD deposited Ge:H layers. A second insight was the effect RF-Power could have on film growth, not only in terms of growth rates but also of crystallinity. To further explore the impact of this process parameter µc-Ge:H layers were deposited on c-Si substrates at varying RF-Power, from 30 to 200 W. All samples had a thickness included between 28 and 33 nm when measured by spectroscopic ellipsometry. The calculated values for X_c are thus directly comparable. Figure 2.2 shows the Raman spectra obtained for µc-Ge:H samples deposited at 30, 60 ,150 and 200 W respectively.

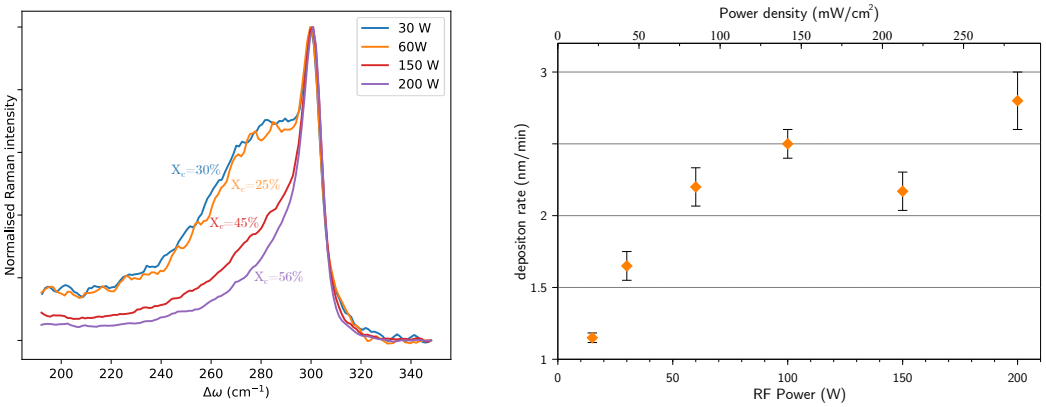

Figure 2.2: Effect of applied RF-Power on Raman spectra, crystallinity and deposition rate of µc-Ge:H at constant dilution factor $R_H = 200$, $T = 250$ °C, $P = 1000$ mTorr, Φ_{tot}= 350 sccm.

The Raman characterization of our films clearly shows higher input power leads to greater crystallinity in high hydrogen dilution conditions. This increase in X_c could be reasonably explained by the increased ion bombardment of the surface which helps rearrange weak bonds at the film's surface. Higher deposition rates usually come at the cost of greater amorphization of the layer as discussed in subsection 2.1, yet above 100 W the deposition rate is quite stable (see figure 2.2), meaning precursors flow is the limiting factor. It is thus deduced that above 100 W, increase in ion bombardment favors crystalline growth more than the increase in deposition rate favors amorphous phase.

Optimization of µc-Ge:H crystallinity by two-step growth

So far it has been shown that structural properties are strongly tied to hydrogen dilution R_H. As shown in figure 2.1(b), increase in hydrogen dilution at constant total gas flow is detrimental to deposition rate as it implies decreasing Φ_{GeH4}. RF-Power can provide a way to noticeably bring the deposition rate back up. However, from 30 to 100 W power consumption is increased by a factor 3.3 while deposition rate only experiences a 50 % gain. A potential method to reach beyond the limitation of hydrogen dilution and RF-Power increase in order to reach higher deposition rates is be to break down deposition into two steps : a slow nucleation step followed by fast growth step.

Cette thèse est accessible à l'adresse : https://theses.insa-lyon.fr/publication/2023ISAL0014/these.pdf
© [A. Wilson], [2023], INSA Lyon, tous droits réservés

µc-Ge:H films were grown on c-Si substrates following pattern :

- a first layer is grown at high R_H (200 or 400) for a duration $t_{nucleation}$ (between 5 and 30 minutes) in order to deposit a thin (5 to 75 nm), highly crystallized layer on the substrate.
- a second layer is grown at lower R_H (100 nm for $R_H = 50$, 75 nm for $R_H = 100$) in order to increase deposition rate while benefiting from the pre-crystallized sub-layer to keep X_c higher than a single-step low R_H film.

Substrate temperature was set to 250 °C, RF-Power to 100 W and Φ_{tot} to 350 sccm. Raman crystallinity was then measured on each *two steps* sample and on single-step layers deposited at each dilution ($R_H = 50, 100, 200, 400$) for reference. As µc-Ge:H has an extremely high absorption coefficient at 473 nm[4] (see subsection 2.2) of around $6 \cdot 10^6$ cm^{-1}, 95 % of the excitation laser is absorbed in the top 60 nm of the film. The *low* R_H top-layer is more than 60 nm thick so that the calculated X_c only accounts for this last layer.

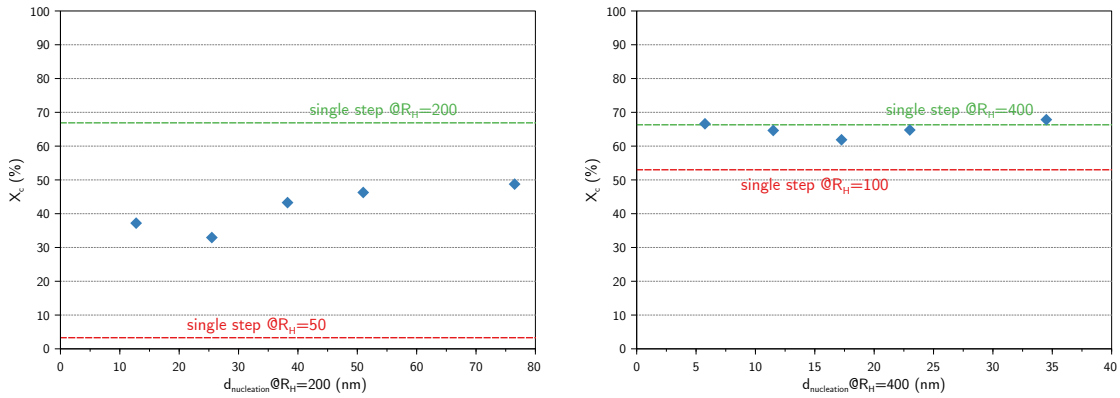

(a) (b)

Figure 2.3: Raman crystallinity for a two-steps growth process (a) with nucleation phase at $R_H = 200$. Nucleation layer thickness $d_{nucleation}$ varies and $d_{R_H 50} = 100$ nm (b) with nucleation phase at $R_H = 400$. Nucleation phase thickness $d_{nucleation}$ varies and $d_{R_H 100} = 75$ nm.

Figure 2.3a and 2.3b show the dependence of X_c on nucleation layer thickness. The red and green dotted line give the measured X_c for a single-step *low* R_H and *high* R_H layer, respectively. The efficiency of the proposed method to improve X_c can be measured by the proximity of the Raman measurement of the two-steps process with the single-step high R_H process.

In the first process, $R_H : 200 \rightarrow 50$, a great improvement of crystallinity is observed when compared to the single-step $R_H = 50$ layer which is fully amorphous. However, the maximum X_c reached is lower than a single layer grown at $R_H = 200$. Nucleation thickness also appears to have little impact on the final value for X_c although $d_{nucleation} > 35$ nm seems to be favorable.

The second process, $R_H : 400 \rightarrow 100$, is more effective as crystallinity is also improved when compared to the single-step $R_H = 100$ layer. The shift is not as important as the first

[4]Wavelength for the Raman excitation LASER

Cette thèse est accessible à l'adresse : https://theses.insa-lyon.fr/publication/2023ISAL0014/these.pdf
© [A. Wilson], [2023], INSA Lyon, tous droits réservés

process, yet the maximum X_c reached is here equal to the single layer grown at $R_H = 400$. This gain is observed no matter the initial layer's thickness in the range studied.

The latter result implies it is possible to reach X_c equivalent to a film grown at $R_H = 400$ while increasing the deposition rate almost by a factor of four (neglecting the time for nucleation layer deposition). In the context of industrial production, this gain in process duration can become a great advantage as long as it does not impact other properties of the film. It may also be an effective method to reduce the impact of the substrate on crystalline growth.

2.2 Optical properties of µc-Ge:H

To understand the potential with respect to near infrared of µc-Ge:H over µc-Si:H and a-Ge:H, one must look into optical properties of this peculiar material. Thick layers of hydrogenated Germanium were deposited on glass and c-Si in order to be studied by spectroscopic ellipsometry. Process parameters used for the deposition are gathered in table 3.6.

Sample	X_c [ ]	Thickness [nm]	t_{dep} [min]	v_{dep} [nm·min^{-1}]	Temperature [°C]	Power [W]	Pressure [mTorr]	R_H [ ]	Φ_{tot} [sccm]
a-Ge:H	0 %	520±10	60	8.5	250	100	1000	50	350
µc-Ge:H	76 %	410±20	180	2.2	250	30	1000	200	350

Table 3.6: Deposition conditions, measured thickness and X_c of Ge:H thin films deposited from a $GeH_4 + H_2$.

In order to restrict the degrees of freedom in our ellipsometry model thickness was measured by SEM. Cross-sectional images of the films were taken under high magnification using the high contrast In-Beam SE (Secondary Electrons) detector mode (see figure 2.4). Due to atomic mass difference between the c-Si substrate and the Ge:H layer the interface can be easily identified and thickness measured accurately.

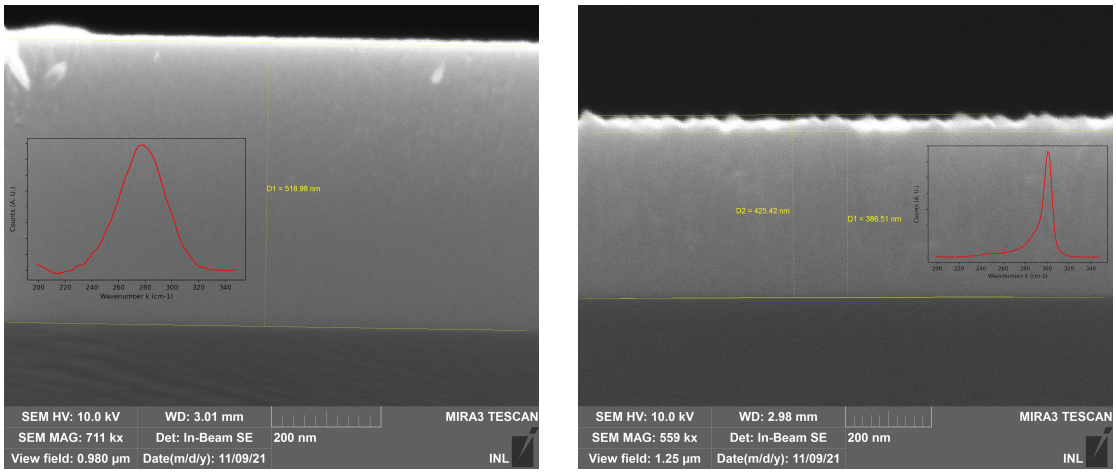

Figure 2.4: Cross-sectionnal view SEM images and Raman spectra of amorphous Germanium (left) and microcrystalline Germanium (right) deposited on c-Si. Surface roughness characteristic of microcrystalline materials can be seen in the second image. Corresponding deposition conditions can be found in table 3.6.

Cette thèse est accessible à l'adresse : https://theses.insa-lyon.fr/publication/2023ISAL0014/these.pdf
© [A. Wilson], [2023], INSA Lyon, tous droits réservés

2.2.1 Refractive index extraction from ellipsometry data

Amorphous Germanium

As an amorphous material, a-Ge:H's optical properties are easy to retrieve. Its optical indices will have no dependence on crystalline volume fraction, and composition is stable, with mostly the hydrogen concentration varying between different deposition conditions. Two approaches were investigated in order to obtain the refractive index $\tilde{n} = n + \imath k$.

The first approach consisted in fitting the whole spectral range of experimental data (figure 2.5a) with one single dispersion formula. The Double New Amorphous dispersion [122] (detailed in chapter 2, section 3.1.3) was selected as it gave consistent results with a-Si:H. The model is built as a 2 layers stack (a-Ge:H dispersion + native oxyde), with a c-Si standard substrate. No roughness was added due to the smooth surface of a-Ge:H thin films. The fitted model yielded a final thickness for our layer of interest of 526 nm with $\chi^2 = 8.7$. The dispersion obtained is shown in figure 2.7. The thickness obtained is in good agreement with the SEM images of the sample (figure 2.4).

The second approach that was used was based on a two step fitting of our data. One will notice that in figure 2.5a no oscillation are found under approximately $\lambda = 850$ nm as absorption is too high. In that region the film is considered as optically thick and a point-by-point calculation for n and k is possible, removing the need for a dispersion formula as long as thickness is known. Above 850 nm a Double New Amorphous dispersion (chapter 2, section 3.1.3) was used as oscillation became predominant. a-Ge:H thickness was set to 525 nm for both models and fitting was done separately before joining the obtained $n(h\nu)$ and $k(h\nu)$. The dispersion obtained is shown in figure 2.5b.

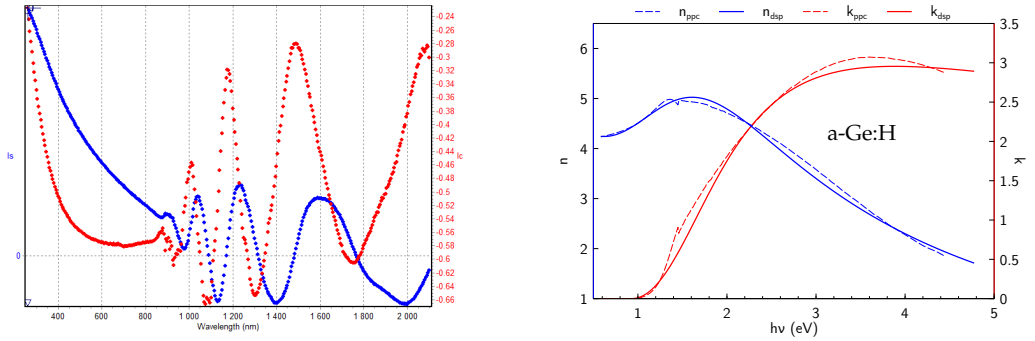

(a) (b)

Figure 2.5: (a) Experimental data from ellipsometry measurement of a thick a-Ge:H layer on c-Si. Under 850 nm the layer can be considered as optically thick and can thus be fitted using point-by-point calculation. (b) Optical indices of amorphous Germanium fitted using a Double New Amorphous dispersion formula (solid line) and using a combination of dispersion formula and point-by-point calculation (dashed line).

The good correspondence between both approaches is a good indicator that our dispersion formula and the model are accurate. In the high energy region, the point-by-point calculation is the most reliable method and the dispersion formula gives a similar $\tilde{n}$. In general, to avoid the discontinuity experienced at the boundaries of our two step approach it is preferable to use directly the optical indices given by the global approach.

Cette thèse est accessible à l'adresse : https://theses.insa-lyon.fr/publication/2023ISAL0014/these.pdf
© [A. Wilson], [2023], INSA Lyon, tous droits réservés

Microcrystalline Germanium

Relying on spectroscopic ellipsometry to find n and k for µc-Ge:H is a much more complex task than working with a-Ge:H. Indeed, the crystalline volume fraction of the film is strongly process-dependent as seen in subsection 2.1. The band structure of c-Ge also leads to a much more complex variation of the refractive compared to c-Si. Spectroscopic ellipsometry modeling of µc-Ge:H layer during growth was reported by Drevillon et al. [69] but no indication regarding the dispersion formula was given. In order to avoid working with too many degrees of freedom, a highly crystallized layer was studied. Its deposition conditions and main properties can be found in table 3.6 as well as in figure 2.4. Only the sample deposited on glass was characterized. The glass substrate's refractive index were measured independently in order to limit the degrees of freedom of our model. The model to yield the most relevant results is given in figure 2.6a. The *void.ref* and *verre_ossila.dsp*[5] account for the transparent substrate, and a user-defined formula (*µcGeH_5am.udf*) consisting of 5 amorphous oscillators (see chapter 2, section 3.1.3) was used for the bulk of our deposited layer. Each oscillator position was tuned to match the position of bulk c-Ge in order to have a good starting point for the fitting process. The final three layers were added to account for surface roughness which can be estimated from SEM images of figure 2.4 to be between 20 and 40 nm in thickness. This model provided a very accurate fit to our experimental data as shown in figure 2.6b, with a $\chi^2 = 1.7$. Calculated thicknesses are given in nanometers in figure 2.6a.

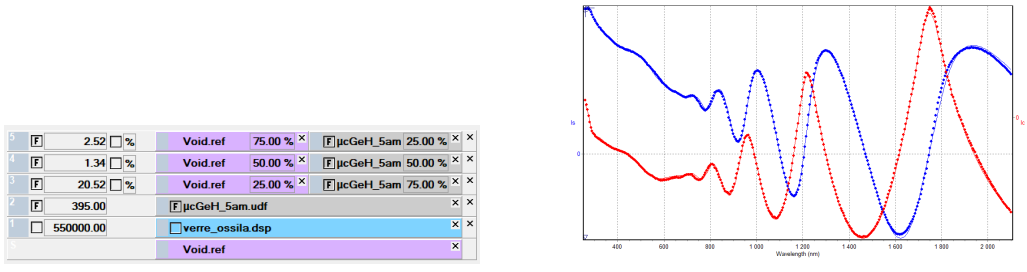

(a) (b)

Figure 2.6: (a) Best ellipsometry model found for fitting µc-Ge:H layers deposited on glass (b) Fitted I_s and I_c (see chapter 2) as a function of photon wavelength, $\chi^2 = 1.7$.

From the fitted custom dispersion formula for our material, one can extract both n and k. The results obtained in the 0.5 eV to 5 eV range are shown in figure 2.7 and compared with the previously obtained coefficients for a-Ge:H. Optical constants for c-Ge have been added to serve as a reference.

Similarly to µc-Si:H, both n and k for µc-Ge:H correspond quite closely to a broadened equivalent of c-Ge. The absorption coefficient $\alpha(\lambda) = 4\pi \cdot k/\lambda$ can then be calculated from the extinction coefficient k.

Figure 2.8 provides the absorption coefficient calculated from the extinction coefficient extracted by ellipsometry. A comparison between a-Ge:H and µc-Ge:H is of particular interest in order to select the best suited material for our needs. In the visible wavelengths, a-Ge:H turns out to have consequently higher absorption coefficient than µc-Ge:H, due to behaving like a direct band-gap material. Above $\lambda = 1060$ nm, µc-Ge:H quickly surpasses a-Ge:H mostly due to its lower band-gap. Higher absorption than c-Ge in most of the studied range

[5]Obtained from experimental measurement on a bulk glass substrate.

Cette thèse est accessible à l'adresse : https://theses.insa-lyon.fr/publication/2023ISAL0014/these.pdf
© [A. Wilson], [2023], INSA Lyon, tous droits réservés

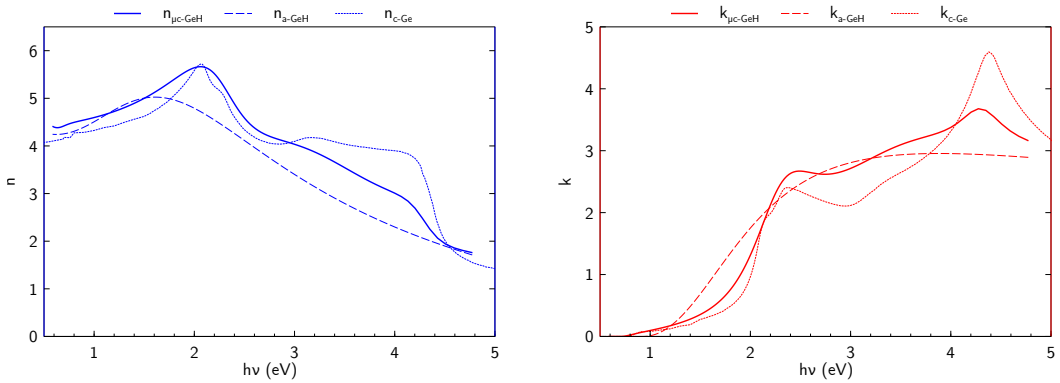

Figure 2.7: Fitted optical coefficients n and k for a-Ge:H and µc-Ge:H as a function of photon energy $h\nu$. Optical indices for c-Ge are given for comparison and taken from [138].

is also observed. It can be attributed to the direct band gap of the remaining amorphous phase combined to the crystalline phase's indirect band gap, as well as band-tail absorption due to defects.

Our spectral range of interest, from 940 and 1340 nm, is in an area where µc-Ge:H would, on average, perform better than a-Ge:H. Albeit absorption is a strong figure of merit for the choice of our material, electronic properties also have to be taken into account.

2.3 Electrical properties of µc-Ge:H

While studying electrical properties of µc-Ge:H an extremely low photo-response was found. Conductivity under dark and under 1 sun illumination was found to be practically indiscernible. Degradation of electrical properties with Germanium was expected since literature mentions on multiple accounts [21, 22] this side effect in Silicon-Germanium alloys (see chapter 1, subsection 5.2).

Influence of deposition parameters on electronic properties through design of experiment

A Design of Experiment (DoE) was implemented in order to test the influence of several parameters on electrical properties such as photo-response and resistivity.

Design of Experiment is a method used to establish the impact of a parameter on a given response while minimizing the number of tests to be performed. It can be used in order to save on both production cost or time. In order for a DoE to be as efficient as possible, the tested parameters have to be independent from each other.

A 3^3 factorial design was chosen in order to to test 3 parameters at 3 levels each [139]. The full screening of these parameters would normally imply trying 27 combinations of parameters, yet a 3^3 factorial design reduces that need down 9 combinations. In our case the parameters chosen were Temperature, R_H and RF-Power. Deposition time was fixed at 60 minutes. For each parameter, three levels were selected as given in table 3.7.

From the chosen levels for each parameter an experiment matrix is built in order for each level (+0,+1 or +2) of a given parameter to be tested only once with each other levels of every parameter. The resulting matrix is given in table 3.8. For each run, the sample's photo-response $\Delta\sigma = \sigma_{light}/\sigma_{dark}$ is measured under 1 sun illumination and resistivity ρ is measured using the Van Der Pauw method (see chapter 2).

Cette thèse est accessible à l'adresse : https://theses.insa-lyon.fr/publication/2023ISAL0014/these.pdf
© [A. Wilson], [2023], INSA Lyon, tous droits réservés

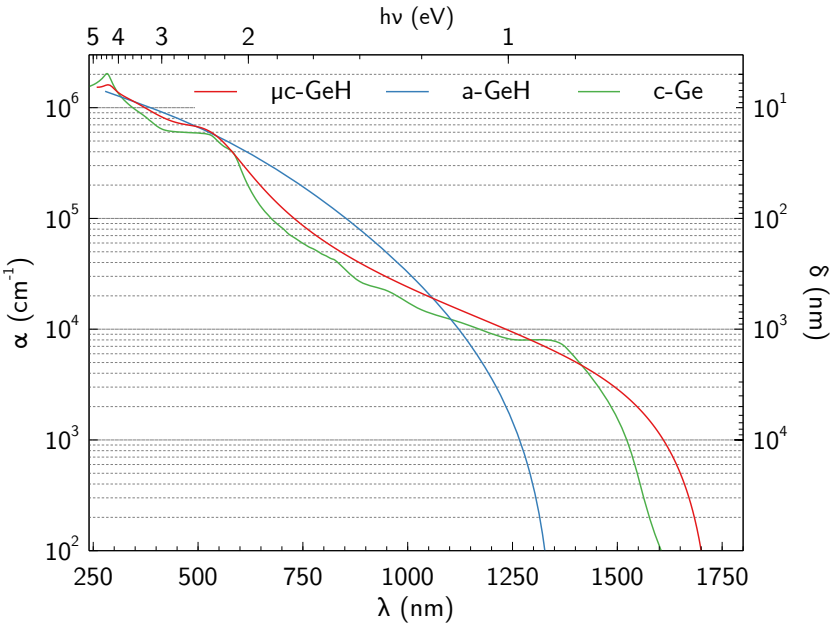

Figure 2.8: Absorption coefficient for a-Ge:H and μc-Ge:H as a function of photon wavelength λ. Spectroscopic ellipsometry is not precise enough to give a reliable value below $\alpha = 10^2\,\mathrm{cm}^{-1}$.

Level	Temperature (°C)	R_H	RF-Power (W)
+0	200	50	30
+1	250	100	50
+2	300	150	100

Table 3.7: DoE parameters and corresponding levels

Experimental results and interpretation

In order to understand these results, the so-called *effect* of every parameter must be calculated. For each level of each parameter the effect of level i is $E_i = \bar{y} - \frac{1}{n}\sum_i^n(y_i)$, with $\bar{y}$ the average of all the responses from the experiment. It represents the average gain in response of the parameter when it is set at level i. The effects of each parameter on photo-response and resistivity are shown in figure 2.9a and 2.9b, respectively.

These results are not encouraging as the average photo-reponse $\Delta\sigma$ was found to be as small as 1.19, meaning conductivity under 1 sun illumination is only 19% higher than under dark for our materials. According to the DoE results, the optimal combination of parameters would be 200 °C, $R_H = 50$, 30 W since the sum of their effects gives the highest $\Delta\sigma = 1.47$. This result is order of magnitude lower than what can be observed in μc-Si:H . One could expect this behavior to be linked to high dark currents and low resistivity of the material. Our study of resistivity ρ shows that even aiming at the most resistive material (in this case with 250 °C, $R_H = 50$, 50 W) yields a corresponding $\Delta\sigma$ is as low as 1.09. This drawback seems to be independent of structural properties as X_c shows no clear correlation with $\Delta\sigma$ (see figure 2.10).

Cette thèse est accessible à l'adresse : https://theses.insa-lyon.fr/publication/2023ISAL0014/these.pdf
© [A. Wilson], [2023], INSA Lyon, tous droits réservés

Run #	Temperature (°C)	R_H	RF-Power (W)	$\Delta\sigma$	ρ ($\Omega \cdot$ cm)
1	200	50	30	1.47	8090
2	200	100	50	1.23	2502
3	200	150	100	1.08	260
4	250	50	50	1.09	96056
5	250	100	100	1.08	1326
6	250	150	30	1.17	2117
7	300	50	100	1.12	11920
8	300	100	50	1.14	5424
9	300	150	30	1.32	1110
$\bar{y}$				1.19	14312

Table 3.8: Deposition parameters for each run of the 3^3 factorial design of experiment.

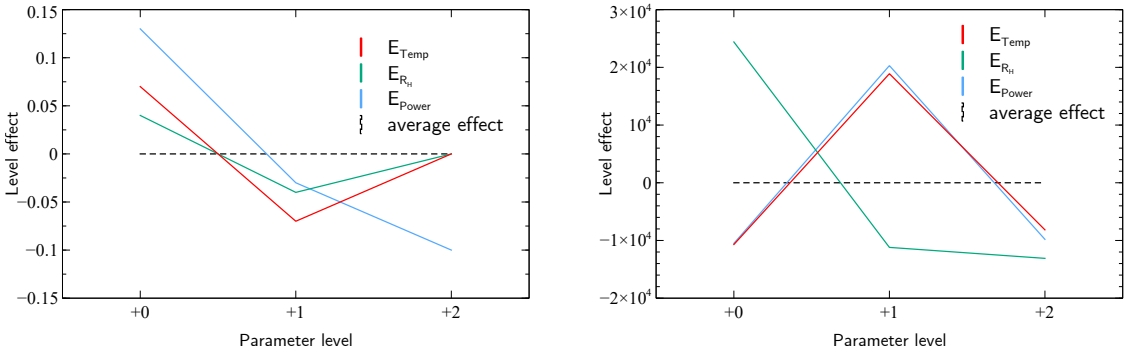

(a) (b)

Figure 2.9: Effect E_i for each parameter tested (Temperature, Dilution and RF-Power) as a function of parameter level $i = \{+0, +1, +2\}$, (a) for photo-response, (b) for resistivity.

2.4 Conclusion : µc-Ge:H thin films

The poor photo-response of µc-Ge:H could be a major drawback for photo-detection applications it could lead to degraded signal to noise ratio. The PECVD deposited µc-Ge:H films studied do not meet the requirements for an effective absorber and thus may not be a viable option for above-IC compatible photodiodes despite its promising optical properties. So far, both µc-Si:H and µc-Ge:H were shown not to be fully appropriate for our intended use, yet both have promising aspects : by working with microcrystalline silicon-germanium alloys, it may be possible to find a compromise between high absorption and sufficient electrical properties.

3 Hydrogenated Silicon- Germanium alloys development

So far two materials have been investigated to serve as an absorber layer in a PIN photodiode. As we aim to reach high quantum efficiency in the near infrared range, effective materials have to be developed for the n-type, intrinsic and p-type layers. The intrinsic layer, also called the absorber layer has to be optimized in order to find the best compromise between photon

Cette thèse est accessible à l'adresse : https://theses.insa-lyon.fr/publication/2023ISAL0014/these.pdf
© [A. Wilson], [2023], INSA Lyon, tous droits réservés

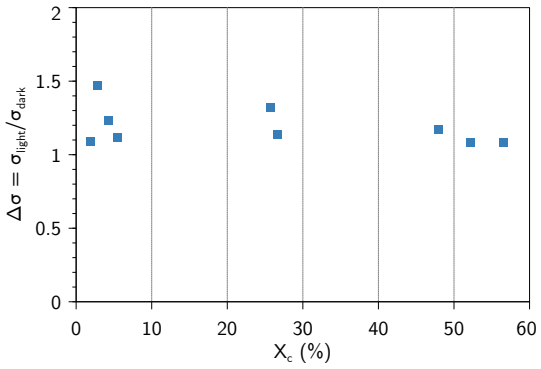

Figure 2.10: Raman crystallinity X_c vs photo-response $\Delta\sigma$ under 1 sun illumination. No clear correlation can be established.

absorption and electron-hole pair extraction from the layer. In the previous sections of this chapter, optoelectronic properties of µc-Si:H and µc-Ge:H were investigated. In the present section, hydrogenated silicon-germanium alloys (μc-$Si_{1-x}Ge_x : H$) are explored as a way to reach a compromise between µc-Si:H's electrical properties and µc-Ge:H's absorption. As introduced in chapter 1, section 5, µc-SiGe:H has been studied in the context of photovoltaic research for bottom cell applications [27, 80, 81]. It was found electrical properties of µc-SiGe:H alloys degrade with Ge incorporation. [23] As with any microcrystalline material the established optical and electrical properties are strongly tied to deposition conditions. Consequently the following section will focus on producing and characterizing state-of-the-art SiGe:H layers for NIR absorption.

3.1 From gas phase $SiH_4 + GeH_4$ to solid $Si_{1-x}Ge_x : H$ films

In order to produce state-of-the-art SiGe:H layers the relation between precursor gas flow and solid phase Germanium concentration was established. The amount of Germanium in the gas phase is typically referred to as Germane Concentration (GC) which is defined as the ratio $GeH_4/(SiH_4 + GeH_4)$. The solid phase germanium concentration x_{Ge} can then be defined as [Ge]/([Ge]+[Si]). x_{Ge} is not directly equal to the atomic Ge composition of the film as hydrogen is not included in the expression.

Stack Number	R_H	Power	Pressure	Φ_{tot}	Temperature
-	-	[W]	[mTorr]	[sccm]	[°C]
#1	25	50	1000		
#2	50	50	1000		
#3	100	50	1000		
#4	100	30	1000	500	200
#5	100	100	1000		
#6	50	100	600		
#7	50	100	800		

Table 3.9: Deposition conditions for the SiGe:H/SiN_x multilayered stacks used for calibration.

Cette thèse est accessible à l'adresse : https://theses.insa-lyon.fr/publication/2023ISAL0014/these.pdf
© [A. Wilson], [2023], INSA Lyon, tous droits réservés

3.1.1 SiGe:H multilayer stack production for chemical analysis

In order to minimize the amount of sample to chemically characterize the following approach was chosen. For every given set of temperature, pressure, power and dilution conditions gathered in table 3.9 a stack of 10 SiGe(100nm)/SiN(35nm) layers was deposited with an increasing Germane Concentration for each SiGe layer in the stack. A schematic cross section on the sample is shown in figure 3.1.

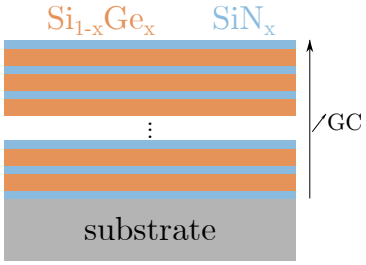

Figure 3.1: Schematic cross section of a SiGe:H/SiN_x stack.

A ToF-SIMS depth composition profile is then obtained by simultaneously etching the film with a Cs+ 3keV ion beam and analyzing the resulting etched products by mass spectrometry. The use of silicon nitride inter-layers helped identify each SiGe:H layer in the stack by marking an abrupt drop in x_{Ge} and also avoided Ge diffusion between adjacent SiGe layers. In order to input the right gas flow rates to setting the value for GC for every layer in the stack, the gas flow rate calculations established in chapter 2, section 1.1.3 were used.

3.1.2 ToF-SIMS Analysis

SEM cross sectional images of the SiGe stacks were obtained as shown in figure 3.2. The thin darker layers represent the low density SiN interlayers while the brighter part of the film represents the SiGe:H layers. Some roughness can be observed in the layer which is most likely due to the microcrystalline nature of the first µc-Si:H layer which produces the well described *cauliflower-like* surface.

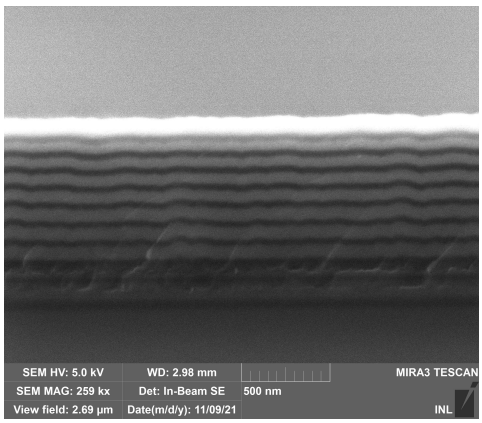

Figure 3.2: Cross-sectionnal SEM image of SiGe/SiN stack #2.

The resulting profiles obtained by ToF-SIMS analysis (chapter 2, section 3.1.2) give the calculated x_{Ge} based on two relations:

Cette thèse est accessible à l'adresse : https://theses.insa-lyon.fr/publication/2023ISAL0014/these.pdf
© [A. Wilson], [2023], INSA Lyon, tous droits réservés

$$[\mathrm{Ge}] + [\mathrm{Si}] = 100\,\% \quad \text{and} \quad [\mathrm{Ge}]/[\mathrm{Si}] = \mathrm{k} \cdot \mathrm{GeCs}^+/\mathrm{SiCs}^+,$$

where k is a proportionality constant calibrated from a reference sample. A depth profile is given in figure 3.3 for stack #1. The depth values of the x-axis are estimated from the average etch rate of the whole stack and thus cannot be used for thickness measurement since the structure is highly heterogeneous.

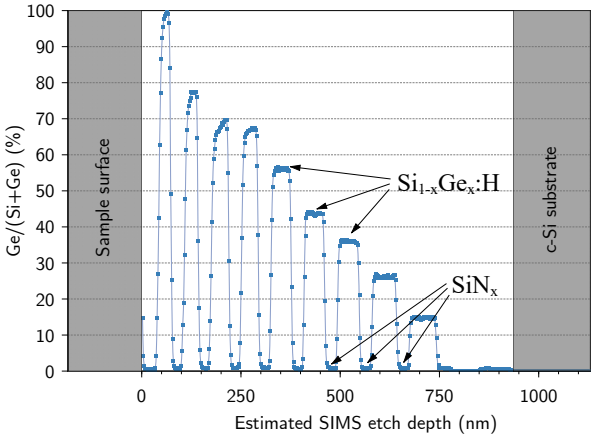

Figure 3.3: ToF-SIMS Ge depth profile obtained from SiGe stack #1 (see table 3.9).

As etch depth increases, a succession of peaks and valleys can clearly be identified, corresponding to the SiGe:H and SiN layers respectively. The fact that the first peak is measured at $x_{Ge} = 100\,\%$ (pure Ge:H) and the last one at $x_{Ge} = 0\,\%$ (pure Si:H) validates the measurement method and confirms negligible Si or Ge diffusion occurs between SiGe:H layers. This result was expected since deposition occurs at only 200 °C. For each peak, the maximum value for x_{Ge} was extracted and used to establish the relation between x_{Ge} and GC.

3.1.3 SiGe:H thin film composition from plasma conditions

All measured x_{Ge} for the 7 samples described in table 3.9 were plotted as a function of GC in figure 3.4. For several samples the layers deposited at $GC < 20\,\%$ yielded a pure Si:H material due to a limitation in gas flow rates in our PECVD setup. A calculated $\Phi_{GeH4+H2}$ below 15 sccm (due mostly to high R_H) led to $\Phi_{GeH4+H2} = 0$ experimentally. The absence of Ge in these layers was confirmed by Electron Energy Loss Spectroscopy (EELS) during Transmission Electron Microscope (TEM) imaging (see figure 3.5). These points have thus been ignored.

The data gathered in figure 3.4 showed Germanium was preferably incorporated into the layer no matter the deposition conditions. Similar experimental evidence was found by Matsui et al. [21] and was explained in terms of the higher deposition rate of GeH_4 compared to SiH_4, in turn a consequence of the lower dissociation energy of $Ge - H$ bonds [70].

By looking at Ge incorporation at increasing R_H (figure 3.4, left) it was found $x_{Ge} = f(GC)$ was independent of hydrogen dilution until $GC = 40\,\%$. Above this threshold, layers deposited at $R_H = 25$ and $R_H = 50$ were less prone to Ge incorporation. A clear discontinuity was observed around $GC = 40 - 50\,\%$ for both of these stacks which could be due to a transition from microcrystalline to amorphous layers as Si:H transitions at lower R_H compared to Ge:H ($R_H = 25$ vs 100 respectively, see sections 1 and 2).

Cette thèse est accessible à l'adresse : https://theses.insa-lyon.fr/publication/2023ISAL0014/these.pdf
© [A. Wilson], [2023], INSA Lyon, tous droits réservés

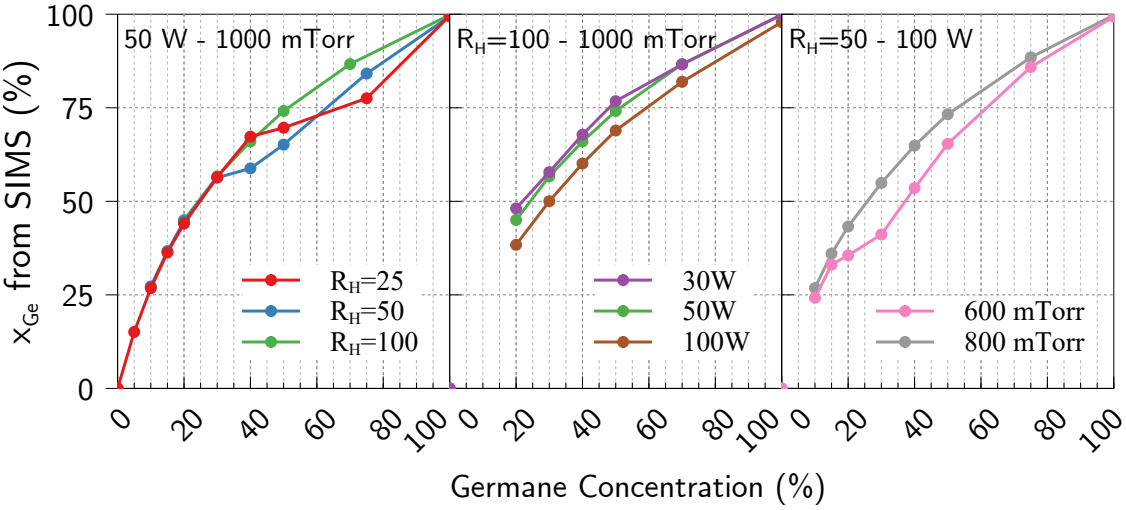

Figure 3.4: $x_{Ge} = f(GC)$ measured by ToF-SIMS for different deposition conditions: (left) at increasing R_H - stacks #1/2/3, (center) at increasing RF Power - stacks #4/3/5, (right) at increasing pressure - stacks #6/7. Details on deposition conditions can be found in table 3.9.

Increasing RF-Power from 30 to 100 W (figure 3.4, center) while keeping R_H at 100 and Pressure at 1 Torr was found to have an impact on Ge incorporation at high power. The greater the power density the closer the experimental data shifted towards a linear relationship between x_{Ge} and GC. Such a behavior can be explained by the increase in ion bombardment brought by high power densities. Ni et al. [38] have shown ion bombardment promotes etching of weaker Ge-Ge bonds while not affecting Si-Si bonds as much.

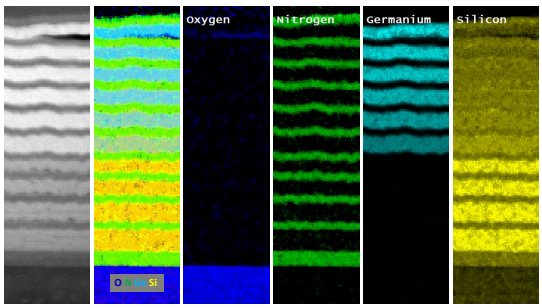

Figure 3.5: EELS TEM image of SiGe/SiN stack #3. The individual layers can be identified due to their composition. The 4 first layers of SiGe:H do not contain any Ge due to an unforeseen hardware limitation.

Another way to tune ion bombardment during deposition is pressure. Similarly to the trend observed with RF-Power, a decrease in Pressure (figure 3.4, right) can increase ion bombardment and promote equivalent Si and Ge incorporation.

3.1.4 Interpolation model for SiGe:H composition

The primary goal of the ToF-SIMS characterization performed on Silicon-Germanium stacks was to establish the relation between x_{Ge} and Germane Concentration. With this data, for a

Cette thèse est accessible à l'adresse : https://theses.insa-lyon.fr/publication/2023ISAL0014/these.pdf
© [A. Wilson], [2023], INSA Lyon, tous droits réservés

given set of deposition conditions it is possible to predict a film's final composition without going through the time-consuming and costly process of ToF-SIMS characterization for every sample. However, the experimental data obtained is discrete (figure 3.4) hence interpolation is necessary to be able to finely tune x_{Ge}.

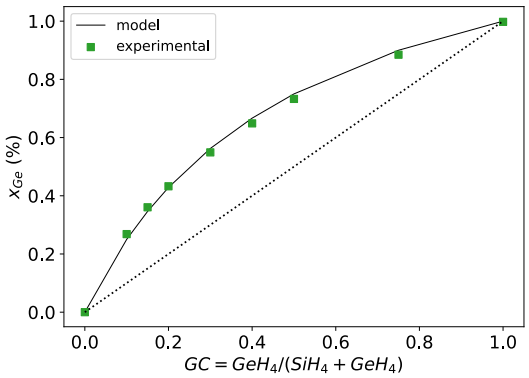

Figure 3.6: Germanium fraction as a function of Germane concentration for stack #7. Experimental data is represented with green squares, the solid black curves corresponding to the fitted model using eq. 3.1 with $R = 3$.

A mathematical expression (see eq. 3.1) was proposed by Matsui et al. [21] to fit experimental data with the incorporation factor R = 5.

$$x_{Ge} = \frac{R \cdot \Phi_{GeH4}}{R \cdot \Phi_{GeH4} + \Phi_{SiH4}} = \frac{R \cdot GC}{R \cdot GC + (1 - GC)} \tag{3.1}$$

The same expression was fitted to the data presented in figure 3.4, expect for stacks #1, #2 and #6 which could not be described by a simple expression. Corresponding R values fitted for each stack is summarized in table 3.10. A R value closer to 1 (dotted line in figure 3.6) would mean there is no preferential incorporation of Ge in SiGe:H alloys.

Stack	#3	#4	#5	#7
R fitted value	3.0	3.2	2.2	3.0

Table 3.10: Fitted R values for each SiGe/SiN multilayer stack according to the expression given in eq. 3.1

By rewriting equation 3.1 as a function of x_{Ge} it becomes possible to input the expected film composition to obtain the suited process parameters (eq. 3.2). From GC all necessary gas flow rates can be computed using the expression defined in chapter 2, section 1.1.3.

$$GC = \left(1 + R \cdot \frac{1 - x_{Ge}}{x_{Ge}}\right)^{-1} \tag{3.2}$$

Although not all SiGe:H stacks could be fitted, the analytical expression for $x_{Ge} = f(GC)$ will be a very useful tool for future photodiode fabrication. In further chapters, Silicon-Germanium layers will be referred to as µc-$Si_{1-x}Ge_x$:H with x being the chosen value for x_{Ge} from which GC, $\Phi_{GeH4+H2}$, Φ_{SiH4} and Φ_{H2} are calculated. Chemical composition of SiGe:H layers now can be finely tuned, the following section will thus focus on measuring the dependence of optical properties on film composition.

Cette thèse est accessible à l'adresse : https://theses.insa-lyon.fr/publication/2023ISAL0014/these.pdf
© [A. Wilson], [2023], INSA Lyon, tous droits réservés

3.2 Optical properties of µc-SiGe:H alloys

In previous section of this chapter, optical properties of microcrystalline Silicon (see 1.3) or microcrystalline Germanium (see 2.2) were shown to be mostly dependent of crystalline volume fraction (X_c). Optical indices could be obtained by Spectroscopic Ellipsometry by fitting the appropriate model to experimental data. This approach is however made more complex in the case of µc-SiGe:H due to an additional degree of freedom brought by the variable composition of the deposited alloy.

3.2.1 µc-SiGe:H sample preparation

In order to study the optical properties of the material, single layers of µc-SiGe:H were deposited on glass and c-Si. Deposition conditions were based on stack #3 as the high hydrogen dilution ($R_H = 100$) ensures film crystallization. The microcrystalline nature was verified by High Resolution TEM imaging of a 193 nm thick µc-SiGe:H layer deposited on a c-Si substrate with $GC = 30\,\%$.

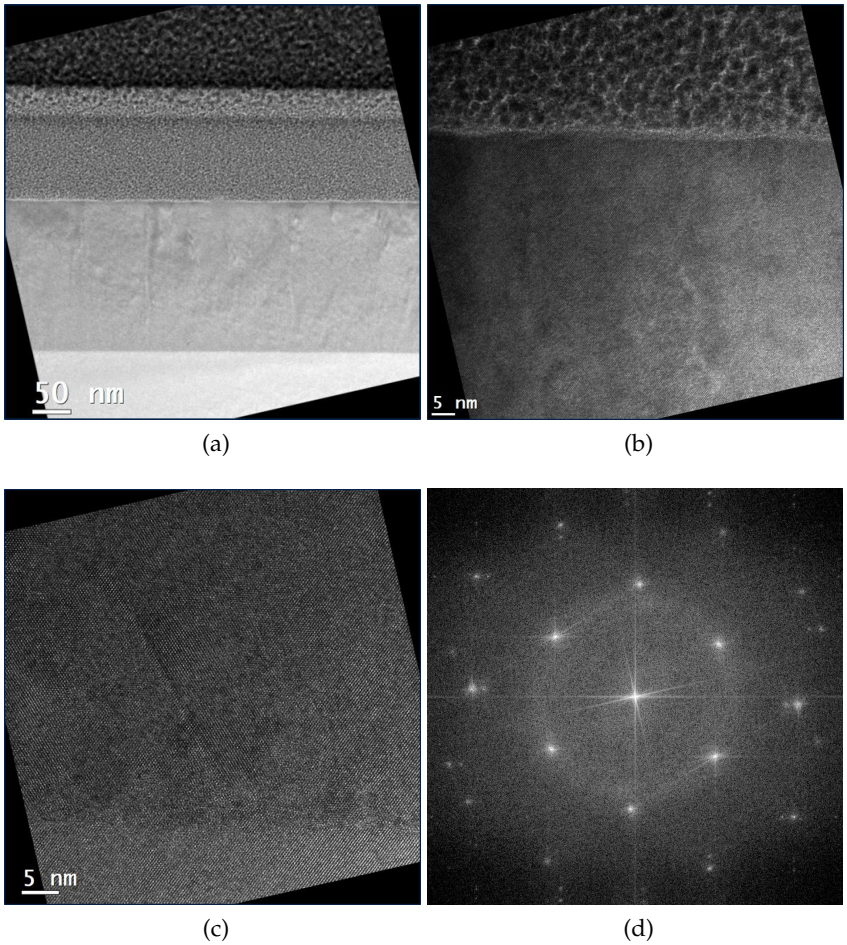

(a) (b)

(c) (d)

Figure 3.7: High Resolution TEM images of a 193 nm µc-SiGe:H film deposited on c-Si. (a) Cross- sectional view of the whole film, (b) atomic structure of sample's surface, (c) atomic structure at the c-Si/SiGe interface, (d) FFT of the layer shown in subfigure (c).

Cette thèse est accessible à l'adresse : https://theses.insa-lyon.fr/publication/2023ISAL0014/these.pdf
© [A. Wilson], [2023], INSA Lyon, tous droits réservés

The resulting HR-TEM images are shown in figure 3.7. On both the high magnification images at the film surface and at the substrate/film interface (figure 3.7b and 3.7c respectively) the crystalline structure can clearly be observed. Amorphous patches can also be identified at the interface and stacking fault (most likely a dislocation) is visible in the center of the image.

A Fast Fourier Transform (FFT) of the film in figure 3.7c was obtained in figure 3.7d. The resulting diffraction pattern confirms the presence of a highly crystalline phase. Satellite spots seen in the periphery of the image are characteristic of stacking faults [140] which naturally occur during microcrystalline material growth.

The presence of a mainly crystalline micro-structure in our films will be used to simplify our ellipsometry models and specifically chose dispersion formulas adapted for crystalline materials.

3.2.2 Optical modelling of µc-SiGe:H alloys

Fitting Method

Similarly to µc-Si:H and µc-Ge:H, we expect the optical indices of µc-SiGe:H to have some resemblance with a broadened version of its crystalline counterpart. The dispersion formula used to model µc-SiGe:H will thus be derived from monocrystalline Silicon-Germanium.

Dispersion formula

The DeltaPsi2 software used for data acquisition and fitting provides an adjustable c-SiGe file [141] for which $\tilde{n} = n + \imath k$ is composition dependent. Figure 3.8 shows the data for n and k at different Ge fractions. This data was used as a mean to calibrate the appropriate dispersion formulas, providing a better starting point for our experimentally measured data. Since the µc-SiGe:H layers are similar to polycrystalline semiconductors a Kato-Adachi dispersion was used, which consists of 3 oscillators (see chapter 2, section 3.1.3).

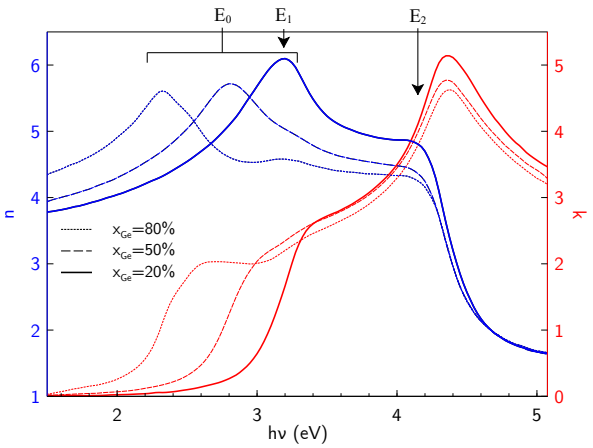

Figure 3.8: n and k optical indices of c-SiGe for $x_{Ge} = 20\,\%$, $50\,\%$ and $80\,\%$

The c-SiGe data can indeed be described as 3 main oscillators corresponding to higher density of states in the band structure :

E_0 Strongly Ge fraction dependent oscillator. Energy position varies from 2.0 eV (pure Ge) to 3.4 eV (pure Si)

Cette thèse est accessible à l'adresse : https://theses.insa-lyon.fr/publication/2023ISAL0014/these.pdf
© [A. Wilson], [2023], INSA Lyon, tous droits réservés

E_1 Weakly Ge fraction dependent oscillator. Energy position stays centered around 3.2 eV (min. 2.5 eV, max. 3.4 eV)

E_2 Weakly Ge fraction dependent oscillator. Energy position stays centered around 4.2 eV (min. 4.1 eV, max. 4.3 eV)

For every given composition x_{Ge}, a specific Kato-Adachi dispersion formula was defined (ex. : *µcSiGeH(x%).dsp*) and fitted to the c-SiGe data corresponding to the same Ge fraction. In order for the dispersion's oscillator to stay as close as possible to the true oscillator positions the values for E_0,E_1 and E_2were bound as described above. Their approximate position is given in figure 3.8. Each dispersion file's parameters were updated with the fitted results.

Model definition

A model similar to those defined for µc-Ge:H and µc-Si:H was built for µc-SiGe:H samples deposited on glass (see figure 3.9). Three layers were used to represent the samples :

1. *verre_ossila.dsp*, the 550 µm thick glass substrate for which n and k were obtained experimentally from a naked glass slide. The thickness and indices of the layer are not fitted.

2. *µcSiGeH(x%).dsp*, the microcrystalline Silicon-Germanium layer of composition x_{Ge}. Both thickness and dispersion parameters are fitted.

3. *Void.ref* + *µcSiGeH(x%).dsp*, the roughness layer accounting for crystallization induced surface roughness. Both thickness and dispersion parameters are fitted.

Although the first layer is not set up as a semi-infinite substrate no interferences will occur in the substrate since its thickness is greater than the coherence length of the light source ($\sim$ 100 µm). Experimental data was acquired ranging from UV to NIR (4.77 eV to 0.59 eV, i.e. 260 nm to 2100 nm) in order to gather robust data on near IR absorption of our films.

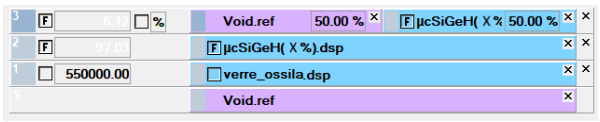

Figure 3.9: Model used for samples of µc-SiGe:H deposited on glass. Screenshot from DeltaPsi2 software.

Results : absorption of µc-SiGe:H alloys

PECVD process parameters used for µc-SiGe:H deposition on glass are gathered in table 3.11 together with corresponding fitted thickness (model layer #2), roughness (model layer #3) and fit quality factor χ^2. Values for *GC* were calculated from the analytical expression 3.2 given above, with $R = 3$. Deposition time $t_{dep.}$ was adapted in order to keep total thickness in the vicinity of 100 nm.

The Kato-Adachi dispersion file for each Ge fraction was thus updated from describing c-SiGe optical properties to µc-SiGe:H optical properties from which n and k were extracted. Figure 3.10a and 3.10b respectively give the fitted n and k as a function of Ge fraction found in µc-SiGe:H. Data for µc-Si:H and µc-Ge:H has been added for reference. The shift of the

Cette thèse est accessible à l'adresse : https://theses.insa-lyon.fr/publication/2023ISAL0014/these.pdf
© [A. Wilson], [2023], INSA Lyon, tous droits réservés

Process Parameters								Fitting results		
Expected x_{Ge}	GC	$t_{dep.}$	R_H	Φ_{tot}	Power	Pressure	Temp.	Thickness	Roughness	χ^2
-	-	[min]	-	[sccm]	[W]	[mTorr]	[°C]	[nm]	[nm]	-
40 %	0.182	45						99.9	10.2	14.4
50 %	0.251	38	100	500	50	1000	250	96.2	11.4	13.5
60 %	0.333	33						84.3	8.9	8.6
80 %	0.574	25.9						89.1	7.6	5.2

Table 3.11: Deposition conditions for µc-SiGe:H thin films used for SE measurements.

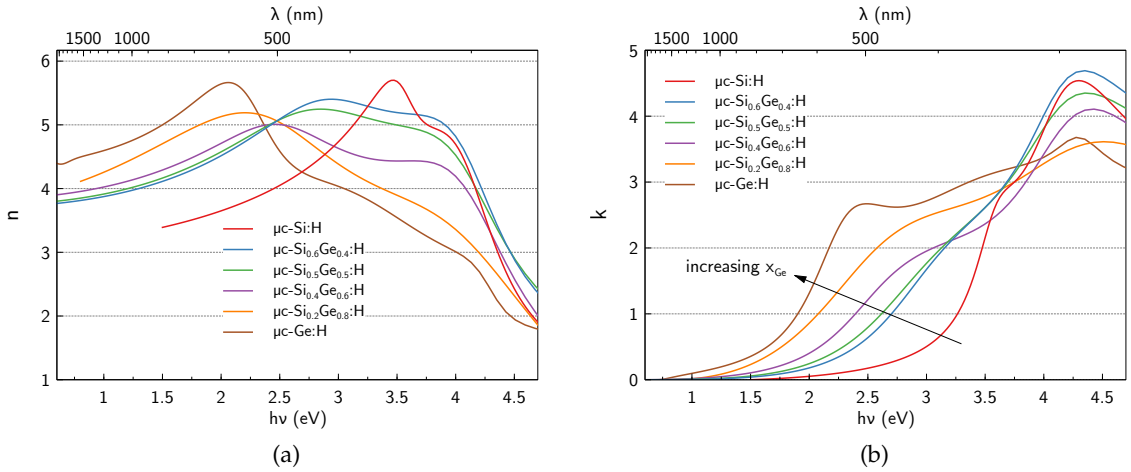

Figure 3.10: Optical indices (a) n and (b) k of µc-SiGe:H alloys of Ge fraction. Data for µc-Si:H and µc-Ge:H obtained in section 1 and 2 of this chapter have been added for reference.

curve to lower energies with increasing Germanium fraction is similar to the one observed for c-SiGe and translates the improved NIR response of Ge rich µc-SiGe:H alloys.

While n and k are useful for optical modeling purposes as well as designing effective anti-reflection coatings, the absorption coefficient is a more useful figure of merit to determine appropriate absorber layer thickness for NIR absorption. The absorption coefficient α can be calculated from the extinction coefficient k given in figure 3.10b using $\alpha(\lambda) = 4\pi k/\lambda$.

The right y-axis of figure 3.11 shows the penetration depth $\delta = 1/\alpha$. Considering light intensity decreases exponentially with material thickness $I = I_0 \cdot exp(-x \cdot \alpha)$, δ corresponds to the thickness needed for absorbing 63.2 % of the incoming photons.

Adding Germanium to µc-SiGe:H alloys is extremely beneficial to the material's performance in the NIR spectral range. At $\lambda = 1000$ nm for instance, shifting from a µc-$Si_{0.6}Ge_{0.4}$:H alloy to a µc-$Si_{0.4}Ge_{0.6}$:H alloys increases absorption from $\alpha = 2 \times 10^3\,cm^{-3}$ to $6 \times 10^3\,cm^{-3}$. These results are in close agreement with those obtained by Matsui et al. [23]. The absence of a sharp drop in absorption at high wavelengths usually seen in crystalline semiconductors can be interpreted as a consequence of sub-bandgap defects of disordered materials [43].

The Ge-rich µc-$Si_{0.2}Ge_{0.8}$:H layer was found to experience and unexpected drop in absorption above $\lambda \approx 1000$ nmwhich contradicts the global tendency of increasing α with x_{Ge}. The issue may originate from an erroneous ellipsometric model/dispersion formula. The alloy may be structurally similar to µc-Ge:H which could not be described accurately by a Kato-Adachi dispersion formula, as seen in section 2.2. Another likely explanation for this behav-

Cette thèse est accessible à l'adresse : https://theses.insa-lyon.fr/publication/2023ISAL0014/these.pdf
© [A. Wilson], [2023], INSA Lyon, tous droits réservés

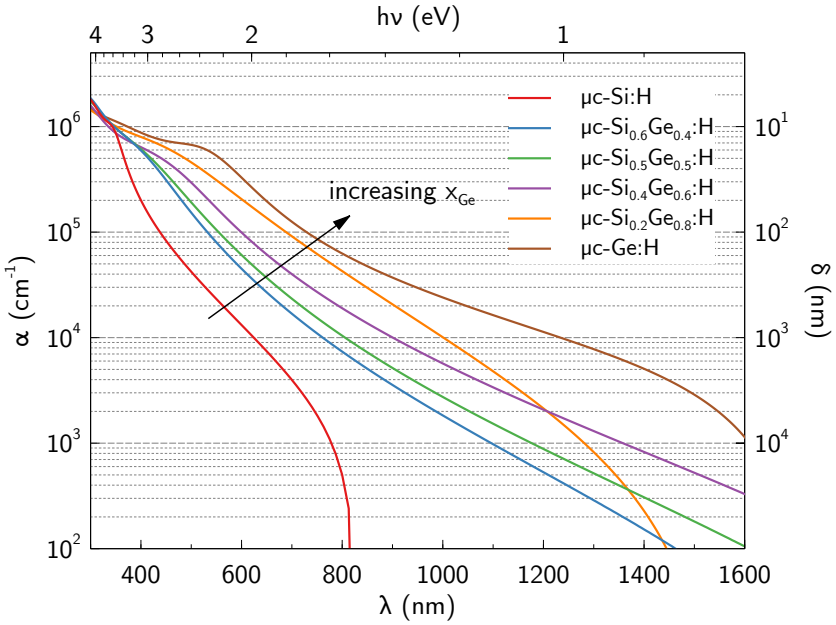

Figure 3.11: Absorption coefficient α of μc-SiGe:H obtained from Spectroscopic Ellipsometry fitted data. Absorption for μc-Si:H and μc-Ge:H from section 1 and 2 of this chapter have been added for reference.

ior may come from a progressive amorphization of the film. R_H was kept constant at 100 for all samples yet Ge incorporation promotes amorphization, meaning the μc-$Si_{0.2}Ge_{0.8}$:H film may not be as crystalline as the μc-$Si_{0.44}Ge_{0.56}$:H sample shown in figure 3.7. As discussed in previous sections of this chapter, the presence of amorphous phase increases band-gap and consequently decreases absorption in the low energy range.

So far in this section it has been shown μc-SiGe:H alloys can be obtained at any given Ge fraction by carefully calibrating the deposition conditions. The resulting film can be optically studied by spectroscopic ellipsometry if precautions are taken in building the model. With increasing Ge fraction NIR absorption is measurably enhanced. A compromise between α and diffusion length L_{diff} should however be found to establish the optimal alloy composition.

3.3 Minority carriers diffusion length in μc-SiGe:H alloys

SSPG measurement method

Diffusion length in amorphous and microcrystalline materials is known to be orders of magnitude lower than those found in crystalline semiconductors. In crystalline silicon solar cells for instance the diffusion length of minority carrier can reach up to several hundred microns, thanks to high mobility and lifetime [128]. The high defect density of microcrystalline semiconductors leads to L_{diff} often being under 1 μm [66]. For electrical characterization of such materials, the Steady State Photocarrier Grating (SSPG) method presented in chapter 2, section 4.2 has proved to be a useful tool. [66, 78, 79] Experiments were performed at the Génie électrique et électronique de Paris (GeePs) laboratory. More information about the experimental setup can also be found in the following paper by Longeaud [79].

Cette thèse est accessible à l'adresse : https://theses.insa-lyon.fr/publication/2023ISAL0014/these.pdf
© [A. Wilson], [2023], INSA Lyon, tous droits réservés

Results : L_{diff} of µc-SiGe:H alloys

µc-SiGe:H samples deposited on glass substrates were characterized using the SSPG method. Deposition conditions for all the measured samples are given in table 3.12.

Expected x_{Ge}	GC	$t_{dep.}$	R_H	Φ_{tot}	Power	Pressure	Temp.
-	-	[min]	-	[sccm]	[W]	[mTorr]	[°C]
0 %	0.0	60	25	250	30	800	200
25 %	0.10	60	50	500	50	1000	200
40 %	0.182	45	100	500	50	1000	250
50 %	0.251	38	100	500	50	1000	250
56 %	0.30	60	100	500	50	1000	200
60 %	0.333	33	100	500	50	1000	250
74 %	0.50	60	100	500	50	1000	200
80 %	0.574	25.9	100	500	50	1000	250

Table 3.12: Deposition conditions for µc-SiGe:H thin film deposited on glass for SSPG measurements

The values obtained for L_{diff} as a function of film composition are plotted in figure 3.12. Despite an overall tendency for diffusion length to decrease with increasing x_{Ge} the experimental results are not very conclusive.

This may be due to anisotropy of microcrystalline film properties. Columnar growth is frequently seen in µc-Si:H films (see chapter 1, section 3.1) however current flow during SSPG is necessarily normal to growth direction. The latter may impact our measurement as current flowing perpendicular to growth columns could interact more frequently with grain boundaries and lead to decreased diffusion lengths. This hypothesis has not been verified so far.

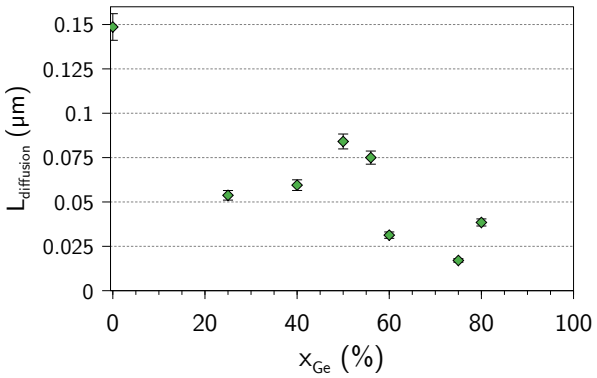

Figure 3.12: Diffusion length as a function of µc-SiGe:H alloy composition obtained from SSPG measurements at room temperature. Error bars correspond the experimental setup's intrinsic uncertainty estimated at 5 %.

SSPG measurements may not be the most reliable method for estimating electrical properties of µc-SiGe:H. In order to figure out the alloy achieving the best compromise between absorption and charge carrier extraction the alloys will be implemented into prototype photodiode devices in chapter 5.

Cette thèse est accessible à l'adresse : https://theses.insa-lyon.fr/publication/2023ISAL0014/these.pdf
© [A. Wilson], [2023], INSA Lyon, tous droits réservés

3.4 Conclusion : µc-SiGe:H thin films

Microcrystalline Silicon-Germanium provides an adjustable material which stands between microcrystalline Germanium's high absorption and microcrystalline Silicon's good electrical properties. The extra degree of freedom brought along with the tunable composition of the material makes its fabrication process more complex and demands a great amount of experimental work to find the best deposition conditions for each nuance of the alloy. In this section, we started by looking at chemical properties of µc-SiGe:H in a wide range of deposition conditions. In depth study of the material's optoelectronic properties was then conducted by focusing on a more narrow set of process parameters where high hydrogen dilution R_H ensured crystalline phase nucleation. µc-SiGe:H alloys are a promising option for efficient NIR absorber layer and will be implemented in the context of photodiode prototype fabrication in chapter 5.

4 Conclusion : Absorber layer materials development

In this chapter, microcrystalline semiconductor layers have been produced by PECVD and characterized. We aimed at producing thin films of semiconductor materials suitable for Near InfraRed (λ from 940 to 1350 nm) absorber layers in future P-I-N photodiode prototypes. In a first attempt to understand and master microcrystalline material growth, amorphous and microcrystalline Silicon films were produced relying on the abundant existing literature. The films obtained showed clear evidence of crystallization and were optically characterized by spectroscopic ellipsometry. Due to its low absorption above $\lambda = 800\,\text{nm}$ µc-Si:H is not a suitable layer for Near InfraRed sensing, yet in the context of P-I-N photodiode production it could act as an efficient n or p-type window layer on the frontside of the device. This opportunity will be explored in the following chapter.

The optical limitations of µc-Si:H have pushed for alternative materials to be studied. Microcrystalline Germanium is a strong candidate for our application since its lower band-gap enhances NIR absorption. Germane, a gas phase precursor of Germanium, is available commercially meaning its production can also be achieved by PECVD. Deposition conditions were tested in order to produce highly crystallized layers. Due to lower covalent bond energy in Germane high hydrogen dilution factor R_H were necessary to transition from amorphous to microcrystalline films. A two-step growth approach was investigated in order to produce films with high X_c without compromising on deposition rate. Optical characterization of Ge thin films by spectroscopic ellipsometry was made possible by defining the appropriate model to describe our samples. The absorption coefficient extracted from the analysis showed the benefits of µc-Ge:H over a-Ge:H for wavelengths over $\lambda = 1000\,\text{nm}$. However, it was found upon inspection of electrical properties that photoconductivity was extremely low due to high dark current and high recombination rates. µc-Ge:H kept this drawback despite our efforts to find more appropriate process parameters.

The final section of this chapter focused on finding an appropriate compromise between optical absorption and electrical properties by working with µc-SiGe:H alloys. The complexity of finely tuning alloy composition makes µc-SiGe:H a more tricky material to produce. A calibration phase was necessary to understand the growth kinetics of the material. Optical characterization by Spectroscopic Ellipsometry of µc-SiGe:H with increasing Ge fraction showed the positive impact on NIR absorption coefficient. An apparent degradation of electrical properties with increasing Germanium content was pointed out by diffusion length measurements, the exact values did not seem truly reliable.

Cette thèse est accessible à l'adresse : https://theses.insa-lyon.fr/publication/2023ISAL0014/these.pdf
© [A. Wilson], [2023], INSA Lyon, tous droits réservés

In the following chapter our work will be devoted to Phosphorus and Boron doping of µc-Si:H and µc-Ge:H thin films to form the pn junction necessary for P-I-N photodiode fabrication. Chapter 5 will then take advantage of the experimental data gathered in the present chapter and implement µc-SiGe:H alloys as the absorber in photodiode prototypes.

Cette thèse est accessible à l'adresse : https://theses.insa-lyon.fr/publication/2023ISAL0014/these.pdf
© [A. Wilson], [2023], INSA Lyon, tous droits réservés

Key Points

Contributions

- ❏ µc-Si:H thin films were produced and optically characterized by Spectroscopic Ellipsometry
- ❏ Highly crystallized Ge:H was deposited from GeH_4 highly diluted in H_2
- ❏ The impact of process parameters on Ge fraction in µc-SiGe:H film was established

Take away message

- ❏ The drop in absorption coefficient of µc-Si:H above $\lambda = 800$ nm does not make it a suitable absorber material
- ❏ The poor electrical properties of µc-Ge:H could compromise its use as an effective absorber despite $\alpha(1\text{ eV})$ reaching up to 10^4 cm^{-1}
- ❏ µc-$Si_{1-x}Ge_x$:H alloys could be a relevant choice for the absorber layer as long as a compromise between absorption and electrical properties can be found by tuning its composition

Cette thèse est accessible à l'adresse : https://theses.insa-lyon.fr/publication/2023ISAL0014/these.pdf
© [A. Wilson], [2023], INSA Lyon, tous droits réservés

Chapter 4

Doped Microcrystalline Semiconductors for pn Junctions

Developing a photodetector prototype from the ground up is a path which can be divided into several building blocks. The first and arguably the most critical of these blocks being the absorber layer material, which has been developed and characterized in the previous chapter. Keeping in mind our final goal is to produce a P-I-N type photodiode two additional materials have to be studied before designing the whole prototype : n and p-type microcrystalline semiconductors.

Crystalline Silicon is commonly doped by means of ion implantation followed be annealing yet this method yields very low activation rates in materials as defective as µc-Si:H [142, 143]. Doping of a non-crystalline material is often achieved by co-deposition, [144–146] where dopant atom precursors are added to the Si or Ge precursors in the initial gas mixture. In addition to being an effective doping method, co-deposition causes the doping to occur directly inside the PECVD reactor chamber in a single step at low temperature without any need for annealing. In the context of our work, using a single equipment to produce both the absorber layer and the doped layers limits the risk of external contamination, reduces process complexity and is time efficient.

In this chapter we will focus on obtaining n and p-type semiconductors by first focusing on phosphine (PH_3) and diborane (B_2H_6) addition to hydrogenated microcrystalline silicon. Considering the challenges of obtaining highly doped p-type µc-Si:H, Boron-doped µc-Ge:H was then explored, yielding encouraging results.

1 Doping requirements for pin structure

The space charge region approach

We aim to obtain microcrystalline layers with high doping levels in order for the space charge regions (SCR) at the P-I and I-N interfaces to extend as far as possible in the intrinsic absorber layer. The electric field in the absorber would then help electron/hole pair separation and collection, thus not relying on the material's low diffusion length. The extent of the SCR in a simple p-n junction can be derived from Poisson's equation [147] :

Cette thèse est accessible à l'adresse : https://theses.insa-lyon.fr/publication/2023ISAL0014/these.pdf
© [A. Wilson], [2023], INSA Lyon, tous droits réservés

$$\Delta V = -\frac{\rho}{\epsilon_{sc}} \quad \text{which yields} \quad W_{SCR} = \sqrt{\frac{2\epsilon_{sc}}{q}\frac{N_D + N_A}{N_A N_D}(V_{bi} - \frac{2k_B T}{q})} \tag{1.1}$$

$$\text{with} \quad V_{bi} = k_B T \cdot ln(\frac{N_D N_A}{n_i^2})$$

where ρ is the volum charge density, ϵ_{sc} is the material permittivity, q the elementary charge, N_D the donor atom density, N_A the acceptor atom density, $N = N_D$ or N_A depending on whether $N_A \gg N_D$ or vice versa, k_B the Boltzmann constant and T the temperature.

If the n-type semiconductor is highly doped and the absorber is p-type, then is is necessary to have $N_D \gg N_A \approx n_i$ in order for the SCR to extend in the region of interest, i.e. the absorber. The SCR length could then be rewritten as :

$$W_{SCR} \approx \sqrt{\frac{2\epsilon_{sc}}{qN}\left(k_B T \cdot ln(\frac{N_D}{n_i}) - \frac{2k_B T}{q}\right)} \tag{1.2}$$

This formula highlights the importance of both a truly intrinsic absorber (low N_A) and a high N_D to obtain a W_{SCR} of the order of magnitude of the absorber thickness.

The Debye length approach

The space charge region approach provides a good description of the change in potential at the P-I or I-N interface when the I and P (or N) regions have opposite doping. Perhaps a more general approach to the problem would be to think about the interface as a sudden change in donor or acceptor density. In such a case the conduction and valence bands do not follow this abrupt change due to the thermal diffusion of free charge carriers. [148, 149] Again, by solving Poisson's equation (1.1) at equilibrium, one finds the potential $\Delta\psi$ as a function of junction depth varies as :

$$\Delta\psi \propto \exp(-x/L_D) \text{ with } L_D = \sqrt{\frac{\epsilon_{sc} k_B T}{q^2 N_{D/A}}}$$

L_D is referred to as the Debye length. It represents the distance over which the free carriers rearrange themselves to shield the rest of the sample from the local electric field. [147] In our case we would rather aim for high Debye lengths in order for the electric field to extend in the absorber over a distance similar to half of its thickness. In any case, this expression confirms our need for highly doped semiconductor layers.

2 *In situ* doping of µc-Si:H

Our first insight into the optical properties of µc-Si:H (see section 1) showed the limited absorption coefficient (see figure 1.6b) of a-Si:H and µc-Si:H made for a poor absorber layer material. These same optical properties could however be taken advantage of by using boron or phosphorus doped Si:H as a window layer in P-I-N photodiodes. The term *window layer* is commonly used in photovoltaics to describe a wide bandgap emitter layer which allows low energy photons to travel the absorber without being absorbed. This design helps reduces absorption in the emitter where recombinations of minority carriers can be extremely high thus degrading the overall quantum efficiency of the device.

Cette thèse est accessible à l'adresse : https://theses.insa-lyon.fr/publication/2023ISAL0014/these.pdf
© [A. Wilson], [2023], INSA Lyon, tous droits réservés

2.1 n-type µc-Si:H

We focused on exploring the growth process as well as the structural and electrical properties of n-type (Phosphorus-doped) µc-Si:H. As previously described in chapter 1, subsection 3.1, undoped µc-Si:H deposited by PECVD typically exhibits an amorphous incubation layer which can span up to 100 nm before nucleation of the crystalline phase.[50] Previous work conducted by other research groups on µc-Si:H/µc-SiGe:H P-I-N sensors have shown that the n and p-type layers are typically designed with a thickness of the order of a few tens of nanometers.[26, 145] It is thus of great interest to understand the structural nature of thin layers as well as the impact of phosphorus doping on their properties. We have studied the impact of deposition process parameters for microcrystalline silicon phosphorous-doped layers, such as power, pressure and hydrogen dilution on film properties. Crystalline volume fraction, active and absolute dopant concentration as well as incubation layer thickness were measured and deposition conditions were found which gave high doping levels as well as a thin incubation layers.

2.1.1 Film deposition and characterization

Films were deposited using a capacitively coupled PECVD setup working at 13,56 MHz. The showerhead-type powered electrode as well as the anode are 300 mm in diameter. The anode is at floating potential due to the reactor's design. All the films were deposited at a temperature of 250 °C, on both glass (soda lime) and monocrystalline silicon. The glass substrates were cleaned using ultrasonic bath in an ethanol solution at 40 °C and rinced with deionized (DI) water while silicon was deoxydized in a 5% HF solution before being rinced with DI water.

All the films were deposited at a temperature of 250 °C, on both glass (soda lime) and monocrystalline silicon. Deposition pressure was varied between 800 and 1000 mTorr and power set at 30 or 100 W. Gases used for deposition include pure silane (SiH_4), pure hydrogen (H_2) and hydrogen-diluted phosphine (0.1 % PH_3 in H_2). We define the hydrogen dilution factor $R_H = \phi_{H_2}/\phi_{SiH_4}$ and the dopant gas ratio $\beta = \phi_{PH_3}/\phi_{SiH_4}$ where ϕ_{PH_3} is the pure (undiluted) phosphine gas flow in sccm. The details for gas flow rate calculation are given in chapter 2, section 1.1.3. Geometrical parameters such as film thickness or roughness were measured by SEM (TESCAN) and AFM (Brucker). The crystalline volume fraction X_c of our films was estimated locally by Raman spectroscopy using a 473 nm laser excitation as detailed in chapter 2, section 2.1. At such wavelength the absorption coefficient in both a-Si:H and µc-Si:H is low enough to ensure the incident photons reach the entire depth of the films, thus providing an averaged value for crystallinity over the whole film thickness. Analysis were performed on glass-deposited films to avoid any contribution of c-Si substrate to the spectrum which would lead to an overestimation of X_c. The absolute concentration in phosphorus atoms in our films was estimated by Time-of-Flight Secondary Ion Mass Spectrometry (ToF-SIMS) measurements (Cs^+ 2keV beam, see chapter 2, section 2.3). Charge carrier concentration n and hence active dopant concentration was measured by Hall effect (Van der Pauw configuration) at room temperature (see chapter 2, section 4.1).

2.1.2 Structural properties of P-doped µc-Si:H

Phosphorus doped µc-Si:H films with varying doping gas ratio β between 0 and 1% were deposited in order to investigate the impact of n-type dopant incorporation on the crystalline

Cette thèse est accessible à l'adresse : https://theses.insa-lyon.fr/publication/2023ISAL0014/these.pdf
© [A. Wilson], [2023], INSA Lyon, tous droits réservés

	Temperature [°C]	Pressure [mTorr]	Power [W]	Power Density [mW.cm^{-2}]	$t_{deposition}$ [min]	Thickness [nm]	β	R_H
R_H 25	250	800	30	42	40	160	0% → 1%	25
low power	250	800	30	42	60	168	0% → 1%	50
high power	250	1000	100	142	60	310	0% → 1%	50

Table 4.1: Deposition conditions for P doped µc-Si:H

volume fraction obtained by raman spectrometry as shown in Figure 2.1. Figure 2.2 represents the calculated Raman crystallinity X_c as a function of β for different deposition conditions. By setting the hydrogen dilution ratio R_H at 25, power at 30 W, pressure at 800 mTorr and $t_{deposition}$ = 40 min, the undoped film ($\beta = 0$) reaches a Raman crystallinity level of 55 % yet adding phosphine to the gas mixture causes a drop in X_c until the film is purely amorphous ($\beta \geq 0.5$). Similar influence on the formation of a crystalline phase has been reported by Guo and Gueng [145] in the case of boron dopant incorporation. In our case, this issue was tackled by working with two deposition conditions, namely *low power* and *high power*, for both of which R_H was increased to 50. The corresponding deposition parameters can be found in Table 4.1.

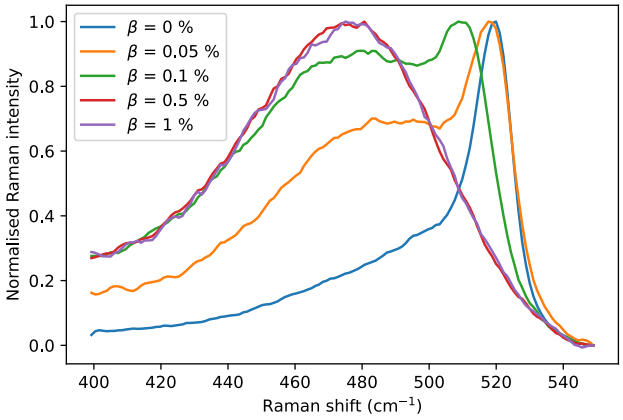

Figure 2.1: Raman spectra of samples deposited using $R_H = 25$ for different gas phase concentration of phosphine $\beta = \phi_{PH_3}/\phi_{SiH_4}$. The redshift and broadening of the Si-Si peak shows the crystalline to amorphous transition

In undoped µc-Si:H, increase in R_H is known to impact strongly X_c until a sharp transition from amorphous to crystalline phase occurs, [43, 150] usually for $R_H > 20$ in our conditions. High compressive stress was observed in P doped µc-Si:H by Wei et al.[151] in similar experimental conditions. This leads us to formulate the hypothesis that the phase transition has a mechanical origin, as phosphorus may prevent the nucleation of crystalline domains, their size (typically in the range of 10 to 20 nm) being unable accommodate the lattice deformation induced by tetravalent P atoms. A greater amount of energy is needed to allow the material to transition from a metastable amorphous phase to a crystalline one. Increasing R_H is a way to provide energy locally [43] without a need for annealing or high temperature processes. We were able to maintain $X_c > 60$ % in the whole range of β dilution. The slow but continuous drop in X_c as β increases for both low and high power films supports the idea that increasing phosphorus concentration while providing a constant amount of energy (or R_H) necessarily

Cette thèse est accessible à l'adresse : https://theses.insa-lyon.fr/publication/2023ISAL0014/these.pdf
© [A. Wilson], [2023], INSA Lyon, tous droits réservés

leads to an increasing amount of amorphous phase in our layers.

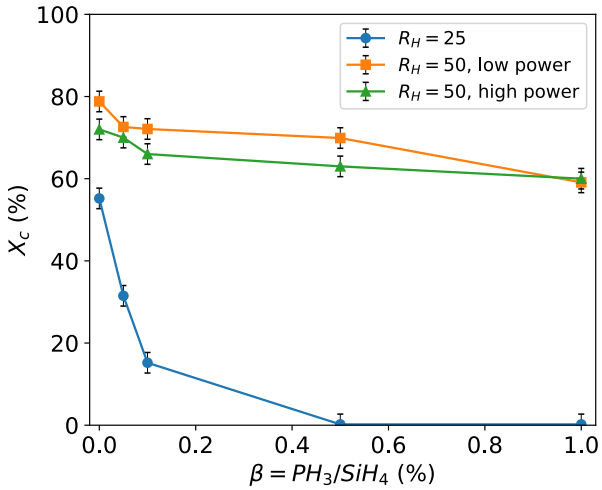

Figure 2.2: Dependence of Raman crystallinity X_c on doping level in different deposition conditions. Film thickness for R_H = 25, low power and high power samples are 160 nm, 168 nm and 310 nm respectively

2.1.3 Incubation layer growth

While in doped samples, low and high power deposition conditions lead to negligible change in X_c at constant β, a strong difference in deposition rates due to the difference in applied power between low power (2.7 nm.min^{-1}) and high power (5.2 nm.min^{-1}) films was noticed. The deposition rate was unaffected by the doping gas ratio. Incubation layer thickness (see chapter 1, section 3.1.5) in both these conditions was studied by depositing 6 layers of increasing thickness on glass substrates while keeping β constant at 0.1%. The impact of doped layer thickness on X_c is shown in Figure 2.3a. Layer thickness was estimated based on the deposition rate obtained via SEM images on thicker samples.

Our measurements show a sharp transition from amorphous to crystalline phase when the low power layer exceeds 35 nm. In high power conditions however crystalline phase is detected in small amounts even for the thinnest layer and increases steadily with film thickness.

In order to verify the region near the substrate remained amorphous even when increasing the thickness of the film Raman spectra were measured on both the frontside and backside of the thicker films. The backside measurements were taken through the glass substrate and its contribution to the spectrum was corrected by subtracting the spectrum of a pristine glass substrate. The optical scattering depth at the excitation wavelength (λ_{exc} = 473 nm) is of the order of α^{-1}, i.e., 35 nm for a-Si:H and 160 nm for µc-Si:H. For thick samples, probing of the layer through Raman scattering is thus sensitive to the chosen side for optical excitation. Figure 2.3b shows the normalized Raman spectra in both cases, for the low power and high power $\beta = 0.1\%$ samples (168 nm and 310 nm respectively). The broadening of the spectrum towards the amorphous region (~ 480 cm^{-1}) supports the existence of an amorphous phase located close to the substrate/film interface. For the low power sample, calculation of X_c yields a value of 67 % from the frontside and 55 % from the backside, while the high power sample yields X_c = 72 % and 57 % from the frontside and backside, respectively. Although

Cette thèse est accessible à l'adresse : https://theses.insa-lyon.fr/publication/2023ISAL0014/these.pdf
© [A. Wilson], [2023], INSA Lyon, tous droits réservés

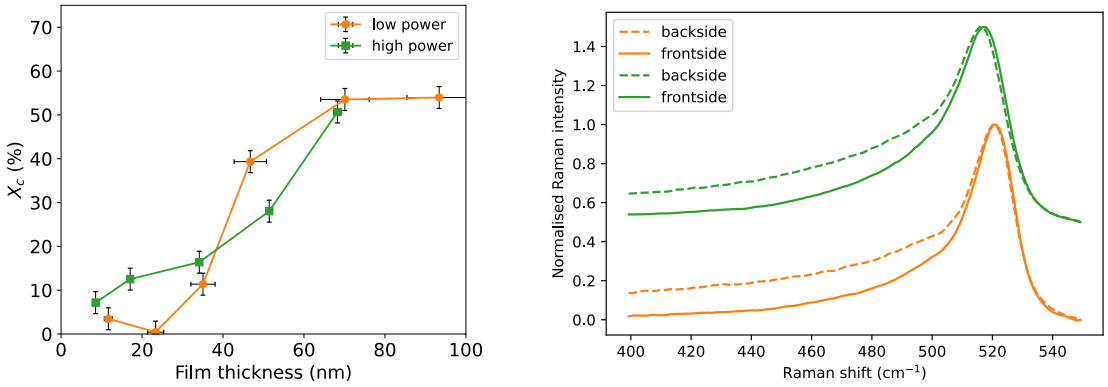

(a) (b)

Figure 2.3: (a) Dependence of Raman crystallinity X_c on deposited film thickness for $\beta = 0.1\%$ (b) Frontside and backside Raman spectra of low and high power deposited films. The noticeable increase in signal intensity in the amorphous region (480 cm^{-1}) reveals the presence of an amorphous phase at the interface with the substrate.

Raman spectroscopy does not provide an estimation of the incubation layer thickness, it supports the model of a thin amorphous layer at the film/substrate interface.

Further results were obtained by AFM measurement of the same films, deposited on c-Si (Figure 2.4). While a-Si:H deposition leads to films with little roughness as shown by Collins et al. [152] and Abelson et al.[153], µc-Si:H growth is in part recognizable due to its *cauliflower-like* surface topography which emerges from the growth of the microcrystalline phase (chapter 1, figure 5.3b). This marked increase in roughness due to the presence of a crystalline phase has been described by Vallat-Sauvain et al. [132] and Matsuda [43] in hydrogenated microcrystalline Silicon and Jordan et al. [154] in hydrogenated microcrystalline Germanium thin films. In low power conditions crystalline nodules totally cover the surface in the 46 nm thin sample while the 26 nm layer shows no sign of crystalline phase. Such a change in surface topology supports our Raman spectroscopy observations regarding the sharpness of the amorphous to crystalline transition (Figure 2.3a). In high power conditions AFM imaging confirms the existence of sparsely distributed crystalline nodules in the 17 nm and 34 nm thin samples.

With the observed differences in the evolution of X_c with film thickness in both conditions as displayed in Figure 2.3 emerges the question of preferable deposition conditions. As crystalline phase is favorable for electronic transport as well as doping, one could argue the low power conditions are to be favored as they yield a higher doping level and a higher X_c for thick films. However, when looking at thinner films high power conditions will lead to a partially crystalline layer, where low power conditions are fully amorphous. Depending on the desired thickness either set of deposition conditions may be preferred. The backside Raman scattering experiment reveals the region close to the substrate stays partially amorphous even with increasing thickness. The extent of that incubation layer is known to be less than the 35 nm necessary to the phase transition in low power conditions (Figure 2.3a).

It must be pointed out that thinner amorphous incubation layers have been obtained for µc-Si:H by using a two step, layer by layer process.[50, 150, 155] However these layers where undoped and as seen in Figure 2.1 the addition of phosphine to the gas mixture prevents

Cette thèse est accessible à l'adresse : https://theses.insa-lyon.fr/publication/2023ISAL0014/these.pdf
© [A. Wilson], [2023], INSA Lyon, tous droits réservés

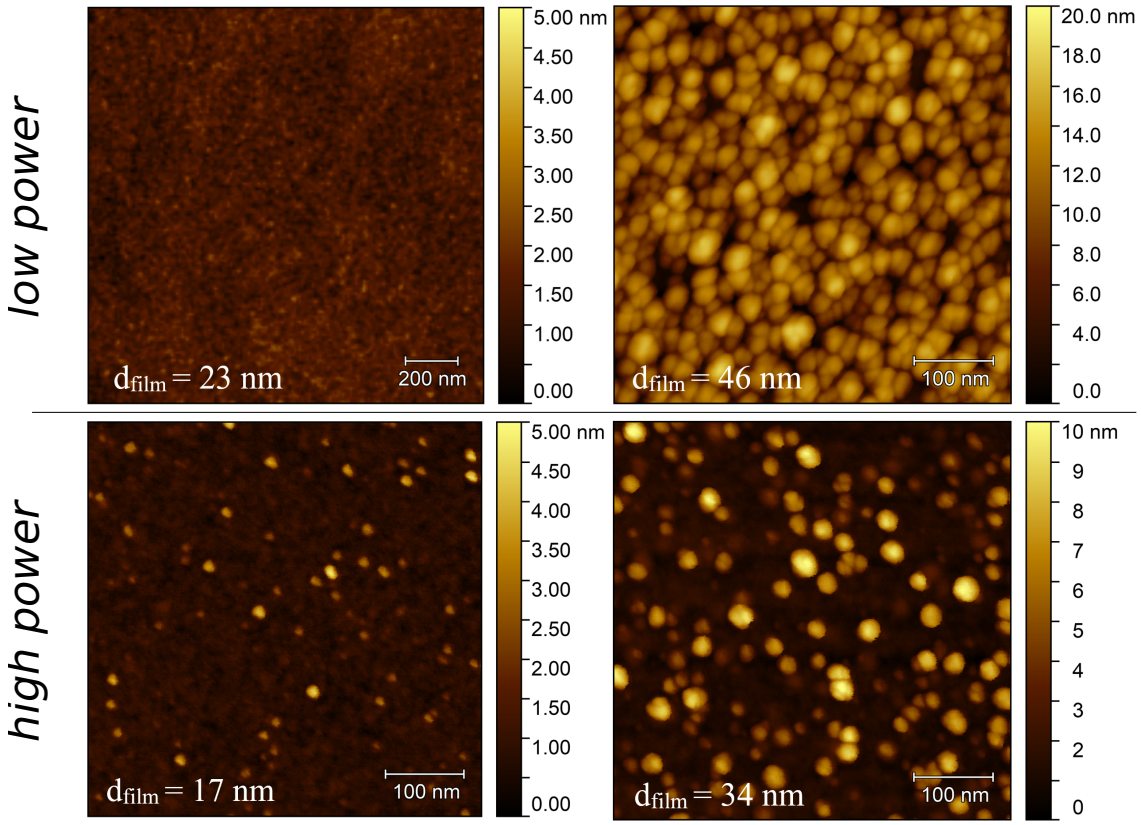

Figure 2.4: AFM surface image of *low power* (top) and *high power* (bottom) deposited films for two samples of increasing film thickness.

crystalline phase nucleation. Thinner incubation layers may also be obtained by further increasing the hydrogen dilution factor R_H, at the cost of a lower deposition rate. The importance of the nature of the substrate must also be mentioned as our Raman spectroscopy measurement cannot be conducted for µc-Si:H films deposited on c-Si. However, similarly to epitaxial growth techniques, the emergence of a crystalline order is favored in presence of an ordered interface. Hence we expect to obtain higher X_c as well as thinner incubation layers for materials deposited on crystalline substrates.

2.1.4 Electrical properties of P doped µc-Si:H layers

Total and active dopant concentration

Electrical properties of our films were measured using a Hall effect setup and chemical composition in terms of absolute phosphorus concentration in the film was measured by SIMS in the entire depth of the films and was found to be homogeneously distributed. Results are shown in figure 2.5a and table 4.2.

High doping levels are achieved with $active\,[P] = n > 10^{20}\text{cm}^{-3}$ for the most doped µc-Si:H layers, with a higher [P] for low power samples. In both set of samples and for the whole range of doping investigated the activation rate of incorporated dopant atoms, i.e. the $active\,[P]\,/\,[P]_{SIMS}$, is over 30 %. It is encouraging considering that µc-Si:H contains numerous structural defects when compared to its mono-crystalline counterpart. At equivalent phosphine level β, our sample exhibit a doping level two orders of magnitude greater than what

Cette thèse est accessible à l'adresse : https://theses.insa-lyon.fr/publication/2023ISAL0014/these.pdf
© [A. Wilson], [2023], INSA Lyon, tous droits réservés

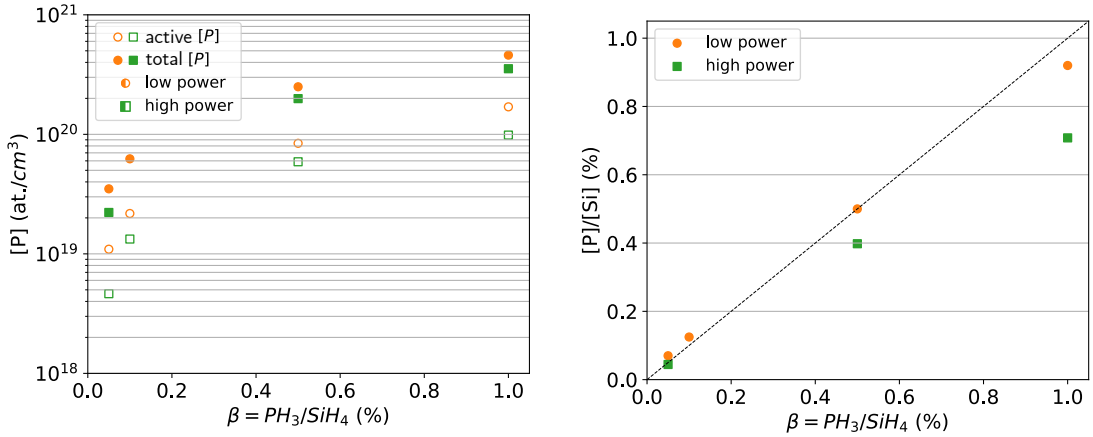

(a) (b)

Figure 2.5: (a) Phosphorus concentration in the deposited films measured by ToF-SIMS , and active P concentration determined by Hall effect, as a function of the phosphine to silane ratio in the PECVD chamber (b) Solid phase phosphorus concentration as a function of gas phase phosphine to silane ratio, the dashed line corresponds to a 1:1 ratio between [P]/[Si] and β

was reported by Wei et al.[151] while Backhausen et al.[156] have reached similar doping levels with β = 2 %. An excess in defects or segregation of phosphorus to grain boundaries would have led to a lower activation rate and thus made it impossible to reach these high doping levels. The detailed values of conductivity σ, mobility μ_H and doping levels n obtained by Hall effect measurement are reported in Table 4.2. The uncertainty is less than 0.1 % for σ and less than 5% for n and μ_H.

Figure 2.5b reveals almost no preferential incorporation of phosphorus in the film compared to silicon. In the studied range, the [P]/[Si] ratio is linearly dependent on the dopant gas flow ratio β with a slight preference for P incorporation in low power ($r = [P]/(\beta \cdot [Si]) =$ 0.94) over high power (r = 0.73) conditions. Such behavior can be explained in terms of bond dissociation energy of Si-H and P-H bonds, as both values are close $\mathrm{E_D(P-H)} = 3.55\,\mathrm{eV} > \mathrm{E_D(Si-H)} = 3$

	low power			*high power*		
β	σ [S·cm^{-1}]	μ_H [cm^2·V^{-1}·s^{-1}]	n_{active} [cm^{-3}]	σ [S·cm^{-1}]	μ_H [cm^2·V^{-1}·s^{-1}]	n_{active} [cm^{-3}]
0.05 %	1.078	0.615	-1.09E+19	0.338	0.454	-4.64E+18
0.10 %	2.195	0.630	-2.18E+19	0.812	0.385	-1.33E+19
0.50 %	8.772	0.651	-8.41E+19	5.690	0.602	-5.90E+19
1.00 %	13.218	0.487	-1.70E+20	9.512	0.602	-9.86E+19

Table 4.2: Hall effect measurement of conductivity (σ), mobility (μ_H) and doping level at room temperature in the Van Der Pauw configuration.

Limitations of Hall effect measurements

Raman scattering experiments provide a depth-averaged information on X_c. However the thick samples (168 nm and 310 nm, for low and high power deposited films, respectively)

Cette thèse est accessible à l'adresse : https://theses.insa-lyon.fr/publication/2023ISAL0014/these.pdf
© [A. Wilson], [2023], INSA Lyon, tous droits réservés

used for Hall effect measurements were analyzed considering the assumption of a homogeneous and isotropic material. In these layers, the amorphous incubation layer may act as a high resistance in parallel to the low resistance microcrystalline layer. As the calculation for the doping level involve film thickness, an under estimation of the effective doping level, and consequently of the activation rate of the crystalline phase is likely. A rough estimation of the order of magnitude of the error committed on doping level measurement can be performed considering the layer is mainly amorphous for the initial 30 nm deposited (Figure 2.3a). The doping level could be underestimated by 18 % and 10 % in low and high power conditions, respectively.

2.1.5 Discussion: Phosphorus doping of Si:H

PECVD conditions suited for deposition of phosphorus highly doped microcrystalline silicon were found. Tendency of P doped µc-Si:H to undergo a crystalline to amorphous transition was prevented by increasing Hydrogen dilution from R_H = 25 to 50, leading to a decrease in deposition rate. In such conditions, AFM and Raman crystallinity measurements revealed that a high power (100 W) and high pressure (1 Torr) regime leads to a more continuous nucleation of crystallites with film thickness contrary to the low power regime (30 W, 0.8 Torr) which grows as an amorphous layer for the first 23 nm before crystalline phase nucleation. Without a fully amorphous incubation layer, high power conditions could be better suited for electrical contact layers in PIN junctions. SIMS and Hall effect measurements show that lower power and pressure (30 W, 800 mTorr) conditions leads to a 20 % higher Phosphorus incorporation in the film from the plasma. However activation rate of incorporated phosphorus does not depend on the deposition conditions chosen and n-type doping levels reaching $1.7 \times 10^{20}\,\mathrm{cm}^{-3}$ was obtained. These newly developed layers were put to use in our prototype structures described in chapter 5. However, Phosphorus doping of µc-Si:H is known to be easier to obtain than its counterpart, i.e. p-type Boron doped µc-Si:H.

2.2 p-type µc-Si:H

The acquired know-how on n-type µc-Si:H growth described in subsection 2.1 has to be completed with p-type µc-Si:H in our goal to produce N-I-P semiconductor stacked layers. In order to obtain Boron-doped Silicon, identical deposition conditions to those used for *low power* deposition of Phosphorus doped µc-Si:H were used (see table 4.1). The dopant gaseous precursor PH_3 was replaced with B_2H_6 (diluted at 1000 ppm in H_2) at a concentration $\beta = B_2H_6/SiH_4$ in the 0.05 % to 0.5 % range.

2.2.1 Structural and electrical study of Boron-doped µc-Si:H

The Raman spectra obtained for each sample are shown in figure 2.6 together with the calculated values for X_c as a function of doping gas ratio β. Unlike n-type µc-Si:H deposited in similar conditions, the layer's micro-structure was found to be strongly affected by Boron incorporation as the deposited layer went from a highly crystallized material ($X_c = 78\,\%$) to a completely amorphous one above $\beta = 0.3\,\%$. This continuous degradation of structural properties with increasing diborane flow has been observed by other groups [146, 158] and was interpreted as a consequence of the local disorder induced by bond length fluctuation. It has also been reported [159] that boron tends to form boron-hydrogen-silicon complex in <p> µc-Si:H which may further add to the local disorder of the material, preventing crystalline phase nucleation.

Cette thèse est accessible à l'adresse : https://theses.insa-lyon.fr/publication/2023ISAL0014/these.pdf
© [A. Wilson], [2023], INSA Lyon, tous droits réservés

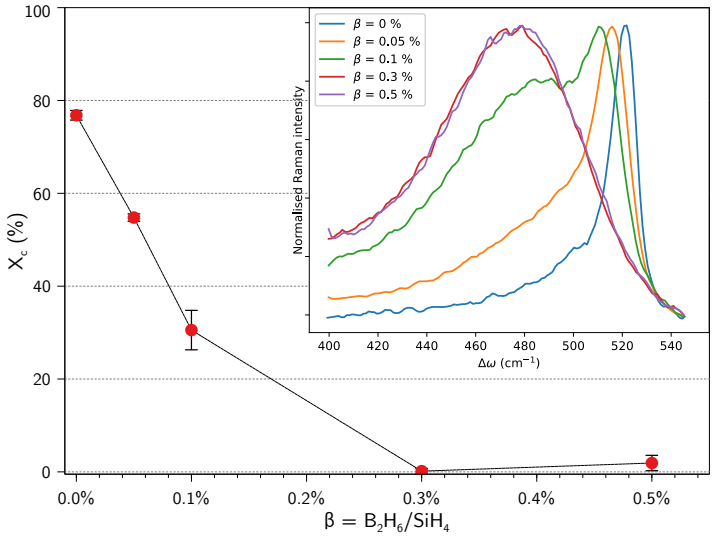

Figure 2.6: Normalized Raman spectra and calculated Raman crystallinity X_c of Boron-doped µc-Si:H for different doping gas ratios β, ranging from 0 % to 0.5 %. The data shows the degradation of the crystalline structure with increasing B_2H_6 concentration.

Similarly, active dopant concentration p was measured by Hall effect as a function of gas phase diborane concentration. The measured doping levels achieved decrease with β despite adding boron to the plasma. The clear correlation between p and the previously measured X_c would seem to imply the loss in active doping level was mostly due to the segregation of boron in the amorphous phase. The layer obtained with the lowest β gave the best results in terms of doping with $p = 3.39 \times 10^{18}$ cm^{-3} while maintaining a relatively high X_c. The plasma-to-film incorporation ratio is however lower ($p/\beta \approx 12\,\%$) than the one observed for <n> µc-Si:H ($n/\beta \approx 30\,\%$) and the maximum doping level remains much lower than n obtained for phosphorus doped µc-Si:H ($n = 1.7 \times 10^{20}$ cm^{-3}).

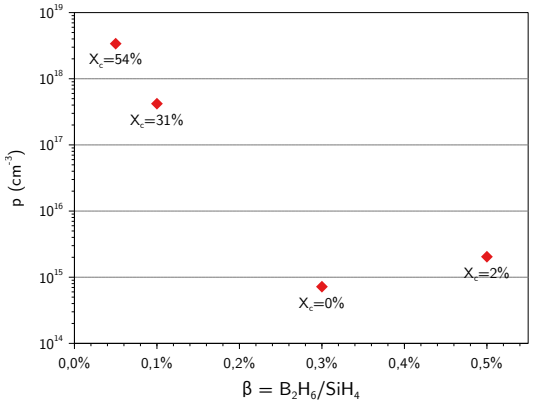

Figure 2.7: Active p-type doping level of Si:H measured by Hall effect as a function of doping gas ratio β.

When working at a high B_2H_6 gas flow, the material became notoriously defective, experiencing severe blistering and dramatic increase in surface roughness. The issue was found to mostly occurs when growing the layers on c-Si substrates. This surface degradation was

Cette thèse est accessible à l'adresse : https://theses.insa-lyon.fr/publication/2023ISAL0014/these.pdf
© [A. Wilson], [2023], INSA Lyon, tous droits réservés

found to be minimal at low-dopant levels ($\beta = 0.05\,\%$) as can be seen in figure 2.8 where Nomarski interference contrast (NIC) microscopy images of two samples highlight the difference in surface roughness seen at the microscopic scale. The much brighter image obtained for the highly doped sample is a consequence of increased irregularity in the z-axis to which NIC microscopy is very sensitive.

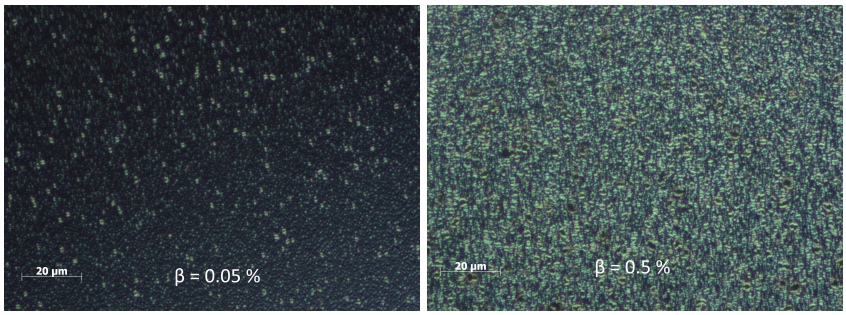

Figure 2.8: Nomarski interference contrast microscopy images of Boron doped µc-Si:H deposited on c-Si show a marked increase in roughness for the highest β values (right).

Looking at the $\beta = 0.5\,\%$ sample at higher magnification with SEM imaging (figure 2.9), it was noticed the film was completely defective with a non-uniform layer including craters and lumps as well as pronounced nano-scale blistering at the µc-Si:H/c-Si interface. While the origin of the inhomogeneity is still unknown, blistering has been described in the past for other PECVD deposited layers [160, 161] and have been attributed to excessive hydrogen desorption at the substrate/film interface, notably during annealing of a-Si:H or silicon nitride at temperatures near 400 °C. The relatively low temperature used during our process (250 °C) may not be sufficient to explain the amount of blistering observed. Since this phenomenon is correlated with diborane injection in the chamber, it would seem boron prevents hydrogen from incorporating uniformly in the layer, causing pockets of hydrogen to form until blisters crack the interface. This mechanism remains a hypothesis so far. As this behavior was not found at low dopant gas flow nor on glass substrates, no further optimization was performed.

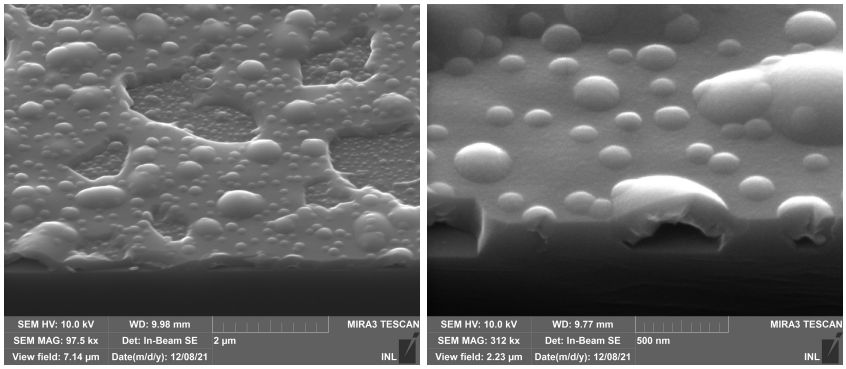

Figure 2.9: SEM image of <p> µc-Si:H deposited at high diborane gas flow ($\beta = 0.5\,\%$) on c-Si substrate and taken at a 45° angle. The severe lack of uniformity of the layer and blisters may in part be due to hydrogen desorption.

Cette thèse est accessible à l'adresse : https://theses.insa-lyon.fr/publication/2023ISAL0014/these.pdf
© [A. Wilson], [2023], INSA Lyon, tous droits réservés

2.2.2 Discussion: Boron doping of Si:H

Boron doping of Si:H is notoriously difficult to obtain, even with a dilution factor as high as $R_H = 50$. The maximum doping level obtain was $p = 3.39 \times 10^{18}\,\mathrm{cm}^{-3}$ which is considerably lower than phosphorus doped µc-Si:H and could limit the electric field extending into the intrinsic absorber of a P-I-N photodiode architecture. Further hydrogen dilution could be a solution to prevent amorphization of the layer at higher β in exchange for lower growth rates. In the context of our work, the active doping level p achieved with $\beta = 0.05\,\%$ is still a viable although not ideal option.

When looking at this issue from the perspective of a photodiode, if the p-type layer is located on the backside of the photodiode, having a high band-gap window layer is not necessary. A boron doped Ge:H or SiGe:H layer could be used providing higher doping levels can be achieved.

3 *In situ* doping of µc-Ge:H

Amorphization of microcrystalline Silicon layer with dopant incorporation has been shown to be an issue no matter the doping type (see figure 2.2 and 2.6 from the previous section). In the case of Phosphorus doping an increase in hydrogen dilution was enough to maintain good crystalline quality. On the other side, Boron doping led to a rapid amorphization at equivalent deposition conditions.

3.1 Boron-doped µc-Ge:H

Looking at p-type semiconductor materials an alternative to p-type µc-Si:H could then be to use µc-Ge:H. The main drawback is the low band gap and high absorption coefficient α of the material described in chapter 3, subsection 2. The use of <p> µc-Ge:H layers could however be beneficial if the stronger absorption of NIR wavelength is compensated by a better doping level leading to a greater electric field in the absorber (see section 1). NIR light absorption could then be kept at a minimum by depositing a ultra-thin layer for the p-type layer.

β	Temperature [°C]	Pressure [mTorr]	Power [W]	$t_{deposition}$ [min]	Thickness[1] [nm]	R_H	Φ_{GeH4} (5%) [sccm]	Φ_{B2H6} (1000 ppm) [sccm]	Φ_{H2} [sccm]
0 %	250	1000	100	90	495	100	70	0	280
1 %	250	1000	100	60	170 ± 10	200	40	20	340
2.5 %	250	1000	100	60	170 ± 10	200	40	50	310
5 %	250	1000	100	60	170 ± 10	200	40	100	260

Table 4.3: PECVD deposition conditions for boron-doped µc-Ge:H layers. Samples were deposited on c-Si and glass substrates.

Similarly to µc-Si:H, B_2H_6 diluted at 1000 ppm was added to the gas mixture commonly used to obtain highly microcrystalline Ge:H layers as described in subsection 2. The doping gas to precursor ratio β is in that case defined as the ratio between the pure gas flow of diborane B_2H_6 and germane GeH_4. As relatively low activation ratios were found for p-type µc-Si:H, β was chosen in the range for 0 % to 5 %. Deposition conditions for the material can be found in table 4.3.

[1] obtained from SEM cross-section images, see figure 3.1

Cette thèse est accessible à l'adresse : https://theses.insa-lyon.fr/publication/2023ISAL0014/these.pdf
© [A. Wilson], [2023], INSA Lyon, tous droits réservés

3.1.1 Structural stability of p-type µc-Ge:H

Raman crystallinity was measured for each sample, results shown in figure 3.2 together with corresponding Raman spectra (figure 3.2b). Evidence for the microcrystalline nature of the film ($X_c \approx 63\,\%$) which does not seem to depend on β was found in the tested range. The intrinsic layer was found to have a similar X_c despite being deposited at lower R_H. It is however difficult to comment on this result as film thickness is not comparable (see table 4.3).

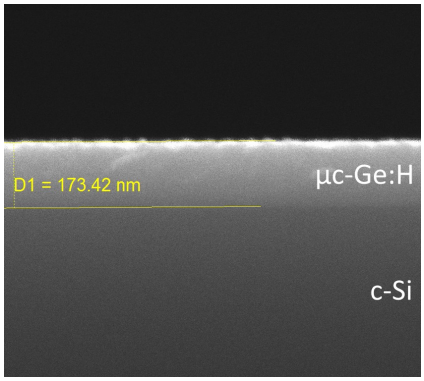

Figure 3.1: SEM cross-sectional image of Boron doped µc-Ge:H deposited on c-Si.

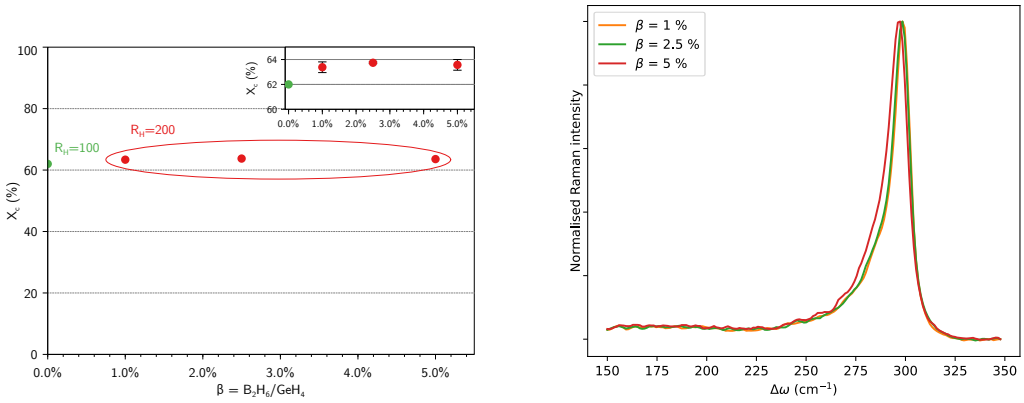

(a) (b)

Figure 3.2: Raman crystallinity X_c (a) and Raman spectra (b) obtained for Boron doped µc-Ge:H thin films on glass.

Although high active doping levels were attained, the p/β ratio obtained is actually as low as 5 %. That is, electrically active Boron is found at $1/40^{th}$ [2] of the Boron / Germanium ratio in the gas mixture. Further SIMS analysis of the samples would be needed to establish whether diborane is simply not well dissociated in the plasma or if incorporated Boron has a low activation rate. In n-type µc-Si:H (see 2.1.4), SIMS measurement showed an incorporation rate of Phosphorus atoms close to 70-90 % with a 0.47 eV difference in dissociation energies. Bond dissociation energies for diborane $D_0(B_2H_5 - H) = 4.35$ eV[162] and for germane $D_0(GeH_3 - H) = 3.6$ eV[163] are significantly different (0.75 eV) but may not justify the low p/β ratio on

[2] since diborane brings two B atoms per molecule.

Cette thèse est accessible à l'adresse : https://theses.insa-lyon.fr/publication/2023ISAL0014/these.pdf
© [A. Wilson], [2023], INSA Lyon, tous droits réservés

its own.

3.1.2 Electrical characterization of p-type µc-Ge:H

Conductivity σ, active doping concentration p and Hall mobility μ_H were obtained by Hall effect measurements at room temperature with 170 nm thick layers deposited on glass. Liquid InGa was used to obtain ohmic contact with the semiconductor layer. Intrinsic µc-Ge:H ($\beta = 0\,\%$) was found to have a relatively high background p-type doping level ($1.6 \times 10^{17}\,\mathrm{cm}^{-3}$) which may be correlated to the high dark currents and low photo-response found in chapter 3, section 2. This background doping may come from *in-situ* contamination during deposition (from previous deposition process involving Phosphorus) or be a direct consequence of large the band tails of µc-Ge:H. It is unlikely this feature comes from exposure to oxygen as an n-type doping would have been expected.

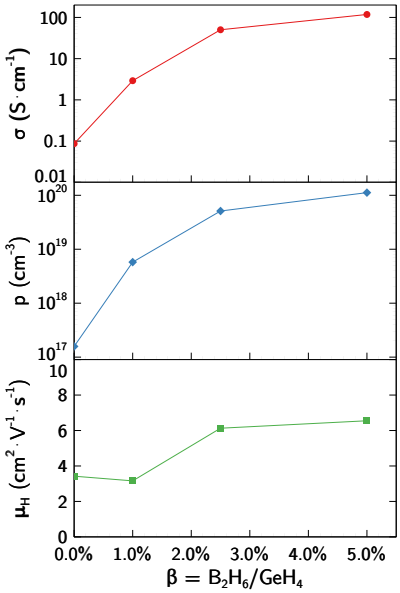

Figure 3.3: Conductivity and mobility measurement by Hall effect of Boron doped µc-Ge:H, solid lines are a guide for the eye.

Doping, conductivity and mobility are plotted in figure 3.3. The conductivity σ increases from $0.086\,\mathrm{S}\cdot\mathrm{cm}^{-1}$ up to $118\,\mathrm{S}\cdot\mathrm{cm}^{-1}$ with diborane addition, which is mainly related to increase in p since μ_H barely varies on the studied range and stays in the order of 3 to $6\,\mathrm{cm}^2/\mathrm{V}\cdot\mathrm{s}$. Interestingly, μ_H increases with β and thus with doping level, as opposed to the usual behavior found in crystalline semiconductors such as Silicon [128]. This result can be interpreted as a decrease in grain-boundary potential barrier height which exists due to trap states, such as previously reported by Kamins and Weis. [164, 165] in the case of Phosphorus doped µc-Si:H. The most interesting result regarding our objective is that p-type doping as high as $p = 1.12 \times 10^{20}\,\mathrm{cm}^{-3}$ was achieved. Compared to the maximum doping level of $3.4 \times 10^{18}\,\mathrm{cm}^{-3}$ obtained for <p> µc-Si:H, boron doping of µc-Ge:H seems quite promising. Indeed, µc-Ge:H films were able to maintain their structural properties despite high diborane gas flow.

Cette thèse est accessible à l'adresse : https://theses.insa-lyon.fr/publication/2023ISAL0014/these.pdf
© [A. Wilson], [2023], INSA Lyon, tous droits réservés

3.1.3 Discussion: Boron doping of Ge:H

In this section it was demonstrated highly microcrystalline Germanium could be obtained while heavily doping the material *in-situ*. Addition of diborane $B_2H_6$to a germane / hydrogen mixture can easily produce p-type semiconductor layers with doping levels reaching over $10^{20}\,cm^{-3}$. No clear impact of Boron's incorporation on the structural properties of the film were found in the studied range, being however limited to by the maximum diborane gas flow rate of 100 sccm. Activation rate of Boron atoms incorporated in the film is believed to be extremely low and may induce unwanted defects states impacting carrier diffusion lengths. Since µc-Ge:H was previously shown to have poor electrical properties (chapter 3, section 3.1.2), replacing p-type µc-Si:H by p-type µc-Ge:H may only be feasible if a sufficiently thin crystalline layer can be obtained so as to limit unwanted absorption and recombination in the Boron-doped part of the P-I-N junction.

4 Conclusion

In this chapter we aimed at developing PECVD-grown n and p-type semiconductor layer for future P-I-N photodiode prototypes. Obtaining thin microcrystalline layers with high doping levels was a key objective to improve both the optical and electrical performances of future devices. An optically thin layer is needed to minimize parasitic absorption in the NIR spectral range while high doping levels has a direct impact on the electrical field in the absorber layer.

In the first section of the chapter, it was showed that Phosphorus prevented the nucleation of crystallites and led to amorphous layers. Adapting the deposition conditions to a high dilution factor R_H helped maintain high crystallinity and reach doping levels $n > 10^{20}\,cm^{-3}$. Boron doping of µc-Si:H was implemented using the same approach but led to a rapid amorphization of the layer with increasing Boron precursor in the gas phase. At low diborane gas flow crystalline layer could however still be obtained, at the cost of doping levels only reaching up to $p = 3.4 \times 10^{18}\,cm^{-3}$.

The drawbacks of p-type µc-Si:H led us to explore another option in the second section : Boron doped µc-Ge:H. Adding diborane to a germane / hydrogen mixture did not significantly affect the crystallinity of the deposited films. While X_c was kept mostly constant (~63 %), Boron incorporation into the layer increased conductivity by 3 decades, with a maximum doping level $p = 1.1 \times 10^{20}\,cm^{-3}$. The main drawback of this material are the low incorporation and activation rates of Boron, which could translate into an increase in electrical defects. The high absorption coefficient of µc-Ge:H (see chapter 3, subsection 2.2) in the visible and NIR spectral range implies <p> µc-Ge:H should only be used as a very thin layer on the backside of the device.

This study of 3 separate materials mostly focused on structural integrity and doping efficiency of our process. Future potential improvements could include band-diagram engineering aspects as well as work function compatibility. One could indeed fine tune the doping and chemical composition of the p/n layers in order to obtain effective hole or electron selective contacts. These aspects would however require to consider the device as a whole in order to optimize each layer with respect to each other. In the final chapter, focus will be put on taking all three building bricks for our photodiode prototype, i.e. the p-type layer, the absorber and the n-type layer, and designing a working device.

Cette thèse est accessible à l'adresse : https://theses.insa-lyon.fr/publication/2023ISAL0014/these.pdf
© [A. Wilson], [2023], INSA Lyon, tous droits réservés

Key Points

Contributions

- ❏ RF-Power was found to influence Phosphorus incorporation in µc-Si:H
- ❏ Boron doping of µc-Si:H leads to a rapid amorphization of the film
- ❏ At high R_H, µc-Ge:H film can be doped with B_2H_6 without degrading structural properties

Take away message

- ❏ Under appropriate conditions, n-type doping of µc-Si:H as high as 1.7×10^{20} cm^{-3} was obtained
- ❏ p-type µc-Si:H doping level did not exceed 3.4×10^{18} cm^{-3} due to amorphization issues
- ❏ High p-type doping level (1.1×10^{20} cm^{-3}) was reached with µc-Ge:H
- ❏ For the doped material to act as a window layer, the absorption of the doped layer should be kept as low as possible

Cette thèse est accessible à l'adresse : https://theses.insa-lyon.fr/publication/2023ISAL0014/these.pdf
© [A. Wilson], [2023], INSA Lyon, tous droits réservés

Chapter 5

Design, Fabrication and Characterization of Photodiode Prototypes

In this final chapter our approach will shift from optimizing individual materials to building a simple photosensitive device. Some aspects of our prototype deemed too far from the scope of our work on microcrystalline semiconductors will not be deeply investigated. Considerations such as band diagram engineering or anti-reflective coating design will thus be left aside.

The three main building blocks of our P-I-N photodiode prototype were individually developed in the previous chapters. Phosphorus and boron doping of µc-Si:H and µc-Ge:H for the N and P layers was addressed in chapter 4 while it was found in chapter 3 that the intrinsic (I) absorber layer should be based on µc-SiGe:H alloys.

1 Prototype design and fabrication

The choices made regarding the design for the prototype will be discussed in this section. The proposed structure is a result of a compromise between opto-electronic performance, production easiness and equipment availability in the lab. A process flow for device production will be detailed and later used for prototype fabrication.

1.1 Prototype design

Several constraints have to be taken into consideration when conceiving the prototype's geometry. These constraints fall into three main categories: robustness, process compatibility and complexity. After some trials the design shown in figure 1.1 was selected. It consists of an ITO coated substrate on which n, i and p-type semiconductor layers are deposited to form the photosensitive part of the device. A central trench is left undeposited for the cathode to be formed directly on the ITO. The 8 anodes are placed on top of the p-type layer. With this architecture, the light has to go through the glass substrate and the ITO to reach the PIN photodiode. This structure could be improved as no surface passivation layer was used.

Such a sample is 20 mm in length, 15 mm in width and 1.1 mm in thickness. It is obtained by a 3 steps lithography-free process schematized in figure 1.2. The selection of the different

Cette thèse est accessible à l'adresse : https://theses.insa-lyon.fr/publication/2023ISAL0014/these.pdf
© [A. Wilson], [2023], INSA Lyon, tous droits réservés

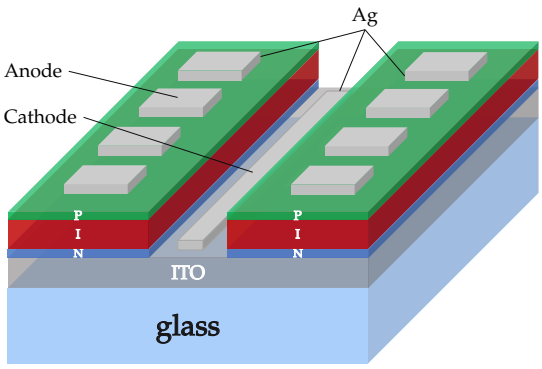

Figure 1.1: Schematic representation of the proposed prototype design for P-I-N photodiodes. Each sample holds 8 electrical contacts defining 8 independent photodiodes.

materials for the device is detailed in the following subsections. This particular structure and process have some key advantages with respect to the constraints defined above, at the cost of a few drawbacks.

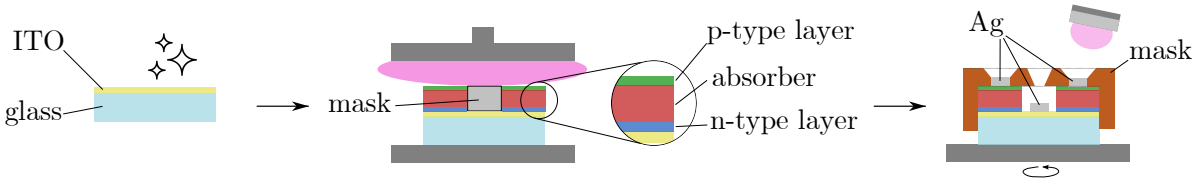

(a) ITO Cleaning

(b) PECVD deposition of N-I-P junction

(c) Sputtering of Silver Contacts

Figure 1.2: Prototype device production process (a) the ITO coated glass is cleaned - see 1.2 (b) the N, I and P parts of the diode are deposition by PECVD with a central mask in order to have access to ITO - see 1.3 (c) Sputtering of metallic anode and cathode by using a 3D printed mask - see 1.4.

Robustness

First and foremost, we need our prototype to have built in redundancy, meaning every sample should contain more than one photodiode in case one of them failed. Unwanted failure can occur due to surface contamination, misalignments or physical damage to part of the sample. With this possibility in mind each sample was designed to hold 8 photodiodes which could be tested independently from one another. The dimensions and spacing for each metal contact is given in figure 1.3

While it may seem obvious for top and bottom photodiodes to be electrically insulated from one another, neighboring cathodes are not separated by any sort of trench. Physically separating all cathodes was deemed unnecessary as the resistance value for the 2 mm gap between adjacent cathodes was found to be over 10 kΩ (due to the low thickness of the PIN layers).

Secondly, the macroscopic dimensions of our pattern for deposition leaves some space for alignment errors. Even if mask positioning is user-dependent the design allows for some variability.

Cette thèse est accessible à l'adresse : https://theses.insa-lyon.fr/publication/2023ISAL0014/these.pdf
© [A. Wilson], [2023], INSA Lyon, tous droits réservés

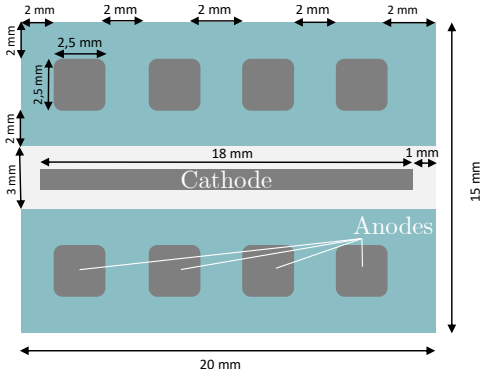

Figure 1.3: Schematic top view of the pattern dimensions defined by mask placement during deposition. The measurements given here correspond to the ideal result.

Process compatibility

In agreement with the general context of this project, the proposed design complies with the CMOS above-IC constraints regarding low temperature processes. [10, 11, 166] Since these constraints are encountered for above-IC image sensor production we need to take them into account for our proof of concept to be valid.

With the design proposed in figure 1.1 only two deposition techniques are used, namely PECVD and sputtering, working at 250°C and ambient temperature respectively.

Complexity

Last but not least, the complexity of the proposed design is minimal. It is achieved by locating all the contacts on the same side of the substrate and by avoiding any etching or lithography steps. Indeed, the masks used for sample production can be directly inserted into the deposition chamber to obtain the desired pattern. This simplicity makes the production process time-efficient and makes the final device performance less dependent on intermediary steps.

1.2 Substrate and front contact selection

Glass substrate

A glass substrate was chosen as the laying ground for our device. 1.1 mm thick commercial glass slides (1.1 mm) commonly used as substrates for perovskite solar cells were chosen. Their transparency throughout the 400 to 2000 nm range (see figure 1.4) makes them an ideal material to use as the prototype's structure requires the incoming light to pass through the substrate (see 1.1). Additionally, the thickness of the substrate helped increase the sturdiness of the sample which made it easier to handle and prevented accidental breakage.

ITO thin film

The prototype design relies on the use of a transparent conductive oxyde (TCO) layer for charge transport from the n-type layer to the cathode. Indium Tin Oxyde (ITO) is a n-type degenerate semiconductor [167] widely used as a TCO in the photovoltaic industry and is thus commercially available. Glass substrate pre-coated with 100 nm of ITO developed by

Cette thèse est accessible à l'adresse : https://theses.insa-lyon.fr/publication/2023ISAL0014/these.pdf
© [A. Wilson], [2023], INSA Lyon, tous droits réservés

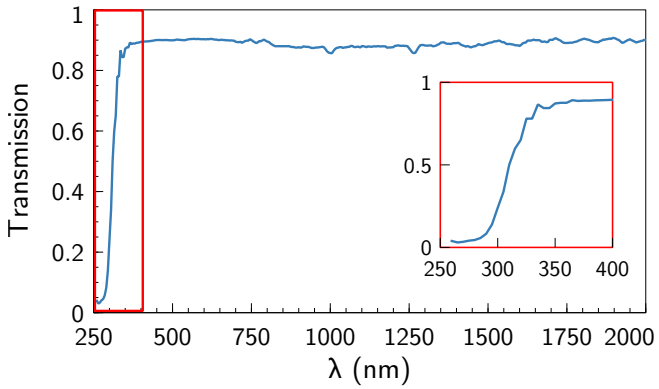

Figure 1.4: UV-NIR transmission of a 550 µm thick glass slide from OSSILA.

OSSILA[1] was thus used in order to avoid developing our own ITO deposition process. Before being used for PECVD material growth, the ITO layer is cleaned according to the process described in chapter 2, section 1.2.3.

The issue with using ITO lies in its optical properties in the NIR domain as optical properties strongly depend on electronic properties such as carrier density. In their 2013 study, Holman et al. [168] showed ITO's extinction coefficient k - and thus absorption - depends on carrier density (see figure 1.5). As carrier density and conductivity increase the film looses in transparency above $\lambda = 600$ nm and particularly above $\lambda = 900$ nm.

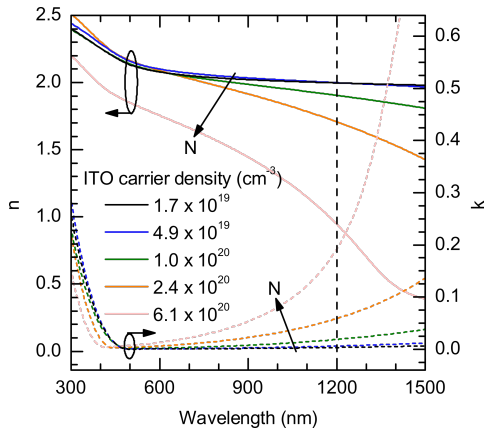

Figure 1.5: Refractive index of sputtered ITO for different carrier density values. Obtained by Holman et al. [168]

The ITO layer used for our prototype was found to have a conductivity $\sigma_{ITO} = 5500$ S.cm. Its refractive index and optical absorption were obtained from spectroscopic ellipsometry data and are shown in figure 1.6. The absorbance is naively calculated for a 100 nm free-standing ITO film with no interference from $A(\lambda) = 1 - \exp(-d_{ITO} \cdot \alpha)$ to get a sense of the losses due to this layer. The refractive index found seem to resemble those of the high carrier density ITO layer from figure 1.5. As a result, ITO absorption in the NIR range is noticeable above 800 nm and becomes extremely detrimental above 1200 nm. This is one of the major downsides of using ITO and will have to be taken into account when discussing further results, especially above the 1200 nm threshold.

[1] www.ossila.com

Cette thèse est accessible à l'adresse : https://theses.insa-lyon.fr/publication/2023ISAL0014/these.pdf
© [A. Wilson], [2023], INSA Lyon, tous droits réservés

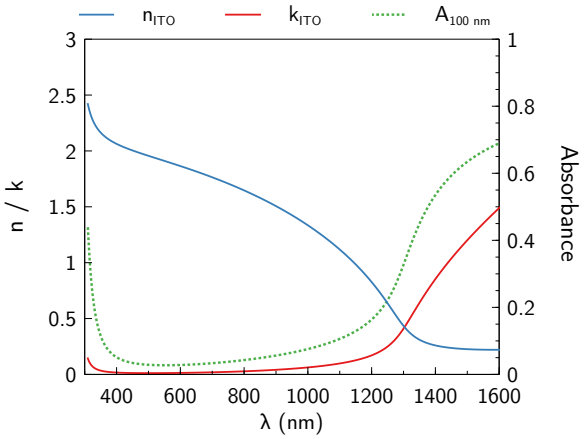

Figure 1.6: Refractive index and absorbance of a 100 nm ITO film, measured by spectroscopic ellipsometry. The absorbance is calculated from the extinction coefficient k.

1.3 N-I-P Junction

The key element of the prototype is the NIR sensitive photodiode. The n-type, intrinsic and p-type layers forming the NIP photodiode are deposited by PECVD during the same run directly on the ITO coated glass substrate. In order to later access the ITO layer for depositing the cathode a central area of 3 mm in width by 20 mm in length must be left undeposited (see figure 1.3). For that purpose, a solid reusable mask cut out of intrinsic monocrystalline silicon was placed across the substrate. After all three N, I and P layers were deposited the c-Si mask was removed to reveal the pristine ITO underneath. The scheme of figure 1.7 provides a simple illustration of the process.

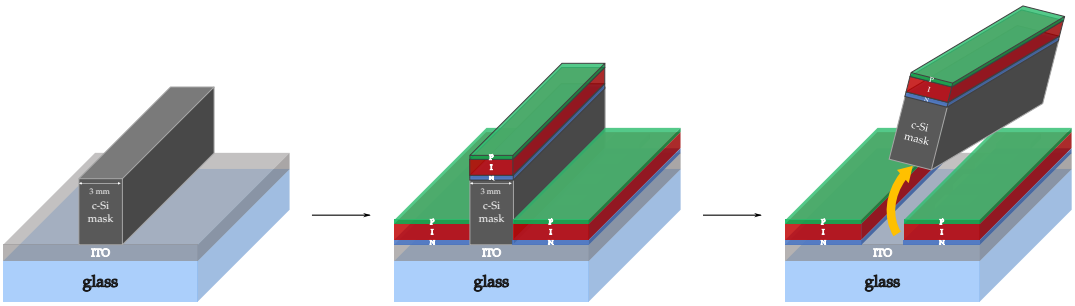

Figure 1.7: (a) The c-Si mask is placed in the center of the ITO coated glass substrate using guides. (b) N, I and P layers are deposited by PECVD. (c) The c-Si mask is removed leaving the central part of the substrate clear of any deposition. Scheme not to scale, the c-Si mask is 3 mm wide and 725 µm thick.

c-Si was selected as the material for the physical mask as it is thermally stable, does not degas and limits any risk of contamination. Metallic masks were avoided due to their tendency to interact strongly with the plasma and locally change the electric field. The thickness of the c-Si mask (725 µm) did create a thickness gradient near its edges. However the gradient did not extend to the photodiode area defined by the anode contacts seen in figure 1.1.

Due to the choice of substrate, the NIP junction is deposited in the following order :

Cette thèse est accessible à l'adresse : https://theses.insa-lyon.fr/publication/2023ISAL0014/these.pdf
© [A. Wilson], [2023], INSA Lyon, tous droits réservés

1. **n-type layer** the first layer will necessarily be a phosphorus doped layer as ITO is itself a degenerate n-type semiconductor [167]. As the incoming light will have to pass through the ITO as well as the n-type layer we must chose a material with low absorption to be used as a window layer. As such phosphorus doped µc-Si:H is most commonly used as the first layer. Ideally the work functions of µc-Si:H would have to be tuned for the Fermi level of ITO and the conduction band of µc-Si:H to be aligned. This layer should be thin (less than 100 nm) and highly crystalline while growing on a polycrystalline surface (ITO) of different composition.

2. **absorber layer** the second layer is an undoped microcrystalline silicon-germanium alloy whose thickness can vary in the 100 nm to 1 µm range. Its composition can be varied to increase absorption in the spectral region of interest. Crystallization of the layer is critical to reach the desired optoelectronic properties and should be helped by the previous microcrystalline layer. In order to minimize dopant contamination of this layer several purge cycles of the chamber are performed between the n-type layer and the absorber layer deposition. However as n-type µc-Si:H is deposited on the reactor walls any ion bombardment occurring during this step will necessarily bring a low amount of phosphorus to the layer, until the reactor wall are in turn coated with µc-SiGe:H. Completely cleaning the reactor would require unloading the samples, thus risking environmental contamination and increasing the complexity of mask alignment.

3. **p-type layer** the structure is completed with the deposition of the p-type layer obtained by boron doping of µc-Si:H or µc-Ge:H. Similarly to the first layer, we aim to have the thinnest possible film (less than 100 nm) to prevent parasitic absorption which would lead to electron-hole pair recombination in the doped areas.

In section 2 and 3 the focus will be set on tuning the thickness, composition and deposition conditions of those three layers in our device.

1.4 Back contact selection

The anodes and cathode of the prototype are deposited in the last step of the production process (figure 1.2). Silver was found to have good ohmic contact with both µc-Si:H and µc-Ge:H no matter the doping type. Additionally, silver is highly reflective in the range of interest which is crucial since it will act as a backside reflector layer, doubling the distance light travels through the absorber.

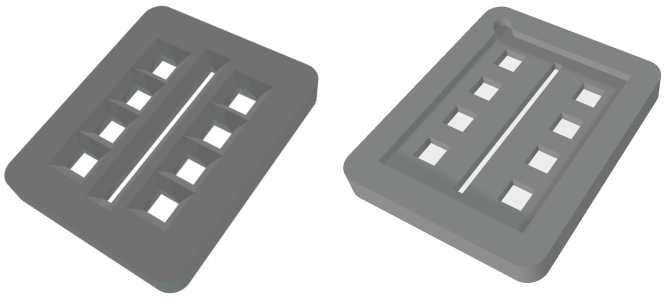

Figure 1.8: Top and bottom view of the 3D printed PLA mask design. The sample sits in the grooved out rectangle seen in the bottom view.

Cette thèse est accessible à l'adresse : https://theses.insa-lyon.fr/publication/2023ISAL0014/these.pdf
© [A. Wilson], [2023], INSA Lyon, tous droits réservés

As only thin layers (300 nm to 1 µm) are needed to complete our structure silver can be deposited by DC sputtering. We take advantage of the process which is done at room temperature to introduce the 3D-printed masks of figure 1.8 in the chamber. The central groove defines the cathode while the square openings define the anodes for each diode. The plastic masks help us implement complex patterns onto the sample's surface without using lithography. The smallest feature which can be made using this technique is of the order of 0.1 mm. Our contacts geometry (figure 1.3) allows for some margin of error, making this approach suitable for our need.

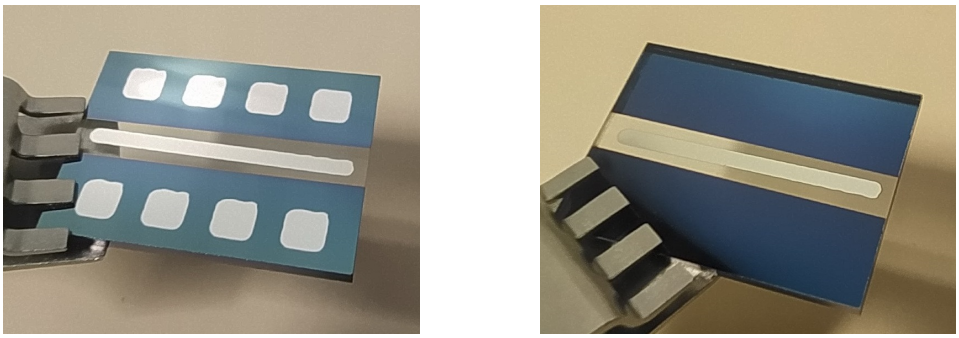

(a) (b)

Figure 1.9: Completed device (a) backside and (b) frontside view.

With this final step the sample is ready to be tested electrically and optically. The backside of the device holds both the cathode and anodes (figure 1.9a), leaving the frontside free of any metal (figure 1.9b).

1.5 Sample testing

Having backside contacts for our prototype greatly simplified the process flow. However it makes sample testing more tedious. To facilitate the electrical measurements of the numerous samples produced, a simple 3D-printed test bench (figure 1.10) was designed which simultaneously established electrical connection with all 8 anodes and the cathode.

The sample is placed in a groove which centers it on the opening window (seen in figure 1.10(b) and 1.10(c)). Nine spring-loaded metal pins held by a polymer plate are then brought in contact with the silver electrodes. Every single photodiode can then be wired to measurement tools by plugging a wire in the side connectors corresponding to the anode and cathode of the desired photodiode.

Overall, the proposed prototype photodiode design is the result of a compromise between manufacturing complexity, CMOS compatibility and device performance. In the following sections, devices produced using this original design will be tested to establish the NIR sensing performance of µc-$Si_{1-x}Ge_x$:H semiconductors thin films.

2 Influence of absorber composition on device performance

Chapter 3 has left us with pending questions regarding the opto-electronic performance of µc-SiGe:H alloys. By implementing different compositions of the alloy as the absorber layer for our previously defined structure we aim to find the optimal absorption to diffusion length compromise in real conditions.

Cette thèse est accessible à l'adresse : https://theses.insa-lyon.fr/publication/2023ISAL0014/these.pdf
© [A. Wilson], [2023], INSA Lyon, tous droits réservés

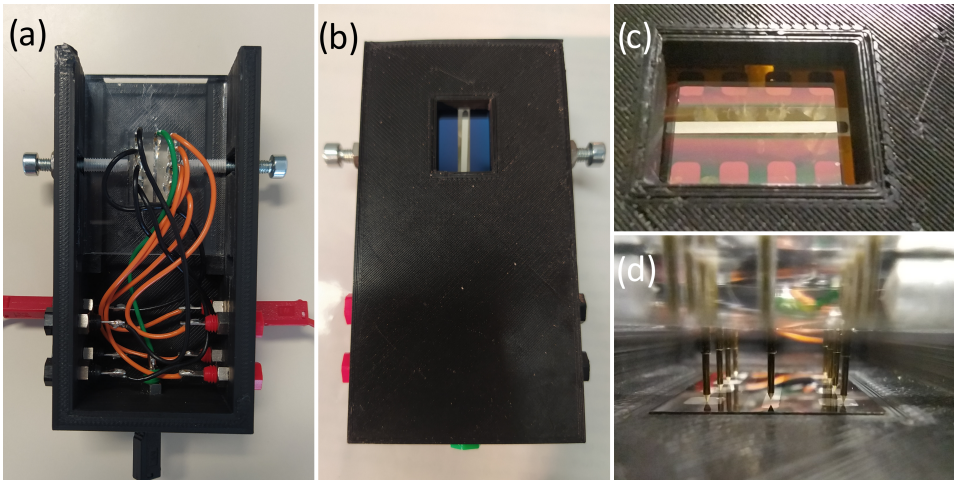

Figure 1.10: 3D-printed opto-electronic test bench design for backside electrical contact. (a) Bottom view with electrical connections (b) Top view with opening window for incident light (c) Close up of the opening window (d) Side view of the 9 spring loaded pins contacting the Ag electrodes.

2.1 Deposition conditions of N-I-P stacks

In order to go through a comprehensive review of µc-SiGe:H alloy compositions, eleven prototypes were produced with identical structure. For all samples, µc-Si:H was selected for the doped N and P layers as good understanding of their growth mechanisms were acquired in chapter 4.

N and P layers

Film thickness for both layers was set to 50 nm to make sure we were no longer in the amorphous incubation layer growth regime (see 2.1.3). Deposition conditions for both N and P layer can be found in table 5.1.

Layer	type	doping gas	β	est. n / p	$t_{dep.}$	R_H	est. thick.	Temp.	Power	Press.	Φ_{tot}
	-	-	-	[cm^{-3}]	[min]	-	[nm]	[°C]	[W]	[mTorr]	[sccm]
P doped µc-Si:H	n-type	PH_3	0.05 %	1.1×10^{19}	18	50	50	250	30	800	350
B doped µc-Si:H	p-type	B_2H_6	0.05 %	3.4×10^{18}	18						

Table 5.1: Deposition conditions for N and P layers used in NIP photodiodes. β is the doping gas to silane ratio defined in chapter 4.

The most crucial parameter for doped films is undoubtedly β, the doping gas to silane ratio. For both films β was set to 0.05 %. In the case of p-type µc-Si:H, this value was the highest which could be achieved without degrading the crystalline quality of the film as discussed in 2.2. On the other hand, n-type µc-Si:H could be reach doping levels as high as $10^{20}\, cm^3$ with higher β. However, high doping levels ($1.1 \times 10^{19}\, cm^3$) were already achieved with β as low as 0.05 % and limiting the amount of PH_3 in the chamber meant reducing the risk of absorber layer contamination mentioned in subsection 1.3.

Cette thèse est accessible à l'adresse : https://theses.insa-lyon.fr/publication/2023ISAL0014/these.pdf
© [A. Wilson], [2023], INSA Lyon, tous droits réservés

Absorber layer

The process parameters for each sample's absorber layer was estimated based on the work presented in chapter 3, section 3. All parameters were kept constant except for germane concentration (GC) which was used to tuned the films' composition. The final Ge fraction x_{Ge} could be estimated using equation 2.1 defined in chapter 3.

$$x_{Ge} = \frac{R \cdot GC}{R \cdot GC + (1 - GC)} \tag{2.1}$$

The germanium incorporation coefficient R was determined experimentally by fitting the function to SIMS measurements. For the deposition condition chosen for absorber deposition (50 W, 1000 mTorr, 500 sccm, $R_H = 100$) R was found to be equal to 3 (see figure 2.1a). We should however mention that in the context of NIP layer stacking, temperature is fixed by the first film to be deposited, i.e, 250 °C in our case. The value for R was however obtained at 200 °C hence we expect some discrepancy between expected x_{Ge} and true x_{Ge}. Raman measurements on µc-SiGe:H films deposited under the same conditions at 200 °C and 250 °C showed the Ge fraction of our films were overestimated by 5 % at most.

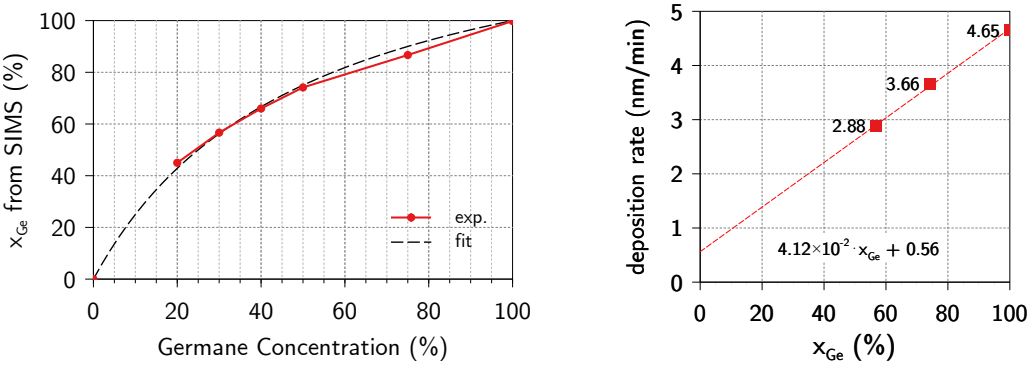

(a) (b)

Figure 2.1: (a) Experimental data and fitted curve for $x_{Ge} = f(GC)$. See chapter 3. (b) Deposition rate extrapolation, used for $x_{Ge} = 40\% \rightarrow 75\%$

Similarly, deposition duration $t_{dep.}$ was obtained from deposition rate, in turned estimated by a linear regression from known samples (see figure 2.1b). The effect of increased temperature, although negligible compared to R_H of RF-Power, may bring additional uncertainty to the estimated thickness.

In order for our results to be quantitatively compared with one another, the target thickness was set to 200 nm as thicker layers could be too limiting for the diffusion length of our layer. A complete overview of the deposition conditions used for each sample is given in table 5.2.

Sample *SiGe25%* was deposited at lower R_H dilution factor due to limitations in minimum gas Germane gas flow. *Ge100%* was deposited at higher R_H to ensure high crystalline quality as mentioned in 2. With our approach we hope to find the best absorber material to fit our need. I should be noted that this optimization is only valid for a 200 nm thick absorber, deposited under these specific conditions. Indeed, an under-performing absorber layer in this setup may turn to be the best option if the layer thickness is increased, say, to 400 nm. With this consideration in mind, structural, electrical and opto-electronic sample characterization were performed.

Cette thèse est accessible à l'adresse : https://theses.insa-lyon.fr/publication/2023ISAL0014/these.pdf
© [A. Wilson], [2023], INSA Lyon, tous droits réservés

Sample	GC -	est. x_{Ge} -	$t_{dep.}$ [min]	R_H -	est. thick. [nm]	Temp. [°C]	RF-Power [W]	Pressure [mTorr]	Φ_{tot} [sccm]
SiGe25%	10.0 %	25 %	69.4	50	200	250	50	1000	500
SiGe40%	18.2 %	40 %	89.8	100					
SiGe45%	21.4 %	45 %	82.3	100					
SiGe50%	25.1 %	50 %	75.9	100					
SiGe55%	30.0 %	55 %	69.4	100					
SiGe60%	33.3 %	60 %	65.8	100					
SiGe65%	38.7 %	65 %	61.7	100					
SiGe70%	43.6 %	70 %	58.0	100					
SiGe75%	49.7 %	75 %	54.6	100					
Ge100%	100 %	100 %	95.4	200					

Table 5.2: Absorption layer deposition conditions for *SiGe* NIP devices. Deposition rate was adapted in order to obtain the desired thickness.

2.2 Structural characterization of prototype photodiodes

2.2.1 Raman spectroscopy of µc-SiGe:H alloys

Characterization of stacked layers

Until now, the µc-SiGe:H films produced had been studied when grown as a standalone layer. Stacking layers is equivalent to changing the nature of the growth substrate for our µc-SiGe:H film hence Raman spectroscopy was used to verify the crystallinity and composition of our absorber. The investigation the structural properties of the aforementioned samples is made more complex by the number of stacked layers. Raman spectroscopy (see chapter 2, section 2.1) was used extensively to characterize µc-Si:H and µc-Ge:H films in chapter 3. This method however probes the sample on a thickness dependent on absorption at the chosen excitation wavelength. For a excitation wavelength $\lambda_{exc} = 473\,\text{nm}$ the penetration depth in µc-SiGe:H alloys is typically in the order of 20 to 100 nm (refer to figure 3.11, chapter 3). The boron doped µc-Si:H top layer however absorbs part of the incoming photons and strongly adds to the output signal in the $\Delta\omega = 400 - 550\,\text{cm}^{-1}$region. The Raman spectrum of the p-type µc-Si:H layer which was deposited on µc-Ge:H (sample *Ge100%*) was used as a reference to remove the parasitic peak from other samples. Examples for the data correction process used are provided in figure 2.2 for samples *SiGe40%* and *SiGe55%*. The resulting spectrum can then be used for further data analysis.

Ge fraction from Raman spectroscopy

Raman spectra were obtained on SiGe devices with absorber Ge fraction ranging from 40 to 70 %. The impact of increasing Ge fraction on Raman data was obtained by relying on the previously defined method for isolating the signal coming from the absorber (see figure 2.3a). Crystalline SiGe alloys typically exhibit three characteristic peak for Ge-Ge, Si-Ge, and Si-Si bonds around 300, 400 and 520 cm^{-1}, respectively [169–171]. Similarly, microcrystalline silicon-germanium also exhibits 3 distinct peaks corresponding to the these bonds [88, 110]. Their position and amplitude can however differ significantly from their monocrystalline counterparts. On top of the well described Ge fraction dependence of peak positions, [111, 112] the Raman shift measured depends on crystalline volume fraction [113]. Peak broadening and red-shifting thus commonly attributed to amorphization for µc-Si:H and µc-Ge:H

Cette thèse est accessible à l'adresse : https://theses.insa-lyon.fr/publication/2023ISAL0014/these.pdf
© [A. Wilson], [2023], INSA Lyon, tous droits réservés

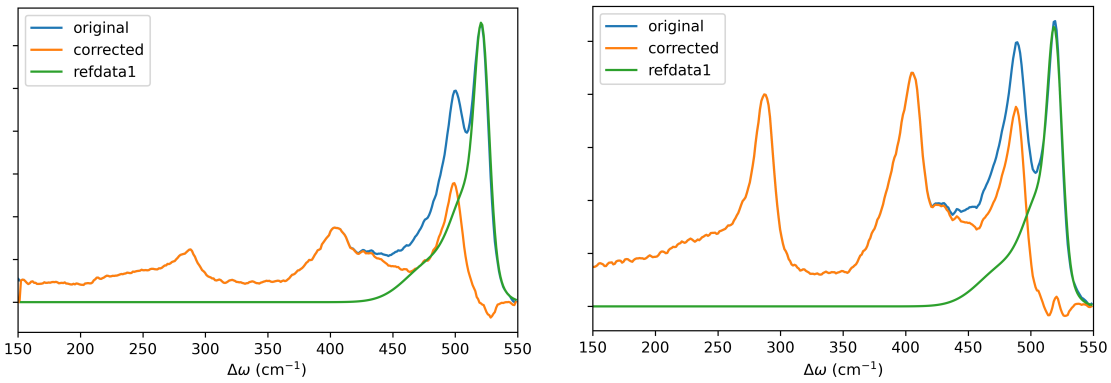

(a) (b)

Figure 2.2: Raw Raman spectra (blue), reference µc-Si:H peak (green) and corrected data (orange) for *SiGe40%* and *SiGe55%* samples. Some artifacts remain in the 520 cm^{-1} region due to peak position mismatch.

is now dependent on two factors. Measurement of a Raman crystallinity X_c from such data was thus deemed unreliable. Qualitative observation of the presence of a highly crystallized phase can however be made as amorphous phase peak broadening lead µc-SiGe:H and a-SiGe:H to have clearly distinguishable Raman spectra. [88, 113]

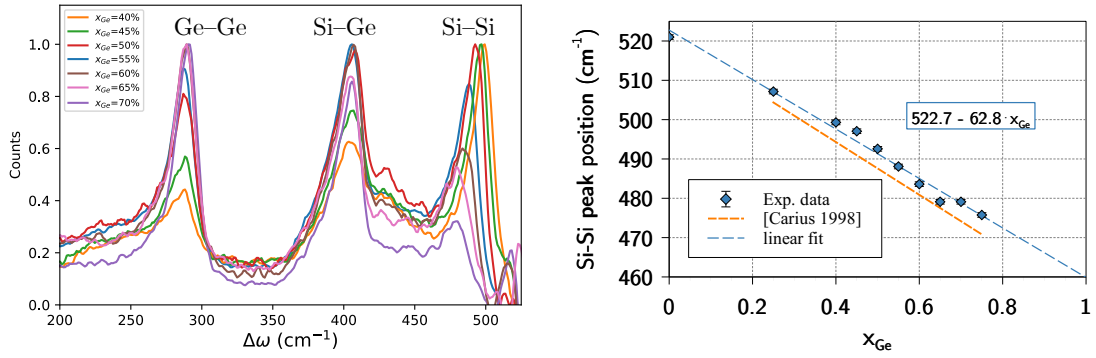

(a) (b)

Figure 2.3: (a) Corrected and normalized Raman spectra for µc-SiGe:H alloys with increasing Ge fraction. The Si-Si peak can simultaneously be seen broadening and shifting to lower $\Delta\omega$ values (b) Si-Si bond peak position as a function of expected Ge fraction. Data from the paper by Carius et al. [88] on µc-SiGe:H is added for reference.

Based on the work performed by several research groups on c-SiGe, poly-crystalline SiGe and µc-SiGe:H [88, 111, 172] it has been established that Raman peak position is composition dependent. While Si-Ge and Ge-Ge peaks are only found to vary in a 20 cm^{-1} window, the Si-Si peak advantageously varies linearly in a 60 cm^{-1} range. Figure 2.3b shows the measured Si-Si peak position for samples in the $x_{Ge} = 0 - 75\,\%$ range, where x_{Ge} is the predicted composition. The linear relation found between expected x_{Ge} and $\Delta\omega_{\text{Si-Si}}$ by this structural analysis method provides experimental evidence that our model is reliable for predicting Ge fraction from Germane concentration 2.1a and finding the appropriate gas flow conditions

Cette thèse est accessible à l'adresse : https://theses.insa-lyon.fr/publication/2023ISAL0014/these.pdf
© [A. Wilson], [2023], INSA Lyon, tous droits réservés

(see chapter 3, section 3.1). This method is not suitable for Ge rich films due to excessive uncertainty in Si-Si peak identification.

A noticeable shift between our data and those taken from Carius et al. [88] is however observed and may have two causes. A difference in crystalline volume fraction between the authors' µc-SiGe:H and ours could explain part the discrepancy. Yet, as discussed in paragraph 2.1, the most likely culprit would be the difference in deposition temperature between the data from our model (200 °C) and the PIN device deposition temperature (250 °C).

2.2.2 TEM analysis of NIP photodiodes

For further insight into the structural properties of the deposited photodiodes TEM analysis (chapter 2, section 2.2) was performed on *SiGe55%* and *SiGe60%* samples (see table 5.2). The TEM lamellae were cut out from regions with no sputtered Ag due to contamination during the FIB milling preparation step.

Film thickness measurements

TEM cross sections obtained from samples *SiGe55%* and *SiGe60%* are shown in figures 2.4a and 2.4b respectively. The ITO, µc-Si:P, µc-SiGe:H and µc-Si:B films can clearly be identified from their contrast in atomic number. Columnar growth features can be seen in both of the sample's absorber layers. No sign of cracks of blisters were found at the interfaces.

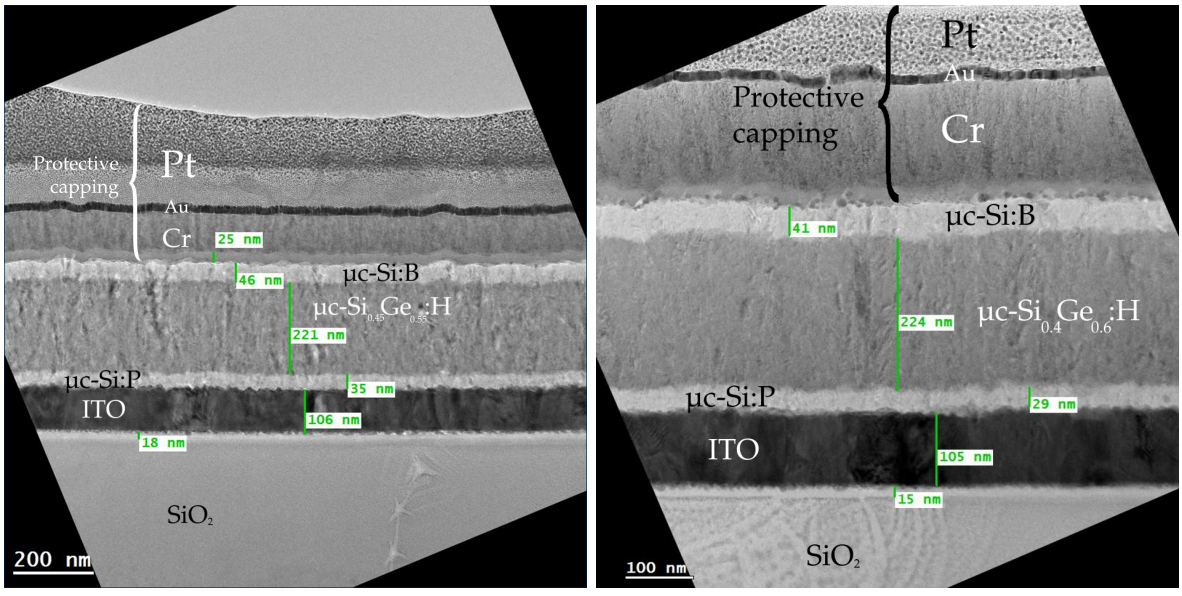

(a) (b)

Figure 2.4: TEM cross section of the glass / ITO / µc-Si:P / µc-SiGe:H / µc-Si:B layer stack for samples (a) *SiGe55%* (b) *SiGe60%*.

Thickness measurements show the goal 50 nm / 200 nm / 50 nm NIP film thickness was not perfectly matched. The n-type µc-Si:H layer was found to be as thin as 29 nm with an average thickness in the order of 33 nm. The crystallization induced interface roughness certainly play a part in the thickness deviation. The p-type µc-Si:H layer which was deposited in almost identical condition was found to be closer to the 50 nm goal thickness (46 nm for

Cette thèse est accessible à l'adresse : https://theses.insa-lyon.fr/publication/2023ISAL0014/these.pdf
© [A. Wilson], [2023], INSA Lyon, tous droits réservés

SiGe55%). We suspect the µc-Si:P film growth kinetics were affected by the underlying ITO film as the growth speed for the film were calibrated with c-Si substrates (see chapter 4).

The absorber layer was measured to be 11 % thicker than was anticipated using our extrapolation model (see section 2.1). Accounting for interface roughness, the absorber layer thickness of sample *SiGe60%* was measured to be 223 ± 8 nm. Both analyzed samples gave comparable results thus only the data regarding *SiGe60%* will be given for the sake of clarity.

Crystalline phase observation

The presence of a microcrystalline absorber has been confirmed previously for all samples using Raman spectroscopy. The high resolution of TEM images of figure 2.5 makes it possible to see the periodic structures characteristic of the crystalline phase.

The Phosphorus doped µc-Si:H layer in figure 2.5a was found to have up to 30 % variation in thickness due to the film's roughness. A crystalline arrangement is seen across the entire thickness of the film and even at the interface with ITO. No sign of extensive amorphous phase was observed and the numerical diffraction pattern exhibits rings characteristic of polycrystals and powders [140]. Many different crystal orientations can be seen in the film but estimating the grain size from those images is difficult.

In figure 2.5b the crystalline phase of the µc-$Si_{0.4}Ge_{0.6}$:H absorber is seen to extend directly from the n-type layer with no sign of an amorphous interface. The numerical diffractogram added shows a ring patter, characteristic of the many crystalline orientations. Similarly figure 2.5c showing the "bulk" of the µc-SiGe:H absorber is found to only exhibit small crystalline phases. The period structure seen in the center of the image was attributed to Moiré patterns created from two overlapping crystalline orientations.

Finally the Boron doped µc-Si:H film was found to also maintain crystallinity through the µc-SiGe:H / µc-Si:H interface. The diffraction pattern has the same ring features discussed previously and the local thickness of the film was found to be strongly affected by the roughness of the interface.

Film composition

STEM EDX mapping (see chapter 2, section 2.2.3) were also used for composition identification. The mapping and line profile shown in figure 2.6 yielded consistent results.

Comparing the counts for Si and Ge, the calculated $x_{Ge} = {}^{[Ge]}/_{[Si]+[Ge]}$ was found to be 59.5 ± 13.3 %. This value is close to the one anticipated, yet the uncertainty means the film composition cannot be given with great precision. For more precise information SIMS analysis would be needed.

The TEM images of the *SiGe60%* sample provided here show our experimental structure matches quite closely the anticipated thicknesses. Considering the parameters were extrapolated from basic models, the final result is satisfactory. Additionally, no critical defects such as cracks, voids or blisters were found in these samples.

2.3 Opto-electronic characterization and modeling

The good agreement between the ideal design for our structure and the experimental prototype obtained meant our samples could undergo further testing. The opto-electronic properties of our devices were investigated using current-voltage characteristics, quantum efficiency and reflectance measurements.

Cette thèse est accessible à l'adresse : https://theses.insa-lyon.fr/publication/2023ISAL0014/these.pdf
© [A. Wilson], [2023], INSA Lyon, tous droits réservés

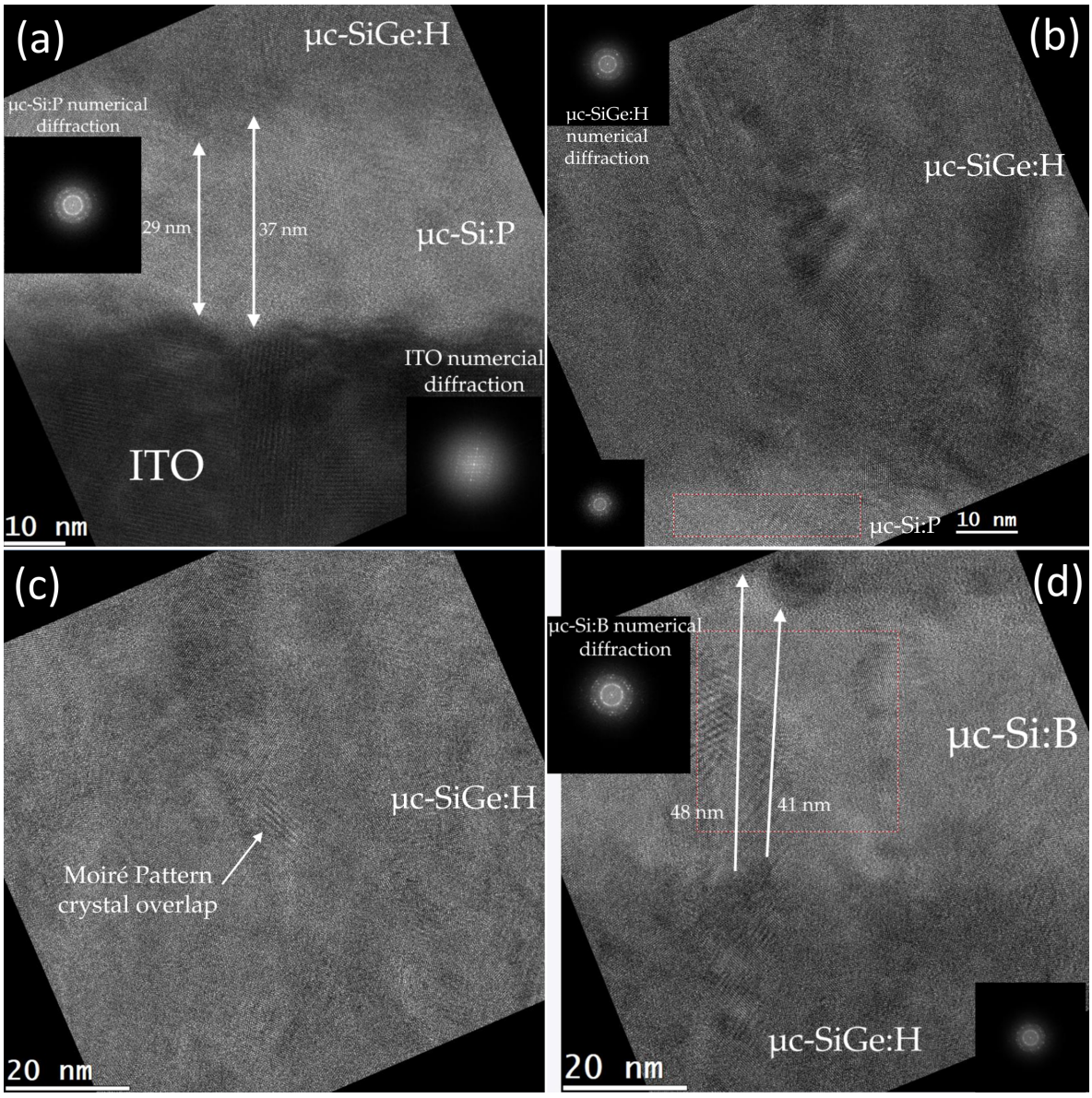

Figure 2.5: High resolution TEM images of sample *SiGe60%*. (a) ITO and µc-Si:P films with numerical diffraction patterns (b) µc-Si:P / µc-SiGe:H interface (c) bulk of the µc-SiGe:H layer (d) µc-SiGe:H / µc-Si:B interface with corresponding diffraction pattern for each layer.

Cette thèse est accessible à l'adresse : https://theses.insa-lyon.fr/publication/2023ISAL0014/these.pdf
© [A. Wilson], [2023], INSA Lyon, tous droits réservés

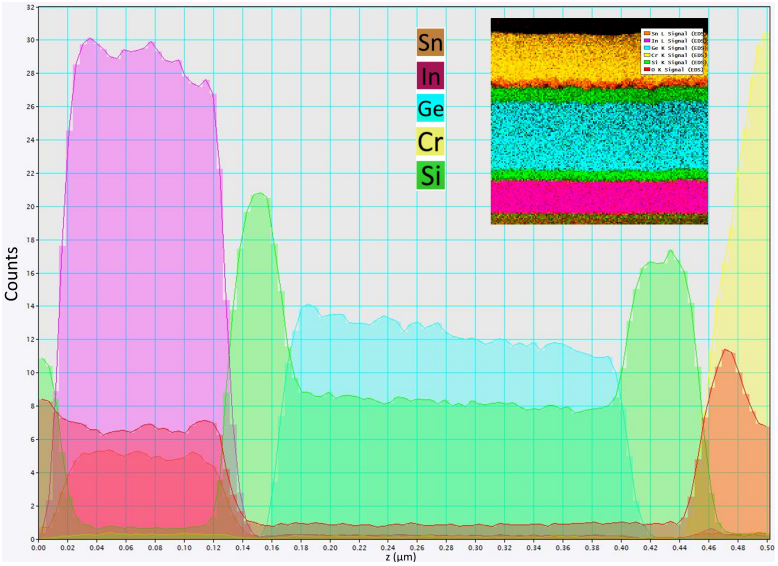

Figure 2.6: Energy Dispersive X-ray Spectroscopy (EDX) mapping and line profile for sample *SiGe60%*.

2.3.1 Electrical characterization

Current-voltage (IV) curves were obtained for the 8 photodiodes of each sample. Examples of such IV curves are shown in figure 2.7a which closely resemble the IV curve of a conventional PN diode. The curves of figure 2.7a were fitted using a single diode equivalent circuit model (figure 2.7b) under dark. [173]

$$I = I_0 \left(\exp\left(\frac{q \cdot (V - R_{series} \cdot I)}{n k_B T} \right) - 1 \right) + \frac{V - R_{series} \cdot I}{R_{shunt}} \tag{2.2}$$

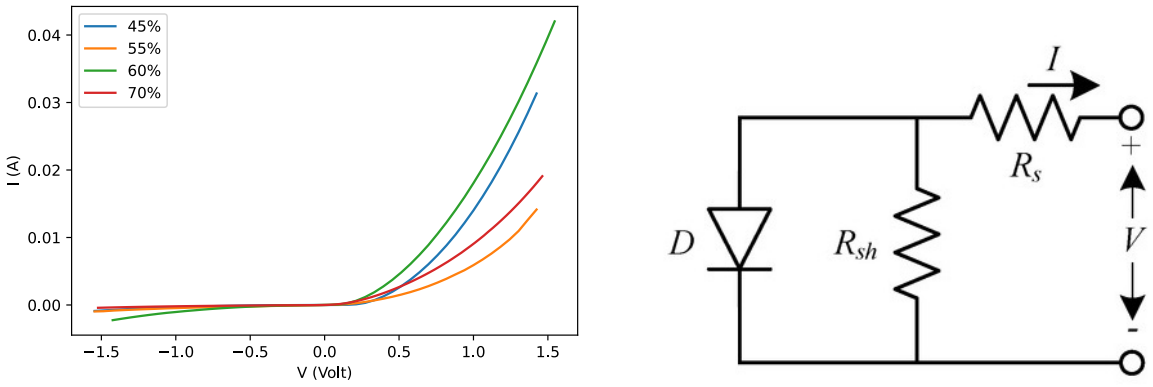

(a) (b)

Figure 2.7: (a) Current-Voltage (IV) characteristic for NIP *SiGe* devices, a diode behavior is observed. (b) Single diode equivalent circuit, from [174].

The extracted values for R_{shunt} and R_{series} are given in table 5.3. Other devices suffered from shunt resistance which could be as low as 20 Ω which drowned the diode characteristic and

Cette thèse est accessible à l'adresse : https://theses.insa-lyon.fr/publication/2023ISAL0014/these.pdf
© [A. Wilson], [2023], INSA Lyon, tous droits réservés

are thus not displayed. The low R_{shunt} on these samples may have been caused by damage to the layers with the test bench contact pins (section 1.5) or by dust contamination due to sample transportation between cleaning and deposition steps.

Sample	R_{shunt}	R_{series}
SiGe40%	12 kΩ	37 Ω
SiGe55%	2.9 kΩ	97 Ω
SiGe60%	3.9 kΩ	33 Ω
SiGe70%	4.8 kΩ	68 Ω

Table 5.3: Fitted R_{shunt} and R_{series} values from previous curves.

Shunt and series resistance of our samples have an impact on the characterizations methods which require a reverse bias to be applied to the structure. Due to the variability in shunt resistance for this batch of sample, future Quantum Efficiency measurements will be performed in short-circuit conditions.

2.3.2 Quantum efficiency of N-I-P Photodiode

Quantum Efficiency (QE) is one of the key figures of merit used to assess the performance of photodiodes in the NIR range. This opto-electronic characterization method provides overall view of the performance of the device by measuring the ratio of extracted charge carriers to incoming photons (see chapter 2, section 3.3). Good QE can only be obtained if good optical properties meet good transport properties.

External Quantum Efficiency measurement

Our samples with increasing absorber Ge fraction were characterized at normal incidence in the $\lambda = 300 - 1100$ nm range. Measurements extending further into the NIR range were conducted further in this chapter on the most promising samples. The External Quantum Efficiency (EQE) for samples ranging from $x_{Ge} = 0$ to 75 % are given in figure 2.8, the *Ge100%* was not displayed due to the EQE values being lower than 0.2 %.

Since EQE accounts number of extracted electrons over the total number of incoming photon some oscillations in the curves appear, corresponding to constructive and destructive interference occurring at specific wavelengths. The period of these oscillations is directly linked to the overall thickness of our NIP junction and the refractive index of our layer. The similarity in oscillation period between all samples is thus due to their similarity in thickness and refractive index. For a given sample, measurements across all functioning photodiode gave fairly repeatable results as shown in figure 2.9. At low wavelengths, the different measurement overlap well yet some discrepancy emerge at higher wavelengths most likely due to variation in the absorber layer thickness during deposition. From the results of figure 2.8 several conclusion can be drawn.

The selected structure for our prototype is functional, EQE measurements can be performed easily and with good repeatability. EQE values as high as 70 % were found for our samples despite the absence of properly designed anti-reflective coatings. This encouraging result means our choice of NIP structure does not only work but is also efficient.

The EQE spectra for pure µc-Si:H and pure µc-Ge:H absorbers gave the worst performance due to poor absorbtion and poor transport properties respectively, as was expected for the study of these materials in sections 1 and 2 of chapter 3.

Cette thèse est accessible à l'adresse : https://theses.insa-lyon.fr/publication/2023ISAL0014/these.pdf
© [A. Wilson], [2023], INSA Lyon, tous droits réservés

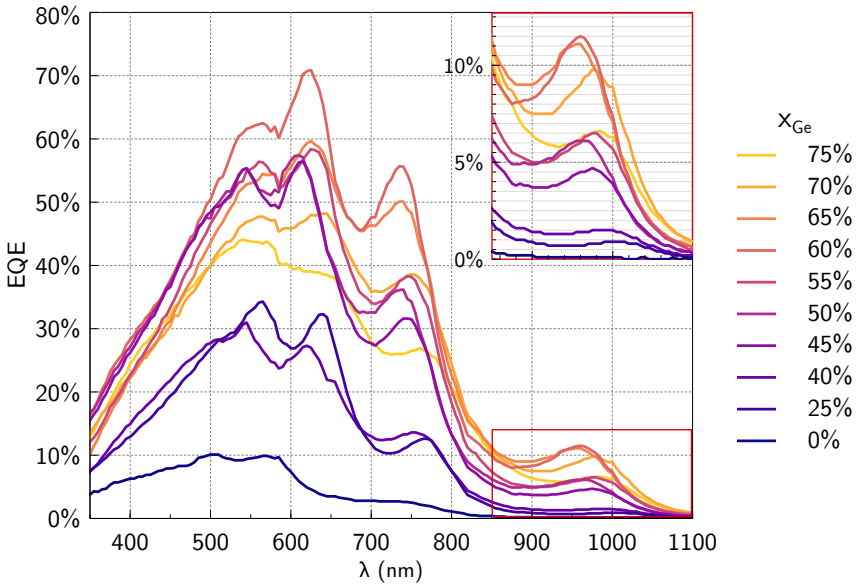

Figure 2.8: External Quantum Efficiency as a function of wavelength for SiGe NIP devices. The absorber is 200 nm thick with its composition x_{Ge} varying in the 0 to 75 % range.

There seems to be an optimum value for the Ge fraction of the absorber layer our prototype. In figure 2.8 the EQE can be seen rapidly increasing over the whole spectral range with increasing x_{Ge} until a composition of 60 % of Germanium in the film. Beyond this point the overall performance of the device starts degrading although the EQE in NIR seems to suffer less than in the visible range. µc-$Si_{0.4}Ge_{0.6}$:H could potentially be the best candidate for our intended use, however one must bear in mind the optimum x_{Ge} may not be identical with a thinner or thicker absorber layer. It could be that a thinner but more Ge-rich absorber could perform better for instance.

The increase of EQE with λ in the 350 to 500 nm range is due to absorption of light in the n-type µc-Si:H layer. Indeed, $\alpha_{\mu\text{c-Si:H}}(400\,\text{nm}) = 2 \times 10^5\,\text{cm}^{-1}$ meaning the penetration depth $\delta = 50$ nm (see chapter 3, figure 3.11). We expect the N layer to absorber 63 % of the incoming light at this given wavelength. With the high doping level n, holes will be recombined in this region. The absence of a passivation layer could also lead free charges generated close to the P-I interface to recombine, thus lowering the EQE in the high energy region.

Finally, the EQE drops continuously above $\lambda = 750\,\text{nm}$. Such behavior may result from excessive absorption in the ITO layer and increase in reflectance. For a better picture of our samples' performance, we must rely on Internal Quantum Efficiency (IQE) measurements.

Internal Quantum Efficiency calculation

Internal Quantum Efficiency (IQE) is a better figure of merit than EQE for studying the performance of our NIP junction since it accounts for losses due to reflectivity and transmission. IQE represents the number of extracted charge for each absorbed photon, rather than for each incoming photon. To calculate the IQE some hypothesis were made. For every wavelength we can write $R + T + A = 1$. As our film were found to have roughness much smaller than λ, scattering of incident light was neglected. Our devices also have a silver back reflector (the anode) which is thick hence $T = 0$. We then have $A(\lambda) = 1 - R(\lambda)$ meaning the IQE can be

Cette thèse est accessible à l'adresse : https://theses.insa-lyon.fr/publication/2023ISAL0014/these.pdf
© [A. Wilson], [2023], INSA Lyon, tous droits réservés

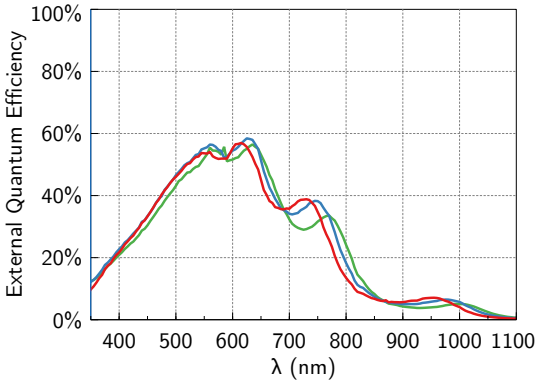

Figure 2.9: EQE measurement repeatability on 3 separate photodiodes of the *SiGe55%* sample. The differences are due to local variations in film thickness.

expressed as follows :

$$IQE(\lambda) = \frac{EQE(\lambda)}{1 - R(\lambda)} \tag{2.3}$$

Where $R(\lambda)$ is the reflection coefficient as a function of wavelength. $R(\lambda)$ can easily be measured using a reflectometer. The spot size must be smaller than the Ag back contact for our calculations to be valid. The IQE is then calculated at every wavelength from the EQE and R data as shown in figure 2.10a. The local maxima in reflectance should align with the minima in EQE. Reflectance measurements made on different photodiodes for each sample since fluctuations in thickness can shift the maxima's position (see figure 2.10b). For each sample, the reflectance and EQE spectra whose peaks and valleys align the best are selected to compute the IQE.

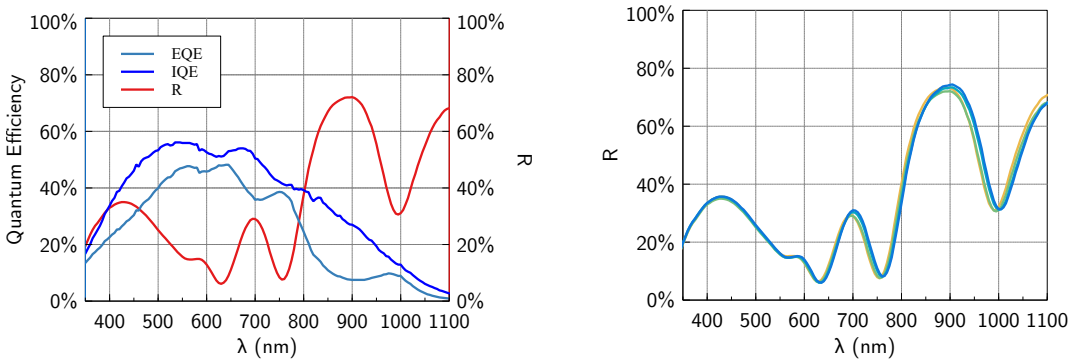

Figure 2.10: (a) Internal Quantum Efficiency calculation for EQE and Reflectance spectra for *SiGe70%*. (b) Repeatability of the reflectance measurement on the *SiGe70%* sample.

This method has drawbacks as R and EQE measurements are done separately and don't probe exactly the same region of the sample. Some misalignment between minima and maxima of both curves can lead to artifact oscillations in the IQE. With this approach IQE is also calculated based one the overall absorption of the device, not the NIP junction's absorption.

Cette thèse est accessible à l'adresse : https://theses.insa-lyon.fr/publication/2023ISAL0014/these.pdf
© [A. Wilson], [2023], INSA Lyon, tous droits réservés

As some light is absorbed in the ITO and Ag layers the IQE is actually underestimated, yet is a readily available and convenient way to obtain it. For a more in depth analysis, optical modeling of the generation rate in the device could tackle the aforementioned issues.

Experimental results

IQE(λ) was calculated for all the previously characterized samples with increasing absorber Ge fraction. The results are given in figure 2.11 and as 2D map in figure 2.12. The trends observed previously for EQE (2.3.2) still hold for IQE :

- high IQE is obtained in the visible range (over 80 % for the best samples). The result is encouraging considering the simplicity of the designed structure.
- the optimal value for alloy composition is µc-$Si_{0.4}Ge_{0.6}$:H. The *SiGe60%* sample performs better throughout the entire spectral range, with IQE(1000 nm) reaching 17.6 %. This is due to the high reflectivity of the sample at these wavelength which was taken into account.
- µc-$Si_{1-x}Ge_x$:H absorbers with x_{Ge} greater than 60 % see their IQE degraded on the whole tested range (see figure 2.12), suggesting the diffusion length in the absorber is becoming noticeably smaller than the absorber thickness.
- the IQE for all devices drops sharply beyond $\lambda = 800$ nm and does not exceed 4 % at $\lambda = 1100$ nm.

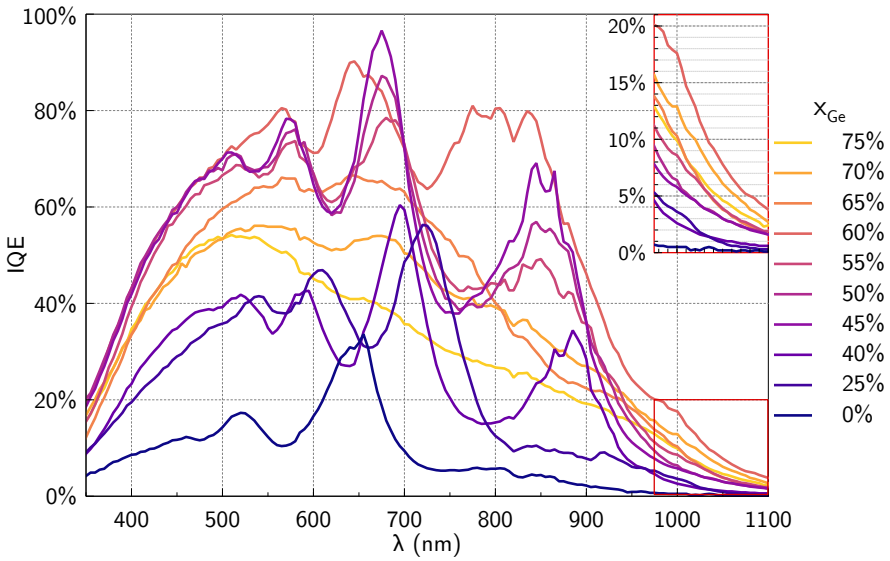

Figure 2.11: Internal Quantum Efficiency as a function of wavelength for SiGe NIP devices with 200 nm thick absorber.

This last point can be explained in terms of the increase in penetration depth $\delta = 1/\alpha$ with λ seen in figure 2.13. In an scenario where 100 % of the incoming light reaches the absorber and no internal interference occur, the maximum percentage of incoming we should be able to capture is :

$$A(\lambda) = 1 - \exp\left(-d_{abs.}/\delta_{x_{Ge}}(\lambda)\right) \tag{2.4}$$

Cette thèse est accessible à l'adresse : https://theses.insa-lyon.fr/publication/2023ISAL0014/these.pdf
© [A. Wilson], [2023], INSA Lyon, tous droits réservés

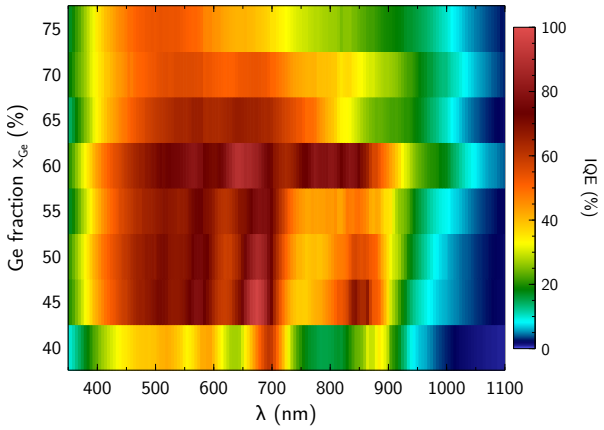

Figure 2.12: IQE heat-map as a function of photon wavelength and absorber Germanium composition. The red areas represent a high IQE while the blue areas correspond to a value close to 0 %. In the NIR region, *SiGe60%* stands out as the best performing device.

For a 400 nm thick[2] µc-$Si_{0.4}Ge_{0.6}$:H absorber at $\lambda = 1000$ nm, $A(\lambda)$ is equal to 20.3 %. This upper bound highlight the need to enhance absorption or to have thicker layers in our device. However, with IQE(1000 nm) = 17.6 % our device is close to reaching this theoretical limit. A more accurate model was developed to model the behavior of the entire photodiode using SILVACO.

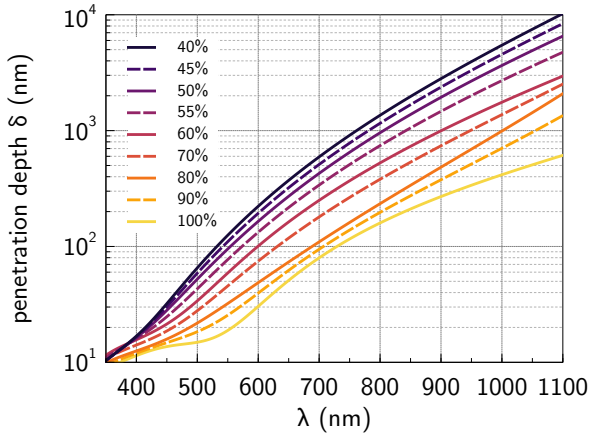

Figure 2.13: Penetration depth δ of photon as a function of wavelength for µc-SiGe:H alloys with $x_{Ge} = 40 - 100$ %. A layer of thickness δ absorbs 63 % of incoming light at corresponding λ. The dashed curves are interpolated values.

2.3.3 Optical modeling of NIP photodiodes

Optical modeling of the glass / ITO / µc-Si:P / µc-$Si_{0.4}Ge_{0.6}$:H / µc-Si:B / Ag stack of sample *SiGe60%* was performed using SILVACO. The goal of these simulations is to distinguish photons reaching the µc-$Si_{0.4}Ge_{0.6}$:H absorber from those absorbed parasitically in the ITO,

[2] 2×200 nm due to the backside reflector doubling the optical path of photons

Cette thèse est accessible à l'adresse : https://theses.insa-lyon.fr/publication/2023ISAL0014/these.pdf
© [A. Wilson], [2023], INSA Lyon, tous droits réservés

µc-Si:H and Ag layers. This is done by obtaining the photogeneration profile at each wavelength, i.e., the number of photogenerated charges as a function of depth and wavelength $n_{photogen}(x, \lambda)$. A detailed presentation of $n_{photogen}(x, \lambda)$ for the *SiGe60%* sample is given in appendix A. The photogeneration profile for a given layer is then integrated as a function of depth and normalized by the incident photon flux. From this data the relative photon absorption can be obtained, representing the proportion of photons absorbed in a given layer as a given λ.

Optical modeling parameters

The information fed into SILVACO consists of the thickness and refractive index for each layer. The thickness for each layer of the *SiGe60%* sample was set based on the TEM cross section presented in section 2.2.2. The refractive index of each layer was taken from the spectroscopic ellipsometry data obtained from individual layers characterized in earlier chapters. Table 5.4 provides an overview of the parameters used for simulation.

Layer	Thickness	Refractive index
glass	semi-∞	$n = 1.643$
ITO	100 nm	from figure 1.6
µc-Si:P	30 nm	from figure 1.6a
µc-$Si_{0.4}Ge_{0.6}$:H	224 nm	from figure 3.10
µc-Si:B	45 nm	from figure 1.6a
Ag	152 nm	from ref. [138]

Table 5.4: Thickness (from TEM) and refractive index for each layer in the modeled device. The refractive index for glass was set to 1.643 on the whole spectral range and absorption was neglected.

The simulation was performed at normal incidence for comparison with experimental measurements. To avoid unwanted interference from the thick glass substrate (1.1 mm) the simulation was done considering the glass as the ambient medium and then corrected by adding the reflection losses due to the air/glass interface. For the sake of simplicity, only planar interfaces were considered in the model.

Modeling results

From the simulation, the contribution to photon absorption of every material in the device could be decomposed. The results are presented in figure 2.14.

The absorption profile of the entire device is probably overestimated in the UV region as absorption from the glass substrate was neglected. The results concerning the µc-$Si_{0.4}Ge_{0.6}$:H layer are of highest interest, since only photons absorbed in the absorber layer have the potential to be collected. Absorption in other layer can be considered as parasitic absorption and should ideally be minimized. As such, the difference between photon absorption in the absorber and in the full stack gives and idea of the optical losses of the structure. In the UV region, the absorption by ITO and µc-Si:P prevails. For µc-Si:P this absorption extends up to $\lambda = 700$ nm but quickly becomes negligible in the visible range. Similarly, µc-Si:B barely contributes to absorption since very little visible light reaches the layer. The absorption in the µc-$Si_{0.4}Ge_{0.6}$:H layer extends until 1150 nm and exhibits sharp oscillations at $\lambda = 605, 740$ and 970 nm due to the layer behaving similarly to a Fabry-Perot cavity [175] at these wavelengths.

Cette thèse est accessible à l'adresse : https://theses.insa-lyon.fr/publication/2023ISAL0014/these.pdf
© [A. Wilson], [2023], INSA Lyon, tous droits réservés

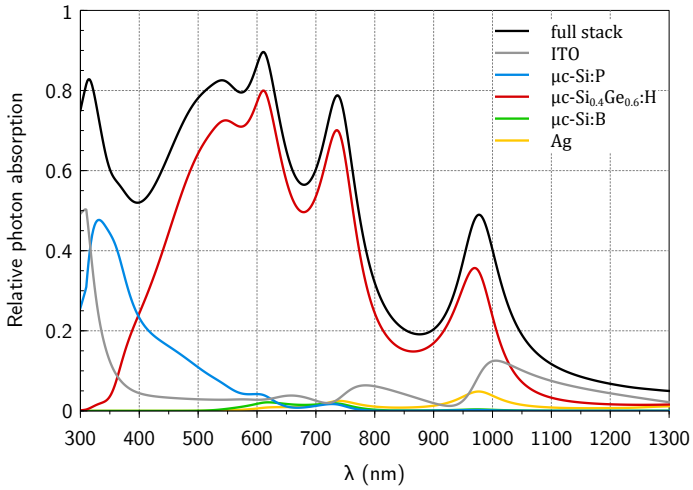

Figure 2.14: Relative photon absorption in each layer of the simulated *SiGe60%* sample. The *full stack* curve corresponds to the absorbance A of the stack, which is equal to $1 - R(\lambda)$.

This relative photon absorption in the absorber layer can be interpreted as an upper bound for the external quantum efficiency since it corresponds to the EQE if no losses due to minority carrier recombination occurred. In the NIR region, ITO, Ag and $Si_{0.4}Ge_{0.6}$:H compete for photon absorption with up to 13 % of the absorption occurring in the ITO layer at $\lambda = 1000$ nm. To a smaller extent, Ag also plays a similar role.

A comparison between the simulated and experimental data is provided in figure 2.15. The reflectance of the entire device is found to be in good agreement with the simulated results in figure 2.15a. In the UV region, $R(\lambda)$ is impacted by the glass substrate, the ITO and the µc-Si:P layer. The discrepancy in that region could be due to the assumption of a constant refractive index for glass. In the visible to NIR region however, the reflectance spectra match closely. The oscillation period of the simulation is almost identical to the experimental data, meaning the indices and thicknesses used were representative of the true properties of our film. Some difference in reflectance amplitude is observed in NIR which could be due to an overestimation of ITO of µc-SiGe:H absorption.

The experimental EQE ($EQE_{exp.}$) can then be compared to the upper bound for EQE (EQE_{max}) obtained from the model. The results provided in figure 2.15b thus compare the maximum sensitivity of the device to the experimental result accounting for recombination of minority carriers. Both profiles are very similar, exhibiting resonances at roughly the same wavelengths. Throughout the visible and NIR range, the absolute difference between $EQE_{exp.}$ and EQE_{max} stays in the 5 to 25 % range and can be attributed to losses due to poor surface passivation, barrier potential at the interfaces and recombination in the absorber. The degradation is stronger in NIR, possibly due to photons being absorbed deeper in the µc-SiGe:H layer. The absence of a sharp resonance peak in $EQE_{exp.}$ at 960 nm could also be due to the true device having non-negligible thickness variation (see section 2.2.2) over the probed area. This could lead to a broadening of the resonance.

Cette thèse est accessible à l'adresse : https://theses.insa-lyon.fr/publication/2023ISAL0014/these.pdf
© [A. Wilson], [2023], INSA Lyon, tous droits réservés

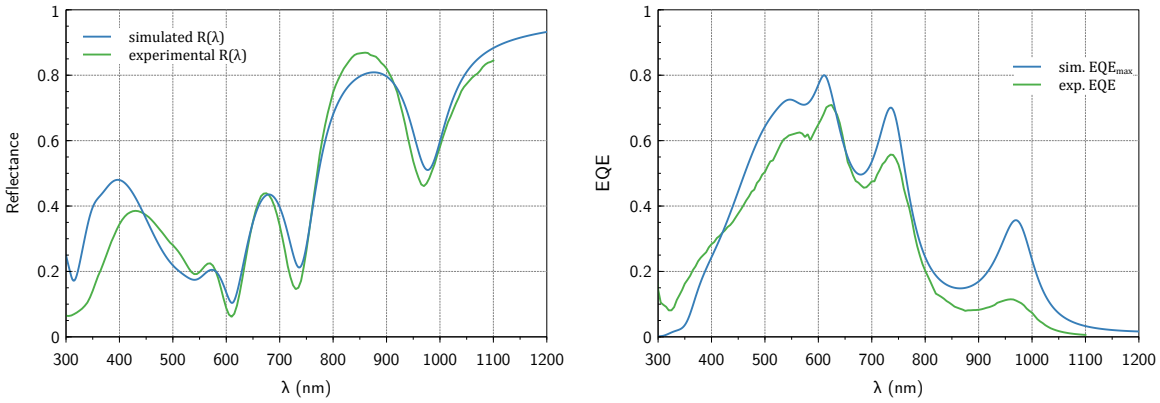

(a) (b)

Figure 2.15: (a) Reflectance (b) EQE experimental and simulated data comparison for sample *SiGe60%*. The thickness used for the simulation are given in table 5.4.

2.4 Discussion : influence of absorber Ge fraction of opto-electronic performance

The results presented in this section on the absorber layer composition's impact on quantum efficiency are first of all a proof of concept of our approach. We were able to produce a set of samples with a sensitivity extending into the NIR spectral range. These results were achieved with a 200 nm thin µc-SiGe:H absorber stacked in a glass/ITO/<n>µc-Si:H/µc-SiGe:H/<p>µc-Si:H/Ag structure.

The high IQE (over 60 %) obtained for different samples in the visible range is an indicator of the viability of our design in terms of bands structure and choice in layer thickness. It can still be improved by studying the work functions of our materials and tuning the anode and cathode contacts to match those work functions.

With the <n>µc-Si:H (50 nm) / µc-SiGe:H (200 nm) / <p>µc-Si:H (50 nm) tested structure, the optimal alloy composition over the entire UV to NIR range was found to be µc-$Si_{0.4}Ge_{0.6}$:H. Below $x_{Ge} = 60\,\%$ the absorption coefficient of the absorber is the limiting factor. Adding Germanium to the layer results increased absorption (see chapter 3, section 3.2). The competition between α and L_{diff} turns in favor of the loss in diffusion length above $x_{Ge} = 60\,\%$ as electrical properties of Ge-rich µc-SiGe:H sharply drop with increasing Ge fraction [23]. An IQE as high as 17.6 % was found for $\lambda = 1000$ nm despite potential parasitic absorption from the ITO and Ag layers.

Optical modeling of the *SiGe60%* sample from experimental data was able to identify more precisely the layers responsible for parasitic absorption, highlighting the role of ITO in that matter. Good agreement between the simulated and experimental data was obtained, improving our comprehension of the device. Comparing the ideal and real EQE showed the sample had less than 15 % photon due to recombination of minority carriers. This value got higher reaching into NIR.

We must keep in mind that this final result is tightly linked to the choice in absorber thickness and may not be the best performing device one can produce with a NIP structure. In the following section, the impact of absorber layer thickness on internal quantum efficiency will be investigated.

Cette thèse est accessible à l'adresse : https://theses.insa-lyon.fr/publication/2023ISAL0014/these.pdf
© [A. Wilson], [2023], INSA Lyon, tous droits réservés

3 Influence of µc-$Si_{0.4}Ge_{0.6}$:H layer thickness on opto-electronic properties

The encouraging results obtained throughout the previous section left pending questions regarding the optimum material. The absorber itself may still be enhanced by changing the deposition conditions leading to another candidate material. This section will thus be dedicated to studying the influence of absorber layer thickness $d_{abs.}$ on internal quantum efficiency.

3.1 Deposition conditions

The deposition process for studying the effect of absorber layer thickness $d_{abs.}$ was based on the one established in the previous section (2.1). The N and P layers were left unchanged, with n-type and p-type µc-Si:H as the doped layers (see table 5.1). The absorber composition was set at $x_{Ge} = 60\,\%$. The choice of this Ge fraction arose from its good performance observed in subsection 2.3.2. Deposition conditions for the absorber layer of each device are given in table 5.5.

Sample	GC -	est. x_{Ge} -	$t_{dep.}$ [min]	$d_{abs.}$ [nm]	R_H -	Temp. [°C]	RF-Power [W]	Pressure [mTorr]	Φ_{tot} [sccm]
SiGe60%100nm	33.3 %	60 %	32.9	100					
SiGe60%200nm	33.3 %	60 %	65.8	200					
SiGe60%300nm	33.3 %	60 %	98.7	300	100	250	50	1000	500
SiGe60%400nm	33.3 %	60 %	131.6	400					
SiGe60%800nm	33.3 %	60 %	263.2	800					

Table 5.5: Absorber layer deposition conditions for *SiGe60%* NIP devices. Thickness was incremented from 100 to 800 nm.

Germane concentration (GC) was kept constant to maintain identical film composition. We expect the diffusion length of the carriers to be independent of absorber thickness. Only deposition duration was changed from one sample to another to ensure the invariant absorber material properties. Structural properties of micro-crystalline materials are known to be thickness dependent. [50, 131] From the Raman data of figure 3.1 film crystallinity does not appear to increase with absorber thickness in the 100 to 400 nm range. This experimental data suggests crystallization has reached a steady state above $d_{abs.} = 100$ nm.

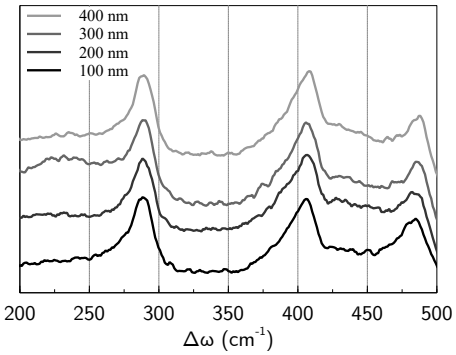

Figure 3.1: Raman spectrum of the absorber layer in NIP devices with increasing µc-SiGe:H thickness.

Cette thèse est accessible à l'adresse : https://theses.insa-lyon.fr/publication/2023ISAL0014/these.pdf
© [A. Wilson], [2023], INSA Lyon, tous droits réservés

3.2 Opto-electronic characterization

3.2.1 I-V characteristic

For all 5 samples detailed in table 5.5 the current-voltage characteristic was obtained in the -1.5 to +1.5 V range. An example of IV curves for each sample is shown in figure 3.2. For all samples a diode behavior is observed with some fluctuations due to R_{shunt} and R_{series}.

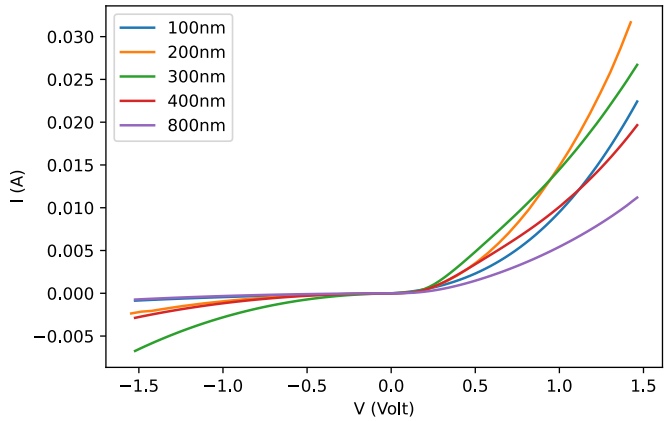

Figure 3.2: IV curves for NIP devices with increasing µc-SiGe:H absorber thickness.

The values for shunt and series resistance were obtained by fitting the IV characteristic with a single diode model as seen in subsection 2.3.1 and are gathered in table 5.6. While R_{shunt} is more likely a consequence of random defects occuring during the production process, R_{series} is due to the sum of silver, ITO and NIP resistance. The impact of the thickness of the intrinsic region on the series resistance R_{series} of the device is clearly visible.

Sample	R_{shunt}	R_{series}
SiGe60%100nm	1.6 kΩ	32 Ω
SiGe60%200nm	4.0 kΩ	24 Ω
SiGe60%300nm	1.9 kΩ	37 Ω
SiGe60%400nm	4.3 kΩ	47 Ω
SiGe60%800nm	7.9 kΩ	76 Ω

Table 5.6: Fitted R_{shunt} and R_{series} values from the sample's IV curves.

3.2.2 Quantum efficiency dependence on absorber thickness

External quantum efficiency and reflectance spectra were obtained for all 5 samples in the 300 to 1100 nm range in short circuit conditions. For each sample, measurements were done on 3 separate photodiodes for robustness and the best measurement was kept for further analysis. The IQE was then calculated according to the method defined earlier in subsection 2.3.2. IQE as a function of photon wavelength is given in figure 3.3 for increasing absorber thickness. Many useful conclusions can be drawn for this data.

At first glance, the 200 nm thick absorber which was tested out in the previous section (2) seems to offer the best opto-electronic compromise. Its IQE is indeed much higher than other samples throughout most of the spectral range. The remaining oscillations in IQE would

Cette thèse est accessible à l'adresse : https://theses.insa-lyon.fr/publication/2023ISAL0014/these.pdf
© [A. Wilson], [2023], INSA Lyon, tous droits réservés

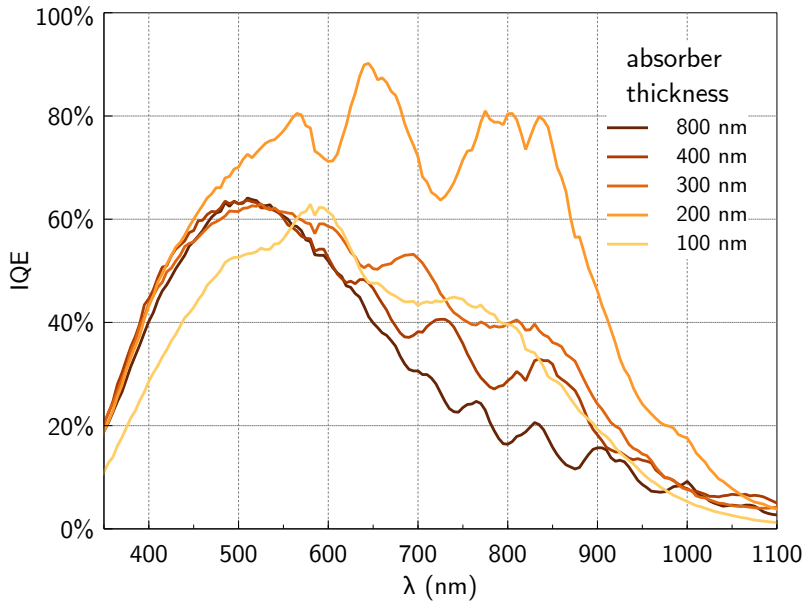

Figure 3.3: Internal Quantum Efficiency as a function of photon wavelength for NIP devices with µc-$Si_{0.4}Ge_{0.6}$:H absorber layer. The thickness of the intrinsic absorber $d_{abs.}$ was increased for 100 to 800 nm.

seem to be due to resonance effects in the absorber layer at certain wavelength similar to those observed in optical simulations of sample *SiGe60%* (section 2.3.3).

The overall IQE first increases with $d_{abs.}$ due to increased absorption until $d_{abs.} \approx L_{diff}$ and then drops as more photo-generated charges recombine before reaching the N and P type layers. This drop is quite slow due to the enhanced absorption. From these results we can therefore suppose $L_{diff}(x_{Ge} = 60\%)$ is in the order of 200 nm.

Focusing on the NIR part of the spectra, we notice *SiGe60%300nm* and *SiGe60%400nm* actually outperform the *SiGe60%200nm* sample at $\lambda = 1100$ nm. Since our end goal is to focus on wavelengths in the 940 to 1340 nm, all three samples are of interest. This result means a thicker sample can perform worse in general but have a sufficient increase in NIR absorption to outperform thinner samples in NIR. The theoretical maximum absorption as a function of photon wavelength and absorber thickness is given in figure 3.4 and was calculated from equation 2.4 of section 2.3.2.

The fact that IQE below $\lambda = 500$ nm is almost totally independent from $d_{abs.}$ is somewhat counter-intuitive. Indeed, from figure 3.4 we know over 95 % of the light reaching the µc-$Si_{0.4}Ge_{0.6}$:H layer should be absorbed since $2 \times d_{abs} \geq 200$ nm. With L_{diff} becoming smaller than $d_{abs.}$ we should thus expect an overall decrease of IQE, even at this specific wavelength. The fact that no significant drop occurs indicates other transport or recombination mechanisms must be at work such as electric field driven charge transport. Simulation of the optical absorption in *SiGe60%200nm* and *SiGe60%400nm* devices are presented in section 2.3.3 and appendix A, respectively. They highlight the relatively low amount of recombination losses in sample *SiGe60%200nm* compared to *SiGe60%400nm*.

Cette thèse est accessible à l'adresse : https://theses.insa-lyon.fr/publication/2023ISAL0014/these.pdf
© [A. Wilson], [2023], INSA Lyon, tous droits réservés

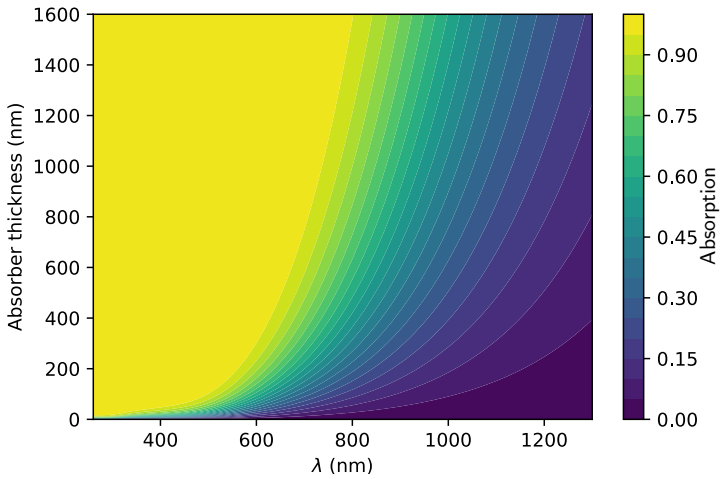

Figure 3.4: Theoretical maximum absorption within the µc-$Si_{0.4}Ge_{0.6}$:H as a function of λ and $d_{abs.}$. Absorption is obtained from equation 2.4. $\alpha_{x_{Ge}}(\lambda)$ is taken from experimental data (3.2) and $d = 2 \times d_{abs.}$ due to the Ag back-reflector of our devices.

3.3 Discussion : Influence of absorber thickness on opto-electronic performances

In this section we produced a set of samples with consisting of glass/ ITO/ <n>µc-Si:H/ µc-$Si_{0.4}Ge_{0.6}$:H/ <p>µc-Si:H/ Ag structure with variable absorber thickness $d_{abs.}$. The tested photodiodes revealed the competition between increase in α and decrease in L_{diff} is dominated by L_{diff} as $d_{abs.} > 200$ nm. This results suggest L_{diff} is in the order of 100 – 200 nm.

An IQE of 5 % at $\lambda = 1100$ nm was however obtained for a 400 nm thick µc-$Si_{0.4}Ge_{0.6}$:H layer. In this case the sacrifice in terms of losses due to recombination was counter-balanced by the gain in absorption. An optical simulation, presented in appendix A provides an upper bound for the EQE of this sample. The behavior of the tested samples in the 500 nm range however show our data cannot simply be explained in terms of diffusion length and other transport or recombination mechanisms need to be integrated in our interpretation.

To overcome the "L_{diff} vs α" conundrum, a final option will be explored : NIP junction polarization.

4 Opto-electronic performance of reverse biased NIP photodiodes

So far in this chapter, the prototype NIP junctions produced were tested in short-circuit conditions, i.e, in absence of any external reverse bias. This measurement method allowed to obtain EQE spectra even for samples with low shunt resistance and helped compare our samples on a common basis. Applying a reverse bias to our photodiodes brings us closer to real-life operating conditions and is therefore the next step forward in this project.

4.1 Experimental setup and sample selection

EQE measurement relies on the amplification of the current in the order of $10^4 - 10^5$ V/A (see chapter 2, section 3.3). If the dark current increases too much, the output voltage saturates the system. The high shunt resistance (> 4 kΩ) found in section 3.2.1 for samples *SiGe60%200nm*, *SiGe60%400nm* and *SiGe60%800nm* limits the dark current when measuring

Cette thèse est accessible à l'adresse : https://theses.insa-lyon.fr/publication/2023ISAL0014/these.pdf
© [A. Wilson], [2023], INSA Lyon, tous droits réservés

the EQE under reverse bias. The dark current values at -1 V as well as the fitted R_{shunt} and R_{series} are reminded in table 5.7.

Sample	R_{shunt}	R_{series}	$I_{dark}(-1\text{V})$
SiGe60%200nm	4.0 kΩ	24 Ω	-0.94 mA
SiGe60%400nm	4.3 kΩ	47 Ω	-1.19 mA
SiGe60%800nm	7.9 kΩ	76 Ω	-0.33 mA

Table 5.7: Fitted R_{shunt}, R_{series} and measured dark current at -1 V obtained from the sample's IV characteristic (figure 3.2). The diodes' surface area are in the order of 7 to 9 mm^2.

The polarized EQE measurements were performed thanks to Dr. Longeaud at GeePs[3] laboratory in Gif-sur-Yvette, France. The experimental setup available at GeePs offered the possibility to characterize our sample up to $\lambda = 1800$ nm. To reach this extended spectral range, the light source intensity is calibrated using a c-Si sensor up to $\lambda = 850$ nm and a c-Ge sensor beyond that point.

EQE measurements are initially done in short circuit conditions and the reverse bias is then gradually increased until breakdown of the photodiode. The breakdown was found to be reversible and no sample were damaged during the process. Unfortunately, due to a different light path in this experimental setup the IQE could not be calculated using the reflectance spectra (only measured up to 1100 nm) as was done so far.

4.2 Quantum efficiency of reverse biased NIP junctions

The external quantum efficiency for all three samples from table 5.7 were measured. Their deposition conditions can be found in table 5.5. Quantitative EQE comparison between samples is difficult even at identical reverse bias since their difference in series resistance means a different voltage is applied across the NIP junction.

4.2.1 Results

The results obtained by polarizing *SiGe60%400nm* exceeded our expectations. Figure 4.1 shows the EQE of the device obtained at increasing reverse bias, working from short circuit to -900 mV in 150 mV steps.

The curve under no bias was found to be almost identical to the one obtain with the setup at INL (whose IQE is given in figure 3.3). With increasing bias ΔV the EQE is improved in the 550 to 1250 nm range. The gain in EQE $G(\lambda, \Delta V) = EQE(\lambda, \Delta V)/EQE(\lambda, 0\,\text{V})$ at a given wavelength increases exponentially with ΔV which makes it all the more appealing to increase bias. At a set polarization value, $G(\lambda, \Delta V)$ was also found to increase with wavelength, meaning the performance improvement due to ΔV affects NIR more than visible light. The calculated gain in EQE is represented in figure 4.2.

Above $\lambda = 900$ nm the EQE was found to be increased by over 250 % at $\Delta V = -900$ mV. This major improvement in device performance is promising for NIR applications. Thanks to the extended spectral range of the experiment, sensitivity was found to extend up to 1250 nm with an EQE of 3.7 % reached for $\lambda = 1125$ nm. The optical modeling of the *SiGe60%400nm* sample provided in appendix A make it possible to compare the maximum theoretical EQE

[3] Génie électrique et électronique de Paris - UMR8507

Cette thèse est accessible à l'adresse : https://theses.insa-lyon.fr/publication/2023ISAL0014/these.pdf
© [A. Wilson], [2023], INSA Lyon, tous droits réservés

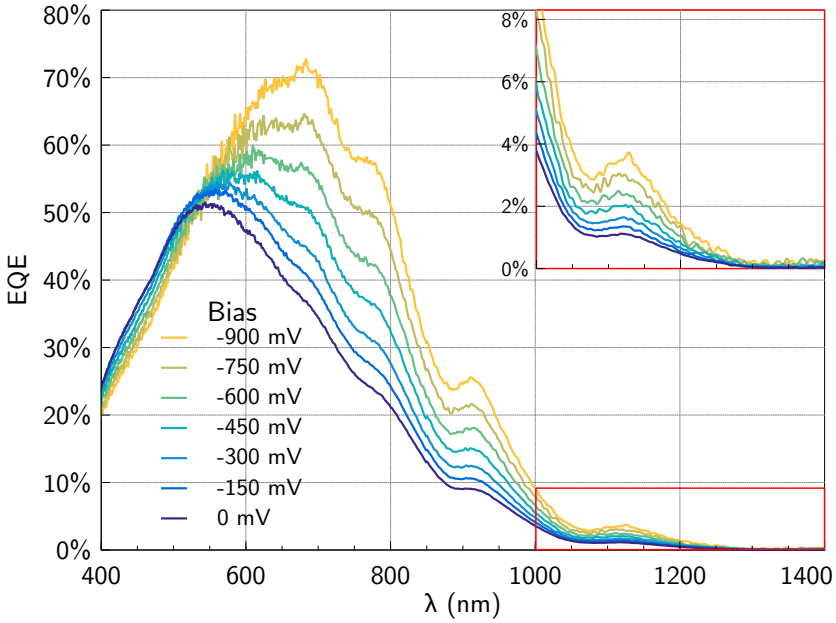

Figure 4.1: Impact on EQE of external reverse bias applied to the NIP junction with a 400 nm µc-$Si_{0.4}Ge_{0.6}$:H absorber (*SiGe60%400nm*)

with the polarized EQE. By applying an external bias, the difference between EQE_{max} and $EQE_{exp.}$ can be greatly reduced, almost reaching 0 in some parts of the spectral range. Increasing ΔV further would this not necessarily result in a constant increase in $G(\lambda, \Delta V)$.

Very similar results were found for samples *SiGe60%200nm* and *SiGe60%800nm*. Unfortunately ΔV could not be increased up to -900 mV due to the photodiodes' breakdown. Similarly to figure 4.1, a gain in EQE was observed on the whole spectral range.

4.2.2 Discussion

As polarization shouldn't affect material absorption, the gain in EQE can be attributed to better charge extraction from the absorber region. In the ideal case, the transport mechanism in the absorber should be governed by drift velocity ($v_{e/h} = \mu_{e/h} \cdot \| \overrightarrow{E} \|$) [176] of charges due to the permanent electric field created by the N-I and I-P interfaces. In practice, the defects in the intrinsic region dampen the electric field and limit its extension to a few hundred nanometers at most for amorphous silicon. [177, 178] The central region of the absorber has no electric field and extraction of charges in this region are thus governed by diffusion length. A schematic representation of the band diagram in the drift velocity regime, the hybrid regime and the diffusion length regime is given in figure 4.3. If the absorber thickness $d_{abs.}$ is smaller than the space charge regions (SCR), the device is governed by drift velocity, and ultimately mobility. We believe that is case for sample *SiGe60%200nm* for which optical modeling showed $EQE_{exp.}$ was similar to EQE_{max}, thus proving charge extraction was efficient. If $d_{abs.}$is slightly greater than the SCR, diffusion length will become important and in the worst case scenario, charge extraction will only rely on L_{diff} (figure 4.3(c)). Of course, our case of a double heterojunction is much more complex than the scheme presented here. Applying a reverse bias to a hybrid regime configuration will extend the electric field in that region and improve charge transport.

This interpretation would help explain the poor gain in EQE in the short wavelength region

Cette thèse est accessible à l'adresse : https://theses.insa-lyon.fr/publication/2023ISAL0014/these.pdf
© [A. Wilson], [2023], INSA Lyon, tous droits réservés

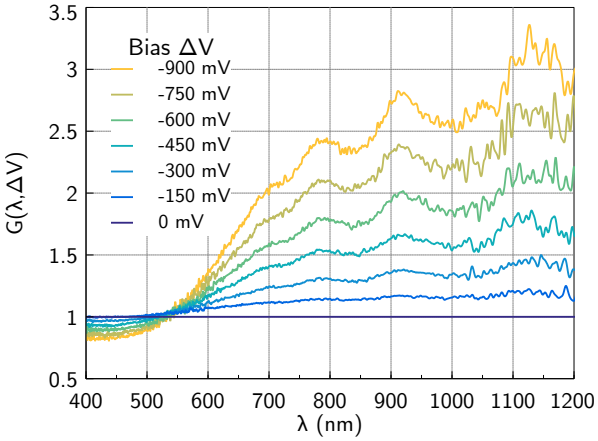

Figure 4.2: Gain in EQE $G(\lambda, \Delta V) = EQE(\lambda, \Delta V)/EQE(\lambda, 0\,\mathrm{V})$ of a NIP junction with a 400 nm µc-$Si_{0.4}Ge_{0.6}$:H absorber (*SiGe60%400nm*).

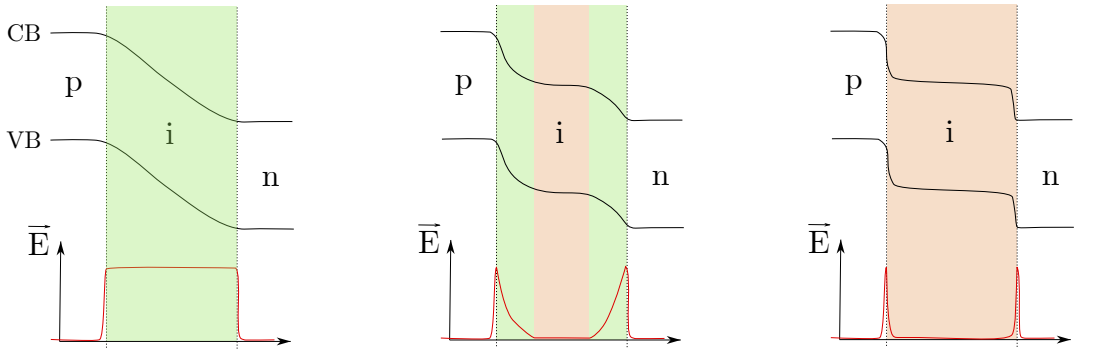

(a) drift velocity regime (b) hybrid regime (c) diffusion length regime

Figure 4.3: The competition between electric field and diffusion length lead to 3 charge transport regimes. A schematic representation of the corresponding band diagram and electric field in 1D is proposed for the simple case of a PIN homojunction.

as high energy photons are already absorbed in the space charge region leading to better charge collection. Adding a bias doesn't improve the EQE as charge collection was already at its maximum. The remaining photons are either being reflected, absorbed in the ITO and n-type layer or the photogenerated charges recombined due to poor interface passivation. The most interesting gain in EQE with ΔV is thus found for higher wavelengths which are absorbed deeper in the layer where the $\overrightarrow{E}$-field was 0 before applying the reverse bias.

With this new understanding of our devices in mind we can influence charge transport in the absorber by improving diffusion length, reducing defect density, increasing N/P layers doping levels or applying an external bias.

5 Conclusion

This final chapter was devoted to make use of the knowledge acquired on intrinsic and doped micro-crystalline semiconductors (chapters 3 and 4) to produce a simple photosensitive device. A simple design for our photodiode was proposed which met the thermal budget con-

Cette thèse est accessible à l'adresse : https://theses.insa-lyon.fr/publication/2023ISAL0014/these.pdf
© [A. Wilson], [2023], INSA Lyon, tous droits réservés

straints of above-IC CMOS image sensors by keeping the whole process under 250 °C. To arrive at this proof of concept, a 3 steps production process was developed while trying to maximize robustness and minimize complexity. To address those two aspects, some compromises had to be made regarding the choice for the electrical contact layers and the dimensions of the photodiodes. The prototype could thus certainly be improved with band diagram engineering, interface passivation and anti-reflective coating design. Although the design was known to be imperfect some encouraging results were obtained.

A set of samples with increasing absorber layer Ge fraction were tested in order to find the µc-SiGe:H alloy offering the best compromise between light absorption and charge extraction. The test structure consisted of glass / ITO(100 nm) / <n>µc-Si:H(50 nm) / µc-$Si_{1-x}Ge_x$:H(200nm) / <p>µc-Si:H(50 nm) / Ag. Electrical testing confirmed our devices to behave as a diodes and internal quantum efficiency measurements revealed their sensitivity could extend to 1100 nm with only a 200 nm thick absorber. As expected, using µc-Si:H or µc-Ge:H as absorber layers led to the worst performances due to optical and electrical limitations respectively. An optimum for film composition was found with a µc-$Si_{0.4}Ge_{0.6}$:H layer with IQE as high as 17.6 % at $\lambda = 1000$ nm. Optical modeling using SILVACO of the device helped gain a better understanding of the limitations of the photodiode. The external quantum efficiency of the device was found to be close to its theoretical maximum in the visible range but started decreasing in NIR.

The impact of absorber thickness on opto-electronic properties was then investigated in an attempt to extend the NIR sensitivity. A structure identical to the previous one was used, with a µc-$Si_{0.4}Ge_{0.6}$:H absorber of variable thickness. The results showed the 200 nm thick absorber still performed better on average, with IQE reaching over 80 % in the visible range. However the 400 nm thick sample was found to perform better at $\lambda = 1100$ nm with an IQE of 5 %.

The sensitivity of the photodiodes tested so far reach our expectations in the visible range but degraded quickly when reaching to NIR, in part due to the ITO layer. The IQE of our samples were obtained under no external bias. Applying a reverse bias to the NIP junction showed a gain of 250 % in EQE could be obtained in the NIR region. The gain in EQE with bias is attributed to the extending electric field in the absorber shifting the charge transport mechanism from being governed by diffusion length to drift velocity. Optical modeling detailed in appendix A proved the existence of a higher bound for the external quantum efficiency of the device. External bias was able to push the experimental EQE close to this theoretical limit.

This chapter has shown that µc-SiGe:H semiconductors deposited by PECVD can indeed be used to produce robust and simple photo-detectors at low thermal budget. The simple design for our photodiode was successful in providing a functional prototype to test the influence of the absorber's composition and thickness on overall opto-electronic properties. The diode behavior and the possibility to polarize our junction for extra characterization is a proof these materials, although highly defective, can be used as sensors.

Cette thèse est accessible à l'adresse : https://theses.insa-lyon.fr/publication/2023ISAL0014/these.pdf
© [A. Wilson], [2023], INSA Lyon, tous droits réservés

Key Points

Contributions

- ❏ A simple design for the prototype photodiode was proposed based on a ITO / NIP / Ag stack
- ❏ The materials developed over the course of the previous chapters were introduced in the NIP diode structure
- ❏ The focus was set on tuning the intrinsic absorber composition and thickness to improve quantum efficiency of the device
- ❏ Optical modeling of the device was performed to provide a better understanding of the source of parasitic absorption in the prototype

Take away message

- ❏ Although minimalistic, the selected design for the photodiode was found to provide reproducible results
- ❏ For a 200 nm thick absorber layer, a 60 % Ge fraction was found to provide the highest IQE (17.6% at 1000 nm)
- ❏ Optical modeling with SILVACO showed good agreement between theoretical and experimental QE
- ❏ With increased absorber thickness, the performance of the device is limited by the poor transport properties of μc-SiGe:H
- ❏ Applying an external reverse bias can overcome the electrical limitations of the material and drastically improve QE in the NIR

Cette thèse est accessible à l'adresse : https://theses.insa-lyon.fr/publication/2023ISAL0014/these.pdf
© [A. Wilson], [2023], INSA Lyon, tous droits réservés

Conclusion and Outlooks

Brief reminder of the Ph.D project objectives

Over the course of this project we sought to develop low thermal budget hydrogenated silicon-germanium thin films, encompassing materials ranging from pure a-Ge:H to µc-$Si_{1-x}Ge_x$:H alloys. Our final goal consisted in integrating these newly developed films into a prototype photodiode whose sensitivity in the NIR spectral range could extend up to 1350 nm. In the context of developing these devices for above-IC CMOS image sensors, we had to make sure the process temperature throughout the fabrication steps did not exceed 350 °C.

Review of the work carried out

In an effort to introduce the topic of microcrystalline materials, a review of the existing literature on PECVD growth of Si, Ge and SiGe thin films was conducted in chapter 1. Si:H thin films have been widely documented over the past 40 years, unlike Ge:H and SiGe:H which were found to be mostly studied in the context of multi-junction solar cells. Examples of the implementation of these materials in devices are however extremely scarce.

Chapter 2 introduced the experimental deposition and characterization techniques used during this project. As a central piece in SiGe:H film deposition, specifications of the PECVD equipment were presented. The hardware was adapted for this project, making it feasible to grow Si:H, SiGe:H or Ge:H films with intrinsic, p-type or n-type doping at low temperature. The wide range of available experimental techniques to characterize amorphous and microcrystalline film was then introduced. Structural and chemical characterization techniques like STEM, Raman Spectroscopy and SIMS were detailed with an emphasis on the specific constraints of our samples. Spectroscopic Ellipsometry, Reflectometry and Quantum Efficiency were used to retrieve the optical properties of the samples while Hall Effect and SSPG were used for electrical characterization. Introducing these analysis methods laid the groundwork for the work carried out over the course of the following chapters.

In chapter 3, we aimed at producing thin films of semiconductor materials suitable for Near Infrared ($\lambda = 940$ to 1350 nm) absorber layers in future P-I-N photodiode prototypes. Due to its low absorption above $\lambda = 800$ nm, µc-Si:H was not a suitable layer for near infrared sensing application. Yet in the context of P-I-N photodiode production it could act as an efficient n or p-type window layer on the frontside of the device. Microcrystalline Germanium was a stronger candidate for our intended use since its lower band-gap significantly enhances NIR absorption. Crystallization of the thin films was more complex to reach for µc-Ge:H than it was for µc-Si:H. Deposition rate was severely impacted by the need for high hydrogen dilution factors. A two-step growth approach was investigated in order to produce films with high X_c without compromising on deposition rate. Optical properties of Ge:H thin films were

Cette thèse est accessible à l'adresse : https://theses.insa-lyon.fr/publication/2023ISAL0014/these.pdf
© [A. Wilson], [2023], INSA Lyon, tous droits réservés

obtained by spectroscopic ellipsometry. The absorption coefficient extracted from the analysis revealed the benefits of µc-Ge:H over a-Ge:H for wavelengths over $\lambda = 1000$ nm. However, it was found upon inspection of electrical properties that photoelectric properties were poor due to high dark current and high recombination rates. µc-Ge:H kept this drawback despite our efforts to find more appropriate process parameters. As a consequence we started focusing on µc-SiGe:H alloys which is a more tricky material to produce. Optical characterization by Spectroscopic Ellipsometry of µc-SiGe:H with increasing Ge fraction showed the positive impact on NIR absorption coefficient. This came at the cost of an apparent degradation of electrical properties with increasing Germanium content.

Having focused on the development of suitable absorber layer materials, the next step consisted in developing PECVD-grown n and p-type semiconductor layer for future P-I-N photodiode prototypes. In chapter 4 we aimed to obtain thin microcrystalline layers with high doping levels. The thickness and doping level criteria were key in improving both the optical and electrical performances of future devices. An optically thin layer is needed to minimize parasitic absorption in the NIR spectral range while high doping levels has a direct impact on the electrical field in the absorber layer. Phosphorus doped µc-Si:H was first obtained despite Phosphorus' tendency to prevent crystalline phase nucleation. Increasing the dilution factor R_H from 25 to 50 helped maintain high crystallinity and reach doping levels $n > 10^{20}$ cm^{-3}. Relying on the same $R_H = 50$ deposition conditions, Boron doped µc-Si:H films stayed fully amorphous at high B_2H_6 gas flow. Low B_2H_6 gas flow could however still lead to a crystalline layer being obtained, at the cost of lower doping levels $p = 3.4 \times 10^{18}$ cm^{-3}. Boron doping of µc-Ge:H was experimented as a consequence of the disadvantages of p-type µc-Si:H. Adding B_2H_6 to a GeH_4 / H_2 mixture did not significantly affect the crystallinity of the deposited films, mostly likely due to the already high R_H needed for µc-Ge:H crystallization. X_c was kept constant (~63 %) while Boron incorporation into the layer increased conductivity by 3 decades, with a maximum doping level $p = 1.1 \times 10^{20}$ cm^{-3}. The high absorption coefficient of µc-Ge:H measured in chapter 3 implies Boron doped µc-Ge:H should only be used as a very thin layer on the backside of the device to limit parasitic absorption.

The material development done over the course of the past chapters lead us to make use of the knowledge acquired on intrinsic and doped micro-crystalline semiconductors to produce a simple photosensitive device. In the first section of chapter 5 a simple design for a photodiode prototype was proposed. This design met the thermal budget constraints of above-IC CMOS image sensors by keeping the whole process under 250 °C. A 3 steps production process was developed (cleaning - PECVD - Sputtering) while trying to maximize robustness and minimize complexity. Some compromises were made regarding the choice for the electrical contact layers and the dimensions of the photodiodes. This design thus leaves room for future improvement such as band diagram engineering, interface passivation and anti-reflective coating design. In order to find the most suitable absorber layer material, samples were produced with absorber layer ranging from pure µc-Si:H to pure µc-Ge:H. The test structure consisted of a glass / ITO / <n>µc-Si:H / µc-$Si_{1-x}Ge_x$:H / <p>µc-Si:H / Ag stack with an absorber roughly 200 nm thick. Light could thus be shined through the glass substrate and reach the NIP diode structure. Silver acted as an electrical contact as well as a back reflector. Electrical testing confirmed our devices to behave as a diodes. Samples with µc-Si:H or µc-Ge:H as absorber layers led to the worst performances due to optical and electrical limitations, respectively. µc-$Si_{1-x}Ge_x$:H absorbers on the other hand yielded encouraging results. A 224 nm µc-$Si_{0.4}Ge_{0.6}$:H layer was found to be optimal with an IQE at $\lambda = 1000$ nm reaching 17.6 %. Modeling of the optical properties of the photodiode with SILVACO was able to give better insight regarding the source of losses due to parasitic absorption and provided a

Cette thèse est accessible à l'adresse : https://theses.insa-lyon.fr/publication/2023ISAL0014/these.pdf
© [A. Wilson], [2023], INSA Lyon, tous droits réservés

theoretical upper bound for the EQE of the device. In an attempt to extend NIR sensitivity, the µc-$Si_{0.4}Ge_{0.6}$:H absorber thickness was varied in the 100 to 800 nm range while keeping the rest of the structure identical to what was previously described. The results showed the 224 nm thick absorber still performed better on average, with IQE reaching over 80 % in the visible range. However the 400 nm thick sample was found to perform better at $\lambda = 1100$ nm with an IQE of 5 %. So far, the tested samples reached our expectations in the visible range but degraded quickly when approaching NIR, in part due to absorption in the ITO layer. However, applying a 0.9 V reverse bias to the sample with a 400 nm thick µc-$Si_{0.4}Ge_{0.6}$:H absorber showed a gain of 250 % in EQE could be obtained in the NIR region up to $\lambda = 1250$ nm. The gain in EQE under bias likely originated from the charge transport mechanism shifting from being governed by diffusion length to drift velocity. Overall, the materials developed in chapters 3 and 4 were successfully implemented in a device, which highlighted the importance of a compromise between optical absorption and charge transport properties. The prototypes developed over the course of this chapter showed that CMOS above-IC compatible NIR photodetectors based on µc-$Si_{1-x}Ge_x$:H alloys are experimentally feasible.

Limitations and perspectives

Simple photodiodes, sensitive up to 1250 nm were obtained from PECVD grown µc-SiGe:H thin films. All semiconductor layers in the devices including n and p-type µc-Si:H and µc-$Si_{1-x}Ge_x$:H alloys were developed and characterized over the course of this project prior to their implementation. This approach proved to be successful, yet pushing the proof of concept further by producing a completed CMOS above-IC image sensor would require us to overcome some limitations. Several aspects of the current µc-SiGe:H thin films and photodiodes could indeed be improved.

First and foremost, the NIR sensitivity should be improved. Currently the highest IQE obtained for any sample at 940 nm is 27.3 %. Even under reverse bias, the best EQE at 1130 nm does not exceed 4 %. This limitation could be significantly improved by replacing ITO as the transparent electrode to prevent parasitic NIR absorption. Working to reducing the defect density in the absorber layer would also increase the extent of the electrical field in the intrinsic layer and ultimately provide better charge extraction, in particular when the electrical field is externally applied. Getting the $\overrightarrow{E}$-field to extend further into the absorber would mean we can increase its thickness to improve light absorption. We suspect transferring the production process to a PECVD setup in which doped layers and intrinsic layers can be deposited in separated chamber would reduce accidental residual doping after phosphorus doped µc-Si:H deposition. Another option to improve NIR absorption would be to consider µc-Ge:H films for the absorber as was done by Krause et al [26]. Unfortunately, every attempt at using this material in our devices was unsuccessful. Beyond Silicon-Germanium alloys, ternary alloys based on SiGeC [179] or SiGeSn [180] could compensate the shortcomings of SiGe in terms of NIR absorption. Both carbon and tin being available as gaseous precursors, they could potentially be deposited by PECVD.

Secondly, dark current characteristics of our photodiodes should be optimized. Due to the simplistic nature of the test structure and its many potential defects, it is difficult to pin-point the root cause for this high dark current under reverse bias. One of the solution which has been suggested by other authors [181] in order to reduce dark current was to add doped a-Si:H interlayers at the electrode-junction interface to act as selective potential barriers. This approach is similar to band diagram engineering which can be performed by tuning the work

Cette thèse est accessible à l'adresse : https://theses.insa-lyon.fr/publication/2023ISAL0014/these.pdf
© [A. Wilson], [2023], INSA Lyon, tous droits réservés

function of each material. On a more speculative note, some concern could be raised regarding the low charge mobility of these material. In the context of an image sensor, the bandwidth of the individual photodiodes (or pixels) should be high enough to ensure all charges are extracted prior to capturing the following image.

If the aforementioned issues are tackled, implementing these materials into a CMOS image sensor could be considered. Appropriate etching solutions and corresponding kinetics would still be to be setup to be able to isolate individual pixels and interconnect them with an underlying CMOS structure. Overall, many aspects of this work would benefit from being investigated further. If these limitations are addressed, we believe low thermal budget microcrystalline silicon-germanium alloys could be a compelling material for above-IC CMOS image sensors.

Cette thèse est accessible à l'adresse : https://theses.insa-lyon.fr/publication/2023ISAL0014/these.pdf
© [A. Wilson], [2023], INSA Lyon, tous droits réservés

Appendix A

Optical modeling of NIP devices with SILVACO

1 Modeling setup

In an effort to confront our experimental data with simulation, optical modeling of the photodiode structure was performed using the TCAD software SILVACO. This work was performed by engineering student Hala Houmsi in the context of her final year project. The modeled glass / ITO / µc-Si:P / µc-$Si_{0.4}Ge_{0.6}$:H / µc-Si:B / Ag photodiode corresponds to the samples produced in chapter 5. The goal of these simulations is to distinguish photons reaching the µc-$Si_{0.4}Ge_{0.6}$:H absorber from those absorbed parasitically in the ITO, µc-Si:H and Ag layers. The 1D model was defined with flat interfaces in order to rely on ray transfer matrix calculations [182] rather than ray tracing. It consists of 6 regions (see table A.1) corresponding to the different media light passes through. The thickness of each layer was obtained from TEM cross sections to match as closely as possible to our devices. The thickness of the Ag layer ensured no transmission occurred in the spectral range of interest.

Region	Thickness	Refractive index
glass	semi-∞	$n = 1.643$
ITO	100 nm	from figure 1.6
µc-Si:P	30 nm	from figure 1.6a
µc-$Si_{0.4}Ge_{0.6}$:H	x nm	from figure 3.10
µc-Si:B	45 nm	from figure 1.6a
Ag	152 nm	from ref. [138]

Table A.1: Medium and corresponding thickness used for each region of the simulated structure.

A beam of N_{ph} photons (10^{12} cm^{-2}) is shined from the glass medium towards the glass/ITO interface at each wavelength. From the successive reflections and transmissions at each interface and using the dispersion relation $\widetilde{n}(\lambda)$ of each medium, the absorption of photons can be calculated at every point in the depth of the photodiode for a given photon wavelength. Assuming each absorbed photon in each layer produces a free charge carrier this absorption profile turns into a photogeneration profile $n_{photogen}(x, \lambda)$ which is function of depth and wavelength.

Cette thèse est accessible à l'adresse : https://theses.insa-lyon.fr/publication/2023ISAL0014/these.pdf
© [A. Wilson], [2023], INSA Lyon, tous droits réservés

2 *SiGe60%200nm* NIP photodiode modeling

The photogeneration profile for sample *SiGe60%200nm* with a 224 nm thick absorber is given in figure A.1 at different wavelengths in the UV to NIR range. The higher $n_{photogen}(x)$ the higher the absorption in that region of space. It can be seen that :

- at $\lambda = 300$ nm, absorption only occurs in the ITO and µc-Si:P layers
- at $\lambda = 500$ nm, most of the absorption takes place in the µc-SiGe:H absorber
- at $\lambda = 700$ nm, the ITO and µc-Si:P layer are almost transparent. The absorber is not completely absorbant meaning the incident and reflected electromagnetic waves will interfere in the bulk of the absorber, creating a type of standing wave with regions of high and low photogeneration.
- at $\lambda = 940$ nm, a similar behavior to the one observed at 700 nm can be seen, the standing wave effect is more intense due to the lower absorption of the material. Part of the photons now reach the Ag layer to be absorbed.
- at $\lambda = 1130$ and 1350 nm, absorption in the ITO prevails, preventing a large amount of photons from reaching the underlying layers. Photogeneration in the absorber drops.

From this data we can see the carriers generated in layers other than µc-SiGe:H will be recombined and lost. The photogeneration rate in the absorber can be extremely uneven due to interferences in the film. Ideally, we could tuned the peaks and valleys of this interference patterns to enhance photogeneration in the space charge region of the absorber. By integrating $n_{photogen}(x)$ on the entire thickness of a layer and normalizing it by the photon source intensity we can get the relative photon absorption (RPA) of each layer at a given wavelength and the reflectance of the whole stack $R_{sim.}$. Since the model used did not account for the air/glass interface, the RPA must be corrected using the Fresnel reflection coefficients of each interface :

$$r_{air/glass/stack} = \frac{r_{air/glass} + r_{glass/stack}}{1 + r_{air/glass} \cdot r_{glass/stack}} \quad \text{with} \quad r_{glass/stack} = \sqrt{R_{sim.}(\lambda)} \tag{2.1}$$

The corrected RPA is then obtained from :

$$RPA_{corr} = RPA_{sim.} \cdot \frac{1}{1 - R_{sim.}} \cdot (1 - \mid r_{air/glass/stack} \mid^2) \tag{2.2}$$

The relative photon absorption for each layer in the stack was presented in chapter 5 and is recalled in figure A.2 for good measure. The impact on total absorption of each individual layer can therefore be identified. In our case, we could wish to maximize the red curve corresponding to the absorber layer.

This simulation and the subsequent results were discussed in chapter 5, section 2.3.3 and will thus not be recalled here.

3 *SiGe60%400nm* NIP photodiode modeling

The same modeling as described above was performed with sample *SiGe60%400nm* were the absorber thickness was set to 448 nm (double the previous one, as deposition time had been doubled during the process). The relative photon absorption obtained in that configuration

Cette thèse est accessible à l'adresse : https://theses.insa-lyon.fr/publication/2023ISAL0014/these.pdf
© [A. Wilson], [2023], INSA Lyon, tous droits réservés

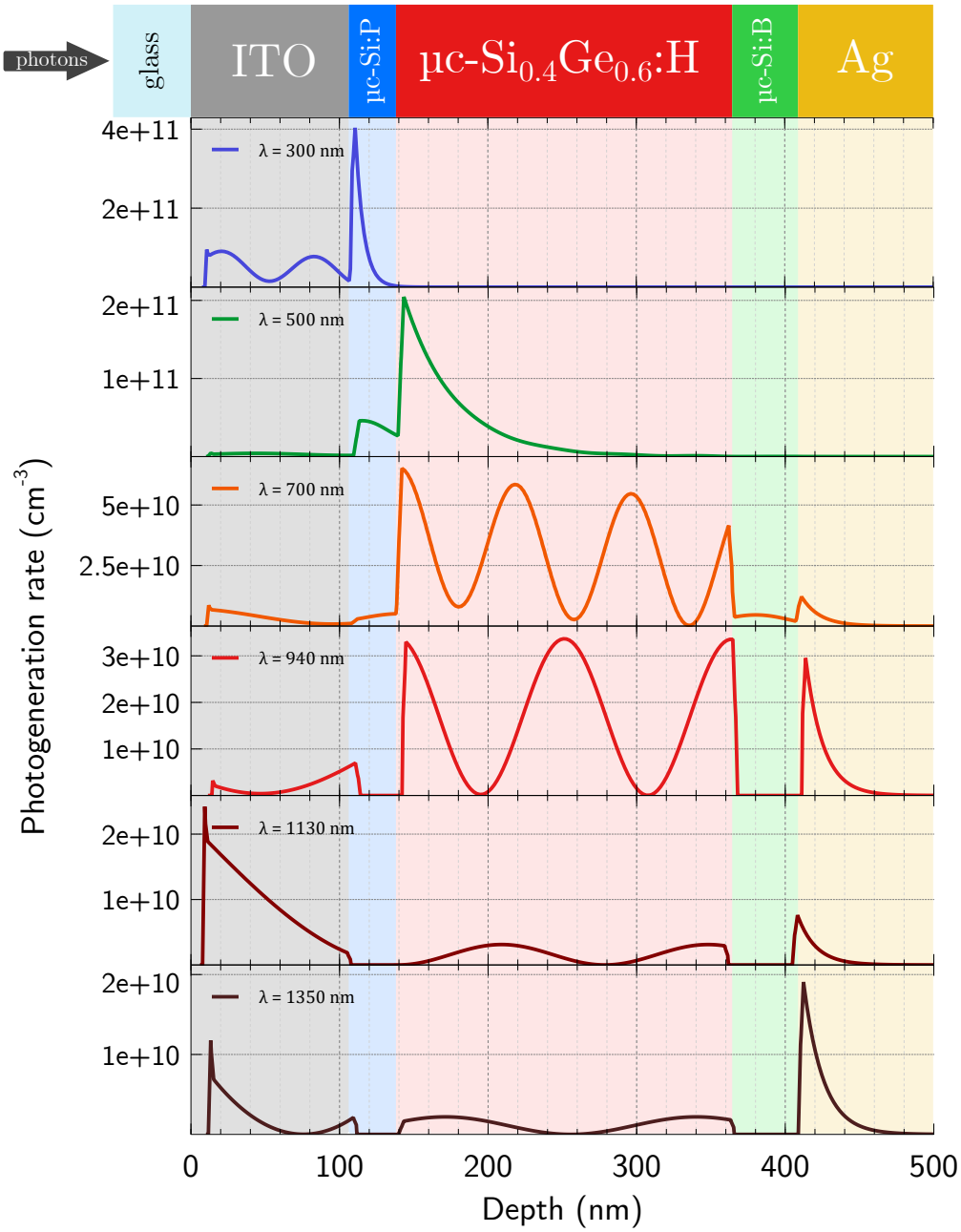

Figure A.1: Photogeneration rate as a function of depth for different wavelengths in the simulated device.

Cette thèse est accessible à l'adresse : https://theses.insa-lyon.fr/publication/2023ISAL0014/these.pdf
© [A. Wilson], [2023], INSA Lyon, tous droits réservés

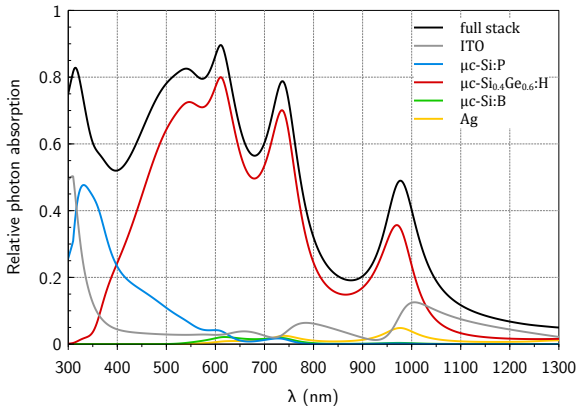

Figure A.2: Relative photon absorption in each layer of the simulated *SiGe60%200nm* sample. The *full stack* curve corresponds to the absorbance A of the stack, which is equal to $1 - R(\lambda)$.

is shown in figure A.1. The parasitic absorption in NIR is found to be also due to ITO in this configuration. By doubling the absorber thickness constructive interference in the film occur more frequently. Four resonance peaks can be identified in the 600 to 1300 nm range. These resonance are reminiscent of a Fabry-Perot cavity [175] in which light bounces back and forth between interfaces, leading to an "optical distance" traveled by photons being greater than a single round trip. This leads to enhanced RPA in the absorber, which corresponds to the maximum theoretical value for the EQE of the device. Since we are aiming at specific wavelengths (940, 1130 or 1350 nm), we could in theory design the absorber to exhibit a resonance at the desired wavelength to maximize EQE.

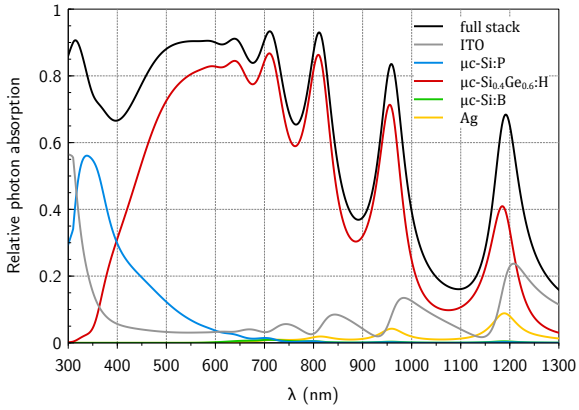

Figure A.1: Relative photon absorption in each layer of the simulated *SiGe60%400nm* sample

In practice, the resonance predicted by our theoretical model exist but are extremely dampened as can be seen in figure A.2a. In this figure, the experimental EQE and theoretical maximum EQE are compared. The fact that the resonances are much lower in intensity for $EQE_{exp.}$ could be a consequence of the thickness distribution of the different layers. Instead of a homogeneous 448 nm layer, the real device has some roughness and some variation in thickness over the probed area (a few mm²). The peak is thus broadened and EQE does not reach the high values predicted by our model.

Additionally, although experimental and simulation data exhibit similar trends , $EQE_{exp.}$

Cette thèse est accessible à l'adresse : https://theses.insa-lyon.fr/publication/2023ISAL0014/these.pdf
© [A. Wilson], [2023], INSA Lyon, tous droits réservés

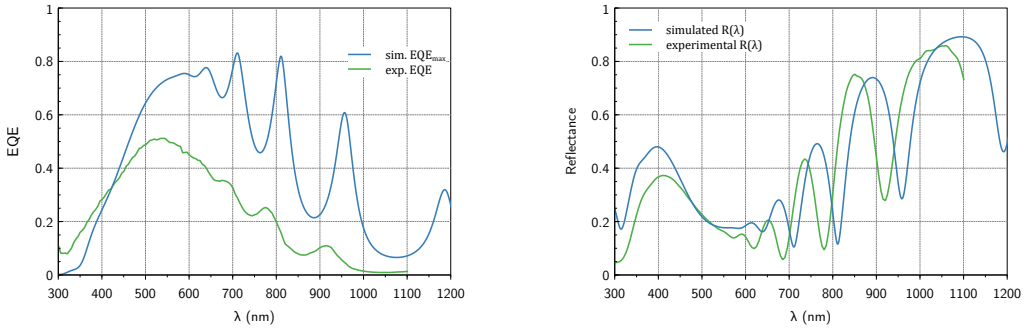

(a) (b)

Figure A.2: (a) Experimental and simulated EQE (b) Experimental and simulated reflectance for sample *SiGe60%400nm.*

remains much lower than the simulated curve. In the visible range, around 50 % of the absorbed charges are lost. This difference cannot be explained solely by the difference in thickness of simulation and experiment revealed by the shift in reflectance data of figure A.2b. This gap between $EQE_{exp.}$ and $EQE_{sim.}$ is an indicator of the poor charge transport properties of the µc-SiGe:H absorber since the simulation was able to identify the proportion of losses due to parasitic absorption. This hypothesis is further confirmed by comparing $EQE_{sim.}$ with the EQE of *SiGe60%400nm* under an external reverse bias (figure A.3). In chapter 5, section 4.2 we argue that the electrical field extending in the absorber due to the external bias improves charge transport by minimizing the residence time of charges in the absorber. From this data we can see that $EQE_{exp.}$ at 700 nm goes from collecting around 50 % of the total photogenerated charges to 100 %. This comparison is qualitative as the model is not perfect (the thickness should be adjusted) but it provides greater insight into the underlying gain mechanisms through bias.

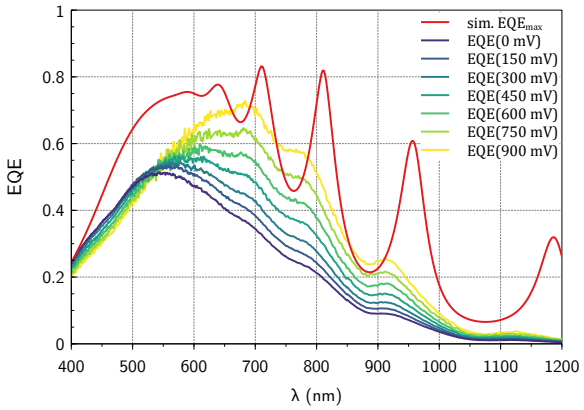

Figure A.3: Experimental EQE with applied reverse bias and simulated EQE for sample *SiGe60%400nm.*

With this theoretical model readily available, we can now actively design the optical behavior of our photodiodes and discard inadequate materials provided we have their refractive index.

Cette thèse est accessible à l'adresse : https://theses.insa-lyon.fr/publication/2023ISAL0014/these.pdf
© [A. Wilson], [2023], INSA Lyon, tous droits réservés

Cette thèse est accessible à l'adresse : https://theses.insa-lyon.fr/publication/2023ISAL0014/these.pdf
© [A. Wilson], [2023], INSA Lyon, tous droits réservés

List of Figures

0.1 Solar irradiance at ground level when the sun is at a 48.2° zenith angle (AM1.5g). The solar spectrum resembles a 5250 °C black body, with absorption bands due to the atmosphere. In particular water vapor in the atmosphere is responsible for 3 dips in the irradiance at 940, 1130 and 1350 nm. . . . 1

0.2 Schematic representation of 3 CMOS types of image sensors (frontside, backside and above-IC), defined by the location of the photodiode. Adapted from STEMMER Imaging. . . . 2

1.1 (a) Simulated (solid and dotted lines) and experimental (points) responsivity for SiGe and Ge photodectectors at -1 V bias [4] (b) Responsivity of a 15 µm thick Ge photodectector at -0.5 V bias [5] . . . 6

1.2 Responsivity for a 10 µm thick c-SiGe PIN photodiode at variable Ge fraction obtained by Silvaco simulation. [9] . . . 7

1.3 Quantum efficiency of PIN solar cells with a : (a) 900 nm thick µc-$Si_{0.6}Ge_{0.4}$:H absorber [21] (b) 1 µm thick µc-$Si_{0.5}Ge_{0.5}$:H absorber [22]. . . . 7

1.4 Quantum efficiency for a PIN photodiode with a 110 nm thin µc-Ge:H absorber deposited by PECVD at different germane concentration GC. Measurements were done under -0.2 V bias at 250 K.[26] . . . 8

1.5 (a) Test structure and (b) quantum efficiency of a µc-Si:H(p)/µc-$Si_{0.27}Ge_{0.63}$:H/c-Si:H(n) solar cell.[27] . . . 8

2.1 Diagram of the evolution of the potential near the plasma-wall interface, with V_S the surface potential and λ_D the Debye length [33]. . . . 10

2.2 INL's capacitive PECVD reactor, with a representation of the chamber's design. . . . 12

2.3 Simplified model for thin film growth on the surface of a substrate during PECVD deposition, adapted from [39] . . . 14

3.1 Diagram of a monocrystalline, microcrystalline and amorphous arrangement of Silicon atoms. . . 15

3.2 Density of the different radicals and ions present in a SiH_4/H_2 steady state plasma. The species marked with a * correspond to ionic species. [43] . . . 16

3.3 Schematic representation of the impact of the gas mixture silane concentration on the morphology of the crystalline phase [41]. . . . 16

3.4 Size (*light:*δ) and volume fraction (*dark:*X_C) of microcrystallites as a function of process conditions. From [43]. . . . 17

3.5 Schematic representation of the three growth models of µc-Si:H [43] . . . 18

3.6 The growth of µc-Si:H starts from an incubation phase where the material is mainly amorphous. 19

3.7 Absorption coefficient of c-Si, a-Si:H and µc-Si:H measured by PDS [40] . . . 20

3.8 Density of state of disordered silicon. The continuum of defects (band tails) prevents the formation of a sharp band-gap [45]. . . . 21

4.1 Band structure of crystalline Germanium at 300 K.[58] . . . 22

4.2 Raman crystallinity (see chapter 2, section 2.1) as a function of ϕ_{GeH_4} for different substrate temperatures. [64] . . . 23

Cette thèse est accessible à l'adresse : https://theses.insa-lyon.fr/publication/2023ISAL0014/these.pdf
© [A. Wilson], [2023], INSA Lyon, tous droits réservés

4.3 Absorption coefficient α for (a) a-Ge:H vs a-Si:H adapted from [75] and (b) µc-Ge:H vs µc-Si:H with crystalline materials as reference (dashed lines) [23] . . . 24
4.4 Mobility lifetime product $\mu_p\tau_p$ of holes for (a) µc-Ge:H deposited at different germane concentration GC [66] and for (b) a-Si:H and µc-Si:H films. [77] . . . 25
4.5 Ambipolar diffusion length of µc-Ge:H deposited at different hydrogen dilution levels.[66] . . . 25
5.1 Ge content of the film as a function of the germane concentration ($GeH_4/(SiH_4/GeH_4)$) of the gas phase under low and high ion bombardment conditions, taken from [38]. The AIST data come from ref. [21]. . . . 27
5.2 (a) Absorption spectrum and (b) Quantum efficiency of p-i-n solar cells of various grades of µc-SiGe:H alloy. [23] . . . 28
5.3 SEM images of the surface of SiGe:H samples deposited at 190 °C, 750 mTorr, 240 mW/cm² and (a) $R_H = 20$ (b) $R_H = 25$ [90]. Images were taken at the same magnification (500 nm scale). . . . 29
5.4 $\Delta\sigma = \sigma_{ph} - \sigma_{dark}$ for: (a) µc-$Si_{1-x}Ge_x$:H [22] (b) proto/nano-crystalline SiGe:H alloy deposited at $GC = GeH_4/(SiH_4 + GeH_4) = 6$ %. $D = R_H$ is the hydrogen dilution factor. [90] . . . 30

1.1 (a) Photo of the PlasmaTherm Vision 310 PECVD equipment used (b) Schematic cross-section of the reactor chamber © PlasmaTherm . . . 32
1.2 Top view of the PECVD chamber bottom electrode after a 120 min deposition (process parameters R_H=20 - 50W - 400 mTorr - Φ_{total}=100 sccm). The radial inhomogeneity is extremely important with a 600 nm thick layer deposited at the edges. . . . 35
1.3 Film growth radial uniformity as a function of : (a) pressure, at fixed $\Phi_{H2} = 500$ sccm, (b) RF-Power, at fixed $R_H = 25$, (c) Φ_{H2}, at 600 mTorr. . . . 36
1.4 Schematic cross-sectional view of the gas flow direction between electrodes in the PECVD reaction chamber. . . . 36
1.5 c-Si substrate cleaning process prior to PECVD deposition. . . . 37
1.6 Glass substrate cleaning process prior to PECVD deposition. . . . 37
1.7 ITO cleaning process prior to PECVD deposition. . . . 38
2.1 Schematic view of the backscattering Raman micro-spectrometer used, adapted from physicsopenlab.org. . . . 39
2.2 (a) Raman spectrum of a-Si:H [105] (b) Raman spectra of µc-Si:H with different crystallite size L. [103] . . . 39
2.3 Fitted Raman spectrum for a µc-Si:H ($X_c = 41.4$ %) film deposited on glass. The fitted curve is the sum of the 3 individual gaussian curves and closely matches our experimental data. . . . 41
2.4 Fitted Raman spectra for a-Ge:H and µc-Ge:H films. [108] . . . 41
2.5 Fitted Raman spectrum for a µc-Ge:H ($X_c = 56.3$ %) film deposited on glass. The fitted curve closely matches our experimental data. . . . 42
2.6 (a) Raman spectrum of a-$Si_{0.65}Ge_{0.35}$:H [113] (b) Raman spectra of µc-SiGe:H films with increasing Ge fraction. [110] . . . 42
2.7 Schematic diagram of a TEM column, taken from [114]. . . . 43
2.8 Annular dark field STEM imaging of a monocrystalline silicon sample. . . . 44
2.9 EELS Image and composition profile of a µc-SiGe:H film deposited on c-Si. . . . 45
2.10 (a) TEM lamella diagram from [116] (b) Micromanipulator lift-out of a lamella. . . . 45
2.11 Schematic diagram of a SIMS instrument, the primary ion beam is generated at the top and secondary ions are analyzed in the mass spectrometer at the bottom, taken from [121]. . . . 47
2.12 ToF-SIMS Depth profile for Phosphorus of an n-type µc-Si:H thin film deposited on glass. . . . 48
3.1 Optical setup of a spectroscopic ellipsometer, taken from [123]. . . . 49
3.2 Building blocks of an ellipsometric model. . . . 49
3.3 Reflectance spectrum of a glass / ITO / µc-Si:H / µc-SiGe / µc-Si:H / Ag stack. . . . 52

Cette thèse est accessible à l'adresse : https://theses.insa-lyon.fr/publication/2023ISAL0014/these.pdf
© [A. Wilson], [2023], INSA Lyon, tous droits réservés

3.4 FILMETRICS F20-UV reflectometer used for reflectance spectra measurement. The sample is placed on the metallic grid on the right side of the image. 53
3.5 Schematic representation of the EQE acquisition, from the light source to the output voltage. . . 54
4.1 Hall effect in a semiconductor thin film. 55
4.2 (a) HMS5000 sample mount and N_2 cooling reservoir (b) Sample mount with 4 pin contacts. . . 56
4.3 Interference fringes from two LASER beams interfering at an angle θ. 57
4.4 SSPG plot of β as a function of Λ for a a-Si:H film [77]. The fitted L_{diff} was found to be equal to 154 nm. 58
4.5 Top view photo of the automated steady state photocarrier grating equipment at GeePs. The LASER beam path has been added in red form better comprehension. 58
4.6 Schematic of the automated steady state photocarrier grating setup at GeePs, taken from geeps.centralesupelec.fr. 59

1.1 Raman spectra comparison of a-Si:H (left), µc-Si:H (center) and standard c-Si (right), obtained for a laser excitation wavelength $\lambda_{exc} = 473$ nm. 62
1.2 (a) Cross-section and (b)-(c) Top view SEM images of 1050 nm thick µc-Si:H deposited on c-Si substrate (sample #264, see table 3.2) 63
1.3 Grazing-Incidence XRD diffractogram of a 339 nm thick µc-Si:H film. Three peaks were identified at 28.4°, 47.3° and 56.1°, respectively. 64
1.4 GI-XRD diffractogram and FWHM of µc-Si:H in two deposition conditions, *low power* (#280, $D_{avg} = 14.3$ nm) and *high power* (#285, $D_{avg} = 6.3$ nm). See table 3.2. 65
1.5 Cross-sectional SEM image of µc-Si:H deposited on c-Si and corresponding ellipsometric data fitted using a Kato-Adachi dispersion formula ($\chi^2 = 1.17$). 65
1.6 (a) Optical indices n and k of a-Si:H, µc-Si:H and c-Si obtained by Spectroscopic Ellipsometry (SE). (b) Absorption coefficient comparison of µc-Si:H and c-Si. The evaluation by SE of α below 10^3 cm^{-1} comes with a lot of uncertainty. 66
2.1 (a) Raman crystallinity, (b) deposition rate and (c) film thickness as a function of R_H. $t_{dep.}$ was set at 20 min., temperature at 250°C and pressure at 1000 mTorr. 68
2.2 Effect of applied RF-Power on Raman spectra, crystallinity and deposition rate of µc-Ge:H at constant dilution factor $R_H = 200$, $T = 250$ °C, $P = 1000$ mTorr, Φ_{tot}= 350 sccm. 69
2.3 Raman crystallinity for a two-steps growth process (a) with nucleation phase at $R_H = 200$. Nucleation layer thickness $d_{nucleation}$ varies and $d_{R_H 50} = 100$ nm (b) with nucleation phase at $R_H = 400$. Nucleation phase thickness $d_{nucleation}$ varies and $d_{R_H 100} = 75$ nm. 70
2.4 Cross-sectionnal view SEM images and Raman spectra of amorphous Germanium (left) and microcrystalline Germanium (right) deposited on c-Si. Surface roughness characteristic of microcrystalline materials can be seen in the second image. Corresponding deposition conditions can be found in table 3.6. 71
2.5 (a) Experimental data from ellipsometry measurement of a thick a-Ge:H layer on c-Si. Under 850 nm the layer can be considered as optically thick and can thus be fitted using point-by-point calculation. (b) Optical indices of amorphous Germanium fitted using a Double New Amorphous dispersion formula (solid line) and using a combination of dispersion formula and point-by-point calculation (dashed line). 72
2.6 (a) Best ellipsometry model found for fitting µc-Ge:H layers deposited on glass (b) Fitted I_s and I_c (see chapter 2) as a function of photon wavelength, $\chi^2 = 1.7$. 73
2.7 Fitted optical coefficients n and k for a-Ge:H and µc-Ge:H as a function of photon energy $h\nu$. Optical indices for c-Ge are given for comparison and taken from [138]. 74
2.8 Absorption coefficient for a-Ge:H and µc-Ge:H as a function of photon wavelength λ. Spectroscopic ellipsometry is not precise enough to give a reliable value below $\alpha = 10^2$ cm^{-1}. 75

Cette thèse est accessible à l'adresse : https://theses.insa-lyon.fr/publication/2023ISAL0014/these.pdf
© [A. Wilson], [2023], INSA Lyon, tous droits réservés

2.9 Effect E_i for each parameter tested (Temperature, Dilution and RF-Power) as a function of parameter level $i = \{+0, +1, +2\}$, (a) for photo-response, (b) for resistivity. 76

2.10 Raman crystallinity X_c vs photo-response $\Delta\sigma$ under 1 sun illumination. No clear correlation can be established. 77

3.1 Schematic cross section of a SiGe:H/SiN_x stack. 78

3.2 Cross-sectionnal SEM image of SiGe/SiN stack #2. 78

3.3 ToF-SIMS Ge depth profile obtained from SiGe stack #1 (see table 3.9). 79

3.4 $x_{Ge} = f(GC)$ measured by ToF-SIMS for different deposition conditions: (left) at increasing R_H - stacks #1/2/3, (center) at increasing RF Power - stacks #4/3/5, (right) at increasing pressure - stacks #6/7. Details on deposition conditions can be found in table 3.9. 80

3.5 EELS TEM image of SiGe/SiN stack #3. The individual layers can be identified due to their composition. The 4 first layers of SiGe:H do not contain any Ge due to an unforeseen hardware limitation. 80

3.6 Germanium fraction as a function of Germane concentration for stack #7. Experimental data is represented with green squares, the solid black curves corresponding to the fitted model using eq. 3.1 with $R = 3$. 81

3.7 High Resolution TEM images of a 193 nm µc-SiGe:H film deposited on c-Si. (a) Cross- sectional view of the whole film, (b) atomic structure of sample's surface, (c) atomic structure at the c-Si/SiGe interface, (d) FFT of the layer shown in subfigure (c). 82

3.8 n and k optical indices of c-SiGe for $x_{Ge} = 20\,\%$, $50\,\%$ and $80\,\%$ 83

3.9 Model used for samples of µc-SiGe:H deposited on glass. Screenshot from DeltaPsi2 software. . 84

3.10 Optical indices (a) n and (b) k of µc-SiGe:H alloys of Ge fraction. Data for µc-Si:H and µc-Ge:H obtained in section 1 and 2 of this chapter have been added for reference. 85

3.11 Absorption coefficient α of µc-SiGe:H obtained from Spectroscopic Ellipsometry fitted data. Absorption for µc-Si:H and µc-Ge:H from section 1 and 2 of this chapter have been added for reference. 86

3.12 Diffusion length as a function of µc-SiGe:H alloy composition obtained from SSPG measurements at room temperature. Error bars correspond the experimental setup's intrinsic uncertainty estimated at 5 %. 87

2.1 Raman spectra of samples deposited using $R_H = 25$ for different gas phase concentration of phosphine $\beta = \phi_{PH_3}/\phi_{SiH_4}$. The redshift and broadening of the Si-Si peak shows the crystalline to amorphous transition 94

2.2 Dependence of Raman crystallinity X_c on doping level in different deposition conditions. Film thickness for R_H = 25, low power and high power samples are 160 nm, 168 nm and 310 nm respectively 95

2.3 (a) Dependence of Raman crystallinity X_c on deposited film thickness for $\beta = 0.1\%$ (b) Frontside and backside Raman spectra of low and high power deposited films. The noticeable increase in signal intensity in the amorphous region (480 cm^{-1}) reveals the presence of an amorphous phase at the interface with the substrate. 96

2.4 AFM surface image of *low power* (top) and *high power* (bottom) deposited films for two samples of increasing film thickness. 97

Cette thèse est accessible à l'adresse : https://theses.insa-lyon.fr/publication/2023ISAL0014/these.pdf
© [A. Wilson], [2023], INSA Lyon, tous droits réservés

2.5 (a) Phosphorus concentration in the deposited films measured by ToF-SIMS , and active P concentration determined by Hall effect, as a function of the phosphine to silane ratio in the PECVD chamber (b) Solid phase phosphorus concentration as a function of gas phase phosphine to silane ratio, the dashed line corresponds to a 1:1 ratio between [P]/[Si] and β 98

2.6 Normalized Raman spectra and calculated Raman crystallinity X_c of Boron-doped µc-Si:H for different doping gas ratios β, ranging from 0 % to 0.5 %. The data shows the degradation of the crystalline structure with increasing B_2H_6 concentration. 100

2.7 Active p-type doping level of Si:H measured by Hall effect as a function of doping gas ratio β. . 100

2.8 Nomarski interference contrast microscopy images of Boron doped µc-Si:H deposited on c-Si show a marked increase in roughness for the highest β values (right). 101

2.9 SEM image of <p> µc-Si:H deposited at high diborane gas flow ($\beta = 0.5\,\%$) on c-Si substrate and taken at a 45° angle. The severe lack of uniformity of the layer and blisters may in part be due to hydrogen desorption. 101

3.1 SEM cross-sectional image of Boron doped µc-Ge:H deposited on c-Si. 103

3.2 Raman crystallinity X_c (a) and Raman spectra (b) obtained for Boron doped µc-Ge:H thin films on glass. 103

3.3 Conductivity and mobility measurement by Hall effect of Boron doped µc-Ge:H, solid lines are a guide for the eye. 104

1.1 Schematic representation of the proposed prototype design for P-I-N photodiodes. Each sample holds 8 electrical contacts defining 8 independent photodiodes. 108

1.2 Prototype device production process (a) the ITO coated glass is cleaned - see 1.2 (b) the N, I and P parts of the diode are deposition by PECVD with a central mask in order to have access to ITO - see 1.3 (c) Sputtering of metallic anode and cathode by using a 3D printed mask - see 1.4. . . . 108

1.3 Schematic top view of the pattern dimensions defined by mask placement during deposition. The measurements given here correspond to the ideal result. 109

1.4 UV-NIR transmission of a 550 µm thick glass slide from OSSILA. 110

1.5 Refractive index of sputtered ITO for different carrier density values. Obtained by Holman et al. [168] 110

1.6 Refractive index and absorbance of a 100 nm ITO film, measured by spectroscopic ellipsometry. The absorbance is calculated from the extinction coefficient k. 111

1.7 (a) The c-Si mask is placed in the center of the ITO coated glass substrate using guides. (b) N, I and P layers are deposited by PECVD. (c) The c-Si mask is removed leaving the central part of the substrate clear of any deposition. Scheme not to scale, the c-Si mask is 3 mm wide and 725 µm thick. 111

1.8 Top and bottom view of the 3D printed PLA mask design. The sample sits in the grooved out rectangle seen in the bottom view. 112

1.9 Completed device (a) backside and (b) frontside view. 113

1.10 3D-printed opto-electronic test bench design for backside electrical contact. (a) Bottom view with electrical connections (b) Top view with opening window for incident light (c) Close up of the opening window (d) Side view of the 9 spring loaded pins contacting the Ag electrodes. . . 114

Cette thèse est accessible à l'adresse : https://theses.insa-lyon.fr/publication/2023ISAL0014/these.pdf
© [A. Wilson], [2023], INSA Lyon, tous droits réservés

2.1 (a) Experimental data and fitted curve for $x_{Ge} = f(GC)$. See chapter 3. (b) Deposition rate extrapolation, used for $x_{Ge} = 40\% \rightarrow 75\%$ . . . 115
2.2 Raw Raman spectra (blue), reference µc-Si:H peak (green) and corrected data (orange) for *SiGe40%* and *SiGe55%* samples. Some artifacts remain in the 520 cm^{-1} region due to peak position mismatch. . . . 117
2.3 (a) Corrected and normalized Raman spectra for µc-SiGe:H alloys with increasing Ge fraction. The Si-Si peak can simultaneously be seen broadening and shifting to lower $\Delta\omega$ values (b) Si-Si bond peak position as a function of expected Ge fraction. Data from the paper by Carius et al. [88] on µc-SiGe:H is added for reference. . . . 117
2.4 TEM cross section of the glass / ITO / µc-Si:P / µc-SiGe:H / µc-Si:B layer stack for samples (a) *SiGe55%* (b) *SiGe60%*. . . . 118
2.5 High resolution TEM images of sample *SiGe60%*. (a) ITO and µc-Si:P films with numerical diffraction patterns (b) µc-Si:P / µc-SiGe:H interface (c) bulk of the µc-SiGe:H layer (d) µc-SiGe:H / µc-Si:B interface with corresponding diffraction pattern for each layer. . . . 120
2.6 Energy Dispersive X-ray Spectroscopy (EDX) mapping and line profile for sample *SiGe60%*. . . . 121
2.7 (a) Current-Voltage (IV) characteristic for NIP *SiGe* devices, a diode behavior is observed. (b) Single diode equivalent circuit, from [174]. . . . 121
2.8 External Quantum Efficiency as a function of wavelength for SiGe NIP devices. The absorber is 200 nm thick with its composition x_{Ge} varying in the 0 to 75 % range. . . . 123
2.9 EQE measurement repeatability on 3 separate photodiodes of the *SiGe55%* sample. The differences are due to local variations in film thickness. . . . 124
2.10 (a) Internal Quantum Efficiency calculation for EQE and Reflectance spectra for *SiGe70%*. (b) Repeatability of the reflectance measurement on the *SiGe70%* sample. . . . 124
2.11 Internal Quantum Efficiency as a function of wavelength for SiGe NIP devices with 200 nm thick absorber. . . . 125
2.12 IQE heat-map as a function of photon wavelength and absorber Germanium composition. The red areas represent a high IQE while the blue areas correspond to a value close to 0 %. In the NIR region, *SiGe60%* stands out as the best performing device. . . . 126
2.13 Penetration depth δ of photon as a function of wavelength for µc-SiGe:H alloys with $x_{Ge} = 40 - 100\,\%$. A layer of thickness δ absorbs 63 % of incoming light at corresponding λ. The dashed curves are interpolated values. . . . 126
2.14 Relative photon absorption in each layer of the simulated *SiGe60%* sample. The *full stack* curve corresponds to the absorbance A of the stack, which is equal to $1 - R(\lambda)$. . . . 128
2.15 (a) Reflectance (b) EQE experimental and simulated data comparison for sample *SiGe60%*. The thickness used for the simulation are given in table 5.4. . . . 129
3.1 Raman spectrum of the absorber layer in NIP devices with increasing µc-SiGe:H thickness. . . . 130
3.2 IV curves for NIP devices with increasing µc-SiGe:H absorber thickness. . . . 131
3.3 Internal Quantum Efficiency as a function of photon wavelength for NIP devices with µc-$Si_{0.4}Ge_{0.6}$:H absorber layer. The thickness of the intrinsic absorber $d_{abs.}$ was increased for 100 to 800 nm. . . . 132
3.4 Theoretical maximum absorption within the µc-$Si_{0.4}Ge_{0.6}$:H as a function of λ and $d_{abs.}$. Absorption is obtained from equation 2.4. $\alpha_{x_{Ge}}(\lambda)$ is taken from experimental data (3.2) and $d = 2 \times d_{abs.}$ due to the Ag back-reflector of our devices. . . . 133
4.1 Impact on EQE of external reverse bias applied to the NIP junction with a 400 nm µc-$Si_{0.4}Ge_{0.6}$:H absorber (*SiGe60%400nm*) . . . 135
4.2 Gain in EQE $G(\lambda, \Delta V) = EQE(\lambda, \Delta V)/EQE(\lambda, 0\,V)$ of a NIP junction with a 400 nm µc-$Si_{0.4}Ge_{0.6}$:H absorber (*SiGe60%400nm*). . . . 136

Cette thèse est accessible à l'adresse : https://theses.insa-lyon.fr/publication/2023ISAL0014/these.pdf
© [A. Wilson], [2023], INSA Lyon, tous droits réservés

4.3 The competition between electric field and diffusion length lead to 3 charge transport regimes. A schematic representation of the corresponding band diagram and electric field in 1D is proposed for the simple case of a PIN homojunction. 136

A.1 Photogeneration rate as a function of depth for different wavelengths in the simulated device. . 145
A.2 Relative photon absorption in each layer of the simulated *SiGe60%200nm* sample. The *full stack* curve corresponds to the absorbance A of the stack, which is equal to $1 - R(\lambda)$. 146
A.1 Relative photon absorption in each layer of the simulated *SiGe60%400nm* sample 146
A.2 (a) Experimental and simulated EQE (b) Experimental and simulated reflectance for sample *SiGe60%400nm.* 147
A.3 Experimental EQE with applied reverse bias and simulated EQE for sample *SiGe60%400nm.* . . 147

List of Tables

1.1 Electron mobility in crystalline, amorphous and microcrystalline silicon (order of magnitude). 19
1.2 Deposition parameters of a-Ge:H and µc-Ge:H films gathered from the literature. Unless stated otherwise, all the films were deposited with a 13,56 MHz capacitively coupled PECVD. 22
1.3 Deposition parameters for µc-SiGe:H films gathered from the literature. 27

2.1 PlasmaTherm Vision 310 PECVD specifications. 32
2.2 Gas lines, concentration and flow rate specifications. 32
2.3 Ecopia HMS5000 specifications. 56

3.1 Typical deposition conditions for Silicon based thin films. A higher R_H yields a microcrystalline structure at the cost of a decreased deposition rate. 62
3.2 Deposition conditions for "thick" µc-Si:H samples #264, #280, #285. 63
3.3 X-ray diffraction peak and corresponding crystallographic parameters for $\lambda_{X-ray} = 1.54$ Å (from [133]) 64
3.4 Model result for µc-Si:H deposited on c-Si modeled with a Kato-Adachi dispersion formula. 66
3.5 Growth rate and Raman crystallinity for silane-based and germane-based plasmas in similar dilution and power deposition conditions. Temperature and Pressure have much less impact on growth rate. 67
3.6 Deposition conditions, measured thickness and X_c of Ge:H thin films deposited from a $GeH_4 + H_2$. 71
3.7 DoE parameters and corresponding levels 75
3.8 Deposition parameters for each run of the 3^3 factorial design of experiment. . . 76
3.9 Deposition conditions for the SiGe:H/SiN_x multilayered stacks used for calibration. 77
3.10 Fitted R values for each SiGe/SiN multilayer stack according to the expression given in eq. 3.1 81

Cette thèse est accessible à l'adresse : https://theses.insa-lyon.fr/publication/2023ISAL0014/these.pdf
© [A. Wilson], [2023], INSA Lyon, tous droits réservés

3.11 Deposition conditions for µc-SiGe:H thin films used for SE measurements. . . . 85
3.12 Deposition conditions for µc-SiGe:H thin film deposited on glass for SSPG measurements 87

4.1 Deposition conditions for P doped µc-Si:H 94
4.2 Hall effect measurement of conductivity (σ), mobility (μ_H) and doping level at room temperature in the Van Der Pauw configuration. 98
4.3 PECVD deposition conditions for boron-doped µc-Ge:H layers. Samples were deposited on c-Si and glass substrates. 102

5.1 Deposition conditions for N and P layers used in NIP photodiodes. β is the doping gas to silane ratio defined in chapter 4. 114
5.2 Absorption layer deposition conditions for *SiGe* NIP devices. Deposition rate was adapted in order to obtain the desired thickness. 116
5.3 Fitted R_{shunt} and R_{series} values from previous curves. 122
5.4 Thickness (from TEM) and refractive index for each layer in the modeled device. The refractive index for glass was set to 1.643 on the whole spectral range and absorption was neglected. 127
5.5 Absorber layer deposition conditions for *SiGe60%* NIP devices. Thickness was incremented from 100 to 800 nm. 130
5.6 Fitted R_{shunt} and R_{series} values from the sample's IV curves. 131
5.7 Fitted R_{shunt}, R_{series} and measured dark current at -1 V obtained from the sample's IV characteristic (figure 3.2). The diodes' surface area are in the order of 7 to 9 mm^2. 134

A.1 Medium and corresponding thickness used for each region of the simulated structure. 143

Cette thèse est accessible à l'adresse : https://theses.insa-lyon.fr/publication/2023ISAL0014/these.pdf
© [A. Wilson], [2023], INSA Lyon, tous droits réservés

Bibliography

[1] M. Bigas et al. "Review of CMOS image sensors". In: *Microelectronics Journal* 37.5 (May 1, 2006), pp. 433–451. DOI: 10.1016/j.mejo.2005.07.002.

[2] Michel Ayraud. "Détecteurs quantiques pour l'ultraviolet, le visible et le proche infrarouge". In: *Optique Photonique* (May 2010). DOI: 10.51257/a-v2-e4065.

[3] D. E. Sawyer and R. H. Rediker. "Narrow Base Germanium Photodiodes". In: *Proceedings of the IRE* 46.6 (June 1958), pp. 1122–1130. DOI: 10.1109/JRPROC.1958.286894.

[4] M Jutzi et al. "SiGe PIN photodetector for infrared optical fiber links operating at 1.25 Gbit/s". In: *Applied Surface Science*. Proceedings of the First International SiGe Technology and Device Meeting (ISTDM 2003) - From Materials and Process Technology to Device and Circuit Technology 224.1 (Mar. 15, 2004), pp. 170–174. DOI: 10.1016/j.apsusc.2003.08.038.

[5] Laurent Vivien et al. "42 GHz p.i.n Germanium photodetector integrated in a silicon-on-insulator waveguide". In: *Optics Express* 17.8 (Apr. 13, 2009), pp. 6252–6257. DOI: 10.1364/OE.17.006252.

[6] Matteo Bosi and Giovanni Attolini. "Germanium: Epitaxy and its applications". In: *Progress in Crystal Growth and Characterization of Materials* 56.3 (Sept. 1, 2010), pp. 146–174. DOI: 10.1016/j.pcrysgrow.2010.09.002.

[7] C Rosenblad et al. "Strain relaxation of graded SiGe buffers grown at very high rates". In: *Materials Science and Engineering: B* 71.1 (Feb. 14, 2000), pp. 20–23. DOI: 10.1016/S0921-5107(99)00343-8.

[8] M Bauer et al. "High Ge content photodetectors on thin SiGe buffers". In: *Materials Science and Engineering: B* 89.1 (Feb. 14, 2002), pp. 77–83. DOI: 10.1016/S0921-5107(01)00761-9.

[9] Jurriaan Schmitz, Balaji Rangarajan, and Alexey Yu Kovalgin. "Fabrication and properties of GeSi and SiON layers for above-IC integrated optics". In: *Solid-State Electronics*. Selected papers from the 15th Ultimate Integration on Silicon (ULIS) conference 108 (June 1, 2015), pp. 8–12. DOI: 10.1016/j.sse.2014.12.022.

[10] Jurriaan Schmitz. "Microchip Post-Processing: There is Plenty of Room at the Top". In: *Future Trends in Microelectronics*. John Wiley & Sons, Ltd, 2013, pp. 110–119.

[11] A.J. Walton et al. "Silicon - Post Processing CMOS Wafers to Create Integrated Sensors, Mems and Electro-Optic Systems". In: *SAIEE Africa Research Journal* 101.1 (Mar. 2010), pp. 3–10. DOI: 10.23919/SAIEE.2010.8532213.

[12] Henry Baltes. "CMOS as sensor technology". In: *Sensors and Actuators A: Physical*. Proceedings of Eurosensors VI 37-38 (June 1, 1993), pp. 51–56. DOI: 10.1016/0924-4247(93)80011-5.

[13] J. A. Theil. "Advances in elevated diode technologies for integrated circuits: progress towards monolithic instruments". In: *IEE Proceedings - Circuits, Devices and Systems* 150.4 (Aug. 1, 2003), pp. 235–249. DOI: 10.1049/ip-cds:20030529.

[14] C. Miazza et al. "Performance analysis of a-Si:H detectors deposited on CMOS chips". In: *MRS Online Proceedings Library* 808.1 (Dec. 1, 2003), pp. 269–274. DOI: 10.1557/PROC-808-A4.46.

[15] Jurriaan Schmitz. "Adding functionality to microchips by wafer post-processing". In: *Nuclear Instruments and Methods in Physics Research Section A: Accelerators, Spectrometers, Detectors and Associated Equipment*. Proceedings of the 8th International Workshop on Radiation Imaging Detectors 576.1 (June 11, 2007), pp. 142–149. DOI: 10.1016/j.nima.2007.01.142.

Cette thèse est accessible à l'adresse : https://theses.insa-lyon.fr/publication/2023ISAL0014/these.pdf
© [A. Wilson], [2023], INSA Lyon, tous droits réservés

[16] Gautam Ganguly and Akihisa Matsuda. "Defect formation during growth of hydrogenated amorphous silicon". In: *Physical Review B* 47.7 (Feb. 15, 1993), pp. 3661–3670. DOI: 10.1103/PhysRevB.47.3661.

[17] Shingo Okamoto et al. "Towards large-area, high-efficiency a-Si/a-SiGe tandem solar cells". In: *Solar Energy Materials* (2001), p. 10.

[18] M. Krause et al. "Role of Bandgap Grading for the Performance of Microcrystalline Silicon Germanium Solar Cells". In: *MRS Online Proceedings Library Archive* 557 (1999). DOI: 10.1557/PROC-557-591.

[19] Amaresh Dey and Debajyoti Das. "Narrow band gap high conducting nc-Si1-xGex:H absorber layers for tandem structure nc-Si solar cells". In: *Journal of Alloys and Compounds* 806 (Oct. 25, 2019), pp. 1529–1535. DOI: 10.1016/j.jallcom.2019.07.320.

[20] B. Rech et al. "Microcrystalline silicon for large area thin film solar cells". In: *Thin Solid Films*. Proceedings of Symposium K on Thin Film Materials for Large Area Electronics of the European Materials Research Society (E-MRS) 2002 Spring Conference 427.1 (Mar. 3, 2003), pp. 157–165. DOI: 10.1016/S0040-6090(02)01210-5.

[21] T. Matsui et al. "Microcrystalline silicon–germanium alloys for solar cell application: Growth and material properties". In: *Journal of Non-Crystalline Solids*. Amorphous and Nanocrystalline Semiconductors - Science and Technology 352.9 (June 15, 2006), pp. 1255–1258. DOI: 10.1016/j.jnoncrysol.2005.11.144.

[22] Yu Cao et al. "Non-uniform distribution in μc-Si1−xGex:H and its influence on thin film and device performance". In: *Solar Energy Materials and Solar Cells* 151 (July 1, 2016), pp. 1–6. DOI: 10.1016/j.solmat.2016.02.009.

[23] Takuya Matsui et al. "Influence of alloy composition on carrier transport and solar cell properties of hydrogenated microcrystalline silicon-germanium thin films". In: *Applied Physics Letters* 89.14 (Oct. 2, 2006), p. 142115. DOI: 10.1063/1.2358318.

[24] Takuya Matsui et al. "Microcrystalline Si1-xGex Solar Cells Exhibiting Enhanced Infrared Response with Reduced Absorber Thickness". In: *Applied Physics Express* 1.3 (Mar. 7, 2008), p. 031501. DOI: 10.1143/APEX.1.031501.

[25] Takuya Matsui et al. "Application of microcrystalline Si1−xGex infrared absorbers in triple junction solar cells". In: *2010 35th IEEE Photovoltaic Specialists Conference*. 2010 35th IEEE Photovoltaic Specialists Conference. June 2010, pp. 000311–000316. DOI: 10.1109/PVSC.2010.5615904.

[26] M. Krause et al. "Microcrystalline Germanium Photodetectors". In: *MRS Proceedings* 664 (2001), A26.5.1. DOI: 10.1557/PROC-664-A26.5.1.

[27] M Isomura et al. "Microcrystalline silicon–germanium solar cells for multi-junction structures". In: *Solar Energy Materials and Solar Cells* 74.1 (Oct. 2002), pp. 519–524. DOI: 10.1016/S0927-0248(02)00069-7.

[28] Jean-Luc Raimbault. *Introduction à la Physique des Plasmas*. 2012. 73 pp.

[29] Simon Jeannot. "Développement de matériaux déposés par PECVD pour les interconnexions optiques dans les circuits intégrés par une approche "back-end"." PhD thesis. 2006. 248 pp.

[30] L. Brahimi. *La physique des plasmas*. Physique & Réussite. Jan. 14, 2016. URL: http://physiquereussite.fr/la-physique-des-plasmas/.

[31] *Physique des plasmas*. In: *Wikipédia*. Mar. 24, 2020.

[32] I.H. Hutchinson. *Introduction to plasma physics*. 2001. URL: http://silas.psfc.mit.edu/introplasma/chap1.html.

[33] P. C. Stangeby and G. M. McCracken. "Plasma boundary phenomena in tokamaks". In: *Nuclear Fusion* 30.7 (July 1990), pp. 1225–1379. DOI: 10.1088/0029-5515/30/7/005.

[34] Yasaman Hamedani et al. "Plasma-Enhanced Chemical Vapor Deposition: Where we are and the Outlook for the Future". In: *Chemical Vapor Deposition - Recent Advances and Applications in Optical, Solar Cells and Solid State Devices* (Aug. 31, 2016). DOI: 10.5772/64654.

[35] H. F. Sterling and R. C. G. Swann. "Chemical vapour deposition promoted by r.f. discharge". In: *Solid-State Electronics* 8.8 (Aug. 1, 1965), pp. 653–654. DOI: 10.1016/0038-1101(65)90033-X.

[36] Aurélien Gaufrès. "Élaboration de carbure de silicium amorphe hydrogéné par PECVD : Optimisation des propriétés optiques, structurales et passivantes pour des applications photovoltaïques". thesis. Lyon, INSA, Jan. 14, 2014.

Cette thèse est accessible à l'adresse : https://theses.insa-lyon.fr/publication/2023ISAL0014/these.pdf
© [A. Wilson], [2023], INSA Lyon, tous droits réservés

[37] Jabbar Ganji, Abdolnabi Kosarian, and Hooman Kaabi. "Mathematical Evaluation of a-Si:H Film Formation in rf-PECVD Systems". In: *Silicon* 12.3 (Mar. 1, 2020), pp. 723–734. DOI: 10.1007/s12633-019-00167-9.

[38] Jian Ni et al. "Microcrystalline silicon–germanium solar cells with spectral sensitivities extending into 1300nm". In: *Solar Energy Materials and Solar Cells* 126 (July 2014), pp. 6–10. DOI: 10.1016/j.solmat.2014.03.029.

[39] A. R. Barron. *Chemistry of Electronic Materials*. 2013.

[40] O Vetterl et al. "Intrinsic microcrystalline silicon: A new material for photovoltaics". In: *Solar Energy Materials and Solar Cells* 62.1 (Apr. 15, 2000), pp. 97–108. DOI: 10.1016/S0927-0248(99)00140-3.

[41] A.V Shah et al. "Material and solar cell research in microcrystalline silicon". In: *Solar Energy Materials and Solar Cells* 78.1 (July 2003), pp. 469–491. DOI: 10.1016/S0927-0248(02)00448-8.

[42] A. Matsuda. "Formation kinetics and control of microcrystallite in μc-Si:H from glow discharge plasma". In: *Journal of Non-Crystalline Solids*. Proceedings of the Tenth International Conference on Amorphous and Liquid Semiconductors 59-60 (Dec. 1, 1983), pp. 767–774. DOI: 10.1016/0022-3093(83)90284-3.

[43] Akihisa Matsuda. "Amorphous and Microcrystalline Silicon". In: *Springer Handbook of Electronic and Photonic Materials*. Ed. by Safa Kasap and Peter Capper. Springer Handbooks. Cham: Springer International Publishing, 2017, pp. 573–587. DOI: 10.1007/978-3-319-48933-9_25.

[44] R. I. Badran et al. "A study of optical properties of hydrogenated microcrystalline silicon films prepared by plasma enhanced chemical vapor deposition technique at different conditions of excited power and pressure". In: *Vacuum* 83.7 (Mar. 24, 2009), pp. 1023–1030. DOI: 10.1016/j.vacuum.2009.01.009.

[45] Mario Moreno et al. "Amorphous, Polymorphous, and Microcrystalline Silicon Thin Films Deposited by Plasma at Low Temperatures". In: *Crystalline and Non-crystalline Solids* (June 29, 2016). DOI: 10.5772/63522.

[46] C. C. Tsai et al. "Control of silicon network structure in plasma deposition". In: *Journal of Non-Crystalline Solids*. Proceedings of the Thirteenth International Conference on Amorphous and Liquid Semiconductors 114 (Dec. 1, 1989), pp. 151–153. DOI: 10.1016/0022-3093(89)90096-3.

[47] Kenjiro Nakamura et al. "Roles of Atomic Hydrogen in Chemical Annealing". In: *Japanese Journal of Applied Physics* 34.2 (Feb. 1995), p. 442. DOI: 10.1143/JJAP.34.442.

[48] Branko Ruscic, David Feller, and Kirk A. Peterson. "Active Thermochemical Tables: dissociation energies of several homonuclear first-row diatomics and related thermochemical values". In: *Theoretical Chemistry Accounts* 133.1 (Nov. 22, 2013), p. 1415. DOI: 10.1007/s00214-013-1415-z.

[49] Akihisa Matsuda. "Growth mechanism of microcrystalline silicon obtained from reactive plasmas". In: *Thin Solid Films* 337.1 (Jan. 11, 1999), pp. 1–6. DOI: 10.1016/S0040-6090(98)01165-1.

[50] P Roca i Cabarrocas. "Plasma enhanced chemical vapor deposition of amorphous, polymorphous and microcrystalline silicon films". In: *Journal of Non-Crystalline Solids* 266-269 (May 1, 2000), pp. 31–37. DOI: 10.1016/S0022-3093(99)00714-0.

[51] A. V. Shah et al. "Thin-film silicon solar cell technology". In: *Progress in Photovoltaics: Research and Applications* 12.2 (2004), pp. 113–142. DOI: 10.1002/pip.533.

[52] Félix Urbain et al. "Multijunction Si photocathodes with tunable photovoltages from 2.0 V to 2.8 V for light induced water splitting". In: *Energy & Environmental Science* 9.1 (Jan. 4, 2016), pp. 145–154. DOI: 10.1039/C5EE02393A.

[53] Kah-Yoong Chan et al. "High-mobility microcrystalline silicon thin-film transistors prepared near the transition to amorphous growth". In: *Journal of Applied Physics* 104.5 (Sept. 1, 2008), p. 054506. DOI: 10.1063/1.2973465.

[54] Kyung Hoon Jun, Reinhard Carius, and Helmut Stiebig. "Optical characteristics of intrinsic microcrystalline silicon". In: *Physical Review B* 66.11 (Sept. 3, 2002), p. 115301. DOI: 10.1103/PhysRevB.66.115301.

[55] J. Tauc, R. Grigorovici, and A. Vancu. "Optical Properties and Electronic Structure of Amorphous Germanium". In: *physica status solidi (b)* 15.2 (1966), pp. 627–637. DOI: 10.1002/pssb.19660150224.

[56] S. Vepřek and V. Mareček. "The preparation of thin layers of Ge and Si by chemical hydrogen plasma transport". In: *Solid-State Electronics* 11.7 (July 1, 1968), pp. 683–684. DOI: 10.1016/0038-1101(68)90071-3.

Cette thèse est accessible à l'adresse : https://theses.insa-lyon.fr/publication/2023ISAL0014/these.pdf
© [A. Wilson], [2023], INSA Lyon, tous droits réservés

[57] V. Dutta, P. Nath, and K. L. Chopra. "Structural and electrical properties of polycrystalline Ge films". In: *physica status solidi (a)* 48.1 (1978), pp. 257–262. DOI: 10.1002/pssa.2210480135.

[58] *Band structure and carrier concentration of Germanium (Ge)*. Ioffe Institute. 2020. URL: http://www.ioffe.ru/SVA/NSM/Semicond/Ge/bandstr.html.

[59] F. H. Karg, H. Böhm, and K. Pierz. "Influence of plasma deposition on structural and electronic properties of a-Ge:H". In: *Journal of Non-Crystalline Solids*. Proceedings of the Thirteenth International Conference on Amorphous and Liquid Semiconductors 114 (Dec. 2, 1989), pp. 477–479. DOI: 10.1016/0022-3093(89)90622-4.

[60] W. A. Turner et al. "Structural, optical, and electrical characterization of improved amorphous hydrogenated germanium". In: *Journal of Applied Physics* 67.12 (June 15, 1990), pp. 7430–7438. DOI: 10.1063/1.344533.

[61] Xinyu Wang et al. "The microstructure evolution of hydrogenated microcrystalline germanium promoted by power gradient method". In: *Journal of Crystal Growth* 455 (Dec. 1, 2016), pp. 136–142. DOI: 10.1016/j.jcrysgro.2016.10.011.

[62] Y. Bouizem et al. "Optoelectronic properties of hydrogenated amorphous germanium deposited by rf-PECVD as a function of applied rf-power". In: *Journal of Physics: Condensed Matter* 17.33 (Aug. 2005), pp. 5149–5158. DOI: 10.1088/0953-8984/17/33/017.

[63] C. Godet et al. "Improvement of plasma-deposited a-Ge : H thin films by hydrogen dilution of germane". In: *Solid State Communications* 74.8 (May 1990), pp. 721–725. DOI: 10.1016/0038-1098(90)90923-Y.

[64] Wolfhard Beyer et al. "Microstructure Effects in Amorphous and Microcrystalline Ge:H Films". In: *MRS Online Proceedings Library Archive* 1245 (2010). DOI: 10.1557/PROC-1245-A04-04.

[65] Erik V. Johnson and Pere Roca i Cabarrocas. "High Quality a-Ge:H Films and Devices Through Enhanced Plasma Chemistry". In: *MRS Online Proceedings Library Archive* 989 (2007). DOI: 10.1557/PROC-0989-A04-04.

[66] R. I. Badran, R. Brüggemann, and R. Carius. "Minority-carrier properties of microcrystalline germanium". In: *Journal of optoelectronics and advanced materials*. Journal of Optoelectronics and Advanced Materials 11 (Oct. 2009), p. 1464.

[67] A. M. Antoine, B. Drevillon, and P. Roca i Cabarrocas. "In situ investigation of the growth of rf glow-discharge deposited amorphous germanium and silicon films". In: *Journal of Applied Physics* 61.7 (Apr. 1, 1987), pp. 2501–2508. DOI: 10.1063/1.337924.

[68] B. Drevillon, C. Godet, and A. M. Antoine. "Ion Bombarment Effect on the Growth of Microcrystalline Germanium". In: *MRS Online Proceedings Library Archive* 75 (1986). DOI: 10.1557/PROC-75-341.

[69] B. Drevillon and C. Godet. "In situ investigation of the microcrystalline germanium nucleation and growth processes". In: *Journal of Applied Physics* 64.1 (July 1, 1988), pp. 145–151. DOI: 10.1063/1.341447.

[70] Daniela Polino, Alessandro Barbato, and Carlo Cavallotti. "Theoretical investigation of germane and germylene decomposition kinetics". In: *Physical Chemistry Chemical Physics* 12.35 (Aug. 25, 2010), pp. 10622–10632. DOI: 10.1039/C002221G.

[71] Alan M. Doncaster and Robin Walsh. "Kinetic determination of the bond dissociation energy d(SiH3–H) and its implications for bond strengths in silanes". In: *Journal of the Chemical Society, Chemical Communications* 20 (Jan. 1, 1979), pp. 904–905. DOI: 10.1039/C39790000904.

[72] B. Bouazzata. "Development of a-/nc-Ge:H: Growth and characterization of a low bandgap material". In: (2020).

[73] Y. Okamoto et al. "Formation of microcrystalline germanium (μc-Ge:H) films from inductively coupled plasma CVD". In: *Applied Surface Science*. 12th International Conference on Solid Films and Surfaces 244.1 (May 15, 2005), pp. 12–15. DOI: 10.1016/j.apsusc.2004.10.060.

[74] Chang Li et al. "Nanocrystalline germanium nip solar cells with spectral sensitivities extending into 1450 nm". In: *Journal of Physics D: Applied Physics* 50.4 (Jan. 2017), p. 045108. DOI: 10.1088/1361-6463/aa4f93.

[75] Robert C. Chittick. "Properties of glow-discharge deposited amorphous germanium and silicon". In: *Journal of Non-Crystalline Solids* 3.3 (May 1, 1970), pp. 255–270. DOI: 10.1016/0022-3093(70)90181-X.

[76] F. J. Morin. "Lattice-Scattering Mobility in Germanium". In: *Physical Review* 93.1 (Jan. 1, 1954), pp. 62–63. DOI: 10.1103/PhysRev.93.62.

Cette thèse est accessible à l'adresse : https://theses.insa-lyon.fr/publication/2023ISAL0014/these.pdf
© [A. Wilson], [2023], INSA Lyon, tous droits réservés

[77] R. Brüggemann. "Steady-state photocarrier grating technique for the minority-carrier characterisation of thin-film semiconductors". In: *Journal of Physics: Conference Series* 253 (Nov. 2010), p. 012081. DOI: 10.1088/1742-6596/253/1/012081.

[78] D. Ritter, K. Weiser, and E. Zeldov. "Steady-state photocarrier grating technique for diffusion-length measurement in semiconductors: Theory and experimental results for amorphous silicon and semi-insulating GaAs". In: *Journal of Applied Physics* 62.11 (Dec. 1, 1987), pp. 4563–4570. DOI: 10.1063/1.339051.

[79] C. Longeaud. "An automated steady state photocarrier grating experiment". In: *Review of Scientific Instruments* 84.5 (May 2013), p. 055101. DOI: 10.1063/1.4803006.

[80] R. Cariou et al. "Low temperature epitaxial growth of SiGe absorber for thin film heterojunction solar cells". In: *Solar Energy Materials and Solar Cells* 134 (Mar. 1, 2015), pp. 15–21. DOI: 10.1016/j.solmat.2014.11.018.

[81] Yu Cao et al. "Hydrogenated microcrystalline silicon germanium as bottom sub-cell absorber for triple junction solar cell". In: *Solar Energy Materials and Solar Cells* 114 (July 2013), pp. 161–164. DOI: 10.1016/j.solmat.2013.03.004.

[82] M. Isomura et al. "Microcrystalline silicon-germanium as a low-gap material for solar cells". In: *Conference Record of the Twenty-Eighth IEEE Photovoltaic Specialists Conference - 2000 (Cat. No.00CH37036)*. 28th IEEE Photovoltaic Specialists Conference. Anchorage, AK, USA: IEEE, 2000, pp. 776–779. DOI: 10.1109/PVSC.2000.915998.

[83] K. D. Mackenzie et al. "Structural, electrical, and optical properties of a-SiGe:H and an inferred electronic band structure". In: *Physical Review B* 31.4 (Feb. 15, 1985), pp. 2198–2212. DOI: 10.1103/PhysRevB.31.2198.

[84] Liping Zhang et al. "Growth of μc-SiGe:H thin films diluted with helium and hydrogen by VHF-PECVD". In: *2008 33rd IEEE Photovoltaic Specialists Conference*. 2008 33rd IEEE Photovoltaic Specialists Conference. May 2008, pp. 1–4. DOI: 10.1109/PVSC.2008.4922820.

[85] Abdelkrim Fedala et al. "Low temperature deposition of microcrystalline silicon germanium Si1-x Gex by RF-PECVD". In: *physica status solidi (c)* (Feb. 4, 2010), NA–NA. DOI: 10.1002/pssc.200982791.

[86] Ismael Cosme et al. "Study of Si and Ge Atoms Termination Using H-Dilution in SiGe:H Alloys Deposited by Radio Frequency (13.56 MHz) Plasma Discharge at Low Temperature". In: *Materials* 13.5 (Mar. 2020), p. 1045. DOI: 10.3390/ma13051045.

[87] G. Ganguly et al. "Hydrogenated microcrystalline silicon germanium: A bottom cell material for amorphous silicon-based tandem solar cells". In: *Applied Physics Letters* 69.27 (Dec. 30, 1996), pp. 4224–4226. DOI: 10.1063/1.116993.

[88] R. Carius et al. "Microcrystalline Silicon-Germanium Alloys for Absorption Layers in Thin Film Solar Cells". In: *MRS Online Proceedings Library Archive* 507 (1998). DOI: 10.1557/PROC-507-813.

[89] M. Krause et al. "Near Infrared Detectors and Solar Cells Based on Microcrystalline Silicon Germanium". In: *MRS Online Proceedings Library Archive* 609 (2000). DOI: 10.1557/PROC-609-A13.7.

[90] Shanshan Fan et al. "Microstructural and Optoelectronic Properties of SiGe:H Films at the Transition Edge Fabricated by PECVD". In: *Crystal Research and Technology* 53.9 (Sept. 2018), p. 1700141. DOI: 10.1002/crat.201700141.

[91] Tianwei Li et al. "Effect of Ge atoms on crystal structure and optoelectronic properties of hydrogenated Si–Ge films". In: *Modern Physics Letters B* 31.19 (May 9, 2017), p. 1740010. DOI: 10.1142/S0217984917400103.

[92] M Krause et al. "Structural and optoelectronic properties of microcrystalline silicon germanium". In: *Journal of Non-Crystalline Solids* 299-302 (Apr. 2002), pp. 158–162. DOI: 10.1016/S0022-3093(01)01195-4.

[93] W. Paul et al. "The mott lecture. Structural and electronic properties of amorphous SiGe:H alloys". In: *Journal of Non-Crystalline Solids* 164-166 (PART 1 1993), pp. 1–10. DOI: 10.1016/0022-3093(93)90479-H.

[94] Debajyoti Das and Amaresh Dey. "Optimization in the nanostructural evolution of hydrogenated silicon germanium thin film in RF-PECVD". In: *Physica E: Low-dimensional Systems and Nanostructures* 111 (July 1, 2019), pp. 20–28. DOI: 10.1016/j.physe.2019.02.024.

[95] H. Li et al. "Optimization of n–i–p protocrystalline SiGe:H thin film solar cells for application in thin film multijunction solar cells". In: *Journal of Non-Crystalline Solids*. Amorphous and Nanocrystalline Semiconductors - Science and Technology 352.9 (June 15, 2006), pp. 1941–1944. DOI: 10.1016/j.jnoncrysol.2006.01.059.

Cette thèse est accessible à l'adresse : https://theses.insa-lyon.fr/publication/2023ISAL0014/these.pdf
© [A. Wilson], [2023], INSA Lyon, tous droits réservés

[96] Qi Hua Fan et al. "High rate deposition of a-Si and a-SiGe solar cells near depletion condition". In: *2010 35th IEEE Photovoltaic Specialists Conference*. 2010 35th IEEE Photovoltaic Specialists Conference. June 2010, pp. 001491–001495. DOI: 10.1109/PVSC.2010.5614457.

[97] Amaresh Dey and Debajyoti Das. "Optoelectronic and structural properties of Ge-rich narrow band gap nc-SixGe1-x absorber layer for tandem structure nc-Si solar cells". In: *Journal of Physics and Chemistry of Solids* 154 (July 1, 2021), p. 110055. DOI: 10.1016/j.jpcs.2021.110055.

[98] A. Salabas, G. Gousset, and L. L. Alves. "Two-dimensional fluid modelling of charged particle transport in radio-frequency capacitively coupled discharges". In: *Plasma Sources Science and Technology* 11.4 (Oct. 2002), pp. 448–465. DOI: 10.1088/0963-0252/11/4/312.

[99] Insook Lee, D. B. Graves, and M. A. Lieberman. "Modeling electromagnetic effects in capacitive discharges". In: *Plasma Sources Science and Technology* 17.1 (Feb. 2008), p. 015018. DOI: 10.1088/0963-0252/17/1/015018.

[100] Karen Reinhardt and Werner Kern. *Handbook of Silicon Wafer Cleaning Technology*. William Andrew, Mar. 16, 2018. 794 pp.

[101] Derek J. Gardiner and Pierre R. Graves, eds. *Practical Raman Spectroscopy*. Berlin, Heidelberg: Springer, 1989. DOI: 10.1007/978-3-642-74040-4.

[102] M. H. Brodsky, Manuel Cardona, and J. J. Cuomo. "Infrared and Raman spectra of the silicon-hydrogen bonds in amorphous silicon prepared by glow discharge and sputtering". In: *Physical Review B* 16.8 (Oct. 15, 1977), pp. 3556–3571. DOI: 10.1103/PhysRevB.16.3556.

[103] E. Bustarret, M. A. Hachicha, and M. Brunel. "Experimental determination of the nanocrystalline volume fraction in silicon thin films from Raman spectroscopy". In: *Applied Physics Letters* 52.20 (May 16, 1988), pp. 1675–1677. DOI: 10.1063/1.99054.

[104] Philippe M. Fauchet. "The Raman Line Shape of Semiconductor Nanocrystals". In: *Light Scattering in Semiconductor Structures and Superlattices*. Ed. by David J. Lockwood and Jeff F. Young. NATO ASI Series. Boston, MA: Springer US, 1991, pp. 229–245. DOI: 10.1007/978-1-4899-3695-0_16.

[105] Zhi Li et al. "Raman characterization of the structural evolution in amorphous and partially nanocrystalline hydrogenated silicon thin films prepared by PECVD". In: *Journal of Raman Spectroscopy* 42.3 (2011), pp. 415–421. DOI: https://doi.org/10.1002/jrs.2711.

[106] V. Paillard et al. "Measurement of the in-depth stress profile in hydrogenated microcrystalline silicon thin films using Raman spectrometry". In: *Journal of Applied Physics* 90.7 (Sept. 24, 2001), pp. 3276–3279. DOI: 10.1063/1.1396828.

[107] Ronald W. Schafer. "What Is a Savitzky-Golay Filter? [Lecture Notes]". In: *IEEE Signal Processing Magazine* 28.4 (July 2011), pp. 111–117. DOI: 10.1109/MSP.2011.941097.

[108] Zhang Hao et al. "On Raman scattering cross section ratio of amorphous to nanocrystalline germanium". In: *Solid State Communications* 313 (June 1, 2020), p. 113897. DOI: 10.1016/j.ssc.2020.113897.

[109] Thierry de Vrijer et al. "The impact of processing conditions and post-deposition oxidation on the opto-electrical properties of hydrogenated amorphous and nano-crystalline Germanium films". In: *Journal of Non-Crystalline Solids* 553 (Feb. 1, 2021), p. 120507. DOI: 10.1016/j.jnoncrysol.2020.120507.

[110] L Houben. "Structural properties of microcrystalline silicon-germanium films". In: *Philosophical Magazine Letters* 79.2 (Feb. 1, 1999), pp. 71–78. DOI: 10.1080/095008399177561.

[111] M. I. Alonso and K. Winer. "Raman spectra of c-SiGe alloys". In: *Physical Review B* 39.14 (May 15, 1989), pp. 10056–10062. DOI: 10.1103/PhysRevB.39.10056.

[112] O. Pagès et al. "Re-examination of the SiGe Raman spectra: Percolation/one-dimensional-cluster scheme and ab initio calculations". In: *Physical Review B* 86.4 (July 5, 2012), p. 045201. DOI: 10.1103/PhysRevB.86.045201.

[113] L. Yang, J. Newton, and B. Fieselmann. "Raman Spectroscopy of a.SiGe:H Alloys". In: *MRS Online Proceedings Library (OPL)* 149 (1989). DOI: 10.1557/PROC-149-497.

[114] Stephen J. Pennycook and Peter D. Nellist. *Scanning Transmission Electron Microscopy: Imaging and Analysis*. Springer Science & Business Media, Mar. 24, 2011. 764 pp.

[115] J. A. Hunt and D. B. Williams. "Electron energy-loss spectrum-imaging". In: *Ultramicroscopy* 38.1 (Oct. 1, 1991), pp. 47–73. DOI: 10.1016/0304-3991(91)90108-I.

Cette thèse est accessible à l'adresse : https://theses.insa-lyon.fr/publication/2023ISAL0014/these.pdf
© [A. Wilson], [2023], INSA Lyon, tous droits réservés

[116] L.A. Giannuzzi and F.A. Stevie. "A review of focused ion beam milling techniques for TEM specimen preparation". In: *Micron* 30.3 (June 1999), pp. 197–204. DOI: 10.1016/S0968-4328(99)00005-0.

[117] Lucille A Gianuzzi, Brian K Kempshall, and Shawn D Anderson. "FIB Lift-Out for Defect Analysis". In: (2002).

[118] S Rubanov and P. R Munroe. "The application of FIB milling for specimen preparation from crystalline germanium". In: *Micron* 35.7 (Oct. 1, 2004), pp. 549–556. DOI: 10.1016/j.micron.2004.03.004.

[119] A. Benninghoven, F. G. Rudenauer, and H. W. Werner. *Secondary Ion Mass Spectrometry: Basic Concepts, Instrumental Aspects, Applications and Trends*. 1st edition. New York: Wiley-Interscience, Feb. 4, 1987. 1264 pp.

[120] Amy V. Walker. "Secondary Ion Mass Spectrometry". In: *Encyclopedia of Spectroscopy and Spectrometry (Second Edition)*. Ed. by John C. Lindon. Oxford: Academic Press, Jan. 1, 2010, pp. 2504–2510. DOI: 10.1016/B978-0-12-374413-5.00022-1.

[121] Fred A. Stevie. *Secondary ion mass spectrometry: applications for depth profiling and surface characterization*. 1. published. Materials characterization and analysis collection. New York: Momentum Press, 2016. 262 pp.

[122] H. Fujiwara. *Spectroscopic Ellipsometry: Principles and Applications*. 2007.

[123] Mithil Mazumder et al. "Spectroscopic Ellipsometry of Asphalt Binder: A Study of Optical Constants". In: *International Journal of Civil Engineering* 18.3 (Mar. 1, 2020), pp. 251–259. DOI: 10.1007/s40999-019-00468-5.

[124] G. E. Jellison, M. F. Chisholm, and S. M. Gorbatkin. "Optical functions of chemical vapor deposited thin-film silicon determined by spectroscopic ellipsometry". In: *Applied Physics Letters* 62.25 (June 21, 1993), pp. 3348–3350. DOI: 10.1063/1.109067.

[125] Emna Kadri et al. "Novel method for the determination of the optical conductivity and dielectric constant of SiGe thin films using Kato-Adachi dispersion model". In: *Phase Transitions* 94.2 (Feb. 1, 2021), pp. 65–76. DOI: 10.1080/01411594.2020.1832224.

[126] A. R. Forouhi and I. Bloomer. "Optical dispersion relations for amorphous semiconductors and amorphous dielectrics". In: *Physical Review B* 34.10 (Nov. 15, 1986), pp. 7018–7026. DOI: 10.1103/PhysRevB.34.7018.

[127] Dieter K. Schroder. "Carrier and Doping Density". In: *Semiconductor Material and Device Characterization*. John Wiley & Sons, Ltd, 2005, pp. 61–125. DOI: 10.1002/0471749095.ch2.

[128] S. M. Sze and Kwok Kwok Ng. *Physics of semiconductor devices*. 3rd ed. Hoboken, N.J: Wiley-Interscience, 2007. 815 pp.

[129] P. G. Le Comber, D. I. Jones, and W. E. Spear. "Hall effect and impurity conduction in substitutionally doped amorphous silicon". In: *The Philosophical Magazine: A Journal of Theoretical Experimental and Applied Physics* 35.5 (May 1, 1977), pp. 1173–1187. DOI: 10.1080/14786437708232943.

[130] B. E. Pieters et al. "Determination of the mobility gap of intrinsic μc-Si:H in p-i-n solar cells". In: *Journal of Applied Physics* 105.4 (Feb. 15, 2009), p. 044502. DOI: 10.1063/1.3078044.

[131] Sanjay K. Ram et al. "Microstructure and surface roughness study of highly crystallized μc-Si:H Films". In: *Thin Solid Films*. Proceedings of Symposium I on Thin Films for Large Area Electronics EMRS 2007 Conference 515.19 (July 16, 2007), pp. 7619–7624. DOI: 10.1016/j.tsf.2007.01.034.

[132] E Vallat-Sauvain et al. "Microstructure and surface roughness of microcrystalline silicon prepared by very high frequency-glow discharge using hydrogen dilution". In: *Journal of Non-Crystalline Solids* 266-269 (May 2000), pp. 125–130. DOI: 10.1016/S0022-3093(99)00769-3.

[133] J. Cárabe et al. "Microstructure of thin films prepared by plasma-enhanced chemical vapour deposition of helium-diluted silane". In: *Applied Surface Science* 143.1 (Apr. 1, 1999), pp. 11–15. DOI: 10.1016/S0169-4332(99)00086-0.

[134] Uwe Holzwarth and Neil Gibson. "The Scherrer equation versus the 'Debye-Scherrer equation'". In: *Nature Nanotechnology* 6.9 (Sept. 2011), pp. 534–534. DOI: 10.1038/nnano.2011.145.

[135] D.N. Wright, E.S. Marstein, and A. Holt. "Double layer anti-reflective coatings for silicon solar cells". In: *Conference Record of the Thirty-first IEEE Photovoltaic Specialists Conference, 2005.* Conference Record of the Thirty-first IEEE Photovoltaic Specialists Conference, 2005. Jan. 2005, pp. 1237–1240. DOI: 10.1109/PVSC.2005.1488363.

[136] Pierre Tomasini. "Thermodynamic Theory of Silicon Chemical Vapor Deposition". In: *Chemistry of Materials* 33.6 (Mar. 23, 2021), pp. 2147–2154. DOI: 10.1021/acs.chemmater.0c04901.

Cette thèse est accessible à l'adresse : https://theses.insa-lyon.fr/publication/2023ISAL0014/these.pdf
© [A. Wilson], [2023], INSA Lyon, tous droits réservés

[137] Stephen A. Campbell. *Fabrication Engineering at the Micro and Nanoscale*. OUP USA, Jan. 10, 2008. 672 pp.

[138] Edward D. Palik. *Handbook of Optical Constants of Solids*. Academic Press, 1998. 1019 pp.

[139] NIST. *Three-level full factorial designs*. URL: https://www.itl.nist.gov/div898/handbook/pri/section3/pri339.htm.

[140] Mohsen Asadi Asadabad et al. *Electron Diffraction*. IntechOpen, Feb. 18, 2016. DOI: 10.5772/61781.

[141] G. E. Jellison, T. E. Haynes, and H. H. Burke. "Optical functions of silicon-germanium alloys determined using spectroscopic ellipsometry". In: *Optical Materials* 2.2 (Apr. 1, 1993), pp. 105–117. DOI: 10.1016/0925-3467(93)90035-Y.

[142] V. Chu et al. "Ion implantation of microcrystalline silicon for low process temperature top gate thin film transistors". In: *Thin Solid Films* 337.1 (Jan. 11, 1999), pp. 203–207. DOI: 10.1016/S0040-6090(98)01177-8.

[143] P. G. Le Comber et al. "Electrical and photoconductive properties of ion implanted amorphous silicon". In: *Journal of Non-Crystalline Solids* 35-36 (Jan. 1, 1980), pp. 327–332. DOI: 10.1016/0022-3093(80)90615-8.

[144] Anna Di Nocera, Alberto Mittiga, and Alfredo Rubino. "Electrical properties of heavily doped μc-Si:H". In: *Journal of Applied Physics* 78.6 (Sept. 15, 1995), pp. 3955–3960. DOI: 10.1063/1.359916.

[145] Q. Guo and X. Geng. "Deposition High Quality P-type Microcrystalline Silicon Thin Films by RF-PECVD". In: *2019 6th International Conference on Systems and Informatics (ICSAI)*. 2019 6th International Conference on Systems and Informatics (ICSAI). Nov. 2019, pp. 263–267. DOI: 10.1109/ICSAI48974.2019.9010228.

[146] R. Saleh and N. H. Nickel. "Raman spectroscopy of B-doped microcrystalline silicon films". In: *Thin Solid Films*. Proceedings of Symposium K on Thin Film Materials for Large Area Electronics of the European Materials Research Society (E-MRS) 2002 Spring Conference 427.1 (Mar. 3, 2003), pp. 266–269. DOI: 10.1016/S0040-6090(02)01203-8.

[147] "*p - n* Junctions". In: S.M. Sze and Kwok K. Ng. *Physics of Semiconductor Devices*. Hoboken, NJ, USA: John Wiley & Sons, Inc., Apr. 10, 2006, pp. 77–133. DOI: 10.1002/9780470068328.ch2.

[148] Yuan Taur and Tak H. Ning. *Fundamentals of Modern VLSI Devices*. 2nd ed. Cambridge University Press, 2009.

[149] W.C. Johnson and P.T. Panousis. "The influence of debye length on the C-V measurement of doping profiles". In: *IEEE Transactions on Electron Devices* 18.10 (Oct. 1971), pp. 965–973. DOI: 10.1109/T-ED.1971.17311.

[150] S. Hamma, D. Colliquet, and P. Rocai Cabarrocas. "Microcrystalline Silicon Growth: Deposition Rate Limiting Factors". In: *MRS Online Proceedings Library Archive* 507 (1998). DOI: 10.1557/PROC-507-505.

[151] Wensheng Wei et al. "Raman spectra of intrinsic and doped hydrogenated nanocrystalline silicon films". In: *Vacuum* 81.5 (Jan. 5, 2007), pp. 656–662. DOI: 10.1016/j.vacuum.2006.09.006.

[152] R. W. Collins and J. M. Cavese. "Surface roughness evolution on glow discharge a-Si:H". In: *Journal of Applied Physics* 61.4 (Feb. 15, 1987), pp. 1662–1664. DOI: 10.1063/1.338059.

[153] J. R. Abelson. "Plasma deposition of hydrogenated amorphous silicon: Studies of the growth surface". In: *Applied Physics A* 56.6 (June 1, 1993), pp. 493–512. DOI: 10.1007/BF00331400.

[154] William B. Jordan et al. "Structural Evolution of Nanocrystalline Germanium Thin Films with Film Thickness and Substrate Temperature". In: *MRS Online Proceedings Library* 762.1 (Feb. 1, 2011), p. 65. DOI: 10.1557/PROC-762-A6.5.

[155] K. Saitoh et al. "Role of the hydrogen plasma treatment in layer-by-layer deposition of microcrystalline silicon". In: *Applied Physics Letters* 71.23 (Dec. 8, 1997), pp. 3403–3405. DOI: 10.1063/1.120324.

[156] U. Backhausen et al. "Hall-Effect Studies on Microcrystalline Silicon with Different Structural Composition and Doping". In: *MRS Online Proceedings Library* 452.1 (Dec. 1, 1996), pp. 833–838. DOI: 10.1557/PROC-452-833.

[157] D. P. Stevenson. "The Strengths of Chemical Bonds". In: *Journal of the American Chemical Society* 77.8 (Apr. 1, 1955), pp. 2350–2350. DOI: 10.1021/ja01613a116.

[158] N. H. Nickel, P. Lengsfeld, and I. Sieber. "Raman spectroscopy of heavily doped polycrystalline silicon thin films". In: *Physical Review B* 61.23 (June 15, 2000), pp. 15558–15561. DOI: 10.1103/PhysRevB.61.15558.

Cette thèse est accessible à l'adresse : https://theses.insa-lyon.fr/publication/2023ISAL0014/these.pdf
© [A. Wilson], [2023], INSA Lyon, tous droits réservés

[159] X. L. Jiang, Y. L. He, and H. L. Zhu. "The effect of passivation of boron dopants by hydrogen in nano-crystalline and micro-crystalline silicon films". In: *Journal of Physics: Condensed Matter* 6.3 (Jan. 1994), p. 713. DOI: 10.1088/0953-8984/6/3/011.

[160] Erwann Fourmond et al. "Impact of ammonia pretreatment of the silicon surface prior to the deposition of silicon nitride layer by pecvd". In: *23rd European Photovoltaic Solar Energy Conference and Exhibition*. Valencia, Spain, Sept. 2008, pp. 1629–1632.

[161] Jiaqi Yan, Erwann Fourmond, and Benjamin Fornacciari. *Study on hydrogenated amorphous silicon prepared by PECVD and crystallization process by thermal annealing*. Projet de Fin d'Etude. 2019.

[162] Paul R. Rablen and John F. Hartwig. "Accurate Borane Sequential Bond Dissociation Energies by High-Level ab Initio Computational Methods". In: *Journal of the American Chemical Society* 118.19 (Jan. 1, 1996), pp. 4648–4653. DOI: 10.1021/ja9542451.

[163] B. Ruscic, M. Schwarz, and J. Berkowitz. "Photoionization studies of GeHn (n=2–4)". In: *The Journal of Chemical Physics* 92.3 (Feb. 1990), pp. 1865–1875. DOI: 10.1063/1.458587.

[164] T. I. Kamins. "Hall Mobility in Chemically Deposited Polycrystalline Silicon". In: *Journal of Applied Physics* 42.11 (Oct. 1, 1971), pp. 4357–4365. DOI: 10.1063/1.1659780.

[165] T Weis et al. "Barrier-limited carrier transport in highly n-doped μc-Si:H thin films". In: *Journal of Non-Crystalline Solids*. 19th International Conference on Amorphous and Microcrystalline Semiconductors 299-302 (Apr. 1, 2002), pp. 380–384. DOI: 10.1016/S0022-3093(01)00954-1.

[166] Piet De Moor. "3D integration of imagers". Conference Talk. Conference Talk. Effectenbeurszaal, June 3, 2014.

[167] Ze Yu et al. "Indium tin oxide as a semiconductor material in efficient p-type dye-sensitized solar cells". In: *NPG Asia Materials* 8.9 (Sept. 2016), e305–e305. DOI: 10.1038/am.2016.89.

[168] Zachary C. Holman et al. "Infrared light management in high-efficiency silicon heterojunction and rear-passivated solar cells". In: *Journal of Applied Physics* 113.1 (Jan. 7, 2013), p. 013107. DOI: 10.1063/1.4772975.

[169] D. Rouchon et al. "Germanium content and strain in Si1−xGex alloys characterized by Raman spectroscopy". In: *Journal of Crystal Growth* 392 (Apr. 15, 2014), pp. 66–73. DOI: 10.1016/j.jcrysgro.2014.01.019.

[170] K. V. Maydell et al. "Microcrystalline SiGe Absorber Layers in Thin-film Silicon Solar Cells". In: *Energy Procedia*. Proceedings of E-MRS Spring Meeting 2013 Symposium D Advanced Inorganic Materials and Structures for Photovoltaics 27-31 May 2013, Strasbourg, France 44 (Jan. 1, 2014), pp. 209–215. DOI: 10.1016/j.egypro.2013.12.029.

[171] M Lorenc and J Sik. "Raman Spectroscopy of SixGe1-x Compositional and Temperaturce Dependence". In: (2002), p. 4.

[172] W. J. Brya. "Raman scattering in Ge-Si alloys". In: *Solid State Communications* 12.4 (Feb. 15, 1973), pp. 253–257. DOI: 10.1016/0038-1098(73)90692-3.

[173] Jeffery L. Gray. "The Physics of the Solar Cell". In: *Handbook of Photovoltaic Science and Engineering*. Apr. 25, 2003, pp. 61–112. DOI: 10.1002/0470014008.ch3.

[174] Efstratios Batzelis. "Non-Iterative Methods for the Extraction of the Single-Diode Model Parameters of Photovoltaic Modules: A Review and Comparative Assessment". In: *Energies* 12.3 (Jan. 2019), p. 358. DOI: 10.3390/en12030358.

[175] M. Vaughan. *The Fabry-Perot Interferometer: History, Theory, Practice and Applications*. CRC Press, Jan. 1, 1989. 612 pp.

[176] Jin-Wei Shi et al. "Separated-transport-recombination p-i-n photodiode for high-speed and high-power performance". In: *IEEE Photonics Technology Letters* 17.8 (Aug. 2005), pp. 1722–1724. DOI: 10.1109/LPT.2005.850886.

[177] Dragica Vasileska. "Drift-Diffusion Model: Introduction". In: (2006), p. 9.

[178] M. Stutzmann. "The defect density in amorphous silicon". In: *Philosophical Magazine B* 60.4 (Oct. 1989), pp. 531–546. DOI: 10.1080/13642818908205926.

[179] J. Kolodzey et al. "Optical and electronic properties of SiGeC alloys grown on Si substrates". In: *Journal of Crystal Growth*. Silicon Molecular Beam Epitaxy 1995 157.1 (Dec. 2, 1995), pp. 386–391. DOI: 10.1016/0022-0248(95)00329-0.

Cette thèse est accessible à l'adresse : https://theses.insa-lyon.fr/publication/2023ISAL0014/these.pdf
© [A. Wilson], [2023], INSA Lyon, tous droits réservés

[180] Tom Wilson et al. "Single and multi-junction solar cells utilizing a 1.0 eV SiGeSn junction". In: 12TH INTERNATIONAL CONFERENCE ON CONCENTRATOR PHOTOVOLTAIC SYSTEMS (CPV-12). Freiburg, Germany, 2016, p. 060006. DOI: 10.1063/1.4962096.

[181] Ghada Dushaq, Ammar Nayfeh, and Mahmoud Rasras. "Metal-germanium-metal photodetector grown on silicon using low temperature RF-PECVD". In: *Optics Express* 25.25 (Dec. 11, 2017), pp. 32110–32119. DOI: 10.1364/OE.25.032110.

[182] Christophe Labbé and Benoit Plancoulaine. *Optique matricielle pour l'analyse des systèmes centrés*. Techniques de l'Ingénieur. Apr. 10, 2017. URL: https://www.techniques-ingenieur.fr/base-documentaire/electronique-photonique-th13/optique-instrumentale-42449210/optique-matricielle-pour-l-analyse-des-systemes-centres-e8250/.

Cette thèse est accessible à l'adresse : https://theses.insa-lyon.fr/publication/2023ISAL0014/these.pdf
© [A. Wilson], [2023], INSA Lyon, tous droits réservés

FOLIO ADMINISTRATIF

THESE DE L'INSA LYON, MEMBRE DE L'UNIVERSITE DE LYON

NOM : WILSON DATE de SOUTENANCE : 15/03/2023

Prénoms : Alestair

TITRE : Développement de couches minces de Germanium et Silicium-Germanium microcristallin pour les détecteurs d'image above-IC en proche infrarouge

NATURE : Doctorat Numéro d'ordre : 2023ISAL0014

Ecole doctorale : ED EEA n°160 - Électronique, Électrotechnique et Automatique

Spécialité : Électronique, micro et nano-électronique, optique et laser

RESUME :
Le marché croissant de l'internet des objets (IoT) encourage le développement de nouveaux capteurs fiables et à faible coût. Les imageurs CMOS ne font pas exception. L'industrie automobile et téléphonique en particulier sont friands d'imageurs pour le proche infrarouge pour observer leur environnement. Leur coût peut être réduit en s'appuyant sur une approche above-IC de l'intégration CMOS dans laquelle les photodiodes du capteur sont produites après les transistors et les interconnexions. Les procédés above-IC sont donc intrinsèquement limités en budget thermique en raison de la structure CMOS sous-jacente à la photodiode.
Dans ce contexte, l'objectif de ce travail est de produire et de caractériser des couches minces de silicium-germanium et de germanium hydrogénés déposés à basse température (< 350 °C) pour imageurs above-IC sensibles dans le proche infrarouge. Une preuve de concept de l'utilisation de ces matériaux pour la détection en proche IR est donnée avec le développement et la caractérisation d'une photodiode. Compte tenu des limitations thermiques, le dépôt chimique en phase vapeur assisté par plasma (PECVD) sera utilisé pour développer des semi-conducteurs amorphes et microcristallins allant du silicium (µc-Si:H) aux alliages de silicium-germanium microcristallin (µc-$Si_{1-x}Ge_x$:H). L'incorporation de germanium est bénéfique pour l'absorption du NIR de la couche mince obtenue en raison de son faible gap par rapport au silicium.
Pour atteindre les objectifs fixés, des couches minces intrinsèques de µc-Ge:H et µc-SiGe:H sont obtenus par PECVD pour être utilisées en tant qu'absorbeur dans de futurs dispositifs. L'étude de ses matériaux se focalise sur l'impact des conditions de dépôt sur les propriétés structurelles, électriques et optiques des couches. La fabrication d'une photodiode nécessitant la réalisation d'une jonction P-I-N, le dopage de type p et de type n de couches microcristallines au phosphore et au bore est donc étudié. En s'appuyant sur ces briques individuelles, une photodiode est conçue pour tester expérimentalement l'efficacité des matériaux développés dans un dispositif réel. Ce prototype de photodiode permet de trouver la composition et l'épaisseur optimale pour l'absorbeur et mais permet également comprendre les mécanismes à l'origine des pertes dans les dispositifs.

MOTS-CLÉS : microcristallin, silicium-germanium, above-IC, PECVD, photodiode, NIR

Laboratoire (s) de recherche : Institut des Nanotechnologies de Lyon

Directeur de thèse: FOURMOND Erwann

Président de jury : MASSINES Françoise

Composition du jury : MASSINES Françoise, ROCA I CABARROCAS Pere, ZIMMERMANN Lars, FOURMOND Erwann

Cette thèse est accessible à l'adresse : https://theses.insa-lyon.fr/publication/2023ISAL0014/these.pdf
© [A. Wilson], [2023], INSA Lyon, tous droits réservés